Periodic Starting Flows

Author:
Tomlinson, R. B.

Publication details:
Report No. UNSW Water Research Laboratory Report No. 168
0858242192 (ISBN)

Publication Date:
1986

DOI:
https://doi.org/10.4225/53/57996f622f17c

License:

The quality of this digital copy is an accurate reproduction of the original print copy

THE UNIVERSITY OF NEW SOUTH WALES
water
research
laboratory
Manly Vale N.S.W. Australia

PERIODIC STARTING FLOWS
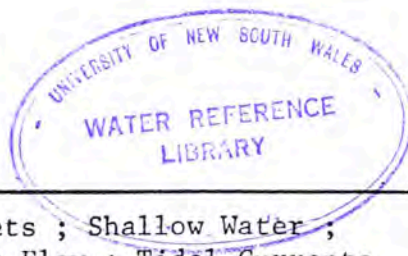
by

R.B. Tomlinson

PERIODIC STARTING FLOWS

by

R.B. Tomlinson

BIBLIOGRAPHIC DATA SHEET	1. REPORT No. 168	2. I.S.B.N. 0/85824/219/2
3. TITLE AND SUBTITLE PERIODIC STARTING FLOWS		**4. REPORT DATE** 1986

5. AUTHOR (S)

R.B. TOMLINSON

6. SPONSORING ORGANISATION

8. ABSTRACT

This report describes research into two-dimensional shallow water periodic starting jet flows and some implications in coastal engineering.

Experiments designed to examine the flow issuing from a rectangular source with sinusoidally varying mass flux were carried out. At the commencement of each cycle a vortex pair was impulsively spun up from the rest and migrated away from the source at the head of a jet-like 'tail'. A characteristic length scale has been determined which describes the gross features of the motion.

A semi-empirical theoretical model is used to describe the growth and motion of the vortex pair cap and the results of numerical simulations are presented. The unsteady jet tail is described using an integral formulation. The cap and jet are initially coupled and behave like a starting jet. A decoupling criterion is defined after which the cap is described as a turbulent vortex pair. The cap motion was found to be unaffected by the flow reversal at the source.

The experiments were carried out for various boundary conditions including linearly varying depth and uniform cross flow. The application of the model to ebb tidal jet flows at coastal inlets is discussed.

9. DISTRIBUTION STATEMENT

For general distribution.

10. DESCRIPTORS Unsteady Flow ; Vortices ; Jets ; Shallow Water ; Experimental Data ; Turbulent Flow ; Tidal Currents

11. IDENTIFIERS

12. CLASSIFICATION Unrestricted	**13. NUMBER OF PAGES** 351	**14. PRICE** $60

ABSTRACT

The behaviour of a two-dimensional shallow water periodic starting jet has been examined. The source mass flux varies sinusoidally. At the commencement of each cycle a vortex pair is impulsively spun up from rest. The vortices migrate away from their source at the head of a jet-like "tail" which is advecting mass and momentum into the vortex pair "cap". The flow was found to maintain symmetry about the jet axis in approximately 70 percent of the experiments.

The investigation has demonstrated that the gross features of the flow can be described in terms of a characteristic length scale which is a function of the fluid density, the peak source momentum flux per unit depth and the flow cycle period.

A semi-empirical theoretical model is developed to describe the growth and motion of the cap which was the dominant feature of the flow. The model allows for mass and momentum contributions to the cap from the unsteady jet. The unsteady jet is modelled independently using an intergral formulation which assumes the jet structure to be self preserving. The cap and jet are initially coupled and behave like a starting jet. They become decoupled when the mean axial velocity at the base of the cap falls below the cap translational velocity. Subsequently the cap can be described as a turbulent vortex pair which is entraining ambient fluid, and is subject to the applied force of bottom frictional resistance.

Laboratory experiments are described which examine the behaviour of the jet for various boundary conditions, including linearly varying depth and a uniform cross-flow. The gross features of the flow were

recorded photographically using dye and surface particles as tracers.

The effect of a cross-flow is to cause a dispersal of the vorticity in the upstream vortex, with the downstream vortex moving away from the source under the influence of the cross-flow and the self-induced motion of the image vortex across the boundary.

The relevence of the vortex pair model to similar naturally occuring flows is discussed. In particular, it is considered that ebb tidal jets at coastal inlets behave in a like manner.

ACKNOWLEDGEMENTS

TABLE OF CONTENTS

LIST OF SYMBOLS

All symbols are defined within the text. Definitions of symbols and subscripts which are not listed will be found in the text, immediately following the use of the symbol or subscript concerned.

A = Planform area of flow

A_c = Inlet channel cross-sectional area

A_J = Jet cross-sectional area variable = HB_J

A_1 = Constant

a = Instability amplification rate

a' = Dimensionless amplification rate

B = Dimensionless vortex pair separation

B_J = Dimensionless jet width

B_N = Nominal dimensionless jet width

B_S = Lagrangian specification of dimensionless nominal jet width near the shock location

$\overline{B}$ = Renormalised vortex pair separation variable

b = Flow width variable

b_c = Vortex pair separation

b_{cc} = Cross-flow channel width

b_o = Inlet channel width

C_1 = Constant dependent on the vorticity distribution

C_2 = Shape constant relating the apparent and real centres of rotation

C_3 = Shape constant related to the vorticity distribution

C_4 = Shape constant related to the vorticity distribution

C_5 = Constant $= \dfrac{\pi C_3}{32\ C_1\ C_2^{\,2}}$

c = Constant

E = Jet entrainment coefficient

E_1 = Jet entrainment parameter $= 2E\,\dfrac{\ell}{b_o}$

E_K = Ekman Number

$E_K{}^*$ = Characteristic Ekman Number

e' = Entrainment coefficient of the vortex pair cap

e = Entrainment parameter $= e'\ c_4/c_3$

F = Linearised friction factor $= \dfrac{f}{8}u_v$

F_1 = Velocity profile integration constant

F_2 = Velocity profile integration constant

$F(y)$ = Lateral jet velocity similarity function

f = Darcy-Weisbach friction coefficient

f_c = Cap friction parameter $= \dfrac{f\,\ell}{8h_o}\,\dfrac{\pi C_3}{4C_1 C_2^{\,2}}$

f_1 = Jet friction parameter $= \dfrac{f\,\ell\,F_2}{8h_o F_1}$

$f*$ = Friction coefficient

g = Gravitational acceleration

H = Dimensionless depth = $1 + \varepsilon \frac{\ell}{h_o} X$

$h(x,y)$ = Flow depth

h_o = Inlet channel depth

I = Hydrodynamic impulse

I_F = Impulse applied to the flow by bottom frictional resistance

K = Vortex Strength

K_1 = Spreading rate coefficient = $\frac{2E}{F_1}$

$K*$ = Characteristic circulation = $\frac{b \ell_o}{T}$

k = Sink strength

k_s = Equivalent grain roughness

L' = Radial length scale

ℓ = Characteristic length scale = $[\frac{1}{\rho} m_o T^2]^{1/3}$

M = Total fluid momentum

M_{JTE} = Dimensiomless jet momentum flux at trailing edge of cap

m = Momentum flux per unit depth

m_o = Maximum momentum flux per unit depth

n = Constant

P $\quad$ = $\quad$ Pressure

P_T $\quad$ = $\quad$ Tidal prism

P_o $\quad$ = $\quad$ Atmospheric pressure

p $\quad$ = $\quad$ Interger constant

Q $\quad$ = $\quad$ Volumetric flow rate

Q_{in} $\quad$ = $\quad$ Constant model supply flow rate

Q_o $\quad$ = $\quad$ Peak model flow rate

Q_{out} $\quad$ = $\quad$ Maximum model outflow rate

Q_{JTE} $\quad$ = $\quad$ Dimensionless jet mass flux at the trailing edge of the vortex pair cap

q $\quad$ = $\quad$ Flow rate per unit depth

q_o $\quad$ = $\quad$ Maximum flow rate per unit depth

R $\quad$ = $\quad$ Vortex core radius

Re* $\quad$ = $\quad$ Characteristic Reynolds Number = $\dfrac{b_o \ell}{\nu T}$

S $\quad$ = $\quad$ Applied stress

S_b $\quad$ = $\quad$ Bottom friction stress

s $\quad$ = $\quad$ Radial distance from the inlet entrance

T $\quad$ = $\quad$ Cycle period

t $\quad$ = $\quad$ Time after commencement of an ebb discharge

U $\quad$ = $\quad$ Dimensionless velocity of vortex pair propagation

U_J = Dimensionless jet axial velocity

U_{JTE} = Dimensionless mean axial velocity of the jet at the trailing edge of the vortex pair cap

U_{LE} = Dimensionless velocity of the leading edge of the vortex pair cap

U_N = Nominal dimensionless jet axial velocity

U_S = Lagrangian specification of dimensionless jet axial velocity near the shock location

U_{TE} = Dimensionles velocity of the trailing edge of the vortex pair cap

$\bar{U}$ = Renormalised cap velocity variable.

$U*$ = Characteristic Velocity = Γ/T

u'' = u_v/u_p

u = A velocity in the x direction

u_c = Jet centreline velocity

u_p = Self-induced velocity of ideal vortex pair

u_v = Self-induced velocity of a real vortex pair

$u(t)$ = Tidal current velocity

u' = Fluctuating component of the velocity in the x direction

$\bar{u}$ = Mean component of velocity in the x direction

V = Velocity along a streamline = $(u^2 + v^2)^{1/2}$

V_c = Dimensionless cross-flow velocity

v = A velocity in the y direction

v_c = Cross-flow velocity

v_i = Velocity due to image vortex across the model boundary

v_T = Downstream translation velocity of a periodic jet subject to a cross-flow

v_e = Lateral entrainment velocity = Eu_c

w = A velocity in the z direction

X = Dimensionless x co-ordinate = x/ℓ

X_c = Dimensionless location of the centreline of the vortex pair

X_S = Dimensionless location of the jet shock

X_{TE} = Dimensionless location of the trailing edge of the vortex pair cap

$\overline{X}$ = Re-normalised dimensionless x co-ordinate

x = Cartesian co-ordinate

y = Cartesian co-ordinate

y_c = Distance to the centroid of a region with uniformly distributed vorticity (one half of the real vortex pair separation)

z = Cartesian co-ordinate

Z = Complex physical co-ordinate = $x+iy$
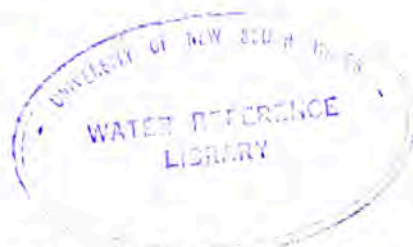
α $\quad$ = Vortex pair cap shape factor = $2\dfrac{(x_{LE}-x_C)}{b_{CAP}}$

α_1 $\quad$ = Slope parameter = $\varepsilon\,\dfrac{\ell}{h_o}$

β $\quad$ = Vorticity amalgamation efficiency factor, Eqation (1.2)

γ $\quad$ = Constant

γ_{LE} $\quad$ = Constant = U/U_{LE}

γ_{TE} $\quad$ = Constant = U/U_{TE}

ΔX $\quad$ = Computational spatial step

$\Delta\tau$ $\quad$ = Computational time step

δ $\quad$ = Boundary layer thickness

δ' $\quad$ = Ekman layer thickness

ε $\quad$ = Bed slope

$\eta(x,y,t)$= Free surface elevation

ν $\quad$ = Fluid kinematic viscosity

ζ $\quad$ = Similarity variable = $\dfrac{y}{b/2}$

ρ $\quad$ = Fluid density

τ $\quad$ = Dimensionless time = t/T

Φ $\quad$ = Complex velocity potential

ϕ $\quad$ = Velocity potential

ψ $\quad$ = Stream function

Ω =   Angular velocity

ω =   Vorticity

ω_c =   Vorticity associated with a non-uniform cross-flow velocity distribution

ω_o =   Absolute vorticity in a region of uniformly distributed vorticity

LIST OF FIGURES

APPENDICES

LIST OF TABLES

1. INTRODUCTION

This work deals with some aspects of the flow induced and main-
tained by a shallow water momentum jet which has a source momentum flux
varying periodically with time. Flows of this type can be referred to
as periodic starting jets. This work is based on observations made by
Wilkinson (1978) in a study of the nearshore hydrodynamics of tidal
inlets.

The hydraulic behaviour of tidal inlets has been extensively exam-
ined by engineers concerned with problems of navigation, sediment move-
ment and coastal structures. The fate of water discharged into the
ocean at an inlet is of particular importance when considered in terms
of the possible pollutant load carried by it. The need to understand
and predict the behaviour of the flow produced in the offshore region
by tidal currents at the inlet has been acknowledged for some time, and
a number of models have been developed to describe the flow structure.
Wilkinson (1978) examined the gross features of the offshore flow
structure in an idealized two-dimensional physical model in which a
sinusoidally reversing flow was discharged from an open channel into a
large stagnant basin. During each period of ebb flow, the discharge
from the simulated inlet developed a structure very similar to that of
a starting jet. A vortex pair was observed to form and ultimately
become the dominant feature of the flow. This vortex pair migrated
away from the entrance despite the influence of the flow reversal on
the flood tide. The flow into the channel during the flood was similar
to a sink flow.

Starting flows have been extensively investigated to provide models for many different natural phenomena. A starting flow occurs with the release of fluid distinguished from the surrounding fluid by its buoyancy or momentum. This release may be instantaneous, resulting in the formation of a vortex ring or pair; maintained, resulting in a starting plume, starting jet, density current or gravity current; or, as is the case for the periodic jet, a gradual time dependent release.

1.1 Literature Review

Previous analyses of the behaviour of jets and plumes have mainly dealt with the final steady state conditions. The initial start-up conditions are generally considered to be short lived and not significant. In some cases, however, the structure that develops at the front of the plume as a result of its impulsive generation may be the dominant feature of the flow. Early studies of atmospheric convection, and in particular thermals, considered the convective processes to be either plume-like with a steady source of heat and moisture, or, instantaneous releases from rest. The first of these approaches ignores the possible mixing that occurs at the top of a thermal and the latter does not account for the advection of mass, momentum and buoyancy from beneath. Turner (1962) predicted that a matching of these two approaches was possible. A similarity solution was found for the cap moving at a constant fraction of the plume velocity. He verified this experimentally and developed a theoretical model representing the frontal cap of a convecting mass as a vortex ring.

Tsang and Wood (1968) have extended this type of analysis to a two-dimensional starting plume consisting of a cap which has a velocity distribution similar to a cylindrical line thermal, and a steady plume

behind it. The theoretical model proposed was based on studies in unsteady self preserving turbulent flows carried out by Wood (1965$_2$). Wood considered the impulse of a starting plume where the vorticity is assumed to be confined to the mixing region and the ambient flow is assumed to be irrotational. By approximating the motion of the cap to that of a solid cylinder an expression for the momentum was obtained. Similarity relationships were developed for the velocity of advance of the cap and its lateral spread. Conservation of momentum for the case of a constant inflow of buoyancy led to a relationship between the rate of advance of the plume, the rate of lateral spread and the rate of inflow of buoyancy. This method does not consider the effect of fluid entrained into the cap. Tsang and Wood (1968) have considered the ambient fluid motion around the cap and have modified it to include the effect of entrainment into the steady tail. Their model also included the effect of experimentally generating the flow from a slot in a solid plane boundary. The motion may then be approximated by an inviscid potential flow model which consists of a line sink along the axis of the tail and the combination of a doublet and a radial source at the centre of the plume cap.

Middleton (1975) has also extended Turner's work on axisymmetric flows. Turner described the motion of the thermal as like that in a spherical vortex. Middleton considered the thermal to be a vortex ring of more general type and found that for a similarity solution to exist there must be diffuse distributions of vorticity and buoyancy, implying a decrease in the total circulation due to the loss of vorticity by diffusion across the axis of symmetry. The total rate of change of circulation was dependent on the balance between this loss, the buoyant generation of vorticity and the ring-wise circulation of the plume advected into the vortex ring. Bulk equations representing this time

rate of increase in circulation, the time rate of increase of ring momentum and buoyancy, and equations (dependent on gross features of the ring structure) representing the velocity of propagation, were used to determine the motion of the vortex ring. The steady plume equations were expressed in Lagrangian terms to enable solutions which give mass, momentum and buoyancy fluxes as functions of both the source conditions and the elapsed time interval since the plume fluid element left the source. Delichatsios (1979) has considered the case of a source where the buoyancy flux varies as a power function of time. Plumes of this type originate from growing fires. The results are consistent with those of Middleton and Turner with the velocity of the leading edge of the plume being less than the velocity inside the plume.

The starting plume model has been applied to flows on horizontal and inclined boundaries. These density or gravity currents are represented in nature by powder snow avalanches, leaks from gas reservoirs, turbidity currents off the continental slope and atmospheric fronts. Recent work by Beghin, Hopfinger and Britter (1981) has shown that two-dimensional starting plume theory is a good description of flow down inclined boundaries.

The starting flows described above have been of the maintained source type. These consist of a frontal cap being supplied with mass, momentum and buoyancy by the steady flow behind. The front has been considered similar in structure and behaviour to starting flows generated from an instantaneous source. Flows of this latter type have been used to describe the motion of isolated masses of buoyant fluid or thermals in atmospheric convection studies. Early experimental work by Scorer (1958), Woodward (1959) and Richards (1963) established the relationships that for mixing thermals the size of the thermal was

proportional to its elevation. Turner (1960) has analysed the behaviour of buoyant vortex rings, assuming the circulation remains constant and the buoyancy acts to increase the momentum of the ring. Turner's model was based on the observations of the first two of the above researchers and his own observations regarding the entrainment of fluid into the rear of the thermal. A self preservation assumption was made. This axisymmetric model was used to describe the flow into and around the thermal, assuming that the flow was instantaneously the same as for a Hill's spherical vortex (Turner,$1964_{1,2}$). The analysis was extended to cover the two-dimensional case of a buoyant vortex pair. Using the description of the motion of a vortex pair by Lamb (1952), and assuming constant circulation, the spread of the thermal was shown to be linear with time.

Richards (1963) argued that circulation cannot be constant and put forward a modified version of Turner's vortex pair model which allowed a decrease in circulation and velocity of propagation with time. This was consistent with the linear growth of cylindrical thermals observed in experiments. Richards (1965) extended his work to the general case of puff motions, and showed that non-buoyant puffs behaved in a similar way. He proposed that the turbulence inside thermals was primarily maintained through their mean motion rather than directly by gravitational instability.

The vortex pair models of Turner and Richards were applied to the observed behaviour of bent-over smoke plumes. These are known to bifurcate, and it was proposed that a vortex pair model can be used for the flow structure in a plane normal to the axis of the plume. The work of Richards (1963), Csanady (1965) and Tsang (1970_2) describes the flow pattern around a buoyant vortex pair (or line thermal). The

motion of the pair was approximated by the impulse momentum equation expressed in the form of a vorticity transport equation for non-viscous fluids (Wood, 1965_2). More recently Jirka and Fong (1981) have provided a comprehensive model linking the gross behaviour of the buoyant plume in a crossflow to the circulating motion in its cross-section, as described by a two-dimensional vortex pair theory. Plume equations were developed similar to those usually applied to bent-over plumes, but include a repulsive force and lateral spread influence due to the vortex pair in the presence of a boundary.

All axisymmetric and two-dimensional thermal models rely on vortex ring or vortex pair formulations with the effects of buoyancy, steady jet "tails" and entrainment, modifying the gross development of the flow, but not substantially affecting the internal structure and characteristic of the vortices. These basic characteristics are described in Lamb (1952) and Batchelor (1967) ,for example. The classical descriptions are at odds, however, with the observed behaviour of real vortex rings, namely, that in reality they slow down and increase in size with time. Maxworthy (1972, 1974 and 1977) has reported on extensive and precise experimental work on the behaviour of laminar and turbulent vortex rings.

From observations of stable laminar rings, Maxworthy (1972) showed that the vorticity is distributed throughout the body of fluid which moves with the ring. This moving body of fluid is continuously entraining new fluid from outside and growing in volume, at the same time depositing some of its own vorticity into a wake. A viscous entrainment model was developed in which the impulse of the moving fluid body remains constant. The ring remained stable for a Reynolds number 600. Maxworthy (1974) extended his study to the development

after the initial stable phase. He showed that the overall growth of a ring was controlled by the entrainment of fluid at the interface between the core and the fluid in the surrounding bubble of co-travelling fluid. The turbulent structure of the core was suppressed by viscous stresses reducing the entrainment at this interface, and resulting in a small growth rate for the ring. Within the bubble the turbulence scale was large and the vorticity low. Mixing occured at the outer edge. Maxworthy showed that most of this entrained fluid was rejected into a wake. The exchange between the core fluid and the turbulent bubble fluid accounted for the loss of the ring impulse which appeared as a momentum deficit in the wake. This drag force was included in the proposed theoretical model. It was assumed that there was a linear ring growth with distance and that the turbulent core and its co-travelling bubble were geometrically similar at all times.

The descriptions of the dynamics of vortex rings can be adapted to analyse vortex pair behaviour as was shown for the case of line thermals. The classical potential theory definition of a vortex pair is that of two line vortices of equal but opposite strength travelling with constant velocity and separation due to their mutual interaction, (Lamb, 1952). Extension of this theory by Turner (1960) and Saffman (1972) ,for example, has included the effect of buoyancy and motion in a stratified environment. The examination of the generation of a vortex pair near a solid boundary must include the influence of the image vortices across the boundary. A pair approaching a solid boundary at right angles will separate, and each vortex will travel in opposite directions parallel to the boundary. Investigations to date have mainly dealt with the behaviour of aircraft wake vortices which have the structure of a vortex pair in a plane normal to the axis of the wake. Departures from the behaviour predicted by the potential theory have

been observed both in reality and in experiments. Barker and Crow (1977) have analysed the influence on the vortex trajectories of a finite core size and variation in the vorticity distribution. Due to the presence of image vortices, the geometry of the orifice or inlet from which the vortex pair is generated has been shown to influence the behaviour of the pair. Sheffield (1977) has established criteria to determine whether or not the vortices will move away from the inlet.

The extension of the analysis of a starting flow to the case where there is a periodically varying time dependence at the source has not yet been undertaken. The description given by Wilkinson (1978) for the early stage of flow development, indicates a general flow pattern likeness to a line thermal or a two-dimensional starting jet. A transition then occurs to a structure similar to a vortex pair which is apparently unaffected by the flow reversal. The analysis of the jet-like tail of such an unsteady starting flow is crucial to the understanding of the behaviour of the vortex pair cap. Delichatsios (1979) has developed a time similarity solution for a round plume with a source buoyancy flux variation which is a power function of time. Killworth and Turner (1982) have used quasi-steady approximations to describe the changes in ambient conditions of a plume with a sinusoidal variation in buoyancy flux discharging into a confined area. Kent (1973) has analysed the integral jet equations for a round jet with source conditions varying continuously from an initial steady state to a final steady state. The main area of interest in jets with varying source conditions has been with high frequency pulsations. These studies (for example - Lai and Simmons, 1980 and Ikeda, 1977) have dealt with either jet noise production due to the formation of coherent vortices in the mixing layer, or with entrainment enhancement.

The descriptions in the literature of real jet flows treated as periodic starting flows are very limited (Onishi and Nishimura 1980_1), and provide only coarse detail of the flow development. The few experimental studies reported have either been related to general engineering considerations (Onishi and Nishimura 1980_2), of a cursory nature (Özsoy 1977), or of a highly specific nature related to plumes with a time varying source of buoyancy in a confined region (Killworth and Turner 1982). The literature does however contain a number of qualitative descriptions of flows induced by periodic (in particular, tidal) action. These mainly deal with the ebb flow at an inlet or estuary and the flow through straits. In the first instance, the models that have been developed have been quasi-steady, assuming that the ebb flow takes the form of a turbulent momentum jet. French (1960) presented a Tollmein type jet solution, which neglects a number of ebb flow features. The influence of bottom friction has been accounted for in models such as Taylor and Dean (1974), Özsoy (1977) and Mehta and Zeh (1980). Gadgil (1971) and Savage and Sobey (1975) analysed the effect of Ekman friction on laminar jets in rotating basins. Variations in bottom topography have been included in the analysis of Özsoy (1977), Beardsley and Hart (1978), Mehta and Zeh (1980) and Joshi (1982) as well as in a number of studies of surface discharge of buoyant plumes such as Stolzenbach and Harlemann (1971).

A realistic model of a tidal flow near an inlet would include currents induced by wave action and local wind conditions. Coriolis force may also influence the jet trajectory. Savage and Sobey (1975) have shown that shallow water jets will not be deflected by coriolis force but in cases where there is a steep bottom slope, separation will occur and deflection may result.

The movement of sediment in a tidal inlet system is complex. As the ebb flow has a turbulent jet structure there will be entrainment bringing sediment towards the entrance in the littoral zone. Also, during the flood tide the movement will be towards the entrance. The relationships between tidal induced movement and that due to wave action and longshore currents have been investigated by Dean and Walton (1974), Oertel (1974) and Sonu and Wright (1975). Similar features to those shown by tidal inlet ebb flows are also evident for flows influenced by buoyancy effects such as those at estuary mouths. Takano (1954,1955), Waldrop and Farmer (1974), Wright and Coleman (1974), and Garvine (1977) provide an analysis and description of river effluent plumes.

The above descriptions of inlet or estuary flows have all considered the ebb flow to be a quasi-steady turbulent jet or plume. The most comprehensive of these studies has been that of Özsoy (1977) who has accounted for bottom friction, bottom topography variability, cross-current deflection and mass transport at the inlet. The treatment of the ebb flow at an inlet as an unsteady jet flow has only been hinted at by previous investigators. The existence of the starting jet and vortex pair structure as described by Wilkinson (1978), has been referred to by Ünlüata and Özsoy (1977), Per Bruun (1978), Mehta and Zeh (1980) and Özsoy and Ünlüata (1982). These descriptions are based on that given in Özsoy's original work. He describes the development of the unsteady jet as follows.

At the beginning of the ebb cycle the water issuing into the ocean approximates a radial source flow. With flow acceleration, separation occurs with vortices forming either side of the discharge. During the later stages of the ebb a turbulent jet will develop with an

impulsively generated vortex pair forming the frontal structure of the jet. Ambient water will be entrained into the jet and the frontal cap, enlarging the structure as it migrates seaward. Özsoy conducted a simple experiment whereby a steady jet was impulsively started and the behaviour described above was observed. A simple approximate calculation of the front velocity was made assuming steady flow for the main part of the jet. A momentum balance for the jet and the frontal cap was obtained.

Observations of such large scale vortex pair-like structures at a tidal inlet are difficult except during the initial spin up phase. This is because of the environmental factors which act to destroy the vortex structure. Wave activity, longshore currents, shoals and irregular bottom topography act against the development of a coherent vortex pair formation. Özsoy (1977) presents aerial photographs of such structures. The ebb discharge was made visible because of the turbidity of the ebb discharge.

Evidence of distinct vortex-like structures exists for flow through straits. Onishi and Nishimura (1980_1) have reported on the phenomena of vortex pair generation and migration at the straits in the Seto Inland Sea of Japan. The existence of the large scale vortices was established with satellite remote sensing and aircraft thermal sensing. The satellite (LANDSAT) scanners also detected turbidity variations in the discharge. The investigations established the presence of coherent vortices being developed in the free shear layer and the amalgamation of these small scale vortices into large scale vortex pairs. The hydrodynamic character of both of these vortex structures was examined and modelled. No mathematical analysis was made of the phenomena. The movement of the vortex pair structure was measured from

the remotely sensed data and compared with the theoretically described self-induced motion by Lamb (1952).

$$u_v = \frac{K}{2 \pi b_c} \tag{1.1}$$

where K = strength of each vortex

$$= \frac{\beta}{2} \int_0^{\frac{T}{2}} u^2(t) \, dt \tag{1.2}$$

b_c = vortex separation

β = amalgamation efficiency factor

u(t) = tidal current velocity

T = tidal period

This investigation was made to examine the tidal flushing characteristics of the straits linking the Seto Inland Sea with the Pacific Ocean and the Japan Sea. This is a highly industrial area and effective disposal of pollutants is highly desirable. From measurements taken, about 10% of the vorticity generated at the Naruto Strait was amalgamated into the large vortex pair. A pair with sufficient strength escaped the influence of the shoreline, and the discharged water trapped in the vortices was transported away from the strait providing an efficient exchange mechanism between the ocean waters and the polluted waters of the Seto Inland Sea.

Onishi and Nishimura (1980$_2$) qualitatively examined the vortex pair generation for Naruto, Tomogashima and Akashi Straits. A small scale physical model was constructed and their experiments confirmed the influence of the formation of the vortex pair on the tidal exchange. They proposed that if the shoreline configuration was such that the pair could not form then the image vortices would trap the ebb

discharge near the strait and tidal exchange would be limited.

1.2 Objectives Of This Study

This thesis deals with an experimental study undertaken to provide a better understanding of the behaviour of periodic starting jets. It is proposed to first give a description of the behaviour of a typical periodic jet as observed during an experiment. This will be in general terms and will include an analysis of the parameters that define the flow. From this background, a theoretical model of the type used in previous starting flow investigations will be developed for the gross behaviour of the flow. A detailed description of the experimental work will then be given and the results compared with those predicted theoretically. Finally, the application of this starting jet model to real tidal flows will be discussed.

2. <u>DESCRIPTION OF THE FLOW</u>

In this chapter a detailed description of the development of the flow during the course of one experiment will be given. The bulk of the present work deals with an idealized theoretical model for a periodic starting flow. However, during the early stages of this study the emphasis was on relating this type of flow to the nearshore hydro-dynamics at a tidal inlet. Thus the terminology used in this thesis is taken from descriptions of the tidal flow emerging from an idealised tidal inlet. The discharge during the half period from flow commence-ment to flow reversal will be called the ebb flow. The half period of flow reversal will be referred to as the flood flow. The finite sized source from which the flow issues will be called the inlet. Other real flow descriptions will be explained as they occur in the text.

The flow description given in this chapter is for the ideal case where the flow remains symmetrical about the jet axis. Ideal flow did not always occur in the experimental program. Flow instabilities resulted in a distortion of the ideal vortex pair development in 28% of the experiments. Asymmetrical flows will be discussed in Chapter 7 and the likelihood of achieving symmetrical flow behaviour in a prototype situation will be discussed in Chapter 10.

The flow under investigation is shown schematically in Figure 2.1. The sinusoidally varying discharge issues from the inlet which is modelled as a rectangular open channel. The fluid in the large shallow basin is initially at rest. The flow per unit depth at the inlet, q , varies with time, t , according to the relationship:

a) Ebb phase
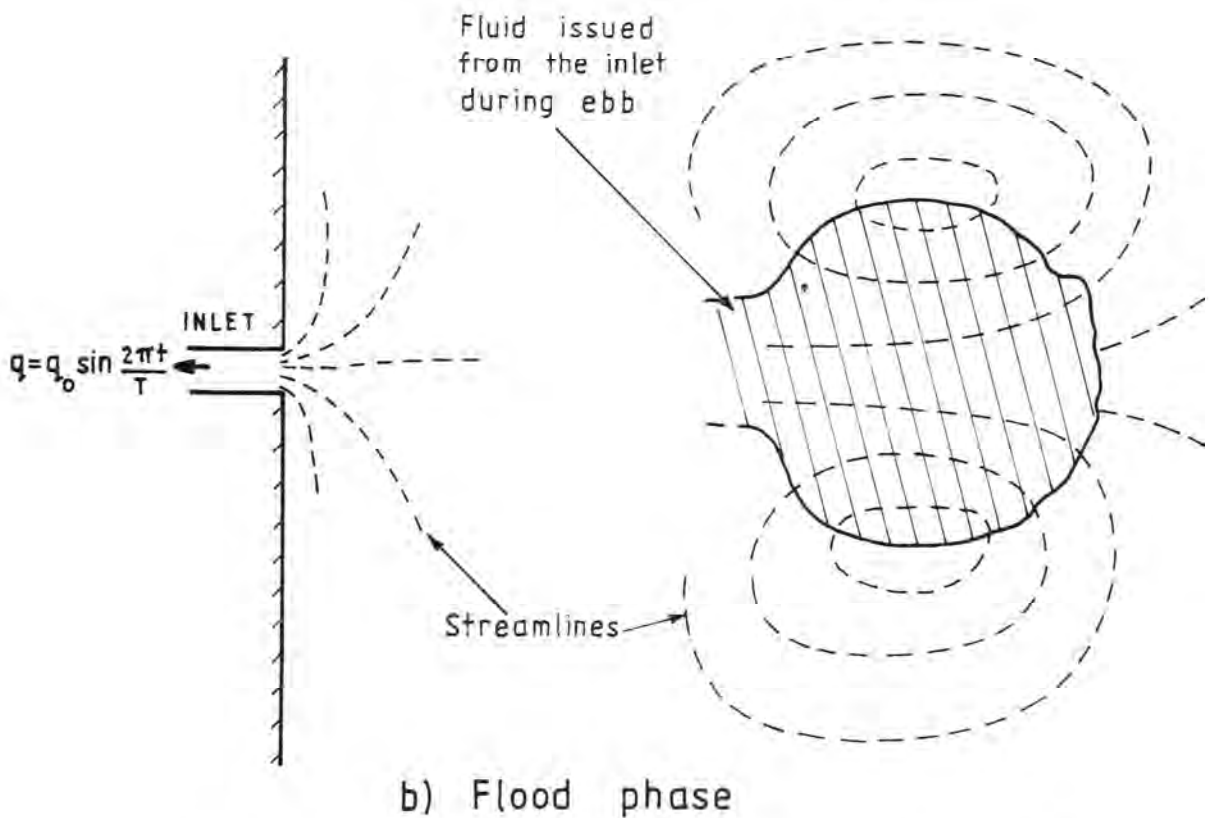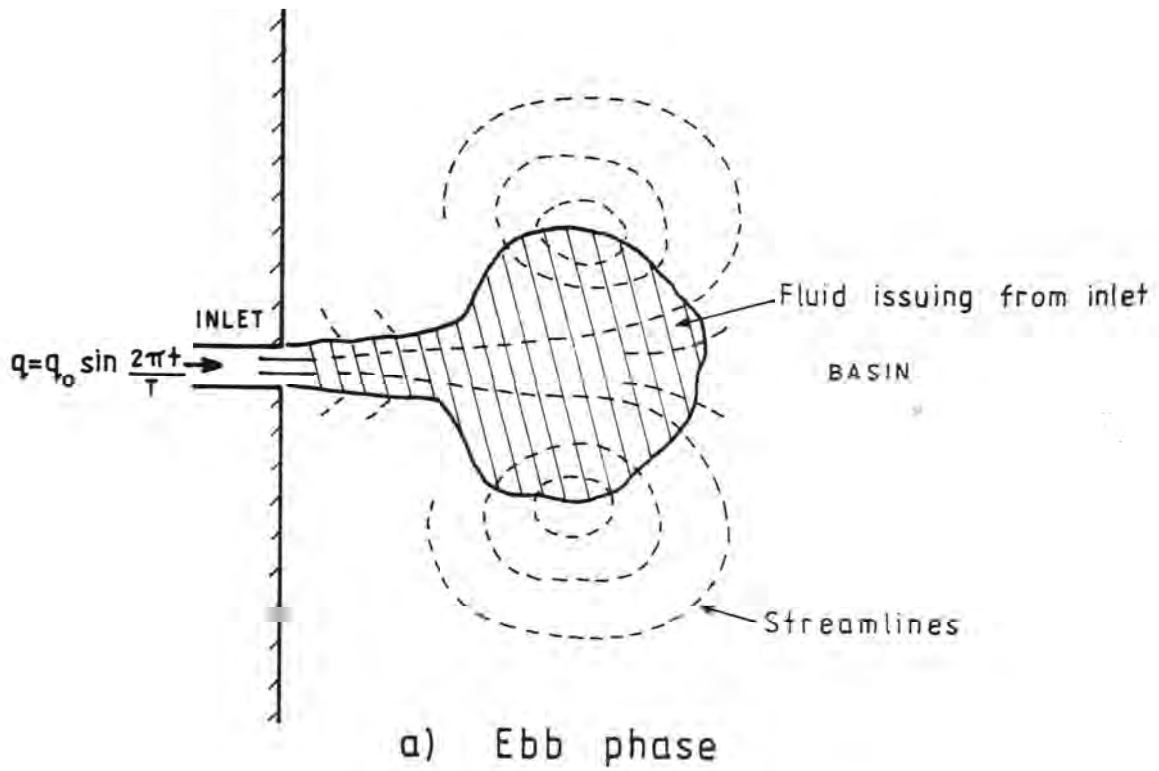
b) Flood phase

SCHEMATIC DIAGRAM OF PERIODIC FLOW
DURING EBB AND FLOOD PHASE

FIGURE 2·1
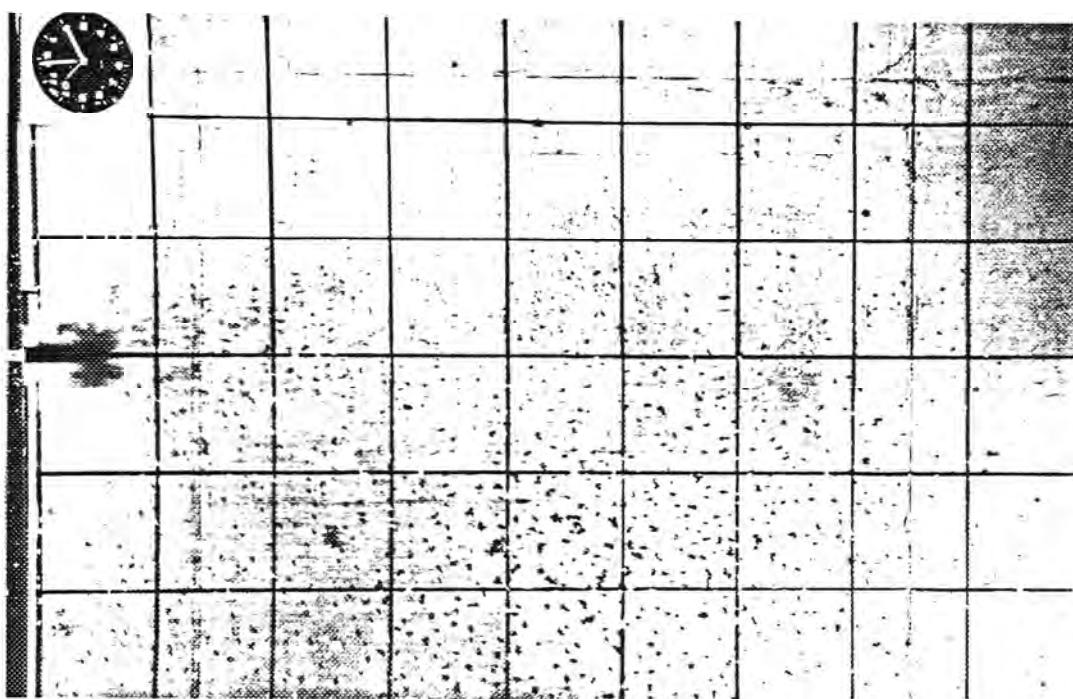
a)   t = 0·05 T
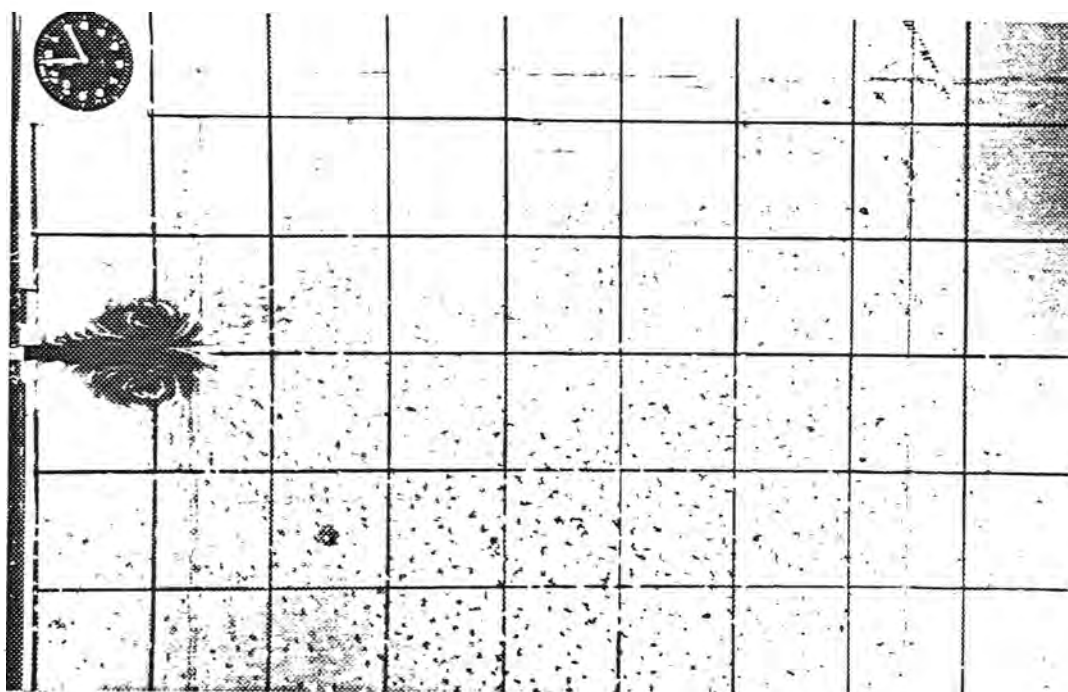
b)   t = 0·18 T

PERIODIC JET FLOW STRUCTURE AT TIME, t,
AFTER COMMENCEMENT OF THE EBB DISCHARGE
Period T = 60 secs. Flow relative to a stationary observer

FIGURE 2·2
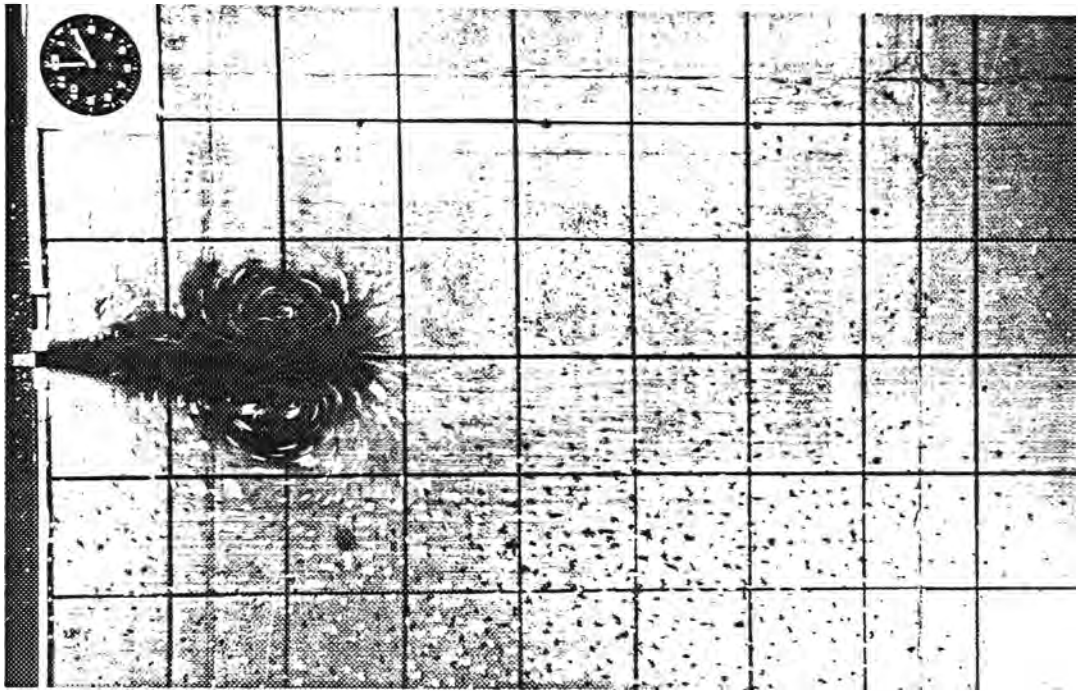
c)   t = 0·34 T

d)   t = 0·5 T

FIGURE 2·2 (Cont.)

e) t = 0·66 T

f) t = 0·82 T

FIGURE 2·2 (Cont.)

g)   t = 1·00 T

FIGURE 2·2 (Cont.)

$$q = q_o \sin \frac{2\pi t}{T} \qquad (2.1)$$
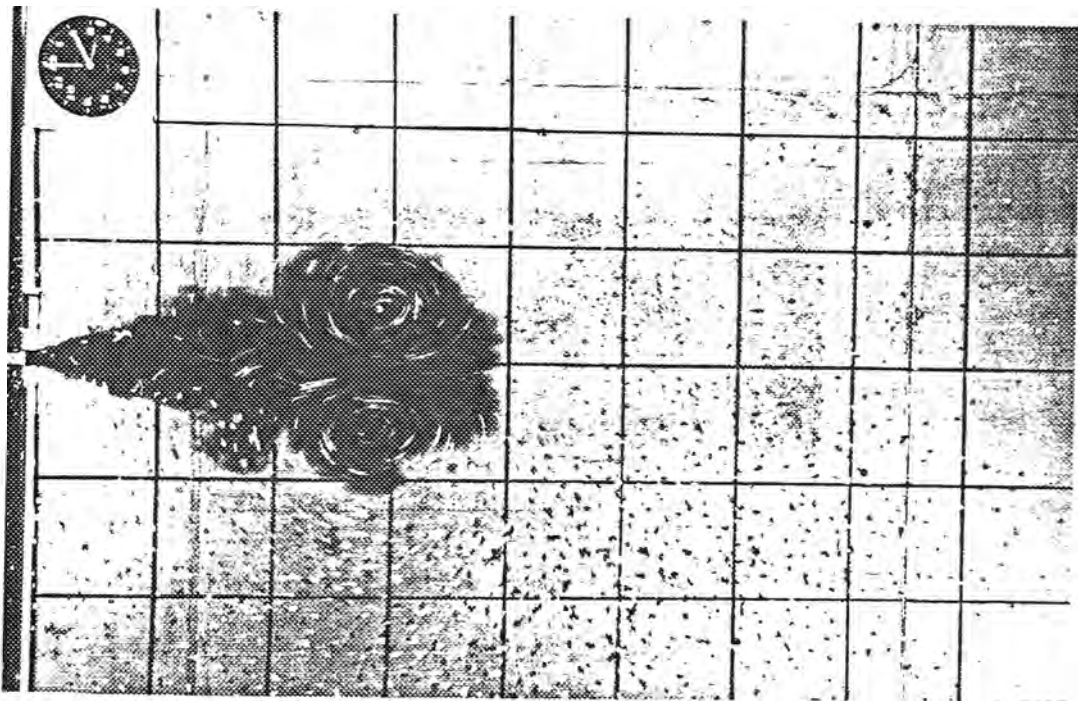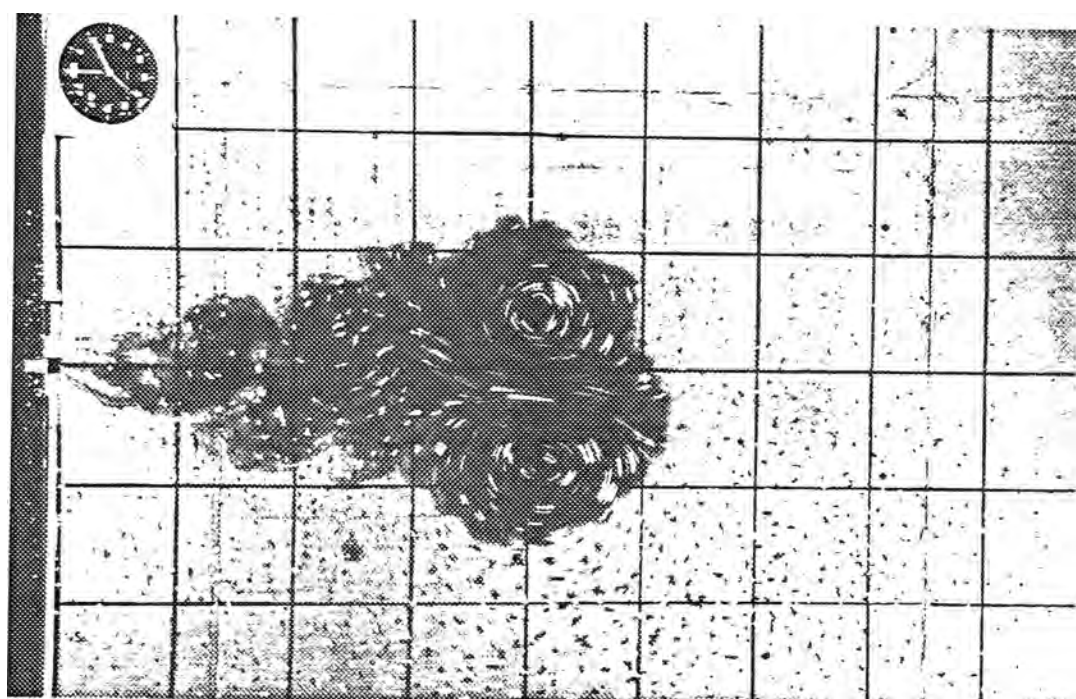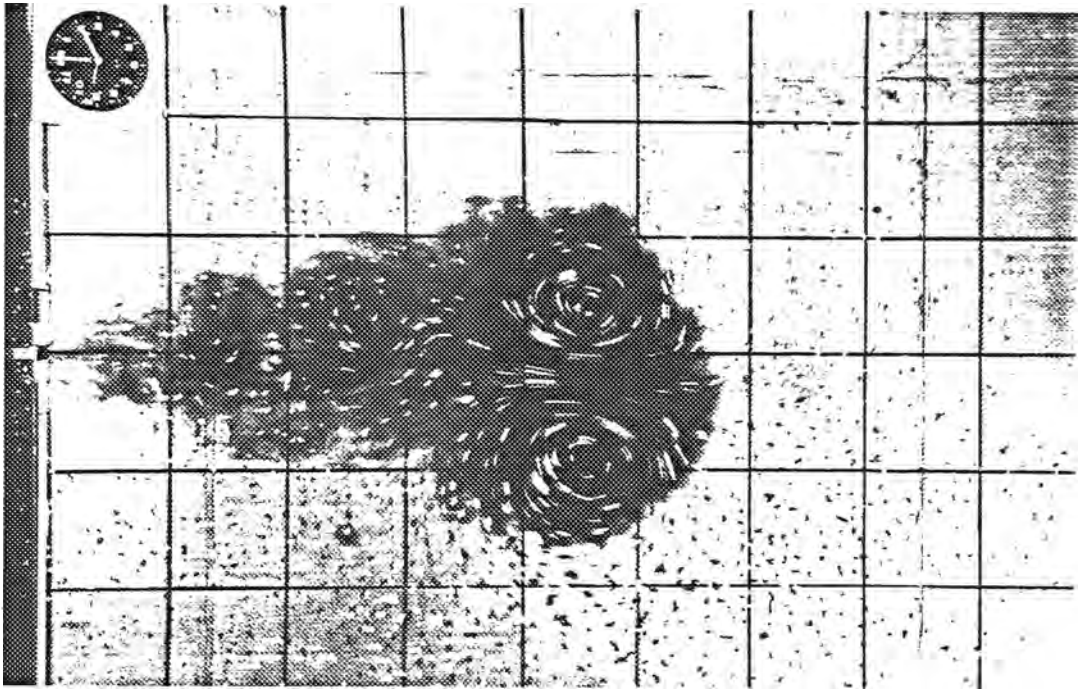
where q_o is the maximum flow rate per unit depth and T is the cycle period.

Figure 2.2 shows the development of the flow over one period. These photographs were taken from a stationary position with an exposure time of 0.03T. The tracers used are dye and confetti. The dye indicates new water entering the basin and the randomly scattered confetti indicates the unsteady velocity distribution in and around the jet. With reference to Figure 2.2, the development of the flow can be described as follows.

As the ebb flow commences a surface of discontinuity is generated due to the separation of the boundary layer that forms on the inlet channel walls. This boundary layer is a region of concentrated vorticity and its detachment at the end of the channel produces a flow instability which leads to the roll up of the vortex sheet. For a short time, the vortex pair remains near the boundary under the influence of image vortices. During this time the strength of the vortices is increasing due to the continued injection of vorticity from the boundary layer. The vortex pair then begins to move away from the source, Figure 2.2b. The fluid which has been ejected from the inlet forms the recirculation cell of the vortex pair, and moves with it. This co-travelling body of fluid is referred to as the vortex pair cap.

During the quarter phase of the flow from $t = 0$ to $t = 0.25T$ the instantaneous flow structure appears similar to that of a constantly maintained source starting jet or plume. The flow bears comparison with that observed by Tsang (1970_1) for a two-dimensional starting

plume, Figure 2.3. The cap is now migrating away from the inlet and is growing in size. It is attached to an unsteady jet "tail". This exhibits similar features to a steady jet with the vorticity generated in the inlet channel diffusing into the zone of potential flow producing turbulence. The jet is entraining ambient fluid and is supplying the vortex pair cap with mass, momentum and vorticity. The entrainment into the jet "tail" is evident in Figures 2.2b and 2.2c.

The vortex pair cap appears to have similar velocity distribution and geometrical shape at different times suggesting that at this stage the flow structure is self-preserving. Under conditions of discharge into a stagnant basin the vortices in the cap are symmetric about an axis perpendicular to the boundary.

The second quarter phase of the flow, $t = 0.25T$ to $t = 0.5T$, is characterised by a continued outflow from the inlet but with a decreasing momentum flux. Under these conditions the flow structure in the jet "tail" will no longer resemble a steady jet. However, observation would indicate that the temporal and spatial variation of the flow properties in the jet "tail" remote from the inlet and near the base of the vortex pair cap have some dependence on the source conditions and the initial steady jet-like flow development. The migration of the vortex pair continues at a slowly decreasing rate, the value of which implies that the jet "tail" is still a source of mass, momentum and vorticity. Figure 2.2c shows that there is still entrainment into the jet.

During this phase the jet begins to meander. It has been proposed earlier that this may be due to the presence of the vortical structures in the free shear layer.
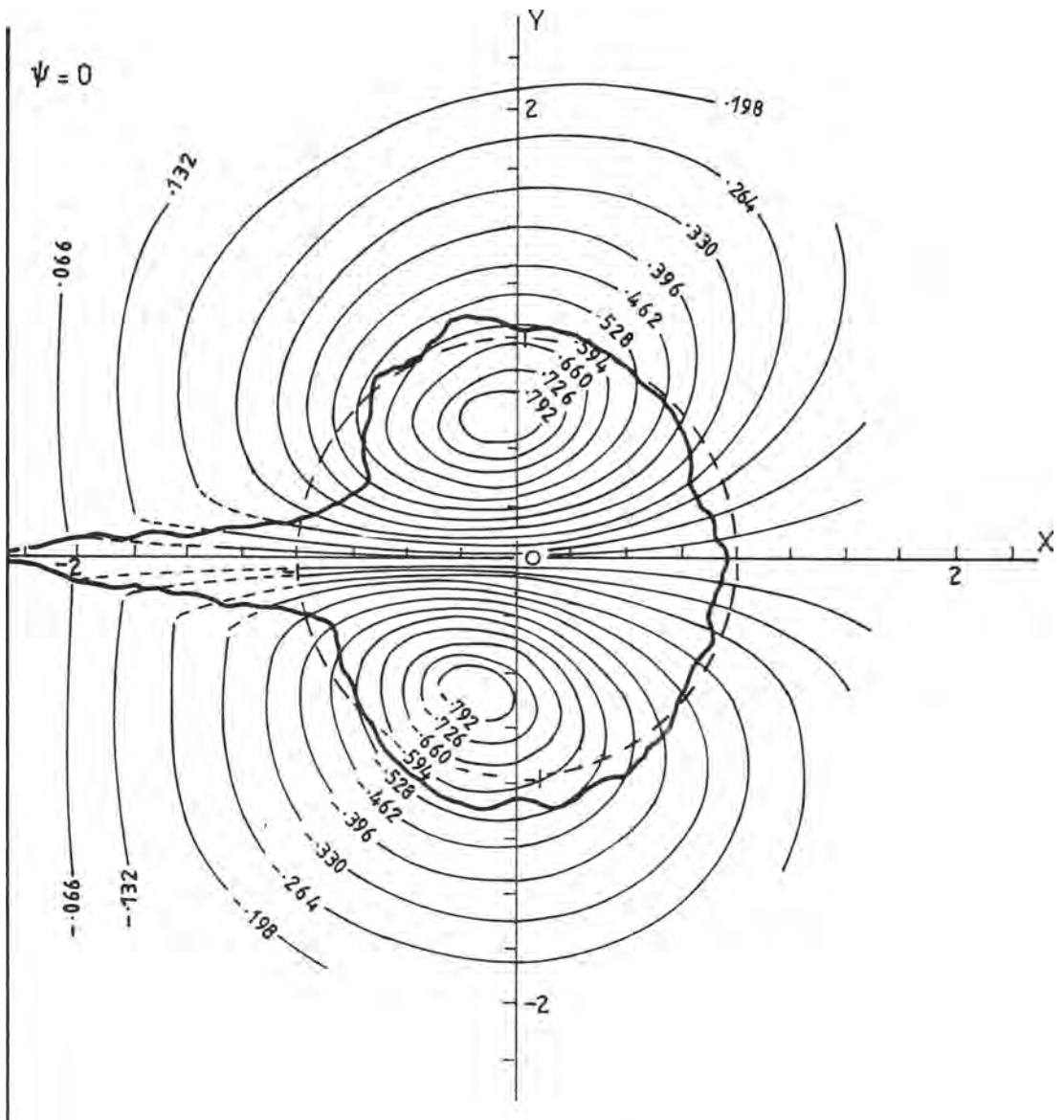
FLOW PATTERN OF A 2-D STARTING PLUME

(After Tsang, 1970₁)

FIGURE 2·3

Winant and Browand (1974) have shown that unstable waves grow in the shear layers formed by the turbulent diffusion of vorticity from the channel boundary layers. These waves roll up into discrete vortical structures. The scale of this turbulence is small compared to the flow structure as a whole. These turbulent vortices will pair up and coalesce forming a larger vortex which engulfs the irrotational ambient fluid, mix and increase the size of the jet flow. The vortices so formed have been observed to become sufficiently large as to induce a meandering motion in the jet at later stages of the flow. The growth of the vortex pair cap does not appear to be influenced by these vortices during the early phase of the flow because the velocity scales associated with each are different. Except under particular circumstances this type of flow instability as shown in Figure 2.4 is not common. Usually the vortex pair is unaffected by jet "tail" instability and exhibits apparent self-similarity during the ebb phase.

The main feature of the flood flow, $t = 0.5T$ to $t = 1.0T$, is that the vortex pair continues to migrate away from the inlet, despite the flow reversal. Although not clearly evident in the photographs (Figures 2.2e,f) this flow into the inlet is similar to a steady radial sink flow. The velocity of the vortex pair is now decreasing more rapidly. The driving force of the advected momentum and vorticity from the jet has been reduced greatly and the vortices will slow down and grow under the influence of entrainment and bottom frictional shear stresses. During this phase the pair appears to remain geometrically similar as before. The movement of dyed fluid indicates that most of the fluid entering the basin during the ebb discharge becomes trapped with the vortex pair. It will move away from the inlet and will not re-enter during the period of flood flow.
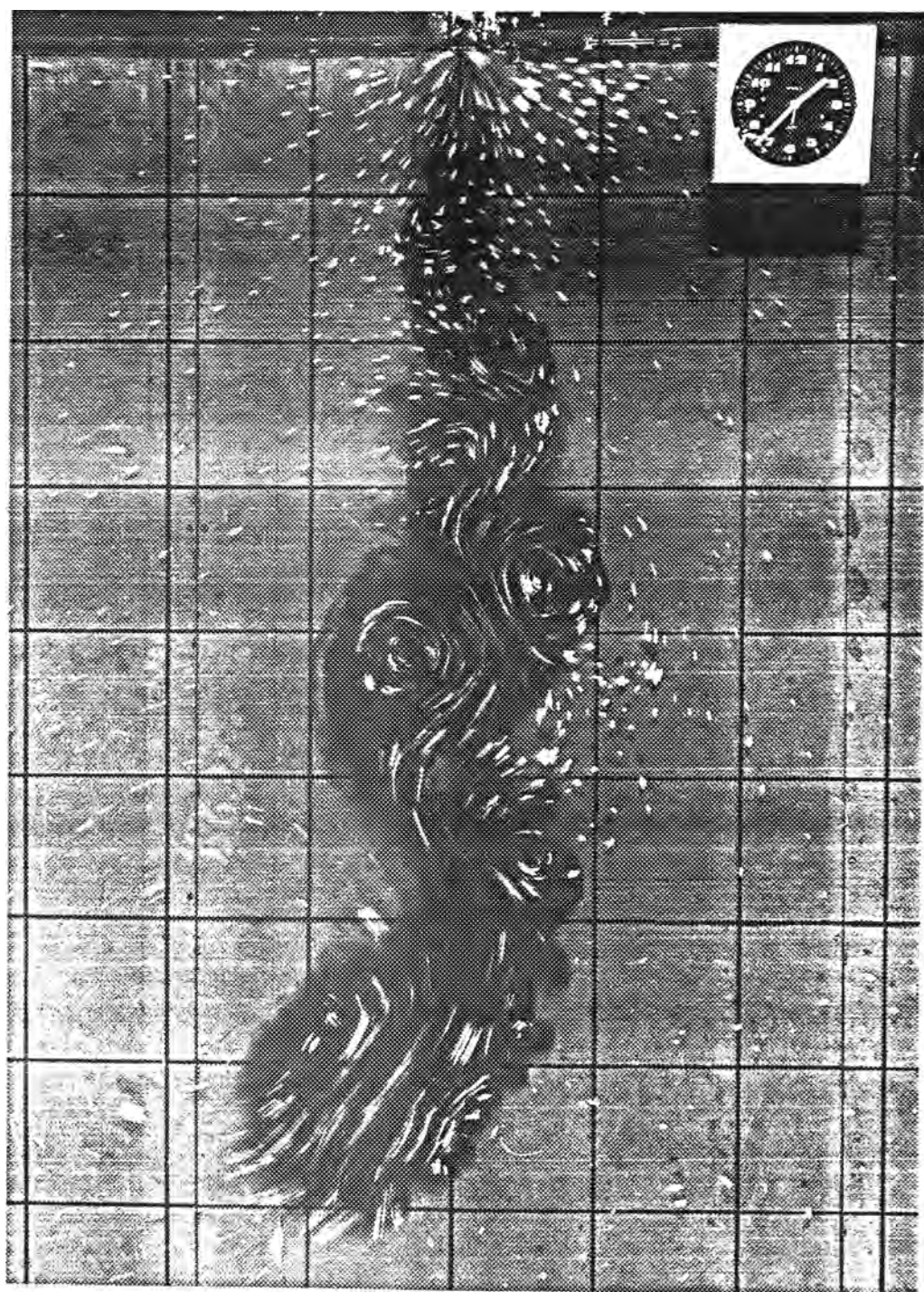
FLOW INSTABILITY IN THE JET "TAIL"

FIGURE 2·4

During subsequent cycles the first vortex pair continues to migrate with decreasing speed. The processes described above are repeated during each cycle, generating a series of vortex pairs. Breakdown of the pair results in most cases from some form of instability. In any given test where such an instability did not occur, the development of the vortex pair structure was limited either by interaction with the model basin boundaries or by mutual interaction with the vortex pair generated during previous or later cycles.

From these observations, it is taken that for the present case of a two-dimensional periodic starting jet, the dynamics of the flow over a complete cycle can be considered as follows. Initially the vortex pair rolls up until its strength is sufficient to move away from the inlet. During the remainder of the ebb phase the flow is like a starting jet with the motion of the vortex pair cap being controlled by the advection of mass, momentum and vorticity from the jet "tail", the entrainment of ambient fluid into the cap, and the bottom frictional resistance to the flow. During the flood phase, the flow back into the inlet can be considered a potential radial sink flow. The influence this flow reversal has on the behaviour of the ebb discharge flow structure will depend on the extent of the flood withdrawal. As the vortex pair cap moves further away from the inlet its motion will become less dependent on the dynamics of the jet tail. Fluid mass and momentum will still be advected into the cap for as long as the velocity in the jet tail at the base of the cap is greater than the translational velocity. The dominant force acting on the cap will then become bottom friction. This combined with a loss of vorticity will cause the flow to slow down and grow in size.

The flow under investigation can be considered as the periodic generation of a turbulent vortex pair with a large scale intermittency. In a later chapter the dynamics of the vortex generation and subsequent development will be analysed in detail. However, at this stage it would be helpful to determine flow parameters which can be used to relate the gross behaviour of one periodic jet to that of another. It is well known that no characteristic length scale can be ascribed to steady jets. If the strength of the jet is periodic then it can be shown that such a scale exists.

The principles of dimensional analysis will now be used to determine characteristic length and time scales and to define parameters which can be used to describe the overall flow behaviour.

2.1 Dimensional Analysis

The behaviour of a two-dimensional jet issuing into a large body of ambient fluid can be described in terms of the following variables:

Q -   the volumetric flow rate at the inlet

b_o -   the inlet channel width

h_o -   the inlet channel depth

ρ -   the fluid density

ν -   the kinematic viscosity.

If the strength of the jet varies periodically there is an additional variable,

T -   the period

A jet discharging periodically into a frictionless basin of uniform depth can be considered two-dimensional. The flow rate per unit depth, $q = Q/h_o$ is given by Equation (2.1). A characteristic momentum flux per unit depth can be defined as:

$$m_o = \frac{\rho \, q_o^2}{b_o} \qquad (2.2)$$

where q_o is the maximum flow rate per unit depth given by Equation (2.1).

It can be shown by dimensional reasoning that a characteristic length scale exists which describes the structure of a periodic jet flow. This length will depend on the momentum flux, the density and the period. Viscous forces will cause a reduction in the net momentum of the flow and the rate of this reduction will be dependent on the Reynolds Number of the flow. It is taken that for large Reynolds Numbers the characteristic length, ℓ , can be expressed mathematically as:

$$\ell = f (m_o, \rho, T) \qquad (2.3)$$

In this equation there are 4 variables expressed in 3 elementary dimensions M, L and T. From the Buckingham Pi-theorem there will be 1 Pi term:

$$\pi = \frac{m_o}{\ell^a T^b \rho^c} \qquad (2.4)$$

where a, b and c are constants.

Solving for a, b and c the dimensionless paramater, π, can be found from which the characteristic length, ℓ, can be defined as:

$$\ell = (\frac{1}{\rho} \, m_o \, T^2)^{1/3} \qquad\qquad (2.5)$$

Physically, this length scales the size of a large Reynolds Number jet after one period from the commencement of the ebb flow.

In steady jet analyses where there is no natural length scale the inlet channel width, b_o, is used as a scale. Thus for a periodic starting flow two length scales ℓ and b_o can be used. The time, t, can be non-dimensionalised with respect to the period, T, as:

$$\tau = t/T \qquad\qquad (2.6)$$

Any flow variable, such as the width, b, at time, t, and distance from the origin, x, can be expressed non-dimensionally as:

$$\frac{b}{b_o} = f \, (\frac{x}{\ell}, \tau) \qquad\qquad (2.7)$$

The length and time scales can be used to derive parameters based on the inlet source conditions which characterise the flow per unit depth.

A characteristic velocity, U*, can be defined as:

$$U* = \ell/T \qquad\qquad (2.8)$$

The characteristic Reynolds Number of the flow, Re*, can be defined in terms of the inlet width, b_o, as:

$$Re* = b_o U*/\nu \qquad (2.9)$$

This will also be the characteristic Reynolds Number for the vortex pair that develops, as b_o will then scale the pair separation. The circulation associated with this vortex is also proportional to $b_o U*$ and a characteristic value, K*, can be defined as:

$$K* = b_o U* \qquad (2.10)$$

The influence of the size of the inlet can be characterised by the ratio of the length to width scales, ℓ/b_o. This parameter becomes important if the concept of similarity is to be used in the analysis of the flow.

Two flow fields are said to be similar if their velocity distribution can be made coincident both in time and distance by the appropriate choice of scales. It is well established that the structure of steady jets is independent of the initial velocity distribution at distances of 20 or more source widths downstream of the discharge point. Turbulence resulting from Kelvin-Helmholtz type instability in the shear zone, spreads in a direction normal to the flow and destroys any initial structure. A similar situation can be expected to exist in the ´tail´ of a periodic starting jet, and provided the dimensions of the inlet are small compared with the size of the flow structures which develop, it can be expected that periodic jets will have a general structural similarity at similar dimensionless times. In reality, the flow being considered is three dimensional and the influence of the

bottom solid boundary on the flow will be depth dependent.

For a flow of constant depth, h_o, it would be expected that the parameter ℓ/h_o would be a relative measure of the influence of bottom frictional forces. This can be confirmed by considering the impulse, I, applied to the flow by bottom friction in one half of a period and comparing this with the total momentum, M, discharged from the inlet. The bottom shear stress, S_b, can be expressed by the usual quadratic law:

$$S_b = \rho \; f* \; U*^2 \tag{2.11}$$

where f* is a friction coefficient and U* is the characteristic velocity. Integrating over the plan area of the flow associated with the discharge between times $t = 0$ and $t = T/2$ gives:

$$I = \int_0^{\frac{T}{2}} \int_0^A \rho f* \; U*^2 \; dA \; dt \tag{2.12}$$

The total momentum, M, is found by integrating the momentum flux;

$$m = m_o \; \sin^2(2\pi t/T)$$

to give:

$$M = \int_0^{\frac{T}{2}} m \; h_o \; dt \tag{2.13}$$

The values of impulse and momentum can be expressed in terms of the characteristic variables using Equations (2.1) and (2.2). The order of magnitude of these two terms are:

$$I = 0 \left[f^* \, \rho \, \frac{\ell^4}{T} \right] \qquad\qquad (2.14)$$

$$M = 0 \left[\frac{h_o}{\ell} \, \rho \, \frac{\ell^4}{T} \right] \qquad\qquad (2.15)$$

Thus

$$\frac{I}{M} = 0 \left[f^* \, \frac{\ell}{h_o} \right] \qquad\qquad (2.16)$$

The depth, normalised with respect to the characteristic length thus becomes a measure of the bottom frictional resistance. Flows with large ℓ/h_o values will be friction dominated. During the early stages of flows with small ℓ/h_o values, the flow will be momentum dominated. The motion of the vortex pair cap at later stages will be influenced by friction to a greater extent. This will act to reduce the impulse of vortex pair and the circulation associated with it.

A measure of the influence of a viscous boundary layer on a rotating body of fluid is given by the Ekman Number (Pedlosky, 1979). This is expressed as the ratio of rotational forces to viscous forces and takes the form:

$$E_K = \frac{\nu}{\Omega \, L'^2} \qquad\qquad (2.17)$$

where Ω is the angular velocity of the rotating fluid and L' is a radial length scale. For a vortex pair consisting of two regions of

uniformly distributed vorticity of characteristic radius, L', separated by distance, b_c, and translating with velocity, u_v, the angular velocity is given by:

$$\Omega = \frac{u_{max}}{L'}$$

$$= u_v \frac{b_c}{L'^2} \tag{2.18}$$

The Ekman Number is thus:

$$E_k \doteq 0 \left[\frac{\nu}{u_v \, b_c} \right] \tag{2.19}$$

A characteristic Ekman Number can be defined as:

$$E_k^* = \frac{\nu}{U^* \, b_o} \tag{2.20}$$

which is the inverse of the characteristic Reynolds Number, Re*.

3. <u>ANALYSIS</u>

In this chapter a theoretical analysis is made of the behaviour of a periodic two-dimensional starting jet issuing into a basin of limited vertical extent. Only the development of the flow generated during one cycle will be considered. It is assumed that the ambient fluid is initially at rest. Interaction with ambient motions induced from previous discharge cycles will be discussed in a later section.

From the description given in Chapter 2, the flow during the first half-cycle can be considered as a starting jet consisting of a two-dimensional jet with a varying source of momentum preceded by a front. This advancing front can be modelled as a vorticity containing region consisting of a pair of Rankine vortices. The front mixes with the ambient fluid, while at the same time additional fluid advected into the front from the jet increases the momentum and circulation of the front. The two components of the starting flow are referred to as the unsteady jet `tail´ and the vortex pair `cap´.

It is proposed to set up an unsteady jet model to give axial velocity and width as a function of time. It will be shown however that a computational limit or shock exists in the numerical solutions to the equations of motion. Solutions can only then be obtained at locations closer to the origin than this limit. A cap model will then be developed which incorporates mass and momentum input from the unsteady jet. Solutions to the cap equations of motion can be obtained provided the junction between the jet and cap remains within the computational limits. An isolated cap model is then developed to describe the cap behaviour after it is decoupled from the jet. This occurs when the mean axial jet velocity falls below the cap translation velocity.

The analysis which follows centres on the classical model for an ideal pair of line vortices as described in standard hydrodynamic texts such as Lamb (1952). In an ideal inviscid fluid a vortex pair translates at a speed, u_p, proportional to the vortex strength, K, and pair separation, $2y_c$. This speed is defined as:

$$u_p = \frac{K}{4\pi y_c} \tag{3.1}$$

Asociated with this motion is a fluid impulse, I, which remains constant for an ideal vortex pair.

In the case of the cap of a periodic starting jet, the vortex pair flow variables - I, u_p, K and y_c - are no longer constant. A model is now constructed to take account of the following properties of a periodic starting jet. The cap is growing due to entrainment of ambient fluid in addition to the fluid advected from the jet tail. The fluid impulse changes with time at a rate equal to the relative influence of the momentum flux being advected from the jet tail and the loss of momentum flux due to the bottom frictional resistance in the shallow basin. The vortex strength also varies depending on the advected vorticity from the tail and the loss of vorticity by turbulent mixing processes in the cap.

The jet tail will influence the behaviour of the cap for as long as the characteristic jet velocity is greater than the translational velocity of the cap. For subsequent times, the flow can no longer be considered a starting flow, and the vortex pair will evolve due to the mutual interaction of the vortices, entrainment and bottom frictional resistance. It will be shown both analytically and experimentally that during this latter phase, the cap will slow down and increase in size.

The equations of motion of the flow will now be developed. Firstly, the equations for an incompressible fluid of limited vertical extent will be considered. These equations will be developed in general terms and then for a shallow water unsteady jet with a sinusoidal variation in source mass flux. From this, the contribution of the jet fluxes to the cap can be determined, and the modified vortex pair equations describing the starting flow will be developed. The vortex pair model will then be re-structured to describe the isolated vortex pair behaviour.

3.1 General Equations of Motion

The flow to be considered is a sheet of fluid of constant and uniform density as defined in Figure 3.1.
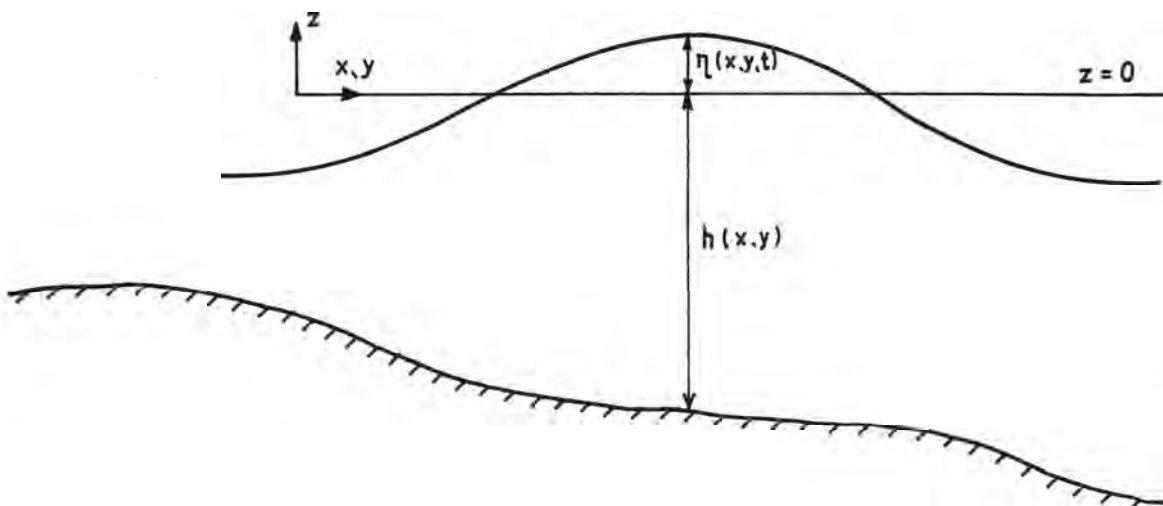
Figure 3.1. Flow Depth Definition Sketch.

The rigid bottom is defined by $z = -h(x,y)$ and the variation in the free surface elevation by $z = \eta(x,y,t)$. It is assumed that the flow is characterized by the parameter ℓ/h_o which was defined in Chapter 2. This can be taken as the ratio of a characteristic horizontal length scale to some characteristic depth of flow. The flow is assumed to be vertically uniform for the condition:

$$\frac{\ell}{h_o} \gg 1 \tag{3.2}$$

This implies that the horizontal velocity components of the flow are independent of z.

The <u>continuity equation</u> for an incompressible flow is:

$$\frac{\partial u}{\partial x} + \frac{\partial v}{\partial y} + \frac{\partial w}{\partial z} = 0 \tag{3.3}$$

where u,v,w are components of the velocity vector in the cartesion coordinate system (x,y,z). These velocities in a turbulent flow have both mean and fluctuating parts defined by:

$$u = \bar{u} + u' \tag{3.4}$$

The general form of the <u>Navier-Stokes equations</u> for a viscous incompressible fluid in which the z direction is directed vertically upwards are:

$$\frac{\partial u}{\partial t} + u\frac{\partial u}{\partial y} + v\frac{\partial u}{\partial y} + w\frac{\partial u}{\partial z} = -\frac{1}{\rho}\frac{\partial P}{\partial x} + \nu\nabla^2 u \tag{3.5a}$$

$$\frac{\partial v}{\partial t} + u\frac{\partial v}{\partial x} + v\frac{\partial v}{\partial y} + w\frac{\partial v}{\partial z} = -\frac{1}{\rho}\frac{\partial P}{\partial y} + \nu\nabla^2 v \tag{3.5b}$$

$$\frac{\partial w}{\partial t} + u\frac{\partial w}{\partial x} + v\frac{\partial w}{\partial y} + w\frac{\partial w}{\partial z} = -g - \frac{1}{\rho}\frac{\partial P}{\partial z} + \nu\nabla^2 w \tag{3.5c}$$

where P is pressure with mean and fluctuating parts, ρ is the fluid density, ν is the kinematic viscosity and ∇^2 is the Laplace operator. Equation 3.5 can be expressed in terms of mean and fluctuating components for an __inviscid__ turbulent flow as shown below for the x-component.

$$\frac{\partial \overline{u}}{\partial t} + \overline{u}\frac{\partial \overline{u}}{\partial x} + \overline{v}\frac{\partial \overline{u}}{\partial y} + \overline{w}\frac{\partial \overline{u}}{\partial z} = -\frac{1}{\rho}\frac{\partial \overline{P}}{\partial x} - \frac{\partial}{\partial x}\overline{u'v'} - \frac{\partial}{\partial y}\overline{v'u'} - \frac{\partial}{\partial z}\overline{w'u'} \tag{3.6}$$

The terms on the right of Equation (3.6) represent the momentum flux of small scale turbulent motion and are usually expressed as a stress applied to the mean flow for example:

$$\overline{v'u'} \equiv -\frac{1}{\rho}S_{xy} \tag{3.7}$$

By rearranging the convective terms and making use of Equation (3.3) the time averaged momentum equations can be expressed (dropping the bar) as:

$$\frac{\partial u}{\partial t} + \frac{\partial u^2}{\partial x} + \frac{\partial vu}{\partial y} + \frac{\partial wu}{\partial z} = -\frac{1}{\rho}\frac{\partial P}{\partial x} + \frac{1}{\rho}[\frac{\partial S_{xx}}{\partial x} + \frac{\partial S_{xy}}{\partial y} + \frac{\partial S_{xz}}{\partial z}] \tag{3.8a}$$

$$\frac{\partial v}{\partial t} + \frac{\partial uv}{\partial x} + \frac{\partial v^2}{\partial y} + \frac{\partial wv}{\partial z} = -\frac{1}{\rho}\frac{\partial P}{\partial y} + \frac{1}{\rho}[\frac{\partial S_{yx}}{\partial x} + \frac{\partial S_{yy}}{\partial y} + \frac{\partial S_{yz}}{\partial z}] \tag{3.8b}$$

$$\frac{\partial w}{\partial t} + \frac{\partial uw}{\partial x} + \frac{\partial vw}{\partial y} + \frac{\partial w^2}{\partial z} = -g - \frac{1}{\rho}\frac{\partial P}{\partial z} + \frac{1}{\rho}[\frac{\partial S_{zx}}{\partial x} + \frac{\partial S_{zy}}{\partial y} + \frac{\partial S_{zz}}{\partial z}] \tag{3.8c}$$

These equations are simplified by invoking the condition that u and v are independent of z, that is, $\ell/h_o \gg 1$. Assuming that the depth is large compared with the variation in the free surface, the vetical particle accelerations are small compared with the gravitational acceleration, that is:

$$\frac{dw}{dt} \ll g \qquad (3.9)$$

Equation (3.8c) then becomes:

$$0 = -g - \frac{1\partial P}{\rho \partial z} \qquad (3.10a)$$

This then reduces to the hydrostatic pressure distribution:

$$P = \rho \, g(\eta - z) + P_o \qquad (3.10b)$$

where P_o is the atmospheric pressure at the water surface.

Equations (3.3) and (3.8 a,b) can now be averaged over the depth of flow from $z = -h(x,y)$ to $z = \eta(x,y,t)$.

3.1.1 Depth Averaged Equations of Motion

The condition that u,v are independent of z allows the continuity equation to be integrated to yield:

$$w = -z\left(\frac{\partial u}{\partial x} + \frac{\partial v}{\partial y}\right) + w_o(x,y,t) \qquad (3.11)$$

where $w_o(x,y,z,t)$ is a constant of the integration.

The condition of zero volume flux through the bottom and free surfaces requires that:

$$w_{z=-h} = -u\frac{\partial h}{\partial x} - v\frac{\partial h}{\partial y} \qquad (3.12a)$$

and

$$w_{z=\eta} = \frac{\partial \eta}{\partial t} + u\frac{\partial \eta}{\partial x} + v\frac{\partial \eta}{\partial y} \qquad (3.12b)$$

Therefore,

$$w_0(x,y,t) = -u\frac{\partial h}{\partial x} - v\frac{\partial h}{\partial y} - h(\frac{\partial u}{\partial x} + \frac{\partial v}{\partial y}) \qquad (3.13)$$

Thus Equation (3.11) becomes:

$$w = -(z+h)(\frac{\partial u}{\partial x} + \frac{\partial v}{\partial y}) - (u\frac{\partial h}{\partial x} + v\frac{\partial h}{\partial y}) \qquad (3.14)$$

Combining this with the free surface boundary condition for z = $\eta(x,y,t)$ and assuming that if $\eta/\eta+h \ll 1$, then $(\eta+h)$ can be replaced by h. The continuity equation then becomes:

$$\frac{\partial}{\partial x}(hu) + \frac{\partial}{\partial y}(hv) = 0 \qquad (3.15)$$

where u and v are depth averaged velocities.

The Momentum Equations (3.8a,b) are integrated vertically making use of Equation (3.11) and the boundary conditions (3.12a) and (3.12b). Replacing $(\eta+h)$ by h as above and expressing in terms of depth averaged velocities gives:

$$h\frac{\partial u}{\partial t} + \frac{\partial hu^2}{\partial x} + \frac{\partial huv}{\partial y} = -gh\frac{\partial \eta}{\partial x} - \frac{1}{\rho}S_{bx} + \frac{h}{\rho}[\frac{\partial S_{xx}}{\partial x} + \frac{\partial S_{xy}}{\partial y}] \qquad (3.16a)$$

$$h\frac{\partial v}{\partial t} + \frac{\partial huv}{\partial x} + \frac{\partial hv^2}{\partial y} = -gh\frac{\partial \eta}{\partial y} - \frac{1}{\rho}S_{by} + \frac{h}{\rho}[\frac{\partial S_{yx}}{\partial x} + \frac{\partial S_{yy}}{\partial y}] \quad (3.16b)$$

$$\text{where} \quad S_{bx} \equiv S_{xz} \ (z=-h) \quad (3.17a)$$

$$S_{by} \equiv S_{yz} \ (z=-h) \quad (3.17b)$$

are the bottom frictional shear stresses.

3.2 Shallow Water Unsteady Jet Equations

For a turbulent jet flow the shallow water equations can be simplified further, as the lateral velocity and length scales are much smaller than the longitudinal scales. Also, the assumption that the surface elevation is small compared with the depth, which itself is small compared to the horizontal length scale (that is, $\eta/\ell \lll 1$) can be invoked. An order of magnitude analysis similar to that used by Özsoy (1977) is carried out reducing Equation (3.16) to:

$$h\frac{\partial u}{\partial t} + \frac{\partial hu^2}{\partial x} + \frac{\partial huv}{\partial y} = -\frac{f}{8}u^2 + \frac{h}{\rho}\frac{\partial S_{xy}}{\partial y} \quad (3.18)$$

where the bottom frictional stress has been expressed in the usual empirically derived quadratic form for flow during the ebb phase. The Darcy-Weisbach friction factor, f, is assumed to be constant.

A solution to Equations (3.15) and (3.18) is now sought in terms of the axial velocity distribution u(x,y,t) and some characteristic jet width b(x,t). In classical turbulent jet theory this is facilitated by introducing the similarity hypothesis for the axial velocity profiles and by defining the characteristic width as the distance from the jet

centreline to the point where the velocity falls to half of its centre-
line value. Self-preservation of velocity profiles will also be
assumed in the present case. This is a reasonable assumption provided
the vertical velocity component is very much less than the horizontal
components.

A number of similarity functions have been introduced by previous
investigators for two and three dimensional jets. The theoretical
solutions of Tollmien (1926) and Schmidt (1941) where later approxi-
mated with Gaussian distributions by Rouse et al. (1952) and others.
Other simpler similarity functions have been proposed based on experi-
mental measurements such as Abramovich (1963). These alllow the velo-
city profile to be limited to a finite distance from the jet centre-
line.

In the present case it is proposed to arbitrarily define a simi-
larity velocity profile which applies over a cross-section of the jet
of finite width b(x,t). This is shown schematically in Figure 3.2.

The boundary conditions applying at the defined nominal limits to
the turbulent region are:

$$v = -v_e + \frac{1}{2}\frac{\partial b}{\partial t} \qquad \text{at} \quad y = +\frac{b(x,t)}{2} \qquad (3.19)$$

$$\text{and} \qquad v = v_e - \frac{1}{2}\frac{\partial b}{\partial t} \qquad \text{at} \quad y = -\frac{b(x,t)}{2} \qquad (3.20)$$

where v_e is the lateral velocity due to the entrainment of surrounding
fluid.
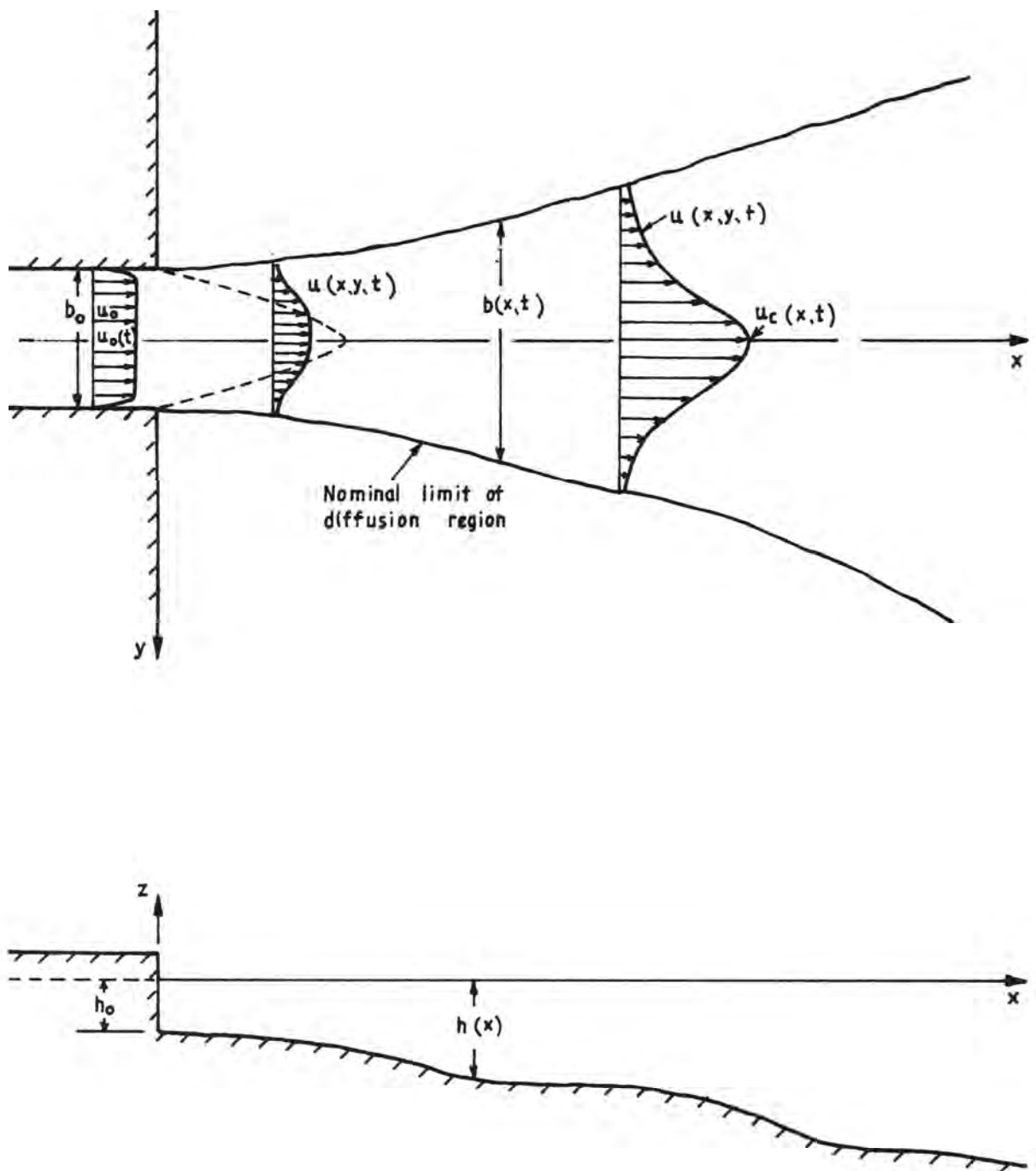
DEFINITION SKETCH FOR
SHALLOW WATER UNSTEADY JET FLOW

FIGURE 3·2

Taking the depth variation to be in the x direction only, the Continuity Equation (3.15) becomes:

$$\int_{-\frac{b}{2}}^{\frac{b}{2}} \frac{\partial hu}{\partial x} \, dy = - \int_{-\frac{b}{2}}^{\frac{b}{2}} \frac{\partial hv}{\partial y} \, dy \tag{3.21}$$

which becomes

$$\frac{\partial}{\partial x} \left(h \int_{-\frac{b}{2}}^{\frac{b}{2}} u \, dy \right) = 2hv_e - h\frac{\partial b}{\partial t} \tag{3.22}$$

Similarly Equation (3.18) afer intergating with respect to y and combining with Equations (3.19) and (3.20) becomes:

$$\frac{\partial}{\partial t} \left(h \int_{-\frac{b}{2}}^{\frac{b}{2}} u \, dy \right) + \frac{\partial}{\partial x} \left(h \int_{-\frac{b}{2}}^{\frac{b}{2}} u^2 \, dy \right) = - \frac{f}{8} \int_{-\frac{b}{2}}^{\frac{b}{2}} u^2 \, dy \tag{3.23}$$

By definition, the lateral shear stress S_{xy} and the velocity u tend to zero as $y \to \pm \ b/2$. The self-similar velocity profile can be expressed as:

$$\frac{u(x,y,t)}{u_c(x,t)} = F(2y/b) \tag{3.24}$$

where u_c is the jet centreline velocity and the function $F(2y/b)$ describes the variation in axial velocity in terms of the similarity variable $(2y/b)$. Use is now made of the entrainment assumption of Morton et al. (1956) which relates the lateral entrainment velocity to the jet axial velocity by:

$$v_e = E \, u_c \qquad (3.25)$$

where E is the entrainment coefficient. Equations (3.22) and (3.23) can now be expressed in terms of u_c as:

$$h\frac{\partial b}{\partial t} + \frac{\partial}{\partial x}(hbu_cF_1) = 2Ehu_c \qquad (3.26)$$

and

$$h\frac{\partial}{\partial t}(bu_cF_1) + \frac{\partial}{\partial x}(hbu_c^2F_2) = -\frac{f}{8}bu_c^2F_2 \qquad (3.27)$$

where

$$F_1 = \int_0^1 \frac{u}{u_c}\,d\xi \qquad (3.28a)$$

$$\left.\begin{array}{c}\end{array}\right\} \quad \xi = \left|\frac{y}{b/2}\right|$$

$$F_2 = \int_0^1 \left(\frac{u}{u_c}\right)^2 d\xi \qquad (3.28b)$$

F_1 and F_2 are constants of integration of the velocity profile normalised with respect to b/2. These values depend on the type of profile assumed. A Top-Hat profile, for example, has $F_1 = F_2 = 1$. At this stage of the analysis the profile is taken to be unknown and will be discussed in a later section.

3.3 General Solution to the Unsteady Jet 'Tail'

In formulating an unsteady model for the motion of the ebb discharge flow structure, the area of interest in the unsteady jet tail is at the 'join' between the jet and the vortex pair cap. Previous investigations by Wood (1965₁), Turner (1962) and Middleton (1975) have shown that a similarity solution is possible for a steady starting flow, implying that the vortex like structure at the head of the

jet will move at a constant fraction of the mean velocity of the jet. The growth of the head will also be in step with that of the jet. Whether such an assumption is valid for an unsteady jet linked to a vortex pair cap is a subject for investigation. Wood (1965_2) was able to show that a similarity solution was possible for the case of an unsteady axisymmetric jet in which the momentum flux is increasing as a power function of time. It would seem reasonable for a periodic jet, that during the phase of flow when the jet momentum flux at the trailing edge of the cap is still increasing at a nearly constant rate, a similarity solution may also exist.

Before the overall behaviour of the periodic starting jet can be considered further it is necessary to examine the behaviour of the unsteady jet `tail` during the ebb flow. The analysis and subsequent discussion which follows in this section, deals with the general case of a two-dimensional unsteady jet taken in isolation from the vortex pair cap. The aim of following analysis is to provide numerical solutions for the contribution of jet `tail` mass and momentum to the vortex pair cap as it migrates away from its origin.

3.3.1 Numerical Solution of Unsteady Jet Equations

Solutions are obtained for an unsteady jet discharging from a virtual origin. The real origin is taken to be located at $x = 0$.

Equations (3.26) and (3.27) are now written in terms of the following dimensionless variables. (The subscript J refers to the general case of an unsteady jet).

$$B_J = \frac{b(x,t)}{b_o} \tag{3.29}$$

$$U_J = \frac{u_c(x,t)}{\ell/T} \tag{3.30}$$

$$X = \frac{x}{\ell} \tag{3.31}$$

$$\tau = \frac{t}{T} \tag{3.32}$$

$$H = \frac{h(x)}{h_o} = 1 + \alpha_1 X \tag{3.33}$$

where $\qquad \alpha_1 = \frac{\partial h(x)}{\partial x}(\ell/h_o)$

The resulting equations are:

$$H\frac{\partial}{\partial \tau}(B_J) + F_1\frac{\partial}{\partial X}(HB_JU_J) = 2E(\ell/b_o)HU_J \tag{3.34}$$

and $\qquad H\frac{\partial}{\partial \tau}(B_JU_J) + \frac{F_2}{F_1}\frac{\partial}{\partial X}(HB_JU^2_J) = -\frac{f\ell}{8h_o}\frac{F_2}{F_1}B_JU^2_J \tag{3.35}$

The boundary condition for a sinusoidally varying source of mass is given by:

$$U_J(\tau)_{X=0} = (\frac{\ell}{b_o})^{1/2} \sin 2\pi\tau \qquad \text{for } 0 < \tau < 0.5$$

$$= 0 \qquad\qquad\qquad \tau > 0.5 \tag{3.36}$$

$$B_J(\tau)_{X=0} = 1.0 \tag{3.37}$$

These equations have been solved numerically. The development of the difference form of the equations and the features of the numerical

solution are given in detail in Appendix 1. However, the main features of the solution will now be outlined.

The equations of motion are solved using an explicit time-integration scheme. The model solves for the variables U_J and HB_J using a finite difference scheme after Keller and Thomee (1962). The Equations of Motion (3.34 and 3.35) can be simplified further if a Top-Hat distribution of velocity is assumed for the previously defined finite width jet cross-section. The velocity U_J then represents the average axial jet velocity. Although a profile similar to that obtained for the classical two-dimensional steady jet would be expected, the Top-Hat distribution allows Equations (3.34) and (3.35) to be combined to give an equation of the form:

$$\frac{\partial U_J}{\partial \tau} - g_1(U_J) \frac{\partial U_J}{\partial X} = g_2(U_J) \tag{3.38}$$

where g_1 and g_2 are known functions of U_J, X and τ. This can be solved for U_J using the above referenced difference technique. The continuity equation can then be solved for the variable HB_J.

The stability criteria for the finite difference form of the above equation as given by Keller and Thomee (1962) can be expressed in terms of the inlet width parameter $(\ell/b_0)^{1/2}$ such that:

$$\frac{\Delta \tau}{\Delta X} \leqslant \frac{F_1}{F_2} (\frac{\ell}{b_0})^{-1/2} \tag{3.39}$$

where $\Delta \tau$ and Δx are the time and spatial computational steps respectively. This criteria is used in the computations with $\Delta x = 0.005$.

3.3.2 Numerical Results

The behaviour of the dimensionless flow variables with distance from the origin, X, for various times, τ, will now be discussed for a typical set of boundary conditions and inlet entrance parameters. A Top-Hat velocity profile has been assumed. Investigation of the sensitivity of the solutions to variation in the entrance parameters has been limited (see Appendix 1).

A feature of the numerical results is the presence of a discontinuity or shock which moves away from the origin with time. This is in accordance with the theory of quasi-linear hyperbolic equations (Jeffrey and Tanuiti, 1964) in which the numerical solutions indicate a tendency for discontinuity even though the initial boundary conditions are smooth. It is clear that this shock condition will not occur in the practical case of a periodic starting jet. Physically, the flow conditions of the vortex pair cap preceding the jet will prevent a sudden discontinuity in the jet fluxes. It follows that the numerical computations will only provide a solution for the location of the join between the vortex pair cap and the jet tail if the join is closer to the origin than the shock location.

The analytical solutions for the unsteady `tail´ of an axisymmetric starting plume developed by Delichatsios (1979) exhibited a similar discontinuity in the buoyancy flux. In that case, the presence of the thermal preceeding the plume precluded the development of the shock in practice. In his discussion on the numerical solution to the intergral equations describing an unsteady laminar viscous jet, Kent (1973) has suggested that the computational discontinuity in the jet fluxes may be understood in relation to a propogating wave of

vorticity, the structure of which is similar to a vortex ring. The present model does not allow this hypothesis to be tested in the two-dimensional inviscid case.

As a general solution for an unsteady jet which is not attached to a vortex pair cap is being sought, the results are evaluated for the dimensionless variable, X, which varies from the origin up to the shock location, X_S. This location will be taken to represent the computational limit for a general unsteady jet solution to exist. It is necessary to modify the source boundary conditions given in Equations (3.36) to avoid the computational singularity that occurs when $\tau = 0.0$ and $\tau = 0.5$. The computations are initiated with a steady jet having a source velocity given by Equation (3.36) for $\tau = 0.01$. In order to obtain solutions in the far field of the inlet after $\tau = 0.5$, the source conditions become steady at $\tau = 0.49$. The variation in nominal jet width, B_J, mean axial velocity, U_J, mass flux HB_JU_J and momentum flux $HB_JU_J^2$ are shown in Figures 3.3 - 3.6. The location of the shock condition is clearly indicated. The jet source velocity variation is shown schematically in Figure 3.4. Numerical sensitivity analysis has shown that for the case of a sinusoidal mass flux variation the speed of the shock is dependent on the computational starting time. However, the values of the jet variables within the computation range are independent of the initial time. As will be discussed later, the mass and momentum fluxes at $\tau = 0.1$ and 0.49 are negligible and may reasonably be assumed not to affect the behaviour of the cap.

This analysis represents an initial investigation into unsteady jet behaviour and as such does not provide a mechanism by which the computational features can be related, if at all, to any physical behaviour. The assumptions made in formulating the intergral

JET PARAMETERS

$\ell/b_o = 15\cdot1$

$\ell/h_o = 36\cdot2$

$E = 0\cdot05$

$f = 0\cdot05$
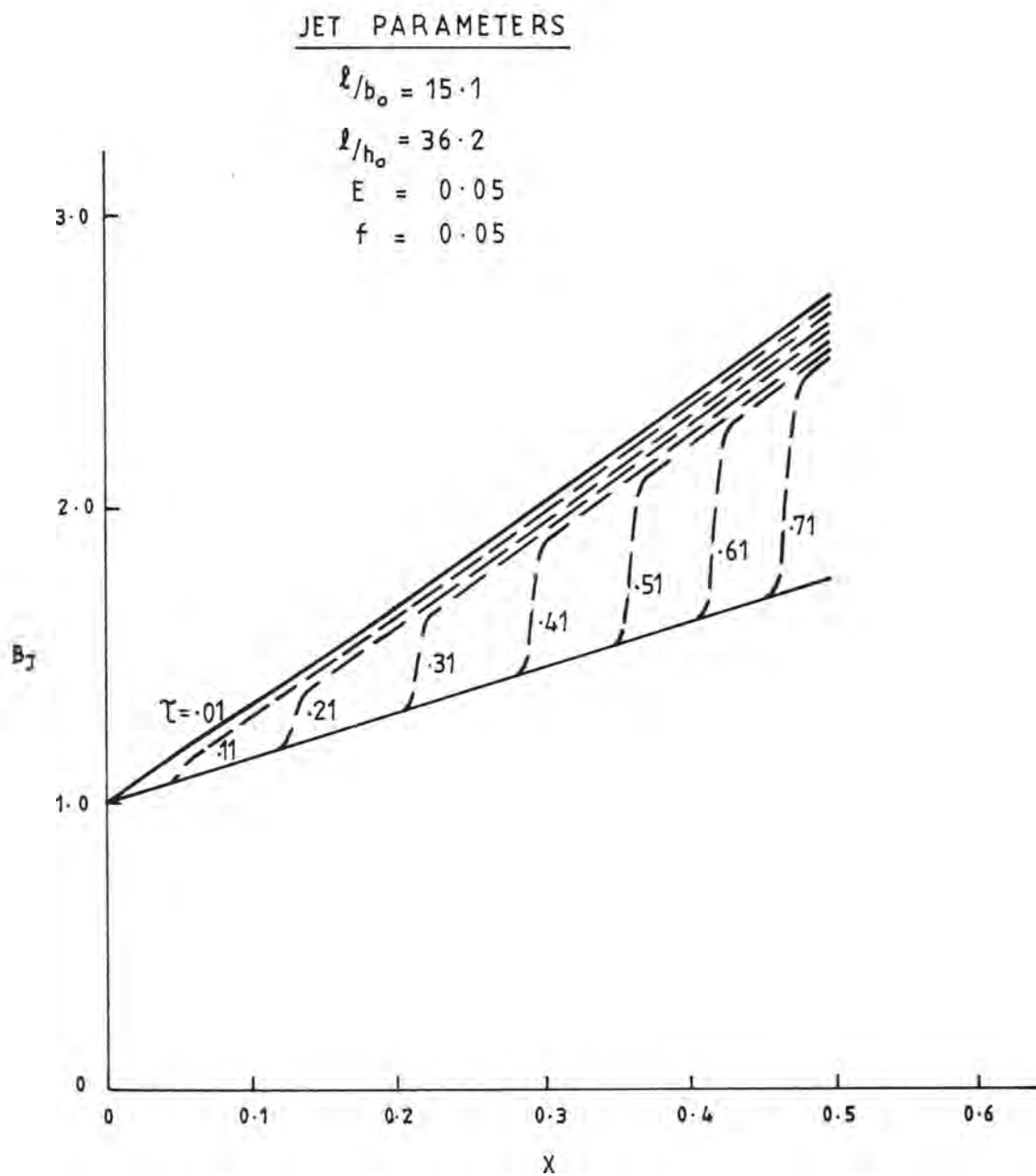
DIMENSIONLESS UNSTEADY JET WIDTH

VERSUS DIMENSIONLESS AXIAL DISTANCE

FIGURE 3·3
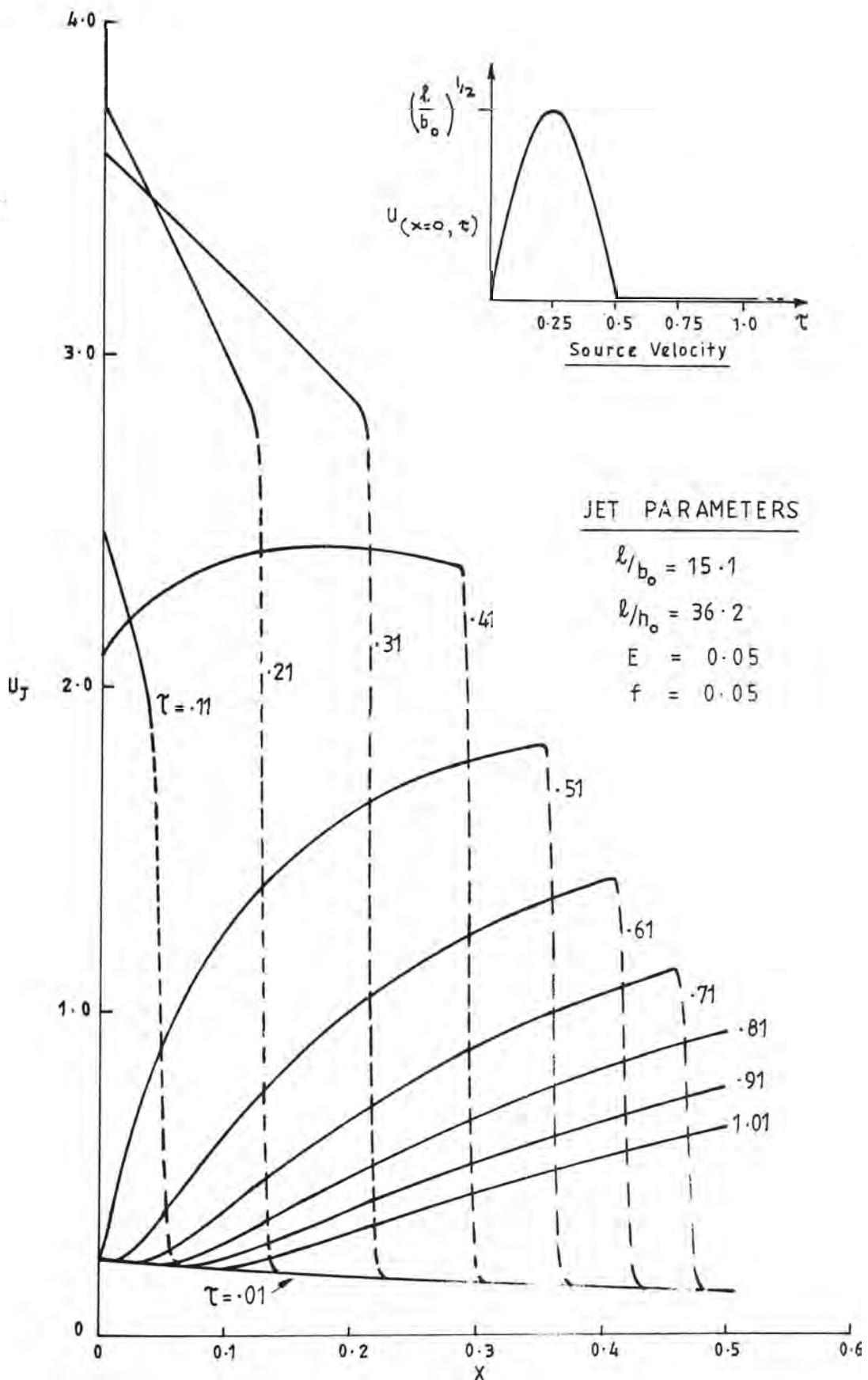
DIMENSIONLESS UNSTEADY JET CENTRELINE VELOCITY
VERSUS DIMENSIONLESS AXIAL DISTANCE

FIGURE 3·4

JET PARAMETERS

$\ell/b_o = 15 \cdot 1$

$\ell/h_o = 36 \cdot 2$

$E = 0 \cdot 05$

$f = 0 \cdot 05$
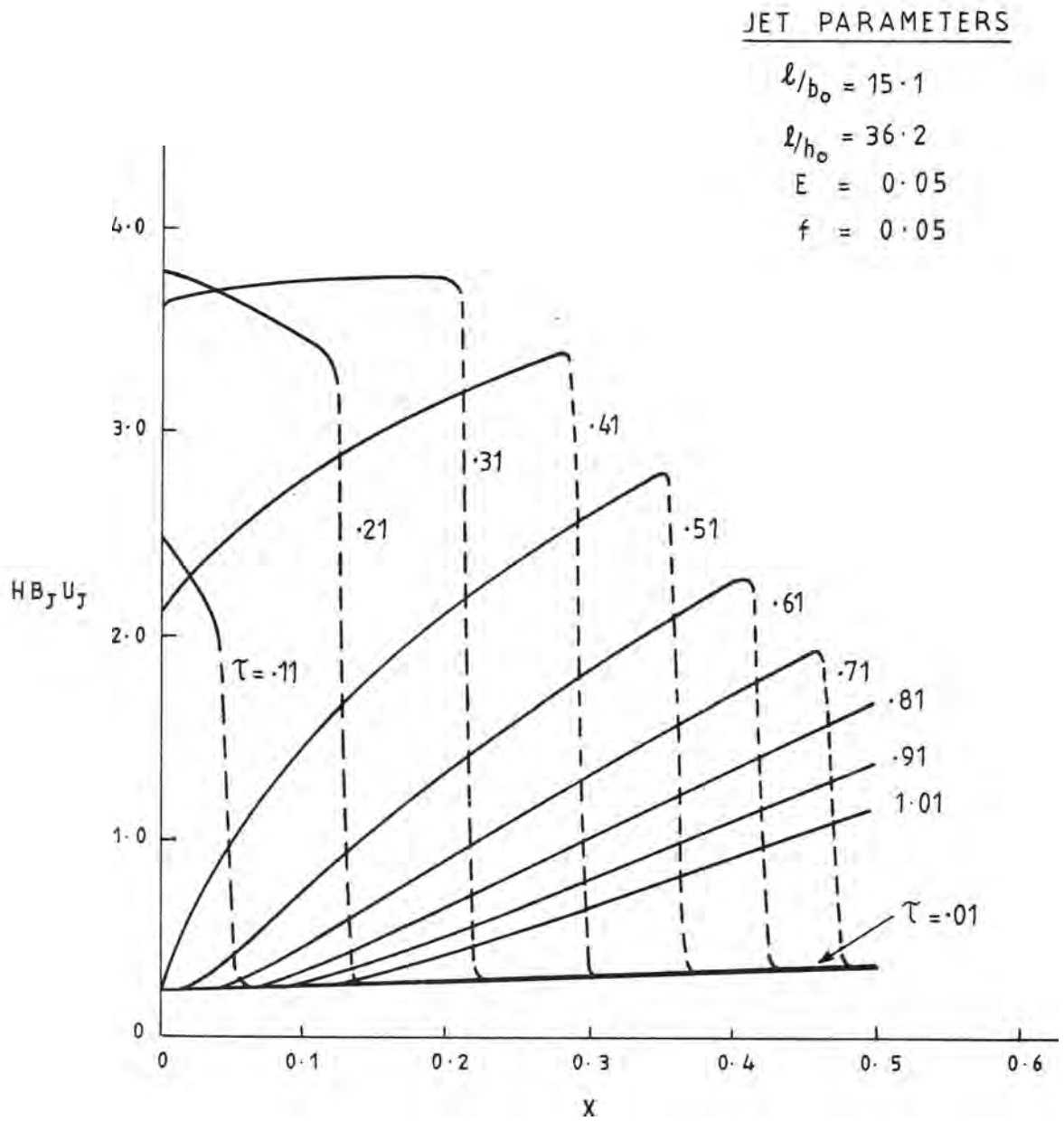
DIMENSIONLESS UNSTEADY JET MASS FLOW RATE

VERSUS DIMENSIONLESS AXIAL DISTANCE

FIGURE 3·5

JET PARAMETERS

$\ell/b_o = 15 \cdot 1$

$\ell/h_o = 36 \cdot 2$

$E = 0 \cdot 05$

$f = 0 \cdot 05$
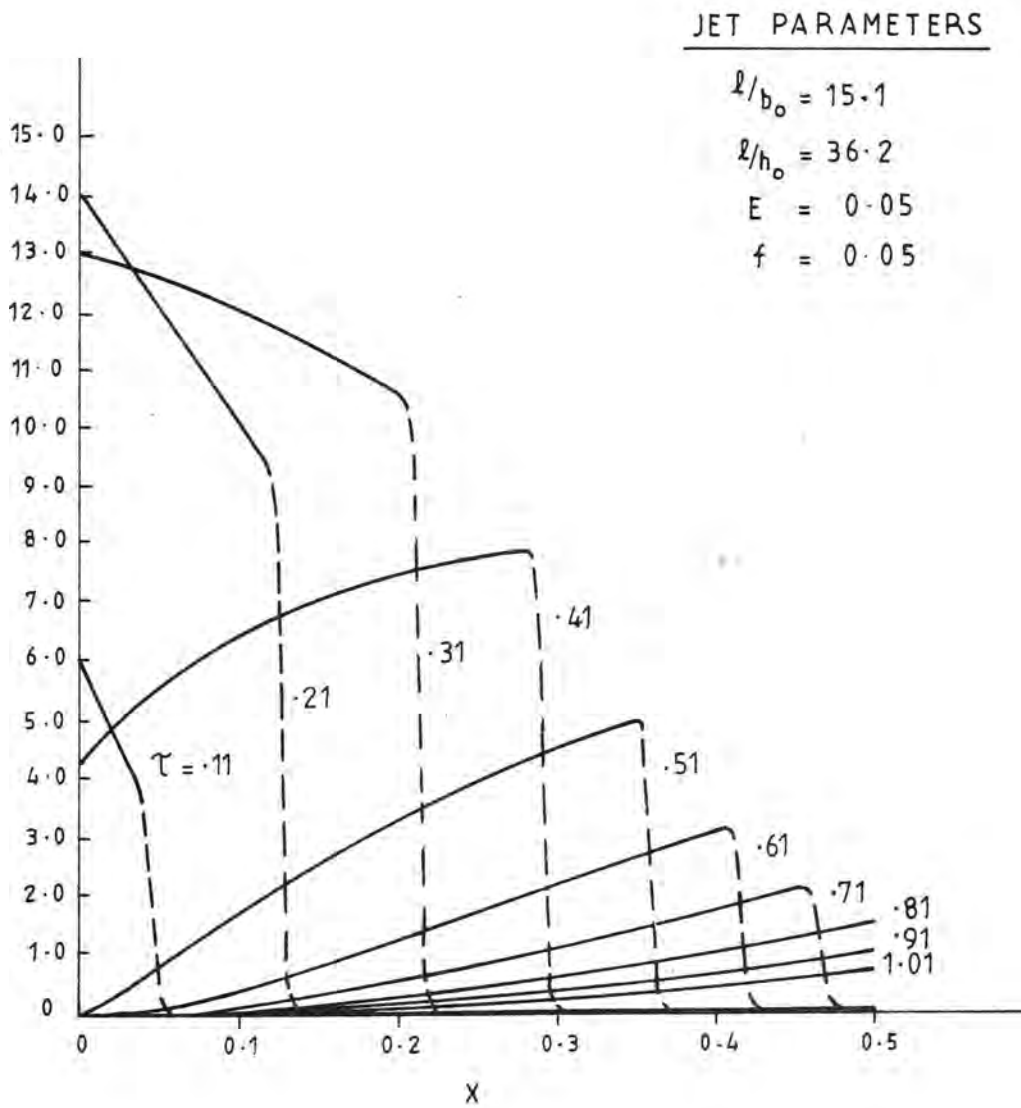
DIMENSIONLESS UNSTEADY JET MOMENTUM FLOW RATE

VERSUS DIMENSIONLESS AXIAL DISTANCE

FIGURE 3·6

equations, in particular, the neglect of the gravitational term $g\frac{\partial}{\partial x}$ and the self-preservation assumption, also place restrictions on the validity of the solutions at the join between the jet `tail´ and the cap. If the join is close to the shock location for instance, the discontinuity in the jet fluxes also invalidates these assumptions.

During the first quarter phase of the cycle ($0 < \tau < 0.25$), the source momentum flux is increasing, and the flow behaves in a quasi-steady manner. This behaviour can be visualized by considering a continuous sequence of steady state solutions corresponding to the instantaneous boundary values. Similar trends were obtained by Kent (1973) in a numerical study of a round viscous jet with source mass flux increasing from one steady state to another. The time similarity Lagrangian formulations developed by Delichatsios (1979) for a round plume with buoyancy increasing as a power function of time, also shows this quasi-steady behaviour.

During the phase of decreasing momentum flux at the source ($0.25 < \tau < 0.5$), however, there is a marked departure from quasi-steady behaviour. Jet velocities now increase with distance from the origin. After the commencement of the flood phase ($\tau > 0.5$), the solutions asymptote to the final steady state boundary condition. The flow variables distant from the origin can be expected to behave independently of the source condition for some time enabling the jet `tail´ model to be used in the starting jet solution for times greater than $\tau = 0.5$. As is shown by Figure 3.4, the jet velocity near the shock location is still relatively high even after one period.

It has been assumed in the formulation of the starting jet model that the behaviour of the vortex pair cap is a function of the

advection into the cap of mass, momentum and vorticity from the jet tail. Numerical solutions to the cap behaviour can only be obtained , however, if the matching point between the cap and the jet is closer to the origin than the computational discontinuity or shock.

Typical numerical results for the location of the shock, X_s, are given in Figure 3.7. The axial jet velocity in the jet behind the shock, U_S, is shown in Figure 3.8, and the ratio of the translational speed of the computational marker, $dX_S/d\tau$, to the jet axial velocity behind the shock, U_S, is given in Figure 3.9. A more comprehensive set of numerical results is presented in Appendix 1. The influence of the inlet width parameter, ℓ/b_o is evident in Figure 3.7 with $dX_S/d\tau$ becoming independent of ℓ/b_o for large values of this parameter. Similar results could be obtained for a section moving at any speed less than the shock speed. This would result in a family of characteristic curves defining the Lagrangian behaviour of the unsteady jet. It will be shown in Chapter 6 that the estimated physical location of the trailing edge of the cap propogates at a speed less than the shock speed and hence appropriate mass and momentum flux contributions can be obtained.

3.4 Equations of Motion of a Starting Jet Issuing into a Basin with Constant Depth

In this section the equations of motion of the vortex pair comprising the cap of a two-dimensional starting jet will be considered. Equations of momentum and continuity will be developed for a vorticity containing region which will be modelled as a pair of turbulent line vortices. These equations will be modified to account for the contribution of momentum and mass from the unsteady jet tail
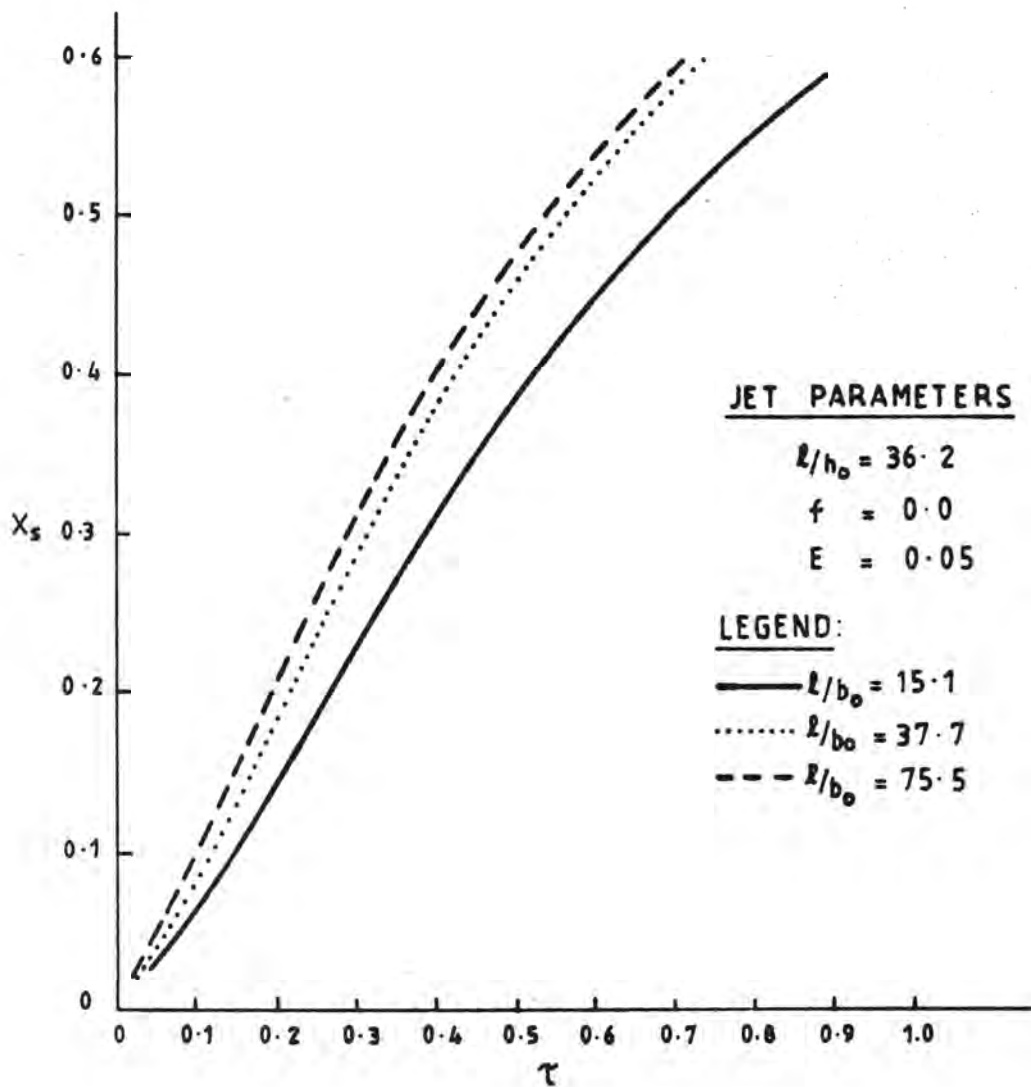
DIMENSIONLESS ADVANCE OF THE JET SHOCK

VERSUS DIMENSIONLESS TIME

FIGURE 3·7
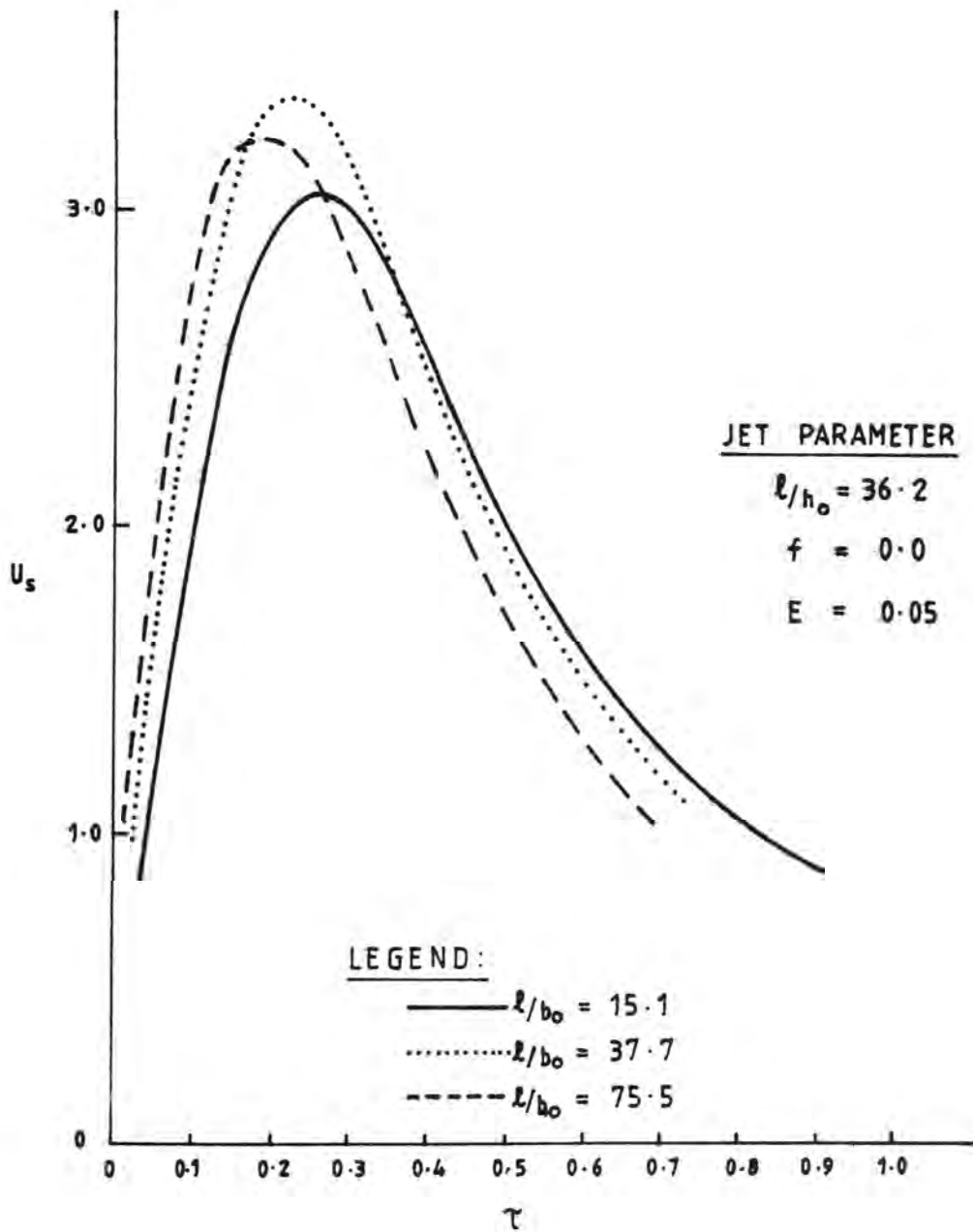
DIMENSIONLESS JET VELOCITY AT THE SHOCK

VERSUS DIMENSIONLESS TIME

FIGURE 3·8
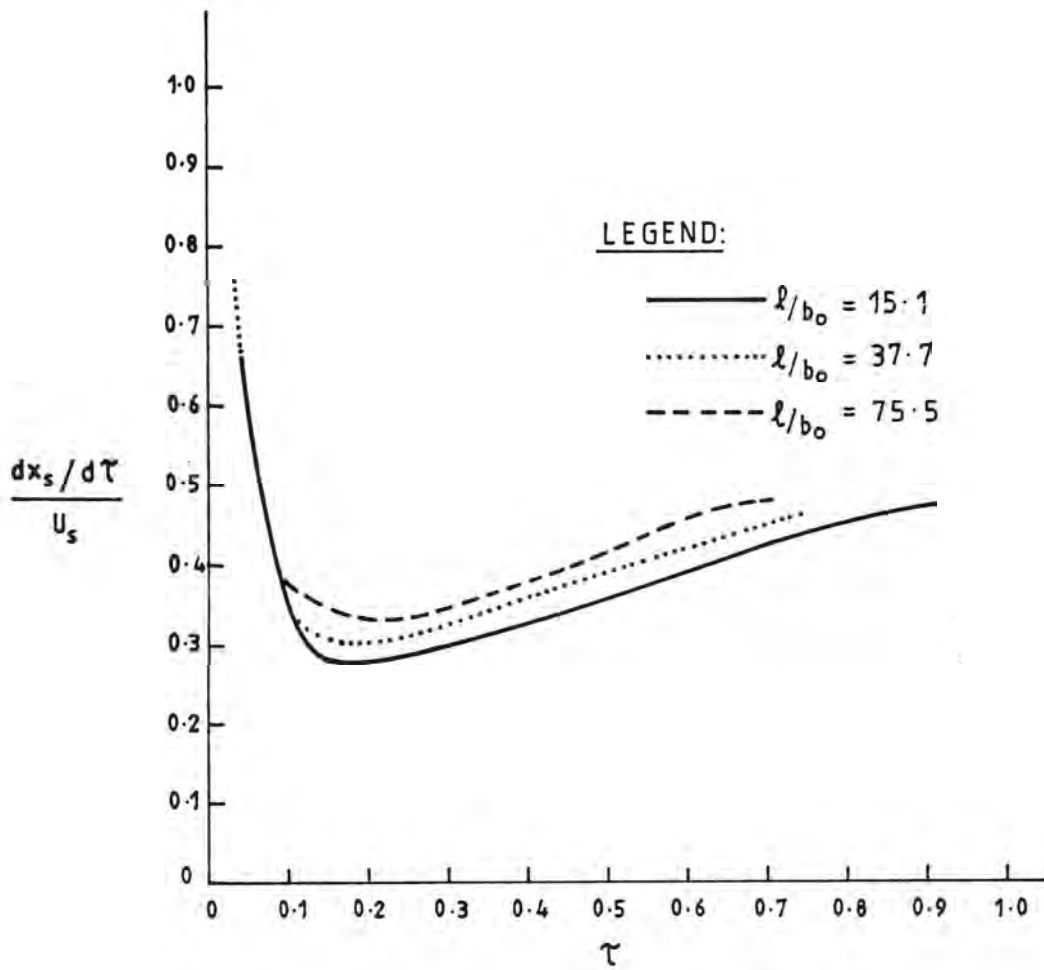
RATIO OF SHOCK SPEED TO JET VELOCITY
VERSUS DIMENSIONLESS TIME

FIGURE 3·9

provided the join between the cap and the jet remains within the computational limits described earlier. The depth of flow is constant and hence the equations represent the change in each variable per unit depth. The case of a linearly increasing depth will be analysed separately.

In developing a model for the starting jet, it has been assumed that the ambient fluid is initially at rest. Clearly this is not the case for successive ebb discharges. However, the assumption of independent flow development during each flow cycle is supported by experimental observation. The development of the starting jet was monitored during the first and fifth cycles - see Chapter 4 - and as willl be shown in Chapter 6 the residual motion set up by a preceding ebb had negligible influence on the gross behaviour of the starting jet.

As stated earlier, the area of main interest in developing a starting jet model for the flow is the join between the jet tail and the vortex pair cap. Similarity formulations for starting flows (Turner (1962), Middleton (1975), Delichatsios (1979), Roman and Bühler (1979) and Demetriou (1983)) give the velocity of the cap as a constant fraction of the characteristic axial velocity of the jet or plume. Whether such a relationship will be approximated during certain phases of the periodic case is still not known. For a source flux which is constant or increasing with time (all of those referenced above), the strength of the vortex pair is always such that the cap will travel at a speed less than the axial jet velocity at the cap. It is possible that the decrease in velocity during the subsequent period of decreasing source momentum flux will be less than the decay of the jet axial velocity. Accordingly the cap and the tail will become decoupled.

3.4.1 Equations of Motion of an Isolated Vortex Pair

The cap of the starting jet is assumed to have a similar structure to a pair of Rankine vortices. An isolated pair is acted upon only by the applied force of bottom frictional resistance. Its motion can then be described in terms of an equation for the mean velocity of propagation of the vortex pair; an equation of momentum conservation and an equation of mass continuity.

The analysis of the flow can be simplified using the self-preservation assumption which states that the shape of the vorticity containing region remains constant at all times.

3.4.1.1 Velocity of Propagation

The velocity of propagation of an ideal vortex pair has been given (Lamb, 1952) as:

$$u_p = \frac{K}{4\pi y_c} \tag{3.40}$$

where K is the strength of each vortex and $2y_c$ is the distance between them. This holds for an irrotational vortex whose rotational core has an infinitesimal area. For a pair of Rankine vortices witn a finite sized rotational core, this relationship will not be adequate. Turner (1960) and other more recent investigators have suggested that for a widely distributed vorticity, the velocity of propogation, u_v, might be represented by a similarity assumption of the form:

$$u_v = \frac{K}{C_1 C_2 b_c} \tag{3.41}$$

where C_1 is a constant dependent on the vorticity distribution, b_c is the apparent separation between the centroid of each vorticity containing region and C_2 is a constant relating the apparent and real vortex separation. These constants will be discussed in full in Chapter 5. For the development of the bulk parameter relationships the velocity of propagation of a turbulent vortex pair will be taken as defined by Equation (3.41).

3.4.1.2 Conservation of Pair Momentum

The hydrodynamical impulse associated with a two-dimensional vorticity containing region (Batchelor, 1967) is given by:

$$\overline{I} = \frac{1}{\rho}\int \overline{X} \times \overline{\omega}\ dA \qquad (3.42)$$

where $\overline{X}$ and $\overline{\omega}$ are the position and vorticity vectors respectively and dA is an element of area. Thus the magnitude of the impulse in the direction of propagation, I, can be expressed as:

$$I = \rho C_2 K b_c \qquad (3.43)$$

The impulse remains constant for an ideal vortex pair. For the case being considered here of a vortex pair moving across a solid boundary parallel to the (x,y) plane, the impulse is no longer constant. A retarding stress vector, $\overline{S}$ with components S_x and S_y, is experienced due to the bottom frictional resistance, such that:

$$\frac{d\overline{I}}{dt} = -\rho \int \overline{S}\ dA \qquad (3.44)$$

This retarding force can be assumed to act on the cap of fluid moving

with the vortex pair. The frictional force per unit bottom area averaged over the flow depth is usually expressed for shallow water flows as an empirically derived quadratic function of the fluid velocity such as:

$$\frac{1}{\rho} S_x = \frac{1}{h_o} \frac{f}{8} u(u^2 + v^2)^{1/2} \tag{3.45}$$

$$\frac{1}{\rho} S_y = \frac{1}{h_o} \frac{f}{8} v(u^2 + v^2)^{1/2} \tag{3.46}$$

where f is the Darcy-Weisbach friction factor, u and v are the local velocities, and h_o is the fluid depth.

Thus, in terms of a cap of fluid moving with the velocity of propagation u_v, the change in impulse of the vorticity containing region in the direction of propagation can be expressed as:

$$\frac{dI}{dt} = -\iint \frac{\rho}{h_o} \frac{f}{8} u^2 dx\, dy \tag{3.47}$$

The area over which the friction force acts can be expressed in terms of the primary flow variables u_v and b_c to give:

$$\frac{dI}{dt} = -\frac{\rho}{h_o} \frac{f}{8} u_v^2 \left[\frac{\pi}{4} C_3\, b_c^2\right] \tag{3.48}$$

where C_3 is a geometrical constant related to the shape of the vorticity containing region.

Combining Equations (3.41), (3.43) and (3.48) gives the conservation of momentum equation for the vortex pair cap as:

$$\frac{d}{dt}[C_1 C_2^2 u_v b_c^2] = -\frac{f}{8h_o} u_v^2 [\frac{\pi}{4}C_3 b_c^2] \tag{3.49}$$

3.4.1.3 Continuity of Mass

An equation for the conservation of mass can be obtained using the entrainment hypothesis for turbulent flows (Townsend, 1976). The cap of fluid surrounding the vortices is assumed to be turbulent and to be growing due to the turbulent entrainment of ambient fluid. Maxworthy (1974) has proposed a number of mechanisms for this entrainment into a turbulent vortex and these will be discussed in a later section. The entrainment hypothesis can be expressed mathematically for the growth of the vortex pair using the entrainment assumption of Morton, Taylor and Turner (1956). This relates the rate of growth of a vorticity containing region to its instantaneous velocity and surface area, by a constant, the entrainment coefficient. In terms of the velocity of propagation, u, and pair separation, b_c, this gives:

$$\frac{d}{dt}[\frac{\pi}{4}C_3 b_c^2] = e'C_4 \pi b_c u_v \tag{3.50}$$

where constant C_4 relates the circumference of the bounded fluid region to that of a circle of diameter b_c, and e' is the entrainment coefficient.

3.4.2 Bulk Form Of the Modified Equations of Motion

The model proposed for a two-dimensional starting flow in shallow, but constant depth will now be outlined. The equations of motion developed in the previous section are modified to account for the contribution of mass and momentum from the unsteady jet tail. A general outline of the turbulent flow is given in Figure 3.10.
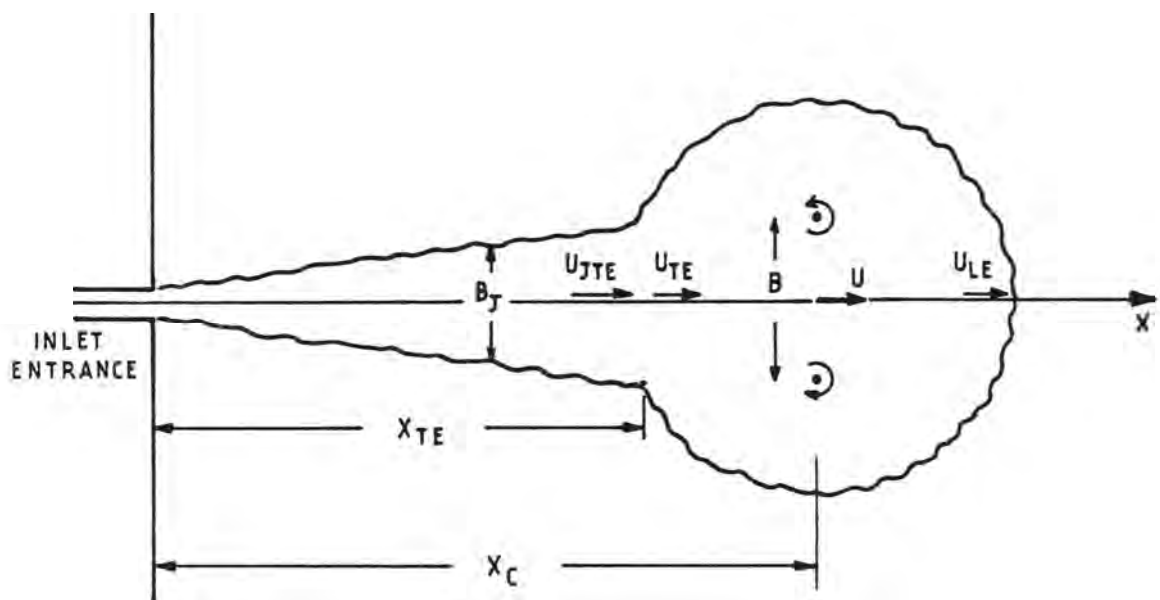
DEFINITION SKETCH FOR A PERIODIC STARTING FLOW
SHOWING THE DIMENSIONLESS VARIABLES
USED IN THE ANALYSIS

FIGURE 3·10

The linear momentum of the vortex pair cap is now being increased by the momentum flux advected from the jet into the cap. It is assumed that this momentum (and mass) is incorporated into the cap at the join between the jet and the cap. The cap variables u_v and b_c are determined at the centre of the cap and hence in order to proceed further with this analysis the cap centreline translation velocity, u_v, must be related to the cap translation velocity at the trailing edge, u_{TE}. It is assumed that as the cap grows its shape remains similar at all times. Thus, u_v can be related to u_{TE} and the cap leading edge velocity, u_{LE}, by constants which are functions of the rate of growth of the cap.

$$u_{TE} = \gamma_{TE} u_v \qquad (3.51a)$$

$$u_{LE} = \gamma_{LE} u_v \qquad (3.51b)$$

At this stage of the analysis it is convenient to re-define the momentum and mass variables for a homogeneous flow as momentum and mass fluxes per unit depth per unit density having dimensions of $L^3 T^{-2}$ and $L^2 T^{-1}$ respectively.

The Conservation of Momentum Equation (3.49) can now be modified to include the momentum contribution from the jet such that:

$$[\frac{dI}{dt}]_{CAP} = -[\text{Friction}]_{CAP} + m_{JET \to CAP} \qquad (3.52)$$

The momentum flux of the jet is added to that of the vortex cap at a rate equal to $(u_{JTE} - u_{TE})$, where u_{JTE} is the mean axial jet velocity at the location of the cap trailing edge. Thus the momentum flux from the jet to the cap is:

$$m_{JET \rightarrow CAP} = m_{JTE}(1 - \frac{u_{TE}}{u_{JTE}}) \qquad (3.53)$$

where m_{JTE} is the jet momentum flux per unit depth at the trailing edge

of the vortex cap. Thus, substituting Equations (3.49) and (3.53) into

Equation (3.52) gives the bulk form of the momentum equation:

$$\frac{d}{dt}[C_2^2 C_1 u_v b_c^2] = -\frac{f}{8h_o} \frac{\pi}{4} C_3 b_c^2 u_v^2 + m_{JTE}(1 - \frac{u_{TE}}{u_{JTE}}) \qquad (3.54)$$

Similarly the Continuity Equation (3.50) is modified to include

the contribution of mass, q, from the jet to the vortex cap given by:

$$q_{JET \rightarrow CAP} = q_{JTE}(1 - \frac{u_{TE}}{u_{JTE}}) \qquad (3.55)$$

Thus the modified form of Equation (3.50) is:

$$\frac{d}{dt}[\frac{\pi}{4} C_3 b_c^2] = (C_4 \pi e') b_c u_v + q_{JTE}(1 - \frac{u_{TE}}{u_{JTE}}) \qquad (3.56)$$

The cap flow variables are non-dimensionalised with respect to the same

inlet parameters as used in the jet analysis. Thus:

$$U(X,\tau) = \frac{u_v}{\ell/T} \qquad (3.57a)$$

$$B(X,\tau) = \frac{b_c}{b_o} \qquad (3.57b)$$

represent the velocity of propagation at the centre of the cap and the

vortex pair separation at that location respectively. Equations (3.56)

and (3.54) are now expressed in terms of the dimensionless variables

defined by Equations (3.29 - 3.32) and Equation (3.57) as:

$$\frac{d\,B^2}{d\tau} = 4e(\frac{\ell}{b_o})BU + \frac{4}{C_3\pi}\frac{\ell}{b_o}Q_{JTE}(1-\frac{\gamma_{TE}U}{U_{JTE}})\qquad(3.58)$$

where $e = e^{-\frac{C_4}{C_3}}$ and,

$$\frac{d}{d\tau}[C_2^2C_1UB^2] = -\frac{f}{8}\frac{\ell}{h_o}\frac{\pi}{4}C_3B^2U^2 + \frac{\ell}{b_o}M_{JTE}(1-\frac{\gamma_{TE}U}{U_{JTE}})\quad(3.59)$$

where M_{JTE} and Q_{JTE} are the dimensionless momentum and mass fluxes per unit density per unit depth.

Numerical solution of Equations (3.58) and (3.59) is now possible provided the relevant constants are known. Constants C_1 – C_4 are geometrical constants relating the size and shape of the vorticity containing region to pair separation, B. These and the growth rate constants e and γ_{TE} can be obtained experimentally as will be discussed in Chapters 5 and 6.

These equations will be valid until the mean jet velocity falls to a value less than the vortex cap velocity. Beyond this the vortex cap can be considered an isolated pair of line vortices for which an analytical solution can be obtained.

3.4.3 Equations of Motion of the Decoupled Vortex Pair Cap

In this section, analytical solutions to the equations of motion for an isolated turbulent vortex pair developed in Section 3.4.1 will be obtained to describe the behaviour of the body of fluid moving with

the vortex pair which has been generated by the unsteady starting flow analysed in the previous sections. The flow is said to decouple from the jet tail for all times after the condition:

$$U_{TE} \geqslant U_{JTE} \tag{3.60}$$

has been met (refer to Figure 3.10).

Equation (3.50) represents the mass continuity equation expressed in dimensionless form. This can be re-written as:

$$\frac{dB^2}{d\tau} = 4e(\frac{\ell}{b_o})BU \tag{3.61}$$

or

$$\frac{dB}{d\tau} = 2e(\frac{\ell}{b_o})U \tag{3.62}$$

The consequence of the entrainment assumption is that the linear scale of the cap increases linearly with distance travelled as can be seen by transforming Equation (3.62) using:

$$U = \frac{dX_c}{d\tau} \tag{3.63}$$

where X_c is the dimensionless location of the centre of the vortex pair cap.

This gives:

$$\frac{dB}{dX_c} = 2e\frac{\ell}{b_o} \tag{3.64}$$

The Momentum Conservation Equation (3.48) can be expressed in dimensionless form as in Equation (3.54) to give:

$$\frac{d}{d\tau}[C_2{}^2 C_1 U B^2] = -\frac{f\ell}{8h_o}\frac{\pi}{4}C_3 U^2 B^2 \tag{3.65}$$

or
$$\frac{d}{d\tau}UB^2 = -C_5\frac{f\ell}{h_o}U^2 B^2 \tag{3.66}$$

where
$$C_5 = \frac{\pi}{32}\frac{C_3}{C_1 C_2{}^2} $$

Using Equation (3.63), Equation (3.61) can be expressed as:

$$\frac{dB^2}{dX_c} = 4e\frac{\ell}{b_o}B \tag{3.67}$$

and Equation (3.66) as:

$$\frac{d}{dX_c}[UB^2] = -C_5\frac{f\ell}{h_o}UB^2 \tag{3.68}$$

Expanding Equation (3.68) and substituting Equations (3.64) and (3.67) to eliminate X_c gives:

$$4e\frac{\ell}{b_o}BU + 2e\frac{\ell}{b_o}B^2\frac{dU}{dB} = -C_5\frac{f\ell}{h_o}UB^2 \tag{3.69}$$

At the time of decoupling, τ_1, the vortex cap is a distance X_1 from the origin and is travelling at a velocity U_1 with a pair separation B_1. For all subsequent times there will not be a contribution of mass and momentum from the jet tail. The vorticity containing region is assumed to grow linearly as a consequence of turbulent entrainment.

Thus Equation (3.69) can be integrated directly using the initial conditions U_1 and B_1:

$$\int_{U_1}^{U} \frac{dU}{U} = \int_{B_1}^{B} [\frac{C_5}{2e\,\ell/b_o} \frac{f\ell}{h_o} + \frac{2}{B}] \; dB \tag{3.70}$$

Integration and simplification leads to:

$$\frac{UB^2}{U_1 B_1^2} = \exp [- \frac{C_5}{2e\,\ell/b_o} \frac{f\ell}{h_o} (B-B_1)] \tag{3.71}$$

Equation (3.64) can be integrated directly to give:

$$B = 2e\frac{\ell}{b_o}X_c + (B_1 - 2e\frac{\ell}{b_o} X_1) \tag{3.72}$$

At this stage it is convenient to express the cap parameters in terms of their values at the point of detachment from the jet , that is:

$$\overline{B} = \frac{B}{B_1} \tag{3.73}$$

$$\overline{U} = \frac{U}{U_1} \tag{3.74}$$

$$\overline{X}_c = \frac{X_c}{X_1} \tag{3.75}$$

and setting the initial conditions as shown in Figure 3.11, as:

$$\overline{U} = \overline{B} = 1 \qquad \text{at} \quad \overline{X}_c = 0 \tag{3.76}$$

Equation (3.72) then becomes:

FIGURE 3·11
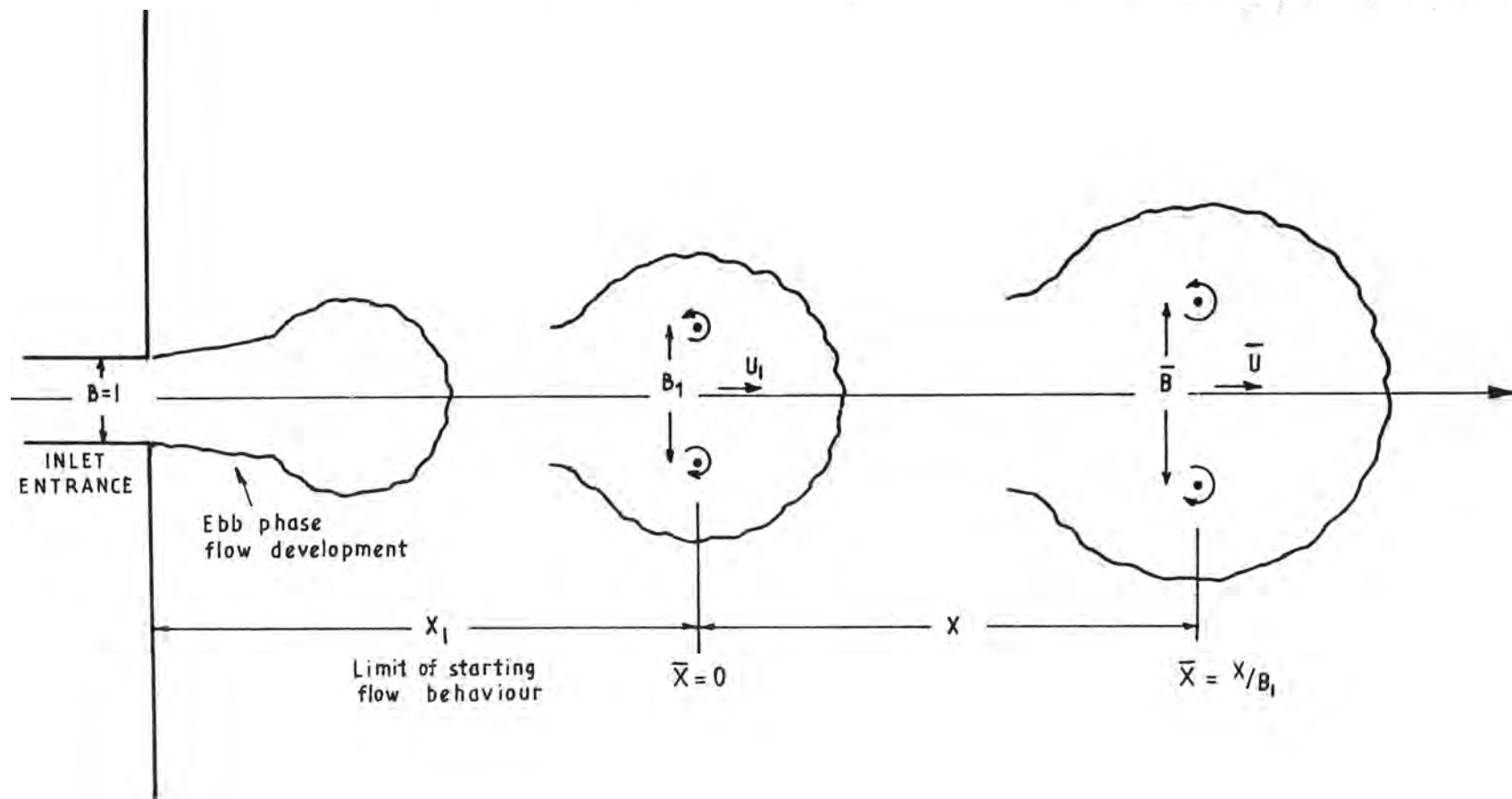
DEFINITION SKETCH FOR THE DECOUPLED VORTEX PAIR CAP FLOW

SHOWING THE RENORMALISED VARIABLES USED IN THE ANALYSIS

$$\overline{B} \;=\; 2e\frac{\ell}{b_o}\overline{X}_c + 1 \tag{3.77}$$

From Equation (3.71):

$$\overline{U} \;=\; \left(2e\frac{\ell}{b_o}\overline{X}_c + 1\right)^{-2} \;\exp\left[-\,C_5\,\frac{f\ell}{h_o}B_1\overline{X}_c\right] \tag{3.78}$$

The functional relationships for other flow variables can now be determined. The impulse is proportional to $\overline{UB}^2$ as:

$$\overline{UB}^2 \;=\; \exp\left[-C_5\,\frac{f\ell}{h_o}B_1\overline{X}_c\right] \tag{3.79}$$

The circulation and the Reynolds Number are both proportional to $\overline{UB}$ as:

$$\overline{UB} \;=\; \left(2e\frac{\ell}{b_o}\overline{X}_c + 1\right)^{-1} \exp\left[-\,C_5\,\frac{f\ell}{h_o}B_1\overline{X}_c\right] \tag{3.80}$$

Simple time relationships can be found for flow over a frictionless boundary by setting $f = 0$ in Equations (3.77 − 3.80) and using the transformation Equation (3.63). These relationships are:

$$\overline{B} \;\sim\; \tau^{1/3} \tag{3.81}$$

and

$$\overline{U} \;\sim\; \tau^{-2/3} \tag{3.82}$$

The circulation and Reynolds Number of the flow vary as :

$$\overline{UB} \;\sim\; \tau^{-1/3} \tag{3.83}$$

The fluid impulse varies as:

$$\overline{UB}^2 \sim \text{constant} \tag{3.84}$$

The constants C_{1-4}, and hence C_5 are, as previously described, dependent on the shape of the vorticity containing region and can be found experimentally or by using numerical results such as Pierrehumbert's (1980). This will be discussed in detail in a later chapter. The entrainment coefficient, e', can be obtained directly from experimental results as:

$$e' = \frac{1}{C_3 \pi B U} \frac{d}{dt} \int_A dA \tag{3.85}$$

where A is the area of the vorticity containing region.

The Darcy-Weisbach friction factor, f, is dependent on the roughness of the boundary and the Reynolds Number based on the flow depth. It is assumed that there is fully turbulent flow in the bottom boundary layer.

The initial conditions for the similarity solution are as defined earlier and shown in Figure 3.11. The initial conditions will be dependent on the ebb phase development and can be taken at a time when the vortex movement is no longer influenced by the momentum advected from the ebb jet as defined by Equation (3.60).

3.5 Vorticity Transport

The model outlined above describes the gross behaviour of a vorticity containing region. The results of the analysis show that it is consistent with recent analyses of vortex motion in that the

circulation is not constant, but decreasing with time. This is an expected result as there are mechanisms acting on the vortices to decrease the circulation. In order to verify the gross parameter analysis these mechanisms will now be considered separately using an approximate first order analysis for the vorticity transport in the vortex pair.

The presence of a solid boundary perpendicular to the axis of rotation of a line vortex of finite core size will result in the formation of an Ekman boundary layer. For flow across a plane boundary, there will be a change of circulation due to the no-slip boundary condition.

Re-writing the shallow water equations of motion for an inviscid flow of constant depth h_o, gives:

$$\frac{du}{dt} = -\frac{1}{\rho h_o} S_x \qquad (3.86a)$$

$$\frac{dv}{dt} = -\frac{1}{\rho h_o} S_y \qquad (3.86b)$$

The vertically integrated vorticity equation can now be obtained by differentiating Equation (3.86a,b) with respect to y and x respectively to give:

$$\frac{d\omega}{dt} = \frac{\partial\omega}{\partial t} + u\frac{\partial\omega}{\partial x} + v\frac{\partial\omega}{\partial y}$$

$$= -\frac{1}{\rho h_o} [\frac{\partial S_y}{\partial x} - \frac{\partial S_x}{\partial y}] \qquad (3.87)$$

where $\qquad \omega = \frac{\partial v}{\partial x} - \frac{\partial u}{\partial y}$

In the absence of internal viscous forces or any other boundary forces the change in vorticity will be due to the action of the bottom stresses S_x, S_y. These are usually expressed as quadratic in the velocity as per Equations (3.45) and (3.46). However, for the present case it is convenient to use a linear relationship similar to the Lorentz linearisation (Groen and Groves, 1962) such that:

$$\frac{1}{\rho} S_x = F u \qquad (3.88a)$$

$$\frac{1}{\rho} S_y = F v . \qquad (3.88b)$$

where the friction factor F is such to make the energy dissipation over the relevant time scale equal to that of the quadratic friction law. An appropriate transformation in the present case would be:

$$F = \frac{f}{8} u_v \qquad (3.89)$$

where u_v is the translation velocity of the vortex pair. Thus the change in vorticity due to bed friction is given by substituting Equations (3.88a) and (3.88b) into Equation (3.87) as:

$$\frac{d\omega}{dt} = -\frac{f}{8h_o} u_v \omega \qquad (3.90)$$

Considering the circulation, K, around one half of the vortex pair:

$$K = \iint_A \omega \, dA \qquad (3.91)$$

where A is the area encompassed by the circuit under consideration. The rate of change of K moving with the fluid (Batchelor 1967, p.268) is:

$$\frac{dK}{dt} = \int_A \frac{du}{dt} \, dA + \int_A \omega \frac{d}{dt}(dA) \qquad (3.92)$$

The differential $\frac{d}{dt}(dA)$ reduces in a first order approximation to:

$$\frac{d}{dt} dA = dA \left[\frac{\partial u}{\partial x} + \frac{\partial v}{\partial y}\right] = 0 \qquad (3.93)$$

Thus the rate of change of circulation is given by:

$$\frac{dK}{dt} = \int_A \frac{d\omega}{dt} \, dA \qquad (3.94)$$

In reality the vorticity containing region grows with time. However, as the growth rate is small during the later stages of the flow, Equation (3.94) is assumed valid to a first order approximation. Thus, substituting Equation (3.90) and (3.91) into Equation (3.94) gives:

$$\frac{dK}{dt} = -\frac{f}{8h_o} u_v K \qquad (3.95)$$

or, by using the relationship, $u_v = \frac{dx_c}{dt}$,

$$\frac{dK}{dx_c} = -\frac{f}{8h_o}K \qquad\qquad (3.96)$$

where x_c is the location of the centre of the vortex pair.

This relationship has the same form as a first approximation for the decay of geostrophic motion under the influence of Ekman-layer friction in the absence of lateral boundaries and forcing (Pedlosky, 1979). Indeed, the mechanisms for decay of an isolated single vortex would be the same, with the Ekman layers (both free surface and bottom layers) acting to pump fluid into the low pressure centre of the vortex and thus compressing the vortex tube reducing its vorticity. The interaction between the two vortices comprising a vortex pair, and their elongated shape, would modify this process.

The growth of the vorticity containing region is due to entrainment of ambient irrotational fluid. Some of the vorticity will be transported by the outer flow to the rear of the vortex pair where it will be annihilated. This loss of vorticity and hence circulation is assumed for the present to be a function of the entrainment velocity. The generalised form of the change of circulation equation is given by Batchelor (1967) as:

$$\frac{dK}{dt} = \int \nabla(-\frac{P}{\rho} + \frac{1}{2}V^2)\ ds + \upsilon\int \nabla^2 V ds \qquad\qquad (3.97)$$

where P is the pressure and $V^2 = u^2 + v^2$ along a streamline.

The second term of this equation represents the viscous diffusion of vorticity through the interior of the fluid. This is assumed negligible relative to the other mechanisms acting. For a flow of constant density, ρ, the rate of change of circulation can be approximated by:

$$\frac{dK}{dt} = \int \nabla \frac{1}{2} V^2 ds \qquad (3.98)$$

where V represents the velocity at points along the separating stream-line $\psi = 0$ of one half of a vortex pair.

Expressed in terms of the entrainment velocity $e' u_v$ and the translation velocity u_v:

$$V^2 = u_v^2 + e'^2 u_v^2 - 2e' u_v^2 \cos\theta \qquad (3.99)$$

where θ is the angle to the positive x-axis.

Assuming the circuit around which the circulation is calculated to be circular then Equation (3.98) becomes:

$$\frac{dK}{dt} = \int_0^\pi V(-e' u_v \cos\theta) \ r \ d\theta \qquad (3.100)$$

where r is the radius of the circuit.
This reduces to:

$$\frac{dK}{dt} = -\frac{\pi}{2} e' u_v^2 \qquad (3.101)$$

Thus the rate of change of circulation as a consequence of mass entrainment and bottom frictional resistance will be of the form:

$$\frac{dK}{dt} = -\frac{f}{8h_o} u_v K - \frac{\pi}{2} e' u_v^2 \qquad (3.102)$$

This can be compared with the rate of circulation change obtained in the previous analysis of the vortex motion.

Equation (3.80) gives the circulation as being proportional to:

$$\overline{UB} = (2e\frac{\ell}{b_o}\overline{X}_c + 1)^{-1} \quad \exp\ [-C_5\ \frac{f\ell}{h_o}\ B_1\overline{X}_c\ ] \tag{3.103}$$

Therefore:

$$\frac{d\overline{K}}{dX_c} \sim \frac{d\overline{UB}}{dX_c} = -C_5\ \frac{f\ell}{h_o}\ B_1(2e\frac{\ell}{b_o}\overline{X}_c + 1)^{-1}\quad \exp\ [-C_5\ \frac{f\ell}{h_o}\ B_1\overline{X}_c]$$

$$= -\ 2e\frac{\ell}{b_o}(2e\frac{\ell}{b_o}\ \overline{X}_c + 1)^{-2}\ \exp\ [-C_5\ \frac{f\ell}{h_o}\ B_1\overline{X}_c] \tag{3.104}$$

or, simplified:

$$\frac{d\overline{K}}{dX_c} \sim -\ C\overline{K} - e\overline{U} \tag{3.105}$$

Using the transformation $\overline{U} = \dfrac{d\overline{X}_c}{d\tau}$ we get:

$$\frac{d\overline{K}}{d\tau} \sim -\ C\overline{KU} - e\overline{U}^2 \tag{3.106}$$

The similarity between Equations (3.102) and (3.106) is to be expected as the Conservation of Momentum Equation (3.65) and the Circulation Equation (3.102) are both forms of the same physical principle.

3.6 Equations for A Starting Jet Issuing Into A Basin with Linearly Varying Depth

The functional relationships for the velocity of propagation and rate of growth of a periodic starting jet propagating in a basin in which the water depth is increasing linearly in the direction of travel will now be considered. The depth variation is given by:

$$h(x) = h_o + x \qquad\qquad (3.107)$$

where h_o is the inlet entrance depth and ε is the bed slope. Expressed in dimensionless form as defined in Section 3.3.1 this is:

$$H = 1 + \alpha_1 X \qquad\qquad (3.108)$$

The main assumption used in the following analysis is that the vortex pair cap behaves as a variable length column of fluid with symmetry about the xz and the yz planes, that is, the vortex pair cap is considered two-dimensional. It is also assumed that the bottom slope, ε, is small.

The entrainment assumption for an isolated vortex pair (Section 3.4.1.3) can be expressed in dimensionless form as:

$$\frac{d}{d\tau}[\frac{\pi}{4}C_3 B^2 H] = (C_4 \pi e^{-\frac{\ell}{b_o}})BHU \qquad\qquad (3.109)$$

The equation of impulse for a column of fluid (Section 3.4.1.2) is similarly:

$$\frac{d}{d\tau}[C_2{}^2 C_1 UHB^2] = -\frac{f \ell}{8h_o{}^4}C_3 U^2 B^2 \qquad\qquad (3.110)$$

3.6.1 Modified Equations of Motion

The equations of an isolated vortex pair are now modified to include the mass and momentum supplied by the unsteady jet to the cap. The procedure adopted for selecting a particular unsteady jet mass and momentum flow is the same as that described in detail in Section 3.4.2

for the case of a constant depth flow. The resulting equations for the general case of flow in a basin of linearly increasing depth are:

$$\frac{d}{d\tau}[HB^2] = 4e\frac{\ell}{b_o}HBU + \frac{4}{C_3\pi}\frac{\ell}{b_o}Q_{JTE}(1-\frac{\gamma_{TE}U}{U_{JTE}}) \qquad (3.111)$$

$$\frac{d}{d\tau}[C_2{}^2C_1HB^2U] = -\frac{f}{8h_o}\frac{\ell}{4}\frac{\pi}{4}C_3B^2U^2 + \frac{\ell}{b_o}M_{JTE}(1-\frac{\gamma_{TE}U}{U_{JTE}}) \qquad (3.112)$$

M_{JTE} and Q_{JTE} are respectively the dimensionless jet momentum flux and mass flux at the trailing edge of the vortex pair cap.

These equations can be solved numerically using a simple Euler method (Chow,1979) for known values of the jet fluxes at the cap. The equations describe the starting flow behaviour up until the jet axial velocity falls below that of the cap.

3.6.2 Numerical Results for the Vortex Pair Cap Motion

The behaviour of the cap is determined by solving the general form of the equations of motion, Equations (3.111) and (3.112). The contributions of jet mass and momentum are taken as a constant for each time step and are obtained from the unsteady jet numerical solutions.

As discussed in Section 3.3 the unsteady jet solution requires an initial steady state to avoid a computational singularity. Numerical solutions for the cap behaviour are also taken to commence at this computational starting time ($\tau = 0.02$ for the cap solutions). The cap is taken to be fully developed at this time with each vortex having acquired a circulation and radius during the intial spin-up time as

defined by the similarity theory of Pullin (1978) given in Appendix 2. Initial cap velocity and separation are then calculated. The sensitivity of the solutions to variation in the computational starting time is discussed in Appendix 2.

The jet solutions are obtained at a location taken to represent the trailing edge of the vortex pair cap which is defined by the assumption of self-preservation of the cap, knowledge of the centreline location at the previous time step and an experimentally determined cap shape factor. This procedure is continued until the jet centreline velocity falls below that of the cap, at which point the right hand terms of Equations (3.111) and (3.112) are dropped. The isolated cap solutions are then obtained for the required time. Solutions are obtained for the dimensionless cap width variable, B , and for the dimensionless location of the cap centreline, X_c. Typical results are shown in Figure 3.12. These results will be discussed in detail in Chapters 5 and 6 in relation to the experimental results.

As discussed in an earlier section, the unsteady jet solution method is limited in that final steady state boundary conditions are required. This clearly is not valid in the physical sense. However, the numerical procedure of decoupling the cap and jet generally occurs when the cap is distant from the inlet. Hence the jet flow variables at this point are still independent of the source flow conditions.

3.6.3 Behaviour of an Isolatd Vortex Pair

Analytical solutions for the functional relationships for the cap velocity and width will now be determined for a vortex pair cap which is decoupled from the starting jet.
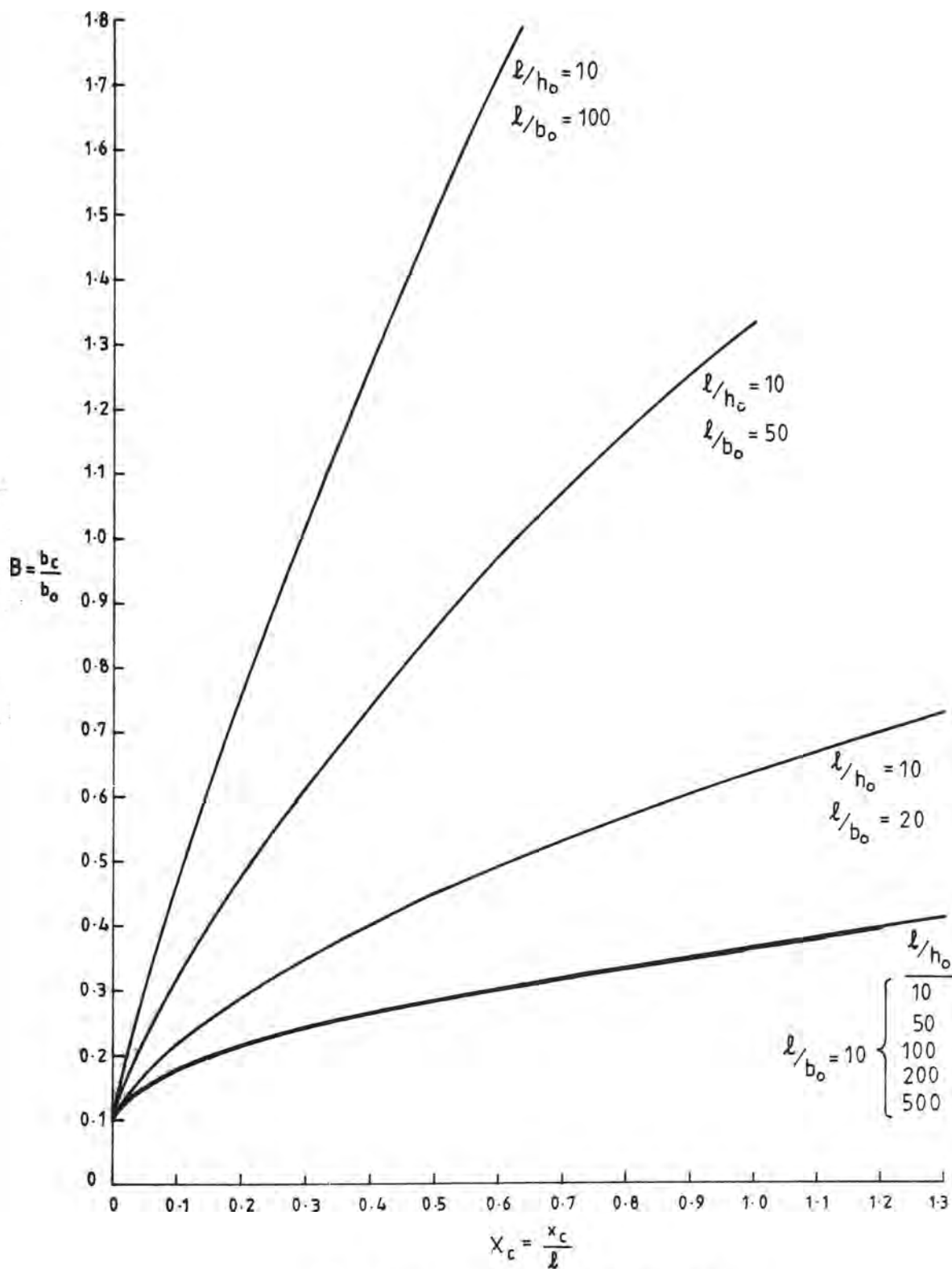
a) Vortex Pair Separation

NUMERICAL RESULTS FOR THE MOTION OF THE VORTEX
PAIR CAP FOR VARIOUS INLET WIDTH AND DEPTH RATIOS

FIGURE 3-12

b) Vortex Pair Cap Advance

FIGURE 3·12(Cont.)
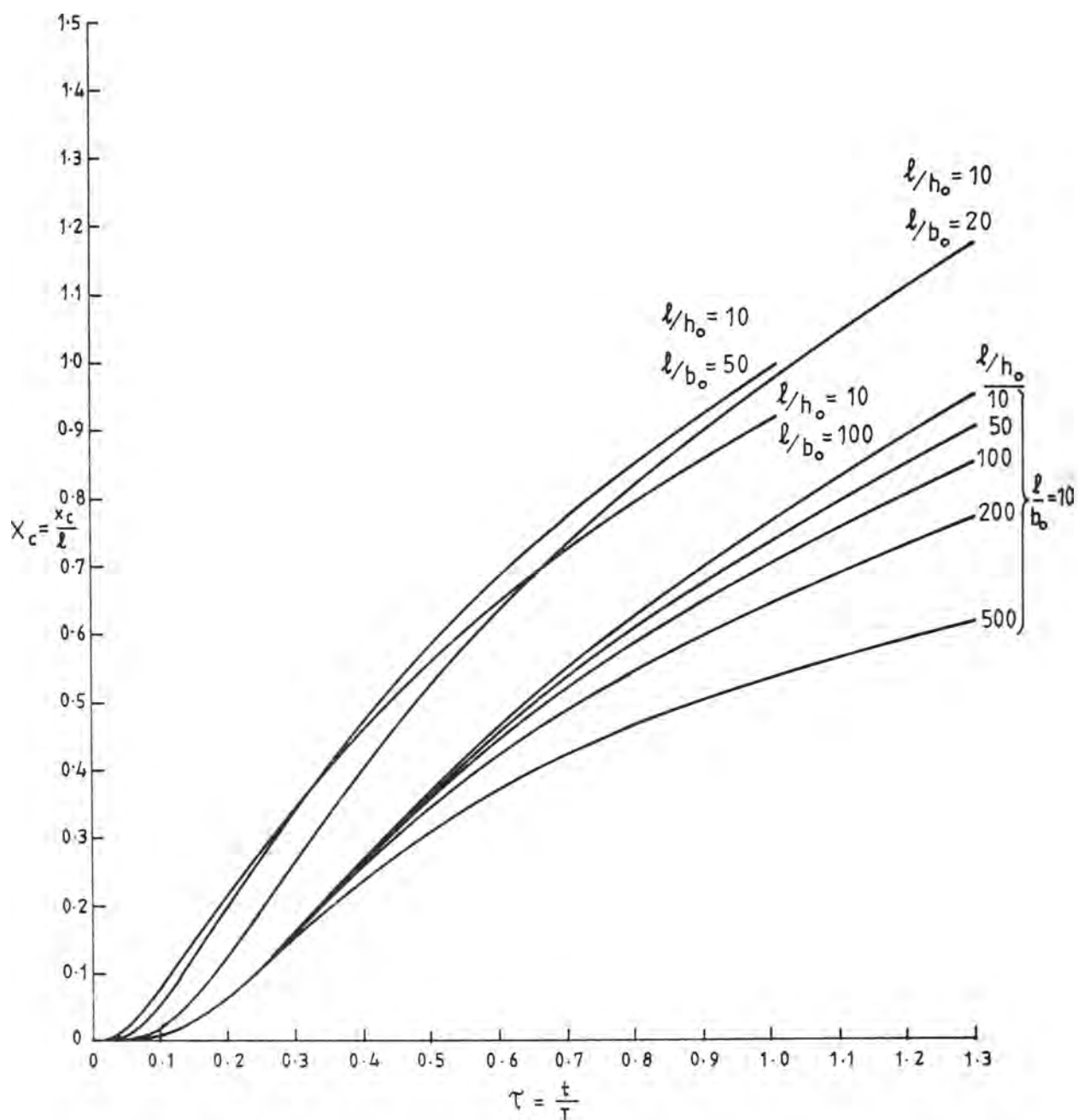
Equation (3.109) can be simplified to give:

$$3H \frac{dB}{d\tau} + B \frac{dH}{d\tau} = 4e\frac{\ell}{b_o}HU \qquad (3.113)$$

Making use of the relationship, $U = \frac{dX_c}{d\tau}$, this becomes:

$$2H \frac{dB}{dX_c} + B \frac{dH}{dX_c} = 4e\frac{\ell}{b_o}H \qquad (3.114)$$

Equation (3.110) is expanded and simplified to:

$$UB \frac{dH}{dX_c} + 2UH \frac{dB}{dX_c} + BH \frac{dU}{dX_c} = - f_c UB \qquad (3.115)$$

where

$$f_c = (\frac{f\ell}{8h_o} \frac{\pi C_3}{4C_2^2 C_1})$$

Equations (3.114) and (3.115) can be reformulated in terms of the depth H as a consequence of the linear depth variation:

$$H = 1 + \alpha_1 X_c \qquad (3.116)$$

or,

$$\frac{dH}{dX_c} = \alpha_1 \qquad (3.117)$$

Thus Equations (3.114) and (3.115) become:

$$2\alpha_1 H \frac{dB}{dH} + \alpha_1 B = 4e\frac{\ell}{b_o}H \qquad (3.118)$$

and

$$\alpha_1 HB \frac{dU}{dH} + 2\alpha_1 HU \frac{dB}{dH} + \alpha_1 UB = - f_c UB \qquad (3.119)$$

Equation (3.118) can be re-arranged and integrated to give:

$$B = (\frac{8e\ell}{3\alpha_1 b_o})H + A_1 H^{-1/2} \qquad (3.120)$$

where A_1 is a constant to be determined. Equations (3.118) and (3.119) can be combined to give:

$$\alpha_1 HB \frac{dU}{dH} = - f_c UB - 4e\frac{\ell}{b_o}UH \tag{3.121}$$

Substituting Equation (3.120) into (3.121) gives:

$$\frac{dU}{dH} = - U[\frac{f_c}{\alpha_1} H^{-1} + \frac{4e\ell}{\alpha_1 b_o} (\frac{8e\ell}{3\alpha_1 b_o} H + A_1 H^{-1/2})^{-1}] \tag{3.122}$$

The initial conditions for this phase of the flow can be set as for the constant depth case. The width B_1, velocity U_1 and depth H_1 are those at location X_1 where the cap becomes decoupled from the jet as defined earlier. Integrating Equation (3.122) gives:

$$\int_{U_1}^{U} \frac{dU}{U} = - \frac{f_c}{\alpha_1} \int_{H_1}^{H} \frac{dH}{H} = \int_{H_1}^{H} \frac{\frac{4e\ell}{\alpha_1 b_o} H^{1/2}}{\frac{8e\ell}{3\alpha_1 b_o} H^{3/2} + A_1} dH \tag{3.123}$$

which becomes:

$$\ln \frac{U}{U_1} = - \frac{f_c}{\alpha_1} \ln \frac{H}{H_1} - \ln \frac{H'}{H'_1} \tag{3.124}$$

where

$$H' = \frac{8e\ell}{\alpha_1 b_o} H^{3/2} + A_1 = BH^{1/2} \tag{3.125}$$

The dimensionless variables are re-normalised as in Section 3.4 in terms of their values at the point of decoupling as $\overline{U} = U/U_1$, $\overline{B} = B/B_1$, and $\overline{H} = H/H_1$. This gives the velocity function as:

$$\overline{U} = \frac{\overline{H}^{-f_c/\alpha_1}}{(\overline{BH}^{1/2})} \tag{3.126}$$

Approximate time power relationships can be obtained by considering the quantity:

$$\overline{UB} = \overline{H}^{-(\frac{f_c}{\alpha_1} + \frac{1}{2})} \qquad (3.127)$$

For $f_c = 0$, this becomes:

$$\overline{UB} = \overline{H}^{-1/2} \qquad (3.128)$$

Now, from Equation (3.120), an approximate relationship for $\overline{B}$ can be obtained at $B_1 \sim 1$ and $H_1 \sim 1$, if the following condition applies:

$$\frac{8e}{3\alpha_1} \frac{\ell}{b_o} \sim 1 \qquad (3.129)$$

Under these circumstances the constant A_1 tends to zero. Thus $\overline{B}$ is proportional to $\overline{H}$. The velocity $\overline{U}$ will be proportional to $\overline{H}^{-3/2}$ and hence varies with time as:

$$\overline{U} \sim \tau^{-3/5} \qquad (3.130)$$

The pair separation $\overline{B}$ varies as:

$$\overline{B} \sim \tau^{2/5} \qquad (3.131)$$

The circulation and Reynolds Number of the flow vary as:

$$\overline{UB} \sim \tau^{-1/5} \qquad (3.132)$$

The impulse varies as:

$$\overline{UB}^2 \sim \tau^{1/5} \qquad (3.133)$$

4. EXPERIMENTAL PROBLEMS AND OBJECTIVES

Experiments were conducted in a laboratory tank to observe the development of a periodic starting jet. These experiments were designed to: provide data on the gross behaviour of the jet; show the influence of variable inlet geometry and source conditions; indicate the velocity distribution in and around the jet and cap; determine the value of constants used in the theoretical model and verify the assumptions made in formulating that model.

4.1 Experimental Apparatus

The main requirement of the experimental set up was to provide a means for qualitative observation and quantitative measurement of a plane periodic starting jet. The flow generated was an idealised model of the discharge from a tidal inlet into the adjacent ocean. A large test area was required to achieve this and to minimise any side boundary effects.

The experiments were performed in a laboratory tank 4.5 m square and 0.8 m deep. The floor of this tank was approximately 1 m above the ground and the sides of the tank were plate glass supported by steel tube frames. A trolley was mounted on the top of the tank walls and was used as a support for the close up photographic work.

A false floor was constructed and placed in the tank. This became the bottom boundary of the basin into which the jet was discharged. The floor was fixed horizontally for experiments with a constant depth or could be raised at the inlet end to provide a uniform bed slope. The dimensions of the false floor were 3 m square and it was

constructed of 5 mm thick asbestos sheeting supported by a timber frame. The false floor was placed in the centre of the tank allowing space in the tank for the cross flow mechanism and the model inlet entrance. A plane vertical boundary along the shoreline (x = 0) was made of galvanised sheet secured to the end of the false floor. A schematic diagram of the tank and false floor is shown in Figure 4.1.

Flow entered the basin via an inlet channel, the details of which are shown in Figure 4.2. This was constructed using 10 mm thick clear PVC material. The inlet entrance was designed so that the width of the rectangular channel could be varied by inserting side blocks of the appropriate thickness. Flow entering the inlet entrance passed through a flow straightener before entering the inlet channel. It was possible to vary the inlet width up to 200 mm. The maximum water depth above the false floor was 100 mm.

4.1.1 Periodic Flow Generating Mechanism

The form of the periodic flow discharging into the basin at the inlet entrance was chosen to represent a typical tidal inlet discharge. The simplest approximation to this is a sinusoidal variation. A convenient way to generate such a flow was to superimpose a sinusoidally varying outflow on a constant inflow at the entrance.

A steady flow Q_{in} was supplied to the inlet through the vertical distributing manifold shown in Figure 4.2. A flow Q_{out} was extracted through the sink at the base of the inlet. Q_{in} was fixed at the required maximum flow, Q_o, for a given experiment. The outflow, Q_{out}, was varied sinusoidally from a maximum flow, $2Q_o$, to zero flow. The resultant flow entered the basin and this flow, Q, varied sinusoidally

PLAN

SECTION A-A
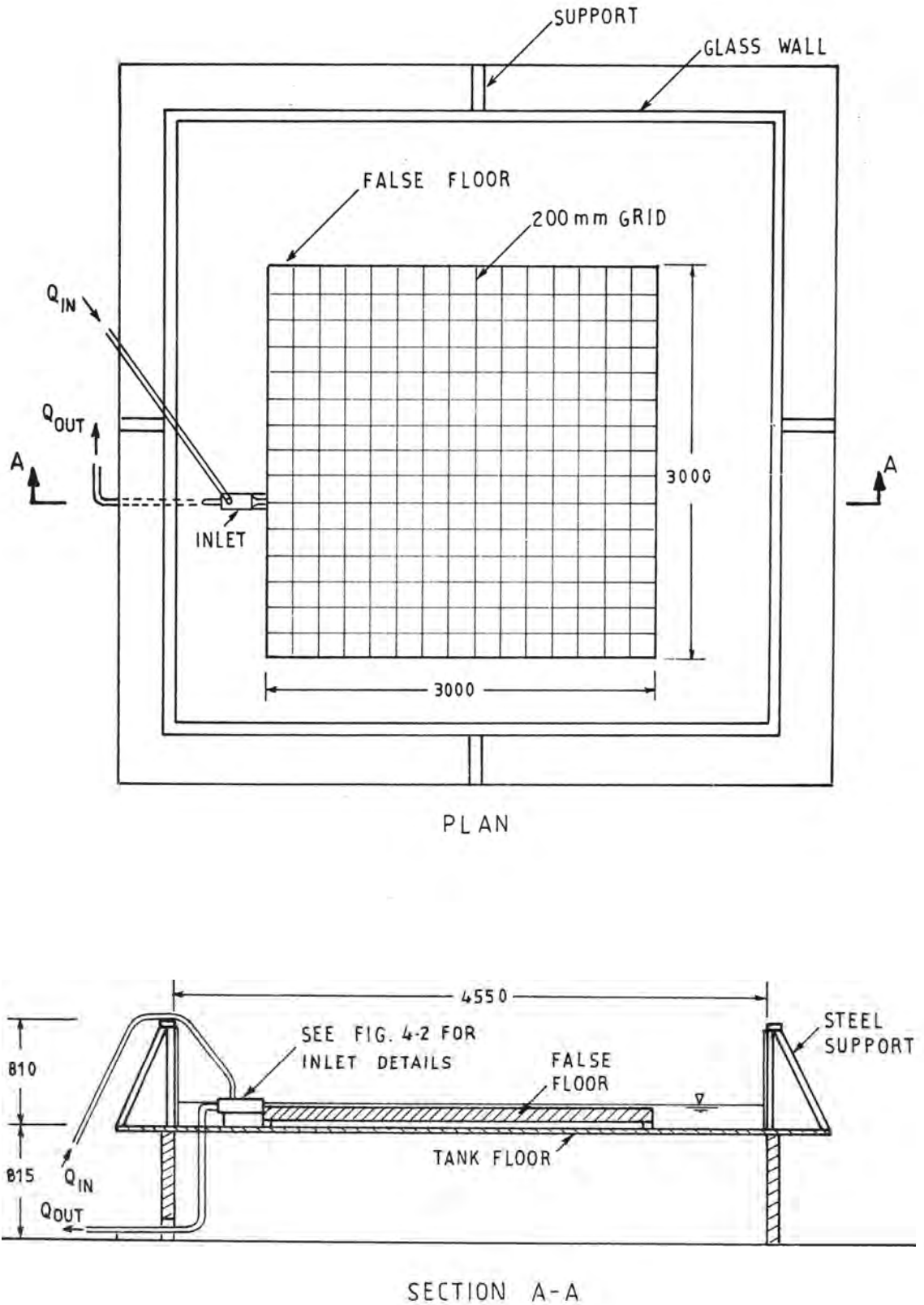
SCHEMATIC DIAGRAM OF TANK SHOWING
FALSE FLOOR AND MODEL INLET

FIGURE 4·1

PLAN

SECTION A-A
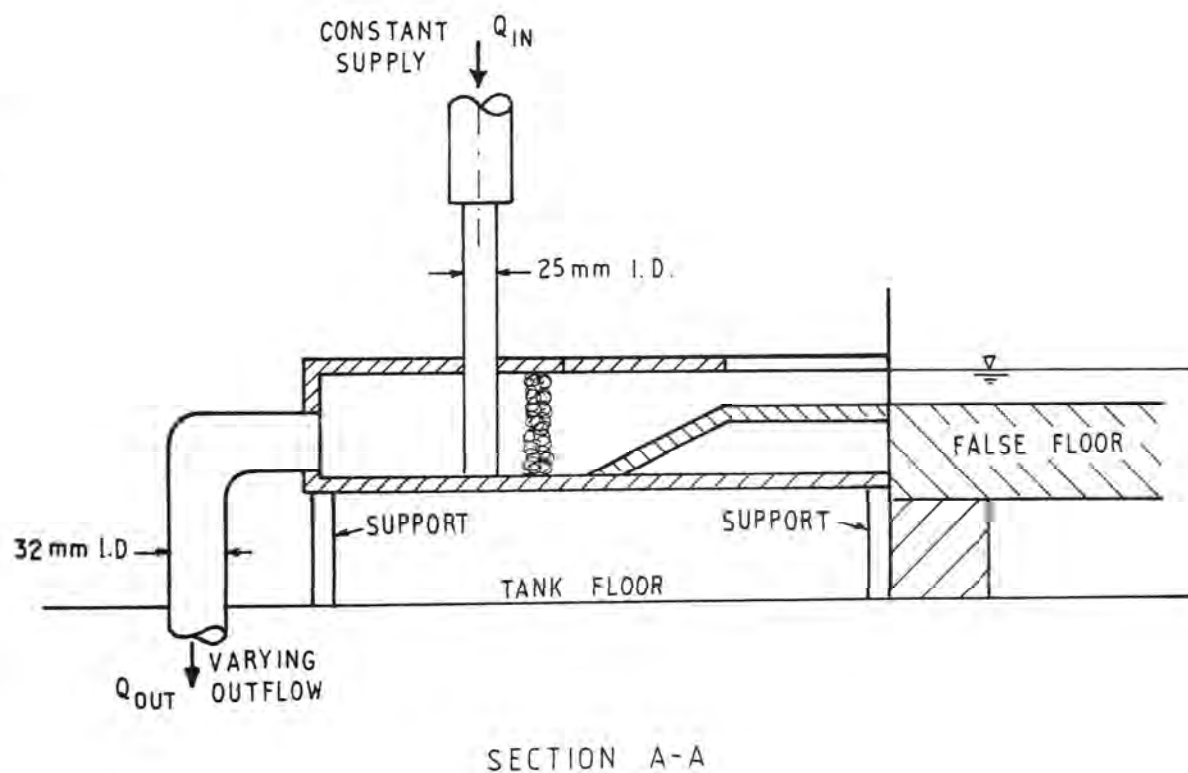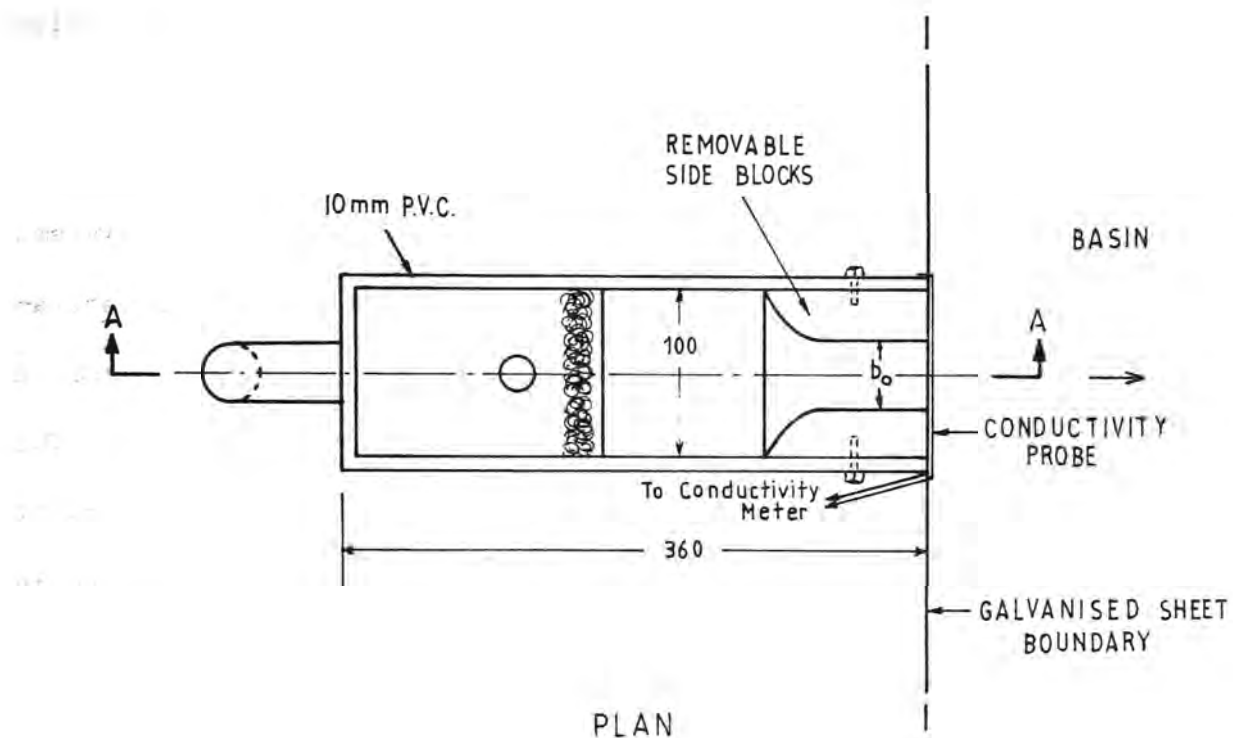
DETAILS OF MODEL INLET

FIGURE 4·2

between values of $+Q_o$ and $-Q_o$. A schematic representation of this superposition of flows is shown in Figure 4.3, and the resulting inlet discharge variation is shown in Figure 4.4.

The inflow, Q_{in}, was obtained from the laboratory supply system. This water originated in Manly Dam, a large reservoir near the laboratory. Water was supplied by gravity to a constant head tank with a 4.3 m available head and then into the laboratory supply system. The outflow, Q_{out}, discharged from the inlet sink via a variable height downstream weir into the laboratory drainage system. The variation in Q_{out} was regulatd by a butterfly valve attached via a crank to a Satchwell control motor. The speed of this motor was 1 revolution per minute and this fixed the period, T, for the majority of the experiments. The speed of the motor could be varied using a Zenith variable transformer to control the supply voltage. The maximum period achieved using this method was 250 secs while still maintaining a constant angular speed.

4.1.2 Inlet Discharge Measurement

The two flow components, Q_{in} and Q_{out}, were monitored separately using venturi metering devices. Venturi meters were used because of their favourable head loss characteristics. The available outflow head was only 1.5 m, which restricted the maximum inlet discharge to 2 x $10^{-4} \, m^3 \, s^{-1}$.

The venturi meters were constructed by the laboratory workshop staff to conform with the specifications laid out in the British Standards Code 1042 - Methods for the Measurement of Fluid Flow in Pipes. The two piezometric tappings were connected to a manometer board which
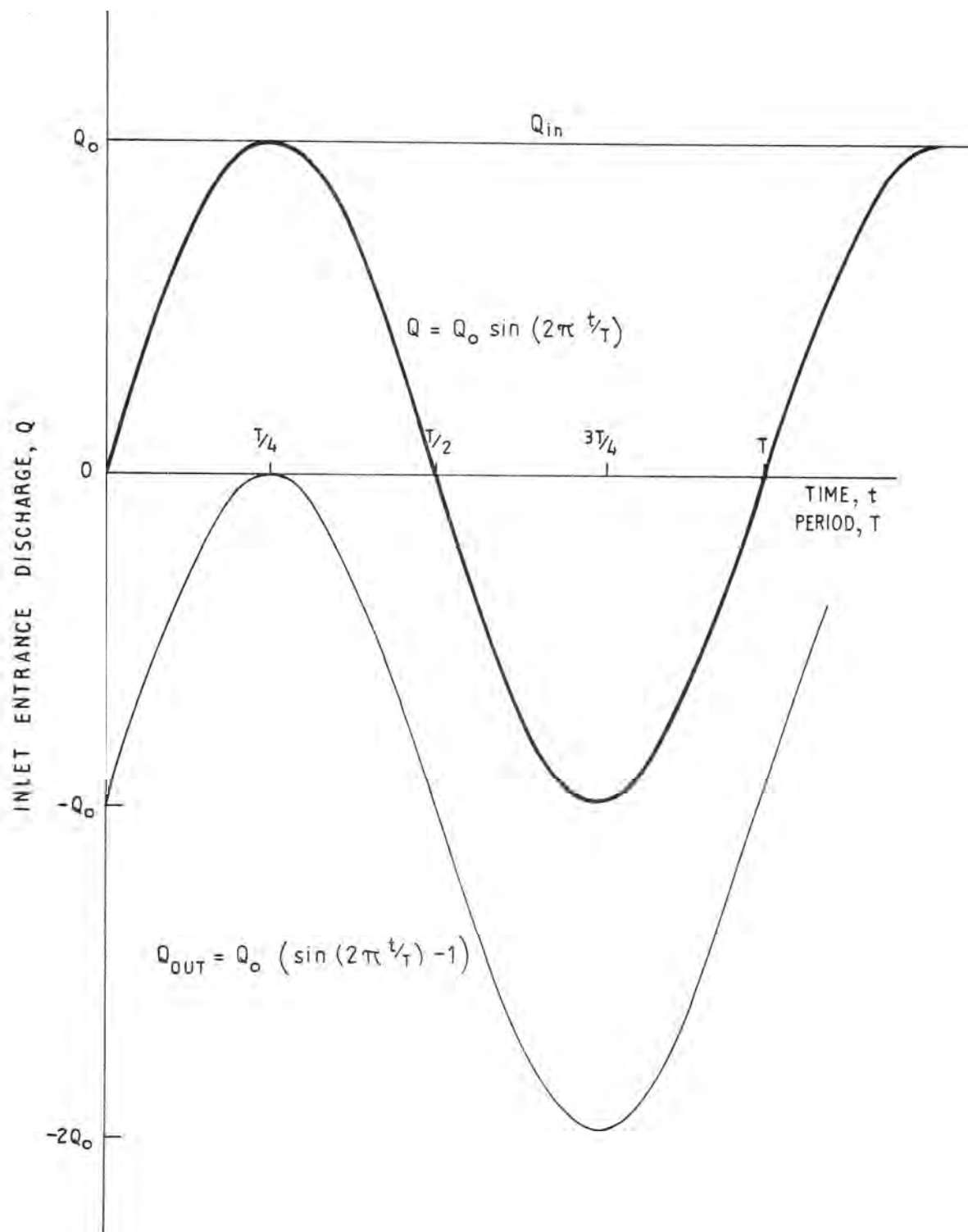
SUPERPOSITION OF INFLOW AND OUTFLOW
TO GENERATE A SINUSOIDALLY VARYING DISCHARGE

FIGURE 4·3
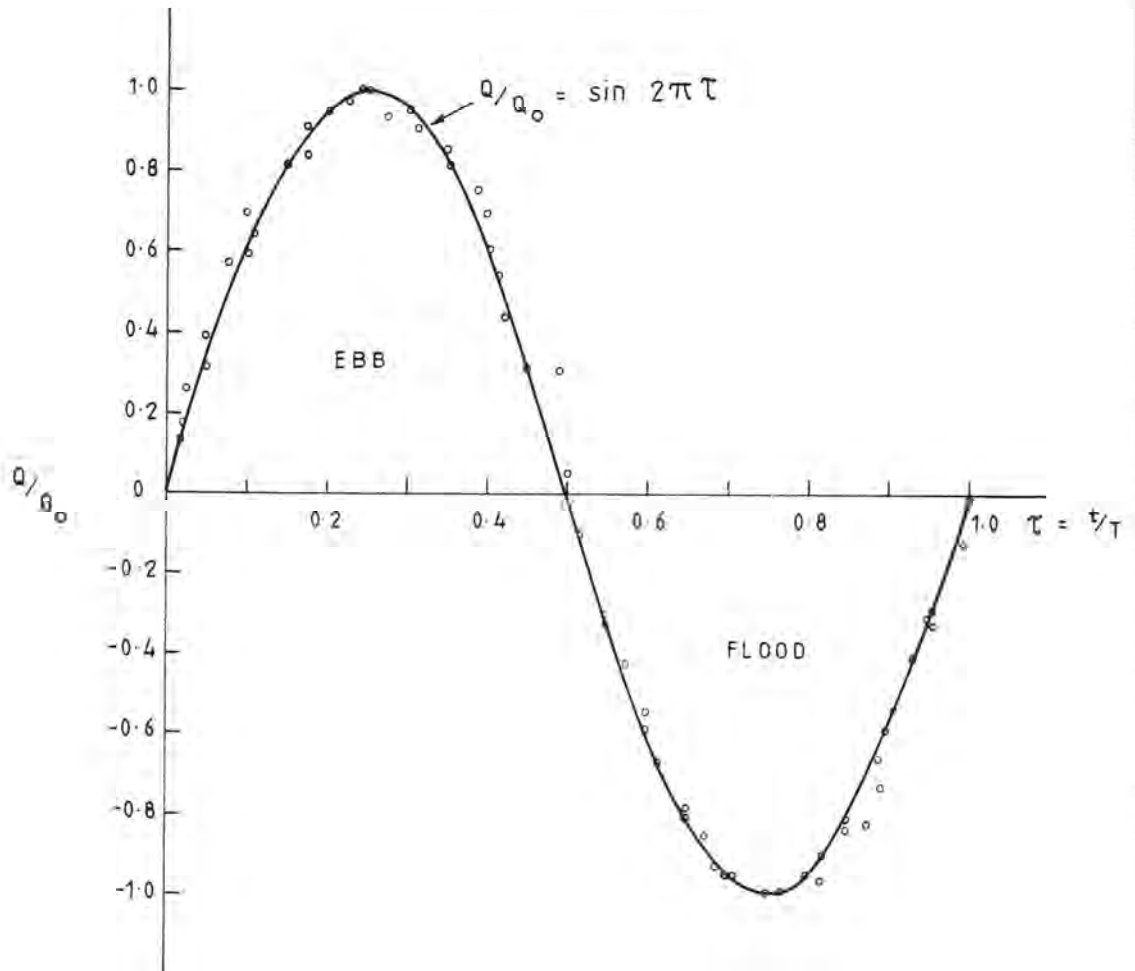
° Data from flow meter calibrations

DIMENSIONLESS MODEL INLET DISCHARGE VARIATION

FIGURE 4·4

could be inclined to increase the sensitivity at low flows. The meters were calibrated by timing the collection of the volume of water discharged for a prescribed piezometric differential head. A meter calibration curve is shown in Figure 4.5. The accuracy of the metered flow was always better than 4%. Direct measurement of the discharge at the inlet entrance was not attempted. The composite discharge variation deduced from the outflow and inflow variations was considered to accurately represent the flow at the inlet entrance. The calibration of the venturi meters was checked regularly. During each experiment the inflow and the maximum outflow were monitored. Over the 5-6 minute period that an experiment was being performed, these values remained constant. A line diagram of the periodic flow generating and measurement system is shown in Figure 4.6.

4.1.3 Cross-Flow Mechanism

A cross-flow parallel to the shoreline (x = 0 boundary) was established using a recirculatory flow system as shown in Figure 4.7. In order to achieve uniform flow across the false floor, an enclosed channel was formed. The width of this channel was set equal to the length of the false floor. To achieve higher cross-flow velocities the width could be reduced. Water collected in an overflow channel at the downstream edge of the false floor was recirculated via a 1.5 H.P. pump to a head box formed by enclosing a section of the test flume as shown in Figure 4.7. The cross-flow velocity profile was measured by releasing confetti and tracking it using the reference grid lines and time exposure photography.
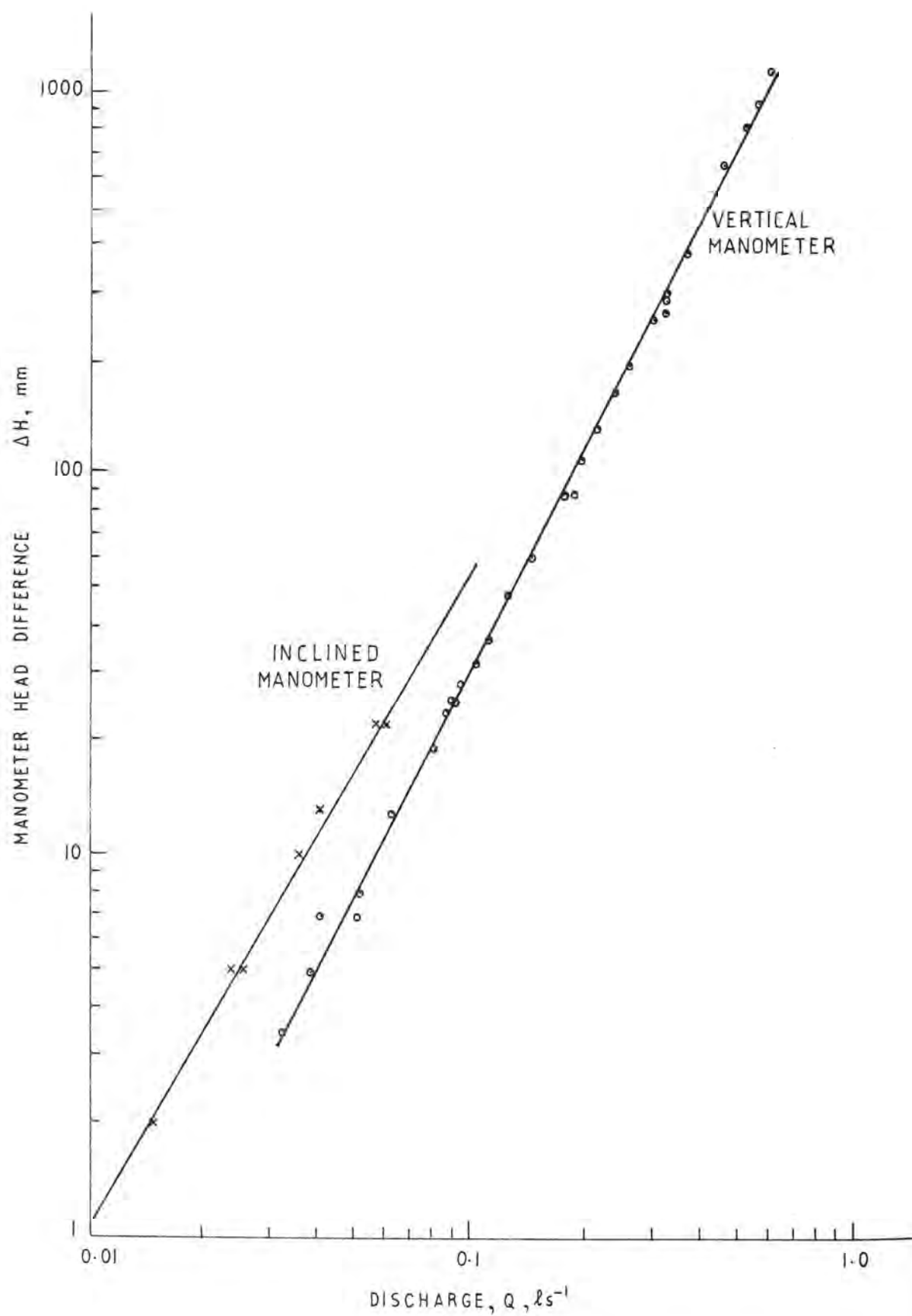
INFLOW VENTURI CALIBRATION

FIGURE 4·5

DIFFERENTIAL HEAD
MANOMETERS

DYE

Q_{IN}

INLET

VARIABLE HEIGHT
FLOW CONTROL WEIR

ISOLATING
VALVE

CRANK

MOTOR

BUTTERFLY VALVE

OUTFLOW
VENTURI METER

Q_{OUT}

MAIN SUPPLY
FROM CONSTANT
HEAD TANK

ISOLATING
VALVE

INFLOW
VENTURI METER

INFLOW CONTROL VALVE
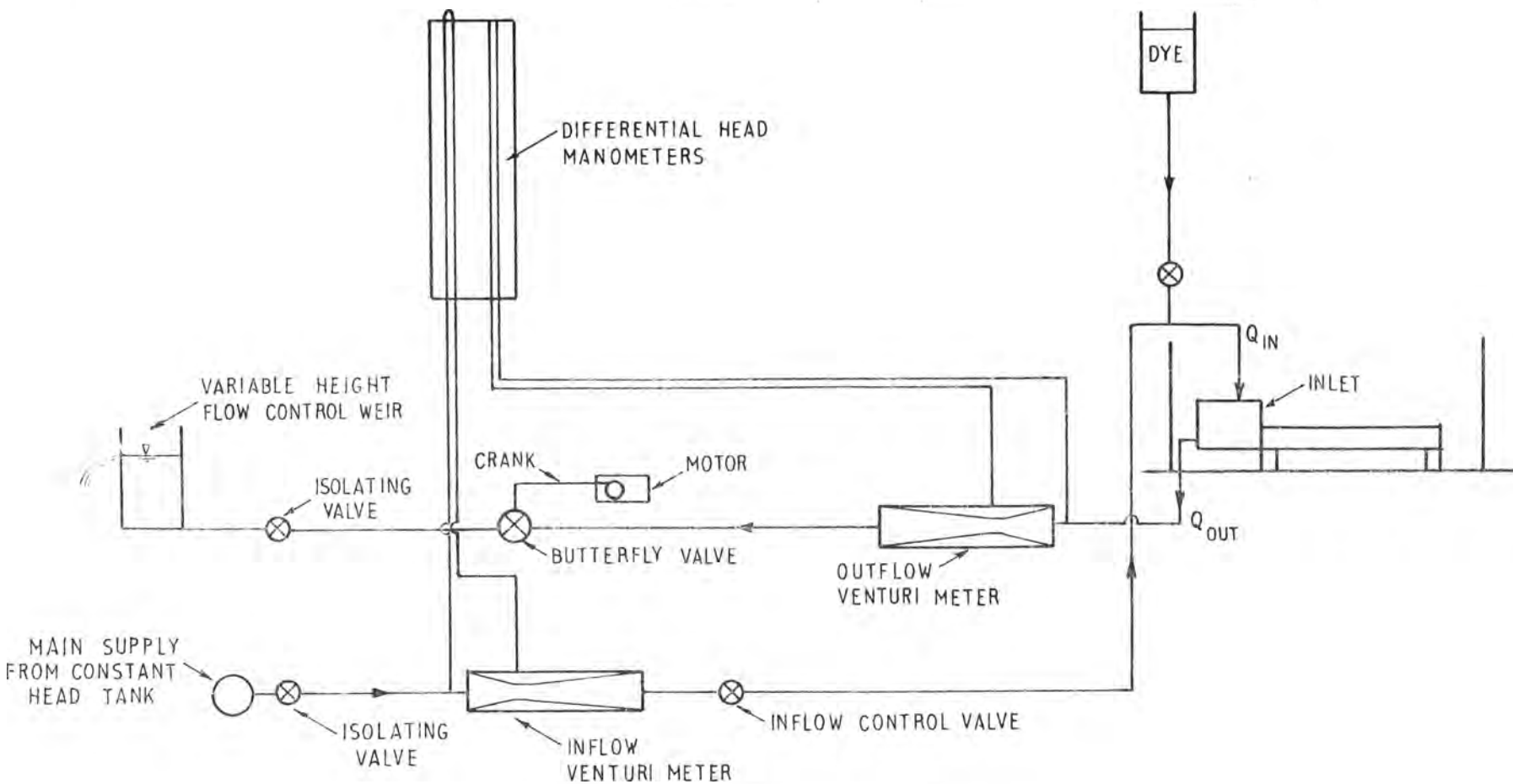
LINE DIAGRAM OF PERIODIC FLOW
GENERATING MECHANISM

FIGURE 4·6
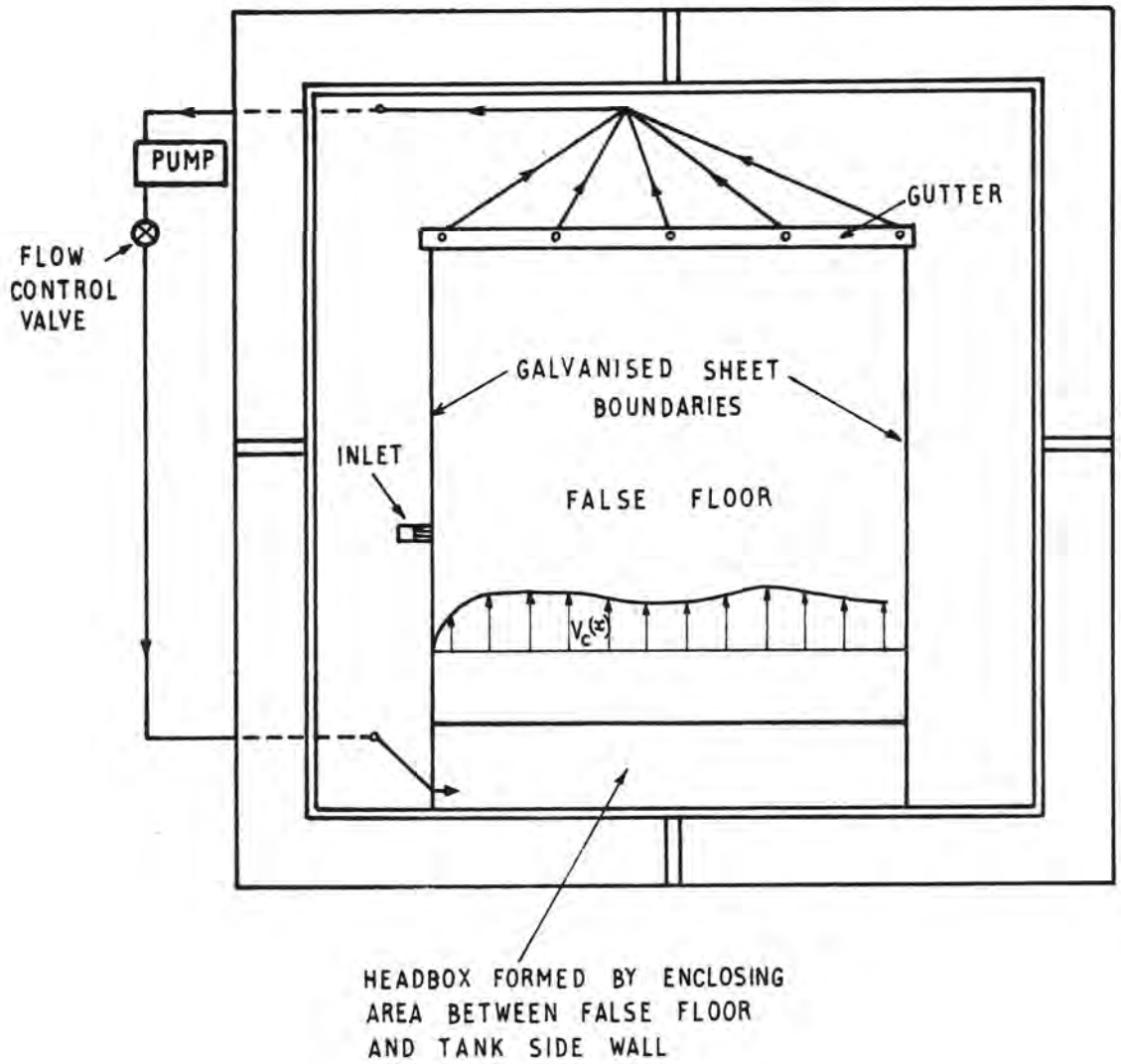
SCHEMATIC DIAGRAM OF CROSS-FLOW

GENERATING MECHANISM

FIGURE 4·7

4.2 Flow Visualisation

A number of techniques were used to visualise the flow. The data obtained was used to make qualitative observations and to provide quantitative measurements of the flow behaviour. The techniques used were dye tracing, surface particle path tracing and hydrogen bubble velocity profile visualisation.

1. Dye was used to distinguish the ebb flow discharge from the clear ambient fluid. A concentrated solution of a blue food dye (Brilliant Blue FCF) was mixed with the constant inflow upstream of the entrance. The main function of the dye was to act as a visual tracer outlining the growth of the vortex pair cap and the location of the leading edge of the flow as it migrated away from the origin. Concentration data in the flow field were not taken, but the concentration was monitored at the entrance channel to provide data on the quantity of discharged ebb fluid that was returned to the inlet during the subsequent flood flow reversal. Conductivity measurements were made using a probe consisting of two 0.142 mm platinum wires. These were stretched horizontally across the entrance channel. The wires were spaced 4 mm apart. A cable connected these to a Radiometer conductivity meter. The output from the meter was fed into a Leeds & Northrop Dual Pen Strip chart recorder which provided a permanent record of the conductivity reading during an experiment. The output speed of the chart was calibrated and found to be within 1% of true, thus providing an effective time base for the records. To link the conductivity readings to the discharge cycle, the second channel of the recorder received input from a potentiometer mounted on the spindle of the butterfly valve controlling the outflow.

As the fluid was meant to be homogeneous, temperature and density measurements of the ambient tank water and the dyed constant inflow were taken just prior to the commencement of a test. The density and temperature difference never exceeded $1 \, kg/m^3$ and $1.4^o C$ respectively.

2. Flow patterns were observed using confetti tracers. It was considered that the confetti gave a good indication of the unsteady flow pattern and, with the aid of time exposure photography could give a reliable estimate of the velocity vectors. Clearly, no indication of the vertical velocity distribution could be given. The tracers were scattered randomly in the field of interest prior to and during the course of an experiment. Dye and tracer movement was monitored photographically from a stationary position 3.5 m above the false floor. The main requirements for the photographic work were as follows: the field of view must cover a sufficiently large area without distortion; the camera was to be remotely controlled ; and the film should give fine grain resolution of the particle traces. To meet these requirements a Nikon FE camera was used. This was fitted with a Nikon MD-1 motor drive unit. Remote control was achieved with a Nikon ML-1 hand-held infra-red transmitter and Nikon ML-1 receiver mounted on the camera. This system was limited as photographs at regular intervals could not be taken, but the advantages of a hand held trigger and the flexibility of timing during an experiment outweighed this disadvantage.

Distortion in the field of view was negligible with a 55 mm Micro-Nikkor lens. The exposure time varied from 0.5 to 2 seconds depending on the source flow parameters. Excellent reproduction of the tracer streaks was achieved using Ilford Pan F (ISO 50) film. Lighting was provided from above using two 1500 W halogen lights. A length scale for the reduction of data was established by a 200 mm grid

painted black on the light grey bottom as shown in Figure 2.2. The distortion of the grid spacing in the photographs was measured to be no greater than 1%.

3. The hydrogen bubble technique was used to determine the velocity distribution in the unsteady jet tail. The low conductivity of the water and the shallow depth used in this study created problems in the application of this technique. Despite the difficulties, this method was employed, being the most accurate technique readily available. The apparatus used is shown schematically in Figure 4.8.

The bubbles were generated by applying a negative voltage to a 0.142 mm platinum wire. 200 mm lengths of this wire were connected between insulated steel pins secured to the floor and were placed at right angles to the axis of the jet at regular intervals. The wires were 15 mm above the bed in 25 mm deep water. The galvanized sheeting making up the boundary of the model basin acted as the anode. Preliminary investigations indicated that the most suitable technique was to pulse each wire in turn at approximately 3 pulses per second. A 100 volt, low current DC power source was applied between the cathode and anode to ionize the water and form hydrogen bubbles. This process was enhanced by filling the tank with a weak solution of sodium sulphate, Na_2SO_4 - approximately 0.15 grams/litre - which increased the conductivity of the water twofold. To prevent any density effects the constant inflow was dosed with a concentrated solution - approximately 20 grams/litre. - giving a similar concentration of salt in the inflow as in the basin water.

BUBBLE TRACE

PLATINUM
WIRE
CATHODES

GALVANISED SHEET ANODE

INLET
ENTRANCE

SYNCHRONISED
CAMERA CONTROL

PULSE
CONTROL

STABILISED D.C
POWER SUPPLY
FOR PULSE CONTROL

A.C MAINS
SUPPLY

ZENITH
VARIABLE
TRANSFORMER

240/240 ISOLATING
TRANSFORMER
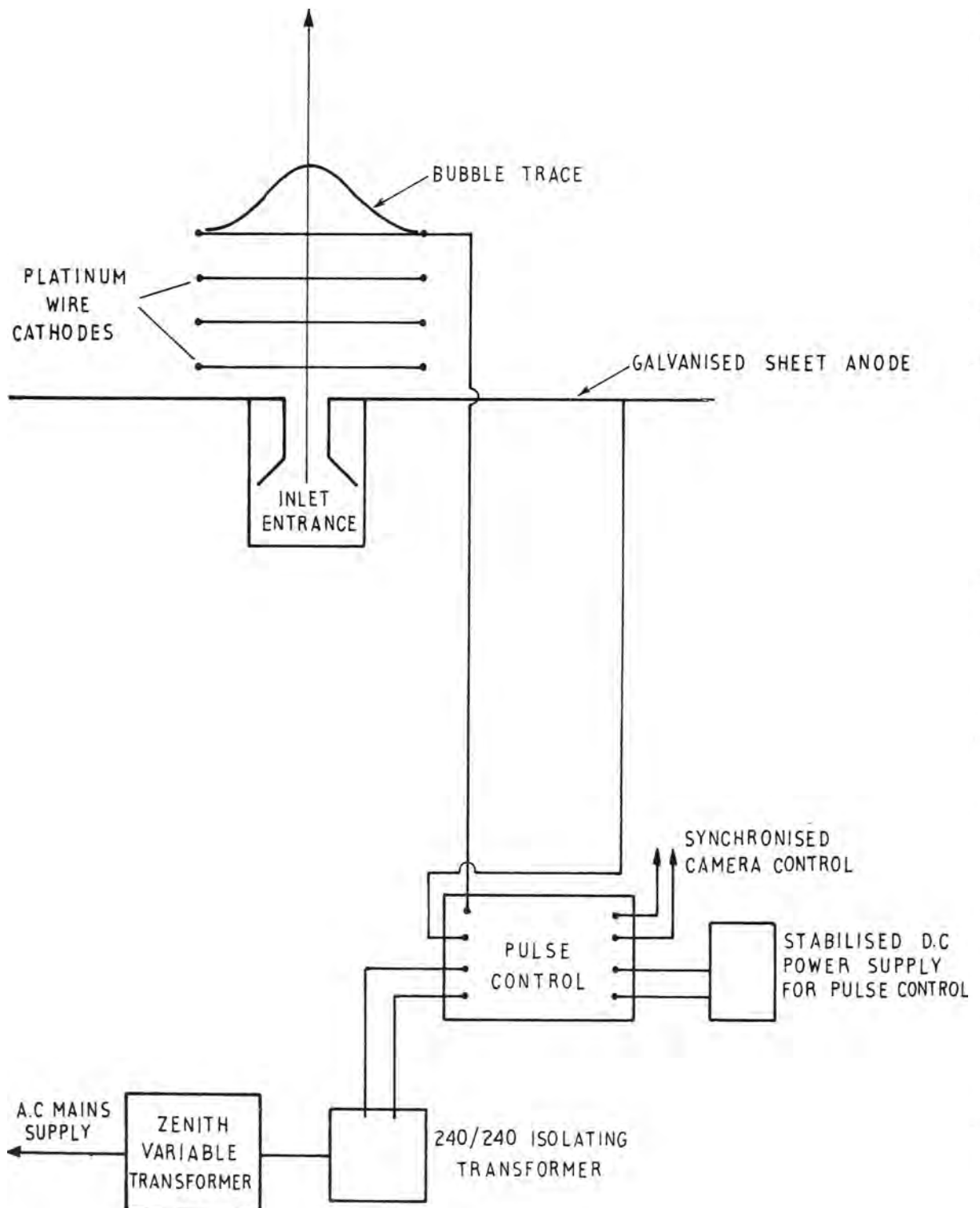
HYDROGEN BUBBLE GENERATION APPARATUS

FIGURE 4·8

The pulse length and interval could be controlled by an electronic pulse timing device which also acted as a trigger for the camera.

The depth of water and the remoteness of the bubble wires from the side walls of the tank made illumination of the bubble traces difficult. This problem was overcome by using a Helium-Neon Laser. The beam was directed into the water by a prism, front face mirror and lens placed in series as shown schematically in Figure 4.9. Divergence of the beam through the cylindrical lens provided a band of light in the plane of the wire parallel to the floor. The beam was aligned to be at the height of the wire and to spread out approximately 50 mm in front of the wire. Bubbles generated at the wire reflected the light with high contrast to the false floor background which was painted black. Colour slide film - Kodak Ektachrome 400 - was used as it was found to be the most sensitive to the red light produced by the laser. An Olympus OM-1 camera system was used for these experiments as its 50 mm lens could be set at an f 1.4 aperture. This was necessary because of the low light intensity of the bubble trace. This camera was motor driven and had synchronous control by the hydrogen bubble pulse control device if required.

It was found that a well-defined photographic record was possible by rapidly pulsing the wire and using a 1/30 second shutter speed to obtain photographs at 2 second intervals. This work was carried out at night for optimum effectiveness of the laser illumination.
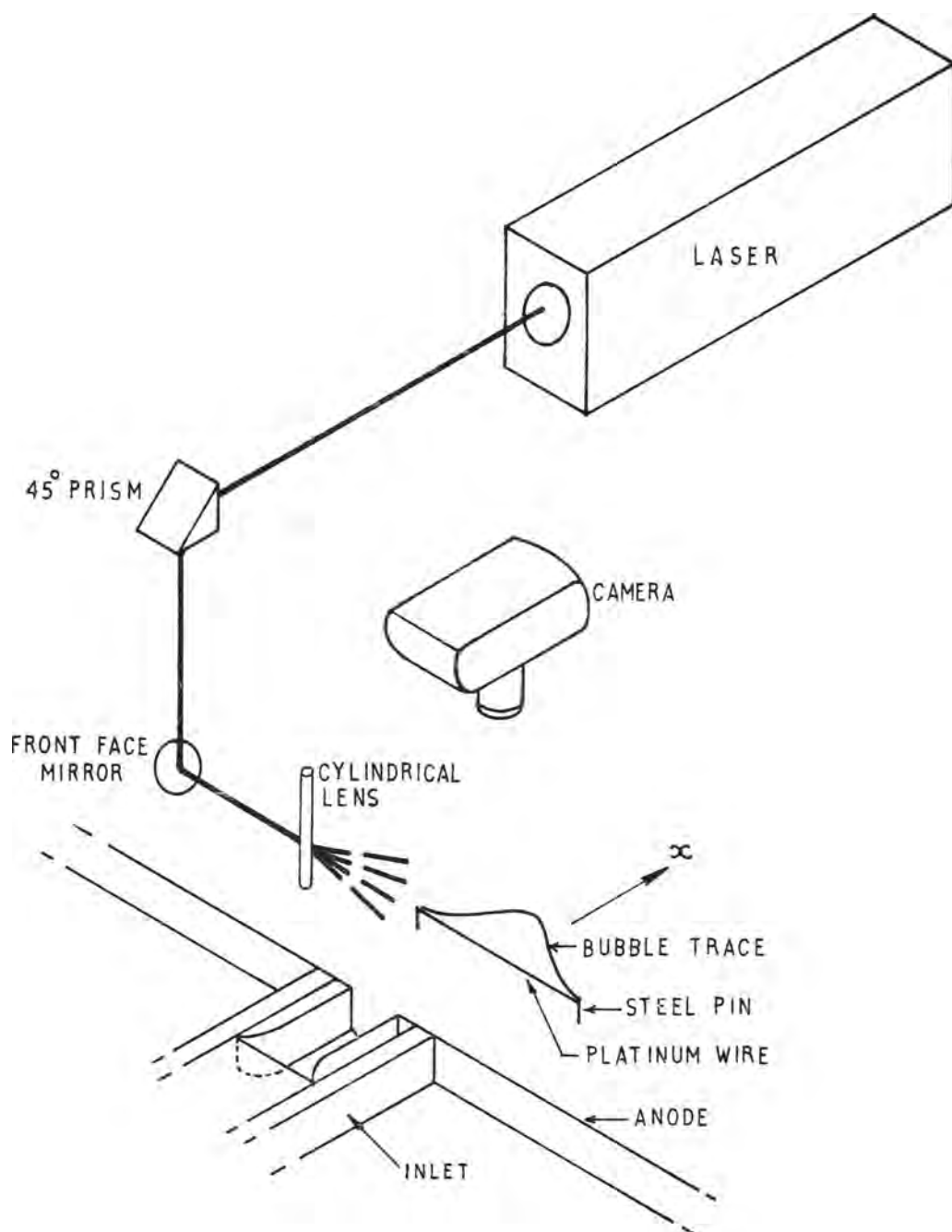
SCHEMATIC OF

HYDROGEN BUBBLE ILLUMINATION APPARATUS

FIGURE 4·9

4.3 Experimental Technique

Experiments were performed using the apparatus described above. The procedure which was followed before, during and after these experiments will now be outlined.

Before filling the tank with water the entrance channel width was fixed and the conductivity probe wires were installed across the channel. The tank was then filled to the desired depth above the false floor. The periodic flow control valves were set for maximum outflow and constant inflow. The required outflow discharge was set by raising or lowering the outflow control weir (see Figure 4.6). The isolating valves on both inflow and outflow lines were then closed. The water in the tank was then allowed to settle to ensure there was no residual disturbance from the filling operation. During this time the photographic and conductivity equipment was set up. Samples were also taken for temperature and density measurements. For experiments with a cross-flow, the recirculating pump was switched on and the required cross-flow velocity established. Sufficient time was allowed to ensure uniform flow before commencing an ebb discharge. At the commencement of an experiment the lighting was switched on and the inflow and outflow isolating valves opened. This set the peak flood flow, $-Q_o$. The dye supply was switched on, the venturi manometer readings checked and the flow rate adjusted if necessary. The surface tracers were then scattered over the area of interest.

The periodic flow control motor was switched on and the photographic record commenced. The ebb flow commenced 15 seconds later (for $T = 60$ seconds). At the completion of one cycle the dye supply was turned off. The flow continued for another three cycles. During the

fourth cycle flood phase, the dye supply was turned on and the photographic record continued from the commencement of the next ebb flow. It was considered that the ambient near-field flow conditions associated with a continuous periodic flow would be established by the fifth cycle. In some cases where the characteristic length was large, the second or third cycle was recorded to avoid any boundary effects due to the finite size of the tank.

The interval between photographs during an experiment depended on the period chosen. For a period T = 60 seconds, photographs were usually taken at 2 or 5 second intervals. If the vortex pair remained coherent, the photographic record was extended to follow the migration of the pair for as long as possible. In most cases, however, the pair became unrecognisable after one period.

At the completion of the experiment the tank was drained. This was necessitated by the spread of the dye. The films were processed immediately in the laboratory darkroom by the author. This revealed any problems with the experiment or the photographic technique, and if necessary the experiment would be repeated. Photographic prints were not made of the negatives because of the numbers involved. Instead, use was made of a micro fiche reader printer. The prints from this machine were foolscap in size and were obtained immediately. Although not as well defined as photographic prints they had sufficient clarity for the data reduction required. Negatives could be viewed with this machine and data reduced directly if needed.

The source of all raw data thus consisted of the photocopies and the conductivity traces. Analysis of the photographic record as shown typically in Figure 2.2, was facilitated by the grid and the clock,

providing the length scale and time base respectively. A typical output from the chart recorder is shown in Figure 4.10. The use made of this data will be discussed in a later section.

closed

open
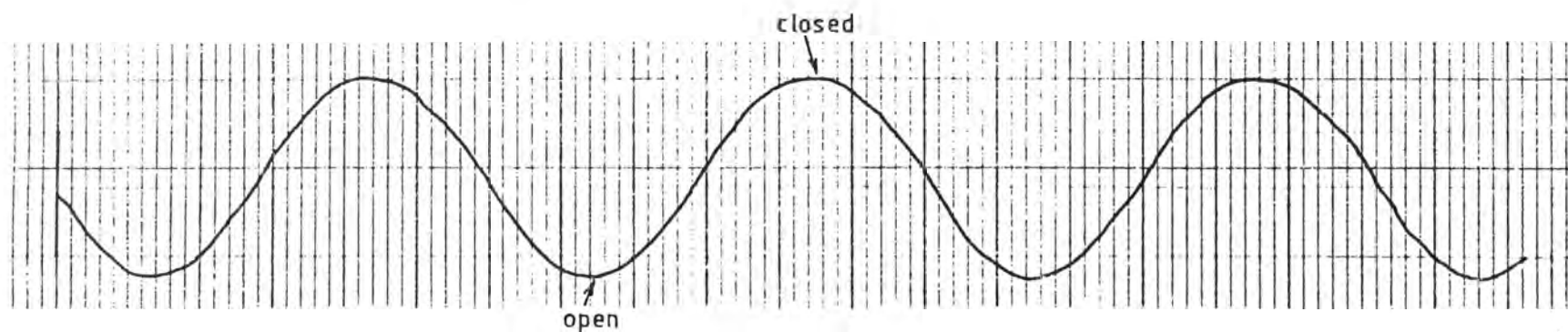
b) FLOW CONTROL VALVE OPERATION

Trace lag

Flood commencement

Dyed ebb discharge commencement

Clear water
ebb discharge
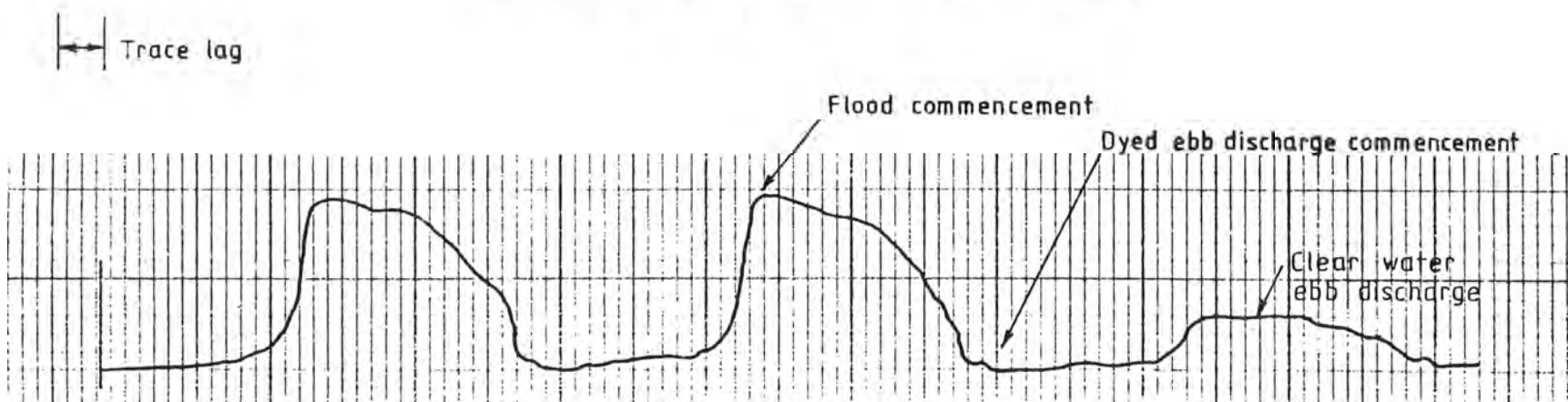
TRACE READ FROM RIGHT TO LEFT

a) SAMPLE OUTPUT FROM CONDUCTIVITY
PROBE ACROSS THE INLET CHANNEL

FIGURE 4·10

5. THE STRUCTURE AND DYNAMICS OF THE VORTEX PAIR CAP

The equations of motion developed in the earlier chapters describe the gross behaviour of a periodic starting flow. Assumptions were made regarding the size and shape of the vorticity containing region associated with such a flow. These enabled the classical theory of vortex pair motion to be applied to turbulent vortices.

In Chapter 6 the experimental results for the gross behaviour of a periodic starting jet will be presented and discussed. But first, the distribution of vorticity in the vortex pair cap will be discussed in relation to the velocity of propagation, the shape of the cap of fluid surrounding the vortex pair and the dynamics of the entrainment and vorticity cancellation processes that occur in a real turbulent flow. A background review of this matter will first be given followed by a discussion of the experimental results obtained for the various shape factors used in the theoretical analysis.

5.1 Background

5.1.1 Velocity of Propagation

The classical theory gives the velocity of propagation of an ideal pair of line vortices as:

$$u_p = \frac{K}{4\pi y_c} \tag{5.1}$$

The ideal line vortex, where all the vorticity is concentrated at a singularity, cannot exist in a real fluid because of viscous diffusion. When viscosity is present, the vorticity is confined to a finite

region called the vortex core. Outside the core, the mean flow can be considered irrotational and the potential theory valid. In two-dimensional inviscid flow, Batchelor (1967) has shown that the behaviour of a line vortex does not depend critically on the finite size of the vortex tube, or the distribution of vorticity. Recent analyses by Saffman (1979) and Pierrehumbert (1980) have shown that this is only valid for a finite core with an equivalent radius less than approximately 0.42 times the vortex separation. For a larger core the velocity of propagation is reduced.

The study of vortex pair models to date has been concerned mainly with the behaviour of aircraft wake vortices. It has been shown that for aircraft wakes the core size can affect the stability of the vortex pair (Widnall et al, 1971), but that the velocity of propagation is independent of the core size. This is because in aircraft wakes the ratio of core radius to vortex separation has been shown to be 0.1 (Spreiter and Sacks, 1951). Experimental studies simulating aircraft wakes have achieved similar ratios. Barker and Crow (1977) and Tomassian (1979), for example, found the ratio in the range of 0.15 to 0.2. This must increase with time, and ultimately the core size will affect the propogation velocity. It has also been shown that axial flow in the core has an important influence on vortex behaviour.

In the present case the origin of the vorticity is the inlet channel boundary layer. The vorticity generated here is advected through a turbulent plane jet and into the vortex pair cap. The vorticity will thus be more widely distributed than in the case of aircraft wake vortices and have a less well defined core region. Turner (1960) has suggested that for a widely distributed vorticity, a similarity assumption of the form:

$$u_v = \frac{K}{C_1(2y_c)} \tag{5.2}$$

might be necessary, where C_1 is a constant dependent on the vorticity distribution, and $2y_c$ the vortex spacing. The velocity of propagation, u_v, thus depends:

i. linearly on the circulation;

ii. inversely on the separation between the vortex centres;

iii. on the distribution of vorticity about the axis of symmetry.

It is expected that as the depth of the flow increases (and hence the length of the line vortices), instabilities of the type described by Widnal et al (1971) will cause a bending of the vortex lines. It has been shown for aircraft wakes that instability leads to a sinusoidal distortion of the vortex lines which increases in amplitude until breakdown of the vortices results. This type of instability will be discussed later in relation to the experimental work.

The velocity of propagation of the distorted vortex lines now consists of a component due to the circulation and separation of the lines and a component due to the sinusoidal fluctuation which is dependent on the core structure. Widnall et al (1971) have shown this velocity to have a form similar to that of the limiting case of a curved vortex line, the vortex ring. The propagation velocity was found to be

$$u_v = \frac{K}{2} k^2 R_o \sin kx \ [\ln \frac{1}{kR} + C] \tag{5.3}$$

where u_v is the propagation velocity, K is the circulation, R the core radius, k and $R_o \sin kx$ the wave number and local amplitude of the disturbance and C a constant dependent on the vorticity distribution in the core. The presence of the bottom boundary layer in real flow will

also cause a three-dimensional distortion of the line vortex. The analysis presented in this thesis was made assuming that the vortex pair remained stable and that axial flow in the core was negligible. Accordingly, the velocity of propagation is taken to be given by Equation (5.2).

5.1.2 The Shape of the Vorticity Containing Region

The flow under investigation is taken to consist of a turbulent pair of vortices of finite core size moving with a self-induced velocity. Associated with this pair is a co-travelling volume of fluid comprising the recirculation cell of the vortex pair. In the present work this volume has been referred to as the vortex pair cap. Vorticity will be distributed throughout the cap due to vorticity diffusion from the vortex core.

The vortex pair cap is defined experimentally as the volume of dyed fluid. This volume may or may not represent the vorticity containing region comprising the pair of vortices and the surrounding recirculation cell. The shape of the vortex core and the vorticty containing region will now be discussed.

5.1.2.1 Vortex Core

In real flows the vorticity is distributed over a finite area, but in a line vortex the vorticity is concentrated at the line singularity. The spread of vorticity in the former case is due to the turbulent diffusion. Moore and Saffman (1971) have shown that for a line vortex under the influence of an imposed strain - such as vorticity of opposite sense - its behaviour is dependent on the shape of the cross-

section of the vortex and the vorticity distribution. A solution was found for the case where vorticity is uniformly distributed within a elliptical cross-section with the major axis parallel to the direction of motion. Saffman (1979) has used these results to derive the properties of a family of elliptical vortex pairs of varying size and separation. Pierrehumbert (1980) has extended Saffman's approximate solution to the case of more general shape. A brief outline of Pierrehumbert's model will now be given.

Pierrehumbert (1980) has considered the case of a vortex pair with vorticity uniformily distributed within the vortex core as shown in Figure 5.1. A solution was found in a frame of reference translating with the vortices if the boundaries of the pair were streamlines. As the stream function, ψ, must be constant on this boundary the shape was determined. Taking the boundaries to be symmetrical about the y axis, and the x axis to be the line of symmetry between the vortices, then the stream function for the boundary g(y) was given by Pierrehumbert as:

$$\psi\,(g(y),y) = \omega_o \int_{y_1}^{y_2} \int_{-g(y)}^{g(y)} \frac{1}{2} \log\,[(x-x')^2 + (y-y')^2]\;dx'dy'$$

$$+ u_v\,y \tag{5.4}$$

where ω_o is the absolute value of the uniformily distributed vorticity and u_v is the velocity of propagation in the x direction. This equation was solved numerically for constant values of the stream function. Figure 5.2a is a reproduction of the numerical results obtained by Pierrehumbert. Figure 5.2b shows the shape of a family of boundaries between rotational and irrotational flow for one vortex. These results
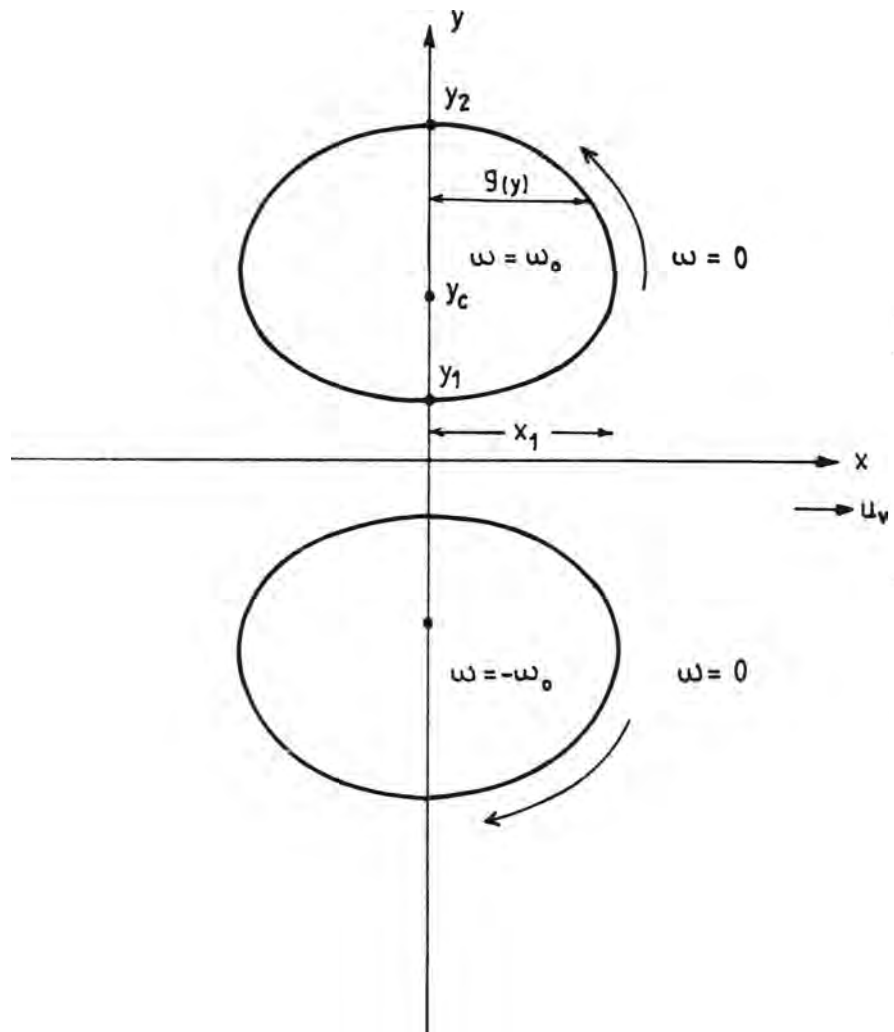
CROSS–SECTION OF VORTEX PAIR WITH
UNIFORMLY DISTRIBUTED VORTICITY

FIGURE 5·1
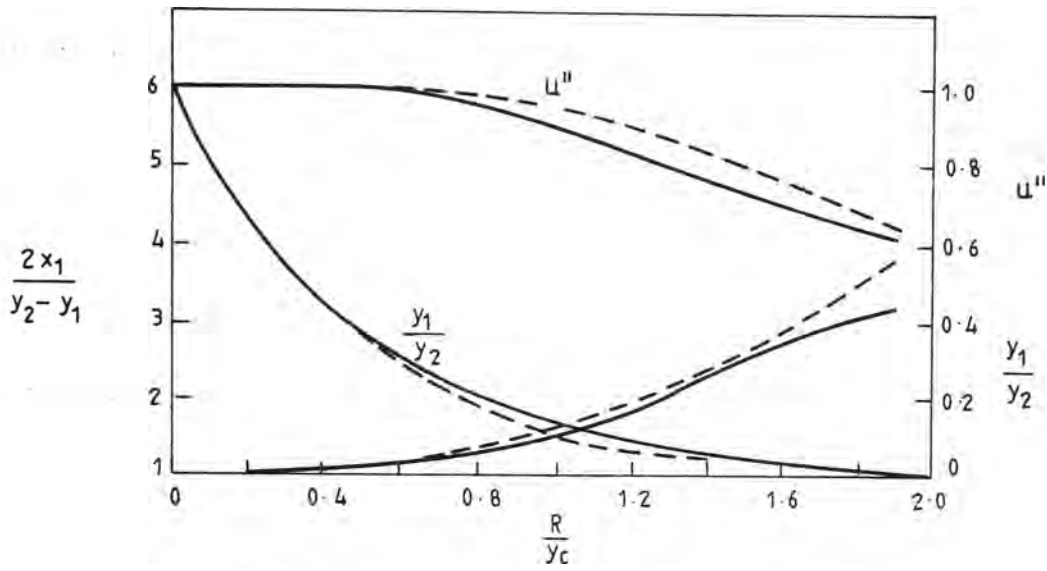
Properties of Vortex Pairs for
various values of R/y_c
(See text for details)
(After Pierrehumbert 1980)

(a)
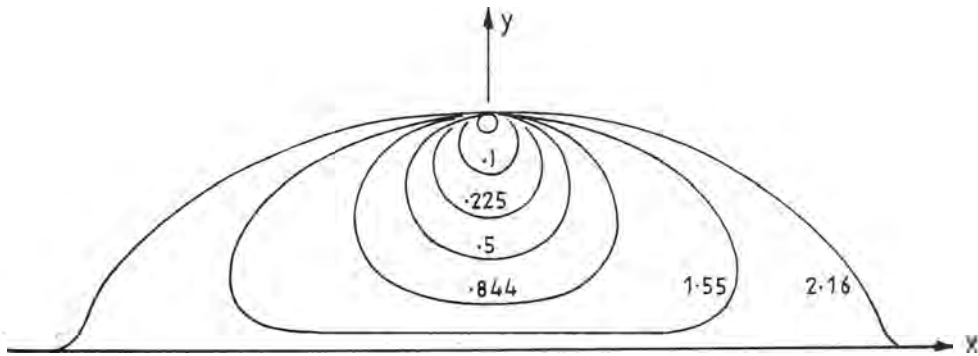
Boundaries between rotational and irrotational
flow of a vortex for various values of R/y_c
(After Pierrehumbert 1980)

(b)

FIGURE 5·2

are expressed in terms of a normalised radius, R/y_c, a normalised velocity, $u" = u_v/u_p$, and a shape factor, $2x_1/(y_2 - y_1)$, where y_c is the half spacing of the vortex centroids and R is the effective radius of the vortex given by:

$$R = (A/\pi)^{1/2} \tag{5.5}$$

where A is the area of each vortex core bounded by the function $g(y)$ given as:

$$A = \int_{y_1}^{y_2} g(y) \, dy \tag{5.6}$$

The velocity, u_p, is the velocity of propagation of an ideal pair of point vortices at $y = \pm y_c$, given by:

$$u_p = \frac{K}{4\pi y_c} \tag{5.7}$$

where
$$K = \omega_o A \tag{5.8}$$

The exact shape of the boundary as derived by Pierrehumbert was found to yield similar vortex pair properties to the approximate ellipse solutions obtained by Saffman (shown in Figure 5.2a as dashed lines).

In the present case it is not possible to experimentally determine the exact shape of the vortex boundaries. The experimental data indicate however that they can be reasonably approximated by ellipses, which are taken to be symmetrical about a line $y = \pm y_c$.

The area of the vortex is then:

$$A = \pi x_1 (y_2 - y_1) \qquad (5.9)$$

The area of fluid carried along with the vortex pair can be determined by evaluating the form of the separating streamline $\psi = 0$ (Figure 5.3). For a pair of line vortices, Lamb (1952) gives this as an oval contour, the equation of which is:

$$\frac{y}{4\pi} + \log[((y - y_c)^2 + x^2)^{1/2} - ((y + y_c)^2 + x^2)^{1/2}] = 0 \qquad (5.10)$$

The semi-axes of the oval are 1.73 y_c and 2.09 y_c. The area enclosed by the contour is $8\pi\gamma \, y_c^2$, where $\gamma \simeq 0.45$. The results of Pierrehumbert indicate that vortices with an effective radius, R, less than about 0.42 y_c can be considered to behave as a pair of line vortices. For values greater than this the vortex properties can be taken from Figure 5.2a. In particular, the velocity of propagation can now be expressed in the similarity form of Equation (5.2), provided structural similarity can be demonstrated as the vortex pair develops in time. The validity of the predictions of Pierrehumbert and Saffman have not been proven experimentally by previous investigators as the majority of research into vortex pairs has dealt with aircraft wake vortices which have core radii much less than 0.42 times the core separation.

5.1.2.2 Vorticity Containing Region

In his development of a generalised momentum equation for a vorticity containing region, Wood (1965[2]) has taken it to be circular. For experiments where dye is used to mark the vorticity containing region, the dyed area can be considered the area of fluid accompanying the
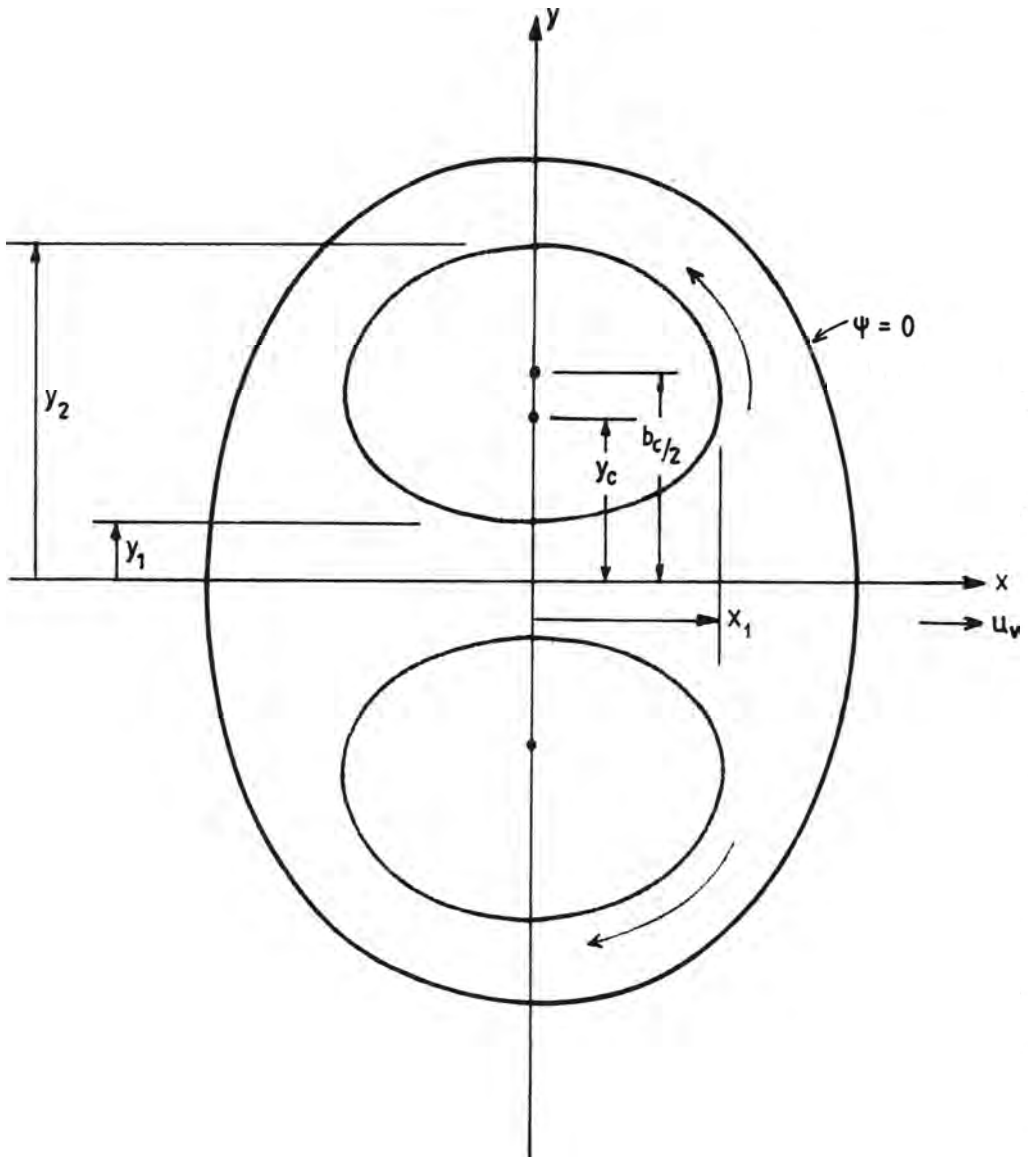
FLUID VOLUME ASSOCIATED WITH

AN IDEAL PAIR OF VORTICES

FIGURE 5·3

vortex pair. The molecular diffusion of the dye is relatively slow compared to that of vorticity, and hence over time the dyed area can be taken as a reasonable approximation to the vorticity containing region.

It is interesting to note from Pierrehumbert's results that in the limiting case of the two vortices just touching on the axis of symmetry, the area of the two vortices is equal to that of the vorticity containing region. The separating streamline in this case will be oval in shape with the long axis in the direction of propagation being approximately twice the length of the minor axis.

5.1.3 The Growth of the Vorticity Containing Region

The growth of the vortex pair cap is, in a periodic jet, due to the mass advected from the jet during the starting flow phase, and the turbulent entrainment of ambient fluid into the cap. The component of growth due to entrainment will now be considered.

The mechanisms for this entrainment are still not fully understood. Maxworthy (1972, 1974) has proposed that for a vorticity containing region comprising a cap of fluid travelling with a small, but finite sized turbulent vortex core, turbulent entrainment occurs at both the interface between the cap and the ambient irrotational flow and the interface between the core and the surrounding cap fluid as shown in Figure 5.4. Vorticity diffuses from the core to the surrounding cap fluid. Mixing between the cap and the ambient fluid causes ambient fluid to be entrained into the cap by an engulfment process. Vorticity which diffuses out of the cap is advected by the ambient fluid to the region behind the cap, where it forms a wake. As the velocity of propagation is dependent on the vorticity distribution,
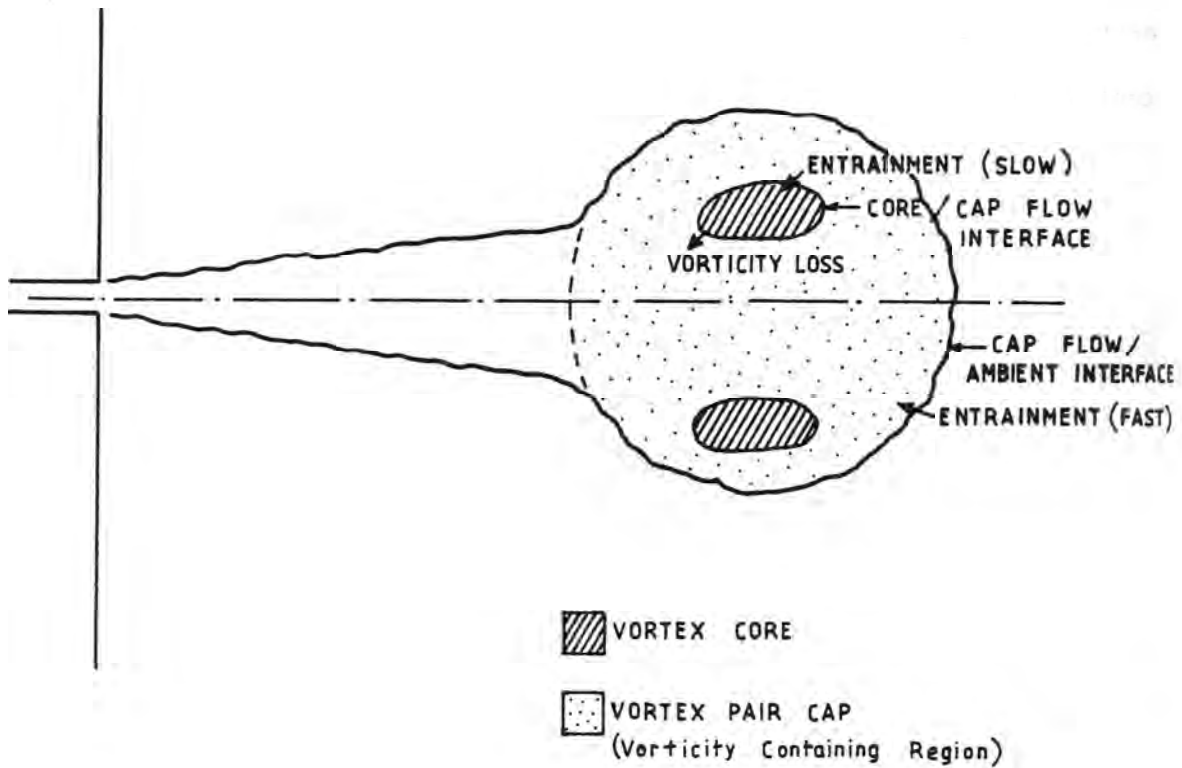
SCHEMATIC DIAGRAM OF

CAP GROWTH MECHANISMS (after Maxworthy, 1977)

FIGURE 5·4

this loss of vorticity results in a slowing down of the pair. It should be noted that in the present case the bottom frictional resistance is another cause of cap deceleration.

The higher rates of shear in the vortex core result in suppression of turbulent mixing between the core and the surrounding cap fluid. Thus the mixing (and hence, the advection of vorticity from the core to the surrounding cap fluid) will be at a slower rate than the mixing between the vortex pair cap (or vorticity containing region) and the ambient fluid. Thus the overall growth of the cap of fluid will be controlled by the loss of vorticity from the core. This explains the slow growth observed in turbulent vortex rings (Maxworthy, 1974), where the core is small compared to the turbulent cap and the vorticity is concentrated.

For a turbulent vortex flow with a more widely distributed vorticity, as is the case in the present study, the mechanisms described above will not explain the higher growth rates observed for both two and three dimensional turbulent vortex motions. A vortex pair or ring which is either impulsively generated at an orifice or which forms the cap of a turbulent starting jet or plume will not have vorticity concentrated in a small core. Instead vorticity will be distributed more uniformly over the whole fluid cap due to the turbulent mixing associated with the method of generation. Thus, mixing at the cap interface will result in a greater loss of vorticity which will be advected behind the cap into a wake and cancelled at the plane of symmetry. The higher level of turbulence in the cap results in the entrainment of a greater quantity of ambient fluid.

The spreading rate for turbulent vortex pairs is usually defined in terms of the spread of the visible edge of the (dyed) vortex cap. A recent study by Wu (1977) has given the entrainment coefficient, or linear spreading constant, as 0.26 on average. Maxworthy's data for vortex rings with a turbulent core showed a spreading rate for the core of the order 0.01. The value obtained by Wu is typical for turbulent starting flows. It is clear that the growth of the vorticity containing region is a function of the distribution of vorticity. Where it is concentrated in a small core, the growth rate is small, whereas for a more widely spread uniform distribution, the growth rate is much greater.

5.2 Experimental Results

In this section experimental results obtained for the shape and dynamics of the vortex pair cap will be presented and discussed in relation to the theoretical predictions outlined above.

5.2.1 Self-Preservation Assumption

The theoretical analysis presented in Chapter 3 was based on the assumption of self-preservation of turbulent flows. Simply stated, this implies that the shape of the turbulence containing region remains constant, and that the distribution of velocity in and around that region also remains constant.

The flow pattern in and around the turbulent region was obtained by analysing the particle traces produced by the time exposure photography. An example of the raw data is shown in Figure 5.5. As the cap is moving relative to a stationary observer, these traces are unsteady.
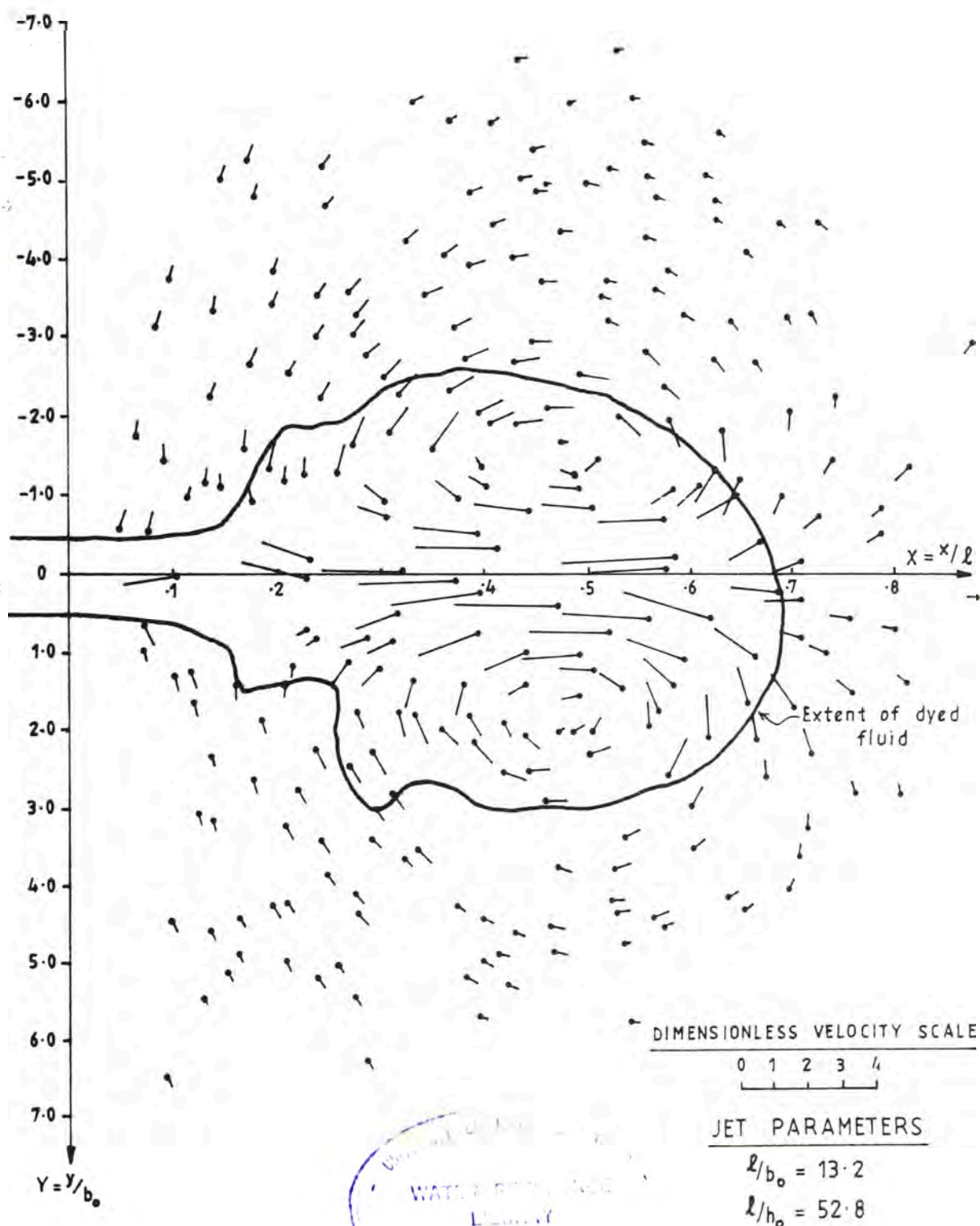
FLOW PATTERN IN AND AROUND THE VORTEX PAIR CAP

RELATIVE TO A STATIONARY FRAME OF REFERENCE

AT TIME $\tau = 0.52$

FIGURE 5·5

A steady flow pattern relative to the vortex pair cap was obtained by vector addition of the unsteady velocity vectors and the cap translation velocity vector. This will allow comparison later with the numerical results obtained by Saffman (1979) and Pierrehumbert (1980) for a family of steady state vortex pairs. An example of the resulting flow pattern is shown in Figure 5.6. This process was very time consuming and was only done for two of the experiments. A quicker method for verifying the self-preservation of the velocity distribution was to determine the unsteady velocity profile for a given section through the cap at various times. One velocity profile was obtained for the velocity in the direction of translation, u, normalised with respect to the translation velocity, u_v, along a line passing through the apparent centres of rotation of the vortices and perpendicular to the axis of symmetry (x axis). The other profile was obtained for the velocity, v , parallel to the y - axis normalised with respect to the translation velocity, along a line parallel to the x-axis passing through the apparent centre of rotation of a vortex. In both cases the length scale was normalised with respect to the distance from the axis of symmetry to the apparent centre of rotation, $\pm b_c/2$. The profiles for two experiments are shown in Figures 5.7 - 5.10.

From these results it can be taken that the flow pattern is self-preserving for all but the initial stages of the flow. Also shown on Figures 5.7 - 5.10 are the locations of the edge of the dyed fluid. (These locations are marked along the appropriate axes). Superposition of velocity profiles from different experiments also shows similarity between starting flows with a range of ℓ/b_o values.

5.1.2 Vortex Pair Separation

DIMENSIONLESS VELOCITY SCALE

0　1　2　3　4

JET PARAMETERS

$\ell/b_o = 13\cdot2$

$\ell/h_o = 52\cdot8$

Extent of dyed fluid

$X = {}^x/\ell$

$Y = {}^y/b_o$
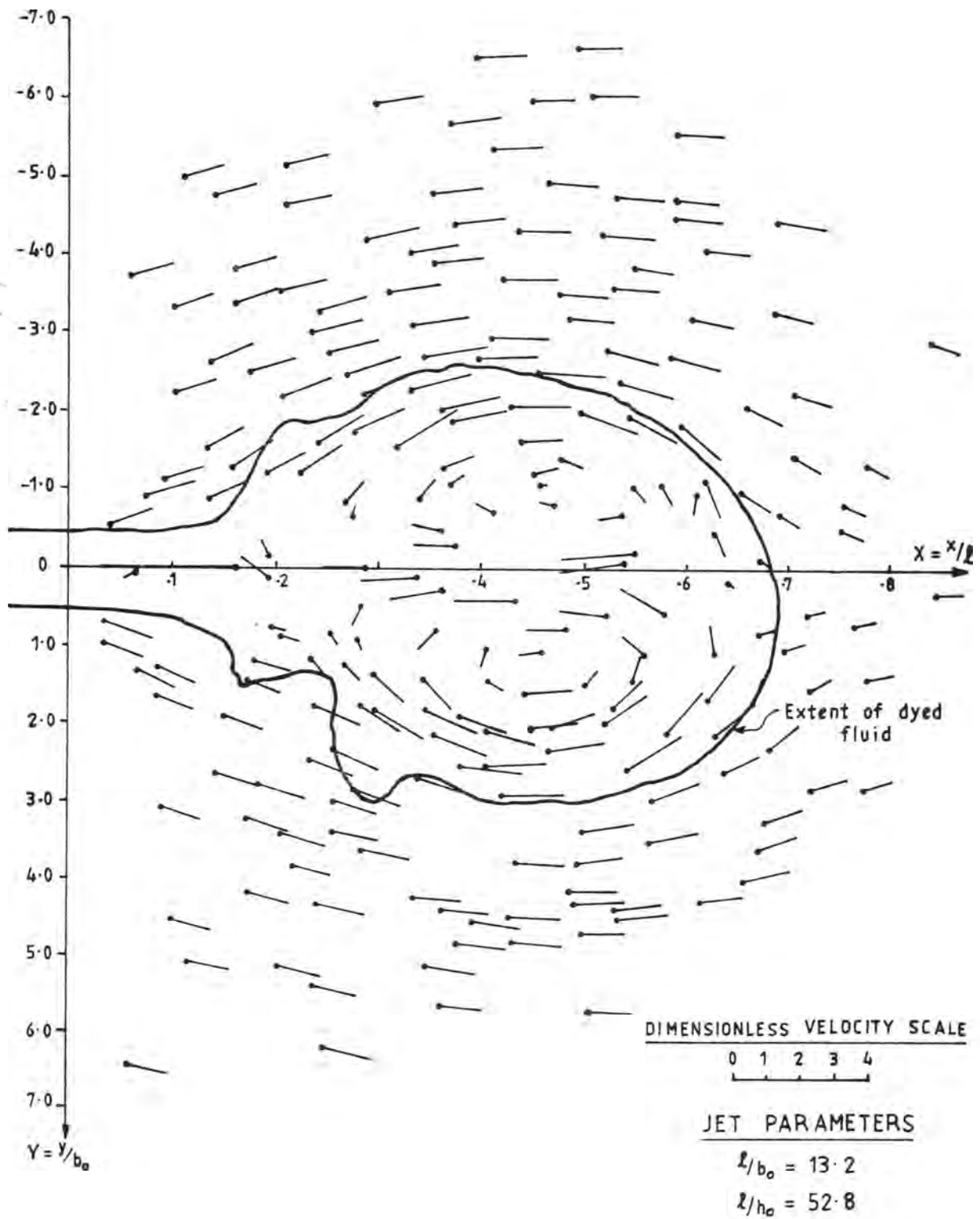
STEADY FLOW PATTERN RELATIVE TO A FRAME
OF REFERENCE MOVING WITH
THE CAP TRANSLATION VELOCITY, U_V.　$\tau = 0\cdot52$

FIGURE 5·6

FIGURE 5·7

NORMALISED VELOCITY PROFILE AT CENTRE OF VORTEX PAIR CAP FOR

VARIOUS TIMES

FIGURE 5.8

NORMALISED RADIAL VELOCITY PROFILE ALONG $y = b_c/2$

FOR VARIOUS TIMES

LEGEND: τ

•	0.15
o	0.20
+	0.25
×	0.30
△	0.35
▽	0.47
⊕	0.52
□	0.57
■	0.65
▲	0.73
▼	0.85
⊟	0.89
⊗	1.00

EXTENT OF DYED FLUID

EXTENT OF DYED FLUID

V/u_v

$2x/b_c$

$\ell/b_o = 13.2$

$\ell/h_o = 52.6$

NORMALISED VELOCITY PROFILE AT CENTRE OF VORTEX PAIR CAP FOR VARIOUS TIMES

FIGURE 5.9

LEGEND: τ

·   0·11
o   0·17
✦   0·20
×   0·25
Δ   0·29
▽   0·33
⊕   0·38
□   0·42
■   0·46
▲   0·50
▼   0·54
⊟   0·59
⊕   0·66
z   0·73
✳   0·82
φ   0·93
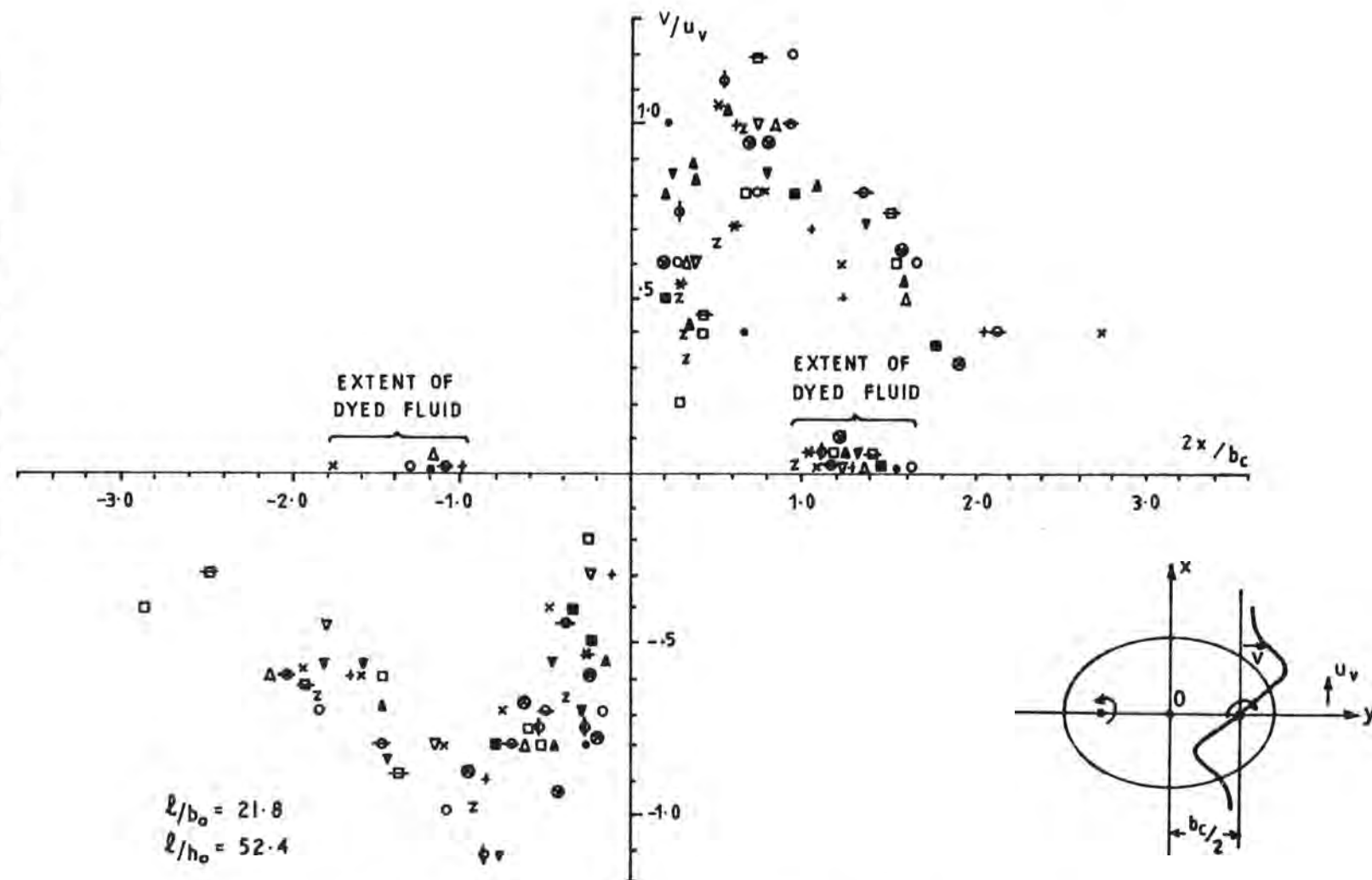
V/u_v

1·0

·5

EXTENT OF
DYED FLUID

EXTENT OF
DYED FLUID

$2x/b_c$

-3·0   -2·0   -1·0   1·0   2·0   3·0

-·5

-1·0

$\ell/b_o = 21·8$
$\ell/h_o = 52·4$

$b_c/2$

FIGURE 5·10

NORMALISED RADIAL VELOCITY PROFILE ALONG $y = b_c/2$

FOR VARIOUS TIMES

Before proceeding further with a discussion of the experimental results it is necessary to clarify the definition of the vortex pair separation. The use of time lapse photography provides a picture of the flow pattern at various times during the flow development, relative to the frame of refernce of a stationary observer. By visual inspection of the flow pattern, the apparent centre of rotation or "eye" of each vortex can be found. The distance between these centres has been used in the analysis as the prime width variable, b_c. The actual centres of rotation have been defined as being located at $\pm y_c$ (Section 5.1.2) - the centroid of the vortices in a frame of reference moving with the vortex pair translation velocity, u_v. Experimentally, the distance $2y_c$ can be found by visual inspection of a flow pattern relative to the frame of reference translating with the vortices (Figure 5.6), and is closer than $b_c/2$ to the axis of symmetry (Figure 5.3). For a flow defined by Figure 5.11, the relationship between these experimentally estimated centres is best shown in Figures 5.12, where the dimensionless variables $B_{CAP} = b_{cap}/b_o$ (cap width), $B = b_c/b_o$ (the apparent separation of the centres of rotation) and $2Y_c = 2y_c/b_o$ (the steady separation of the vortex centres), are plotted against $X_c = x_c/\ell$ (the distance from the inlet to the cap centreline), for the two experiments that were analysed completely.

Saffman (1979) has estimated that for an elliptical vortex pair the displacement of the apparent centre of rotation from each the vortex centre is given in terms of dimensionless variables by:

$$\frac{b_c}{2} - y_c = (\frac{\pi u_v}{K}) [x_1 + \frac{(y_2 - y_1)}{2}] \frac{(y_2 - y_1)}{2} \tag{5.11}$$

where x_1 and $\frac{(y_2 - y_1)}{2}$ are the major and minor semi-axes of the vortex as
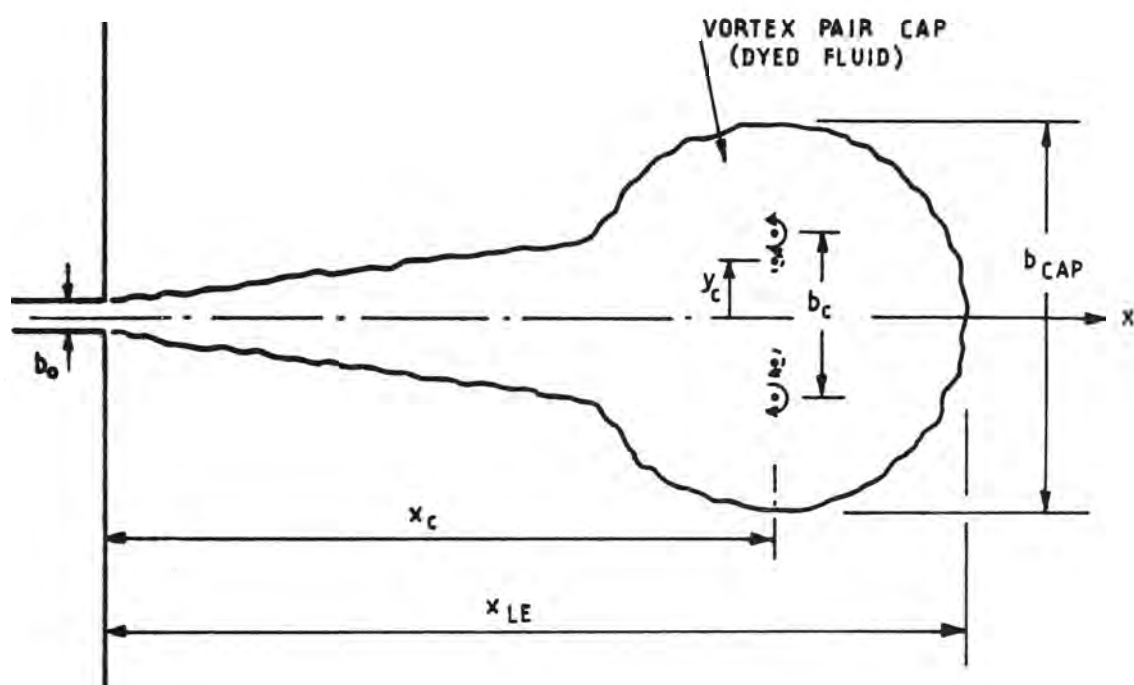
DEFINITION SKETCH FOR VARIABLES DESCRIBING
THE VORTEX PAIR CAP
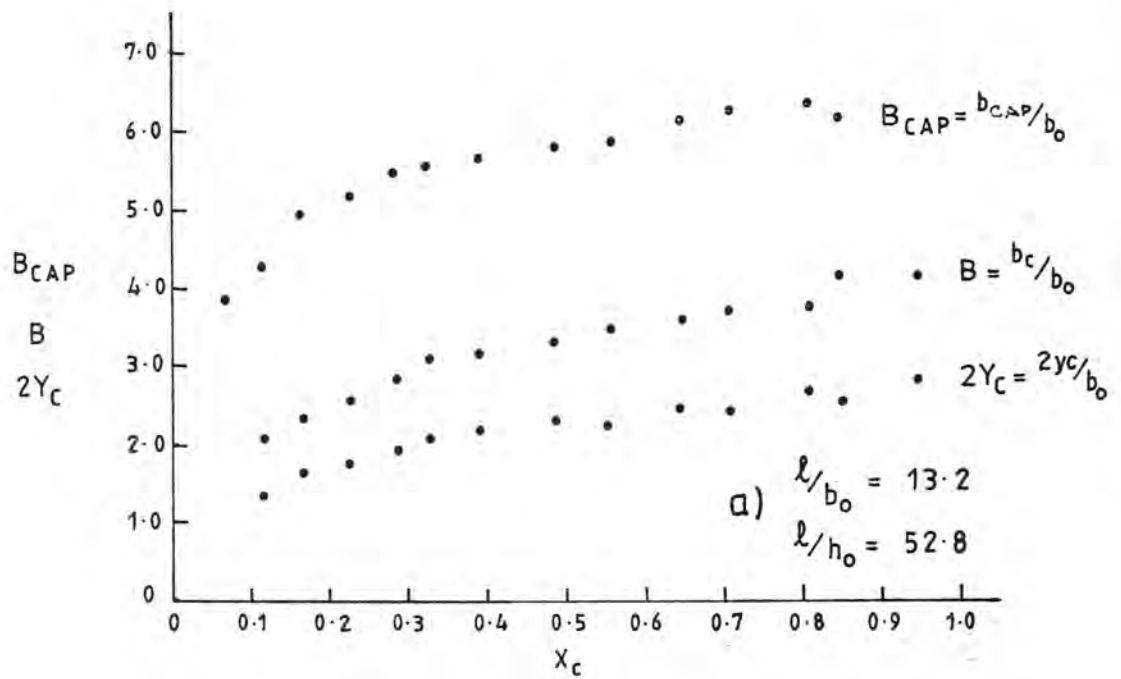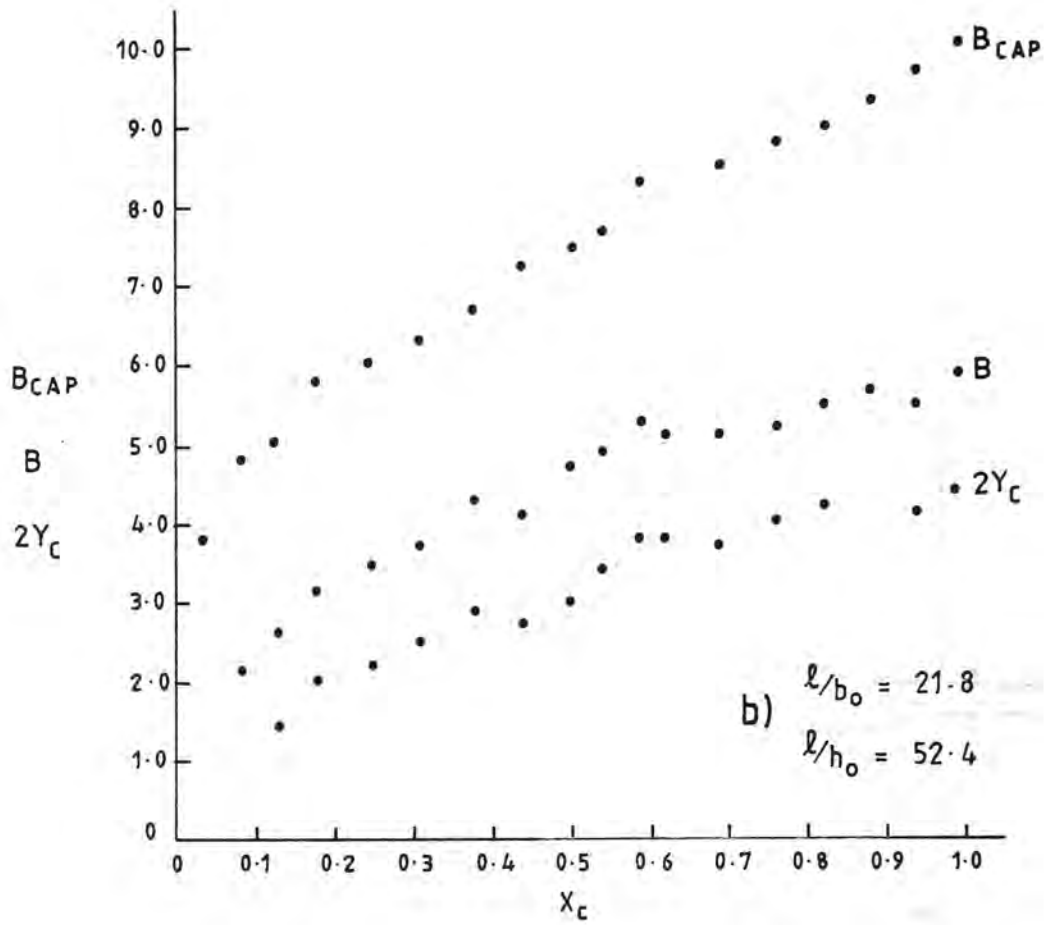
FIGURE 5·11

EXPERIMENTAL RESULTS FOR THE REAL AND
APPARENT VORTEX PAIR SEPARATION

FIGURE 5·12

shown in Figures 5.1 and 5.2. The distance between the apparent and real centres of rotation , $(\frac{b_c}{2}-y_c)$, can be estimated from Equation (5.11) by taking $u_v \simeq K/2\pi y_c$ thus giving:

$$\frac{y_c}{b_c} - 2(\frac{y_c}{b_c})^2 = \frac{1}{4}[\frac{2x_1}{b_c} + (\frac{y_2-y_1}{b_c})] \ (\frac{y_2-y_1}{b_c}) \tag{5.12}$$

This implies that in a similarity formulation the apparent and real centres are related by a constant. The results shown in Figure 5.12 are in fair agreement with this, considering the experimental method used for determining the centres of rotation. The variable b_c is the more readily determined measure of the pair separation and as such has been used as the prime width variable.

The similarity form for the translation velocity, u_v, (Equation 5.2) can now be expressed as:

$$u_v = \frac{K}{C_1(C_2 b_c)} \tag{5.13}$$

where C_2 is the similarity constant $\frac{2y_c}{b_c}$ which is defined by Equation (5.12).

5.2.3 Velocity Distribution

The velocity distribution relative to a frame of reference moving with the vortices shown in Figure 5.6 indicates that the rotational flow identified by the dyed region is confined to a cap of fluid which is nearly circular in shape. The vortex core appears elliptical in cross-section. Moore & Saffman (1971) have shown this to be the

equilibrium state for a vortex pair. The assumption is made in this study that the vorticity is uniformly distributed within each elliptical core and that a core is symmetrical about a line parallel to the x-axis passing through y_c. Thus, an estimate can be made of the semi axis of the ellipse by determining the width of the vortex core from Figures 5.7 - 5.10.

The characteristic indication of a core in a stationary frame of reference is the change of the absolute velocity from zero in the centre of the core ($x = 0$, $y = \pm y_c$), to a maximum value at the outer edge of the core. Examining Figures 5.8 and 5.10, it is possible to say that close to $x = 0$ the dependence of velocity, v , on x is linear. Similarly, for the axial velocity, u, a linear dependence on y is indicated. This linear dependence enables the size of the vorticity regions to be estimated from these similarity profiles as follows.

The x semi-axis is estimated directly from the radial velocity profiles (Figures 5.8 and 5.10, for example) by determining the distance between the velocity peaks. An average value for $x_1 = 0.40 b_c$ was obtained for all of the experiments.

The y semi-axis is not so easily determined. The outer boundary of the vortex core is estimated from the centreline velocity profiles at $y_2 = 0.72 b_c$ on average. The velocity profiles do not reveal any information regarding the location of the inner boundary other than that its limit is the axis of symmetry. However the observed presence of dyed fluid between the vortices indicates that the entire inner region is rotational. The value of y_1 can be estimated from Equation (5.12) once the parameter $\dfrac{y_c}{b_c}$ has been determined. The average value of

y_c taken from the plotted unsteady velocity profiles is $y_c = 0.32 b_c$. Substituting $\frac{y_c}{b_c} = 0.32$, $\frac{y_2}{b_c} = 0.72$, and $\frac{x_1}{b_c} = 0.80$ into Equation (5.12) yields an estimate for the location of the inner boundary at $\frac{y_1}{b_c} = 0.28$.

These results can be compared with the numerical solutions of Saffman (1979) and Pierrehumbert (1980). Assuming an elliptical cross-section for the core, the area, A, is given by:

$$A = \frac{\pi}{2}(0.72-0.28)(0.40) \, b_c^{\,2}$$

$$= 0.28 \, b_c^{\,2} \qquad\qquad (5.14)$$

The effective radius, R, is then:

$$R = (A/\pi)^{1/2}$$

$$= 0.30 b_c \qquad\qquad (5.15)$$

The parameter, $R/y_c = 0.93$, describes the properties of the vortex core as shown in Figure 5.2a. Saffman's approximate results give $2x_1/(y_2-y_1) = 1.50$ and $y_1/y_2 = 0.15$ for this value of R/y_c. This compares with the experimental estimates of 1.83 and 0.39 respectively. In the limit ($y_1 = 0$), the corresponding experimental parameter values are $R/y_c = 1.18$, $2x_1/(y_2-y_1) = 1.11$ and $y_1/y_2 = 0$.

Although not in good numerical agreement the experimental results show that the vortex pair cap (taken to be the vorticity containing region) has a similar shape to that of the vorticity containing region predicted by Saffman and Pierrehumbert. A detailed comparison with their results is not possible without a more precise measurement of the

velocity distribution. Tsang (1970_1) has shown for two-dimensional starting plumes that the vorticity is widely spread throughout the cap, but is not uniformly distributed. If this is so for the present case, the poor agreement with Pierrehumbert's results would be expected.

An estimate of the circulation of the vortices can be found by determining the vorticity, ω_0, along the x-axis defined by:

$$\omega = \frac{\partial v}{\partial x} - \frac{\partial u}{\partial y} \tag{5.16}$$

where v is normal to the axis. Then, assuming a uniformly distributed vorticity in the core, the vorticity can be estimated from Figures 5.7 - 5.10 as:

$$\omega_0 = [\frac{\partial(v/u_v)}{\partial(2x/b_c)} - \frac{\partial(u/u_v)}{\partial(2y/b_c)}] \frac{2u_v}{b_c}$$

$$= 9.3 \frac{u_v}{b_c} \tag{5.17}$$

The circulation of the core is given by:

$$K = \int_A \omega \, dA \tag{5.18}$$

Assuming an elliptical section, the cross-sectional area of the core is $A \simeq 0.28 b_c$ as before.

Thus:

$$K = 2.6 \, u_v b_c \tag{5.19}$$

The induced ambient flow about the vortex pair cap (Figure 5.5) is similar to the doublet flow proposed for a cylindrical two-dimensional starting plume by Tsang (1970_1) (Figure 2.3). In the mixing region of the cap the flow is turbulent and rotational. Outside this region the ambient flow is close to a potential flow. Tsang (1970_2) has conducted extensive studies to establish the velocity distribution around a buoyant vortex pair. His experiments agreed well with his proposed doublet flow and those of Richards (1963) and Csanady (1965). It is reasonable to assume a similar inviscid potential flow for the present case for the region outside the vortex core. A doublet flow relative to a stationary reference frame of the form:

$$\psi \ \propto \ - \ \frac{\cos\theta}{r} \tag{5.20}$$

implies a velocity dependence for the potential flow outside the cap and along the centreline of the cap of the form:

$$v \ = \ \frac{1}{r}\frac{\partial\psi}{\partial\theta} \qquad \text{along} \ \ \theta \ = \ \frac{\pi}{2}$$

$$\propto \ \frac{1}{r^2} \tag{5.21}$$

A curve of this form has been plotted on Figures 5.7 for the ambient flow region. The velocity distributions suggest that a streamfunction of the form:

$$\psi \ = \ - \ 0.48 b_c^2 u_v \frac{\cos\theta}{r} \tag{5.22}$$

provides a reasonable description of the flow field.

5.2.4 <u>Shape</u> <u>and</u> <u>Size</u> <u>of</u> <u>the</u> <u>Vortex</u> <u>Pair</u> <u>Cap</u>

Interpretation of the normalised velocity profiles has shown that each vortex core within the vortex pair cap has an elongated shape assumed to be elliptical. The shape of the cap is assumed nearly circular. However, the shape of the rear half of the cap cannot be determined from the photographic record, because dyed fluid which is trapped in the bottom boundary layer obscures the shape of the rear portion of the cap. The shape can be defined in terms of the location of the leading edge of the dyed fluid, x_{LE} , the location of the centre of rotation of the vortices, x_C , and the maximum width of the dyed fluid, b_{CAP} (see Figure 5.11). A shape factor, α, is defined as:

$$\alpha = \frac{2(x_{LE}-x_C)}{b_{CAP}} \tag{5.23}$$

This has been determined for all experiments at all times. A sample data reduction is given in Appendix 3. The variation in α during one experiment was not systematic and can be attributable to the turbulent billowing of the dyed fluid, which made measurements of the width of the cap difficult. A mean value of α was determined for each experiment and an overall average mean value for all experiments was found to be $\alpha = 0.98 \pm 0.13$. The assumption of a nearly circular cap as defined by $\alpha \simeq 1.0$ is thus valid. The apparent elongation of the cap towards the later stages of the flow development is not evident from the determination of α, or from the core shape determination of the previous section. This elongation would seem to be due to the bottom boundary layer effect which artificially elongates the cap in the photographic record. The factor, α, is considered a reliable estimate of the cap shape.

In all previous studies (e.g. Wood (1968), Tsang and Wood (1968) and Tsang (1970$_2$)), it was assumed that the shape of vorticity containing region is nearly circular and that it is represented by the dyed patch. Referring to Figures 5.7 - 5.10 it can be seen that the dyed region is marginally larger than the extent of the vortex core as defined by the absolute maximum velocity. The average width of the dyed cap is $1.69b_c \pm 0.22b_c$ whereas the estimated distance between the outer extent of each vortex core is $1.35b_c$. The core width can only be estimated as there is a transition region between the rotational flow in the core and the potential flow around it. The similarity profiles, however, are not well enough defined to proceed any further with this discussion.

In summary, the dyed fluid can be taken to represent the vorticity containing region which in the present case is circular in shape and comprises two vortices occupying nearly all of the body of fluid travelling with them.

5.2.5 Evaluation of Constants $C_1 - C_4$

The theoretical model developed in Chapter 3 for the gross behaviour of a periodic starting jet is semi-empirical in that certain constants were introduced enabling the cap motion to be described by means of a irrotational model. Numerical values of these constants will now be determined using the experimental data and also the numerical data of Pierrehumbert (1980).

C_1: This constant relates the velocity of propagation of the cap to the vortex strength and the pair separation as in Equation (5.2). Pierrehumbert has shown, (Figure 5.2a), that in the case of uniformly

distributed vorticity this is a function of the size and shape of the vortex core. In applying Pierrehumbert's results it has been assumed that the core of each vortex is elliptical in shape and that the centroid of the ellipse corresponds to the real centre of rotation of the vortex. Thus, from the velocity profiles shown in Figures 5.7 - 5.10, the parameter R/y_c (defined in Section 5.1.2.1) has the approximate value 0.93. From Figure 5.2a the value of the normalised velocity, u", is 0.90. The constant C_1 is related to u" by:

$$C_1 = \frac{2\pi}{u''}$$

$$= 6.98 \qquad\qquad (5.24)$$

Although Pierrehumbert's results are not directly applicable in this case, it was shown earlier that there is reasonable agreement with the experimental results. Also the parameter R/y_c is not very sensitive to variation in y_1 (which was the variable not determined from the similarity profiles).

C_2: This constant relates the apparent separation of the vortex pair centres of rotation, b_c, to the distance between the real centres, $2y_c$, in a frame of reference translating with the vortices. This has been defined by Equation (5.12). Experimentally it can be determined by considering Figures 5.7 and 5.9. The location of $y = \pm y_c$ is found where the velocity profile crosses the line $u/u_v = 1.0$. The average values of y_c taken from all of the plotted unsteady profiles is $y_c = 0.32 b_c$.

$$C_2 = 0.64$$

C_3: Under the self-preservation assumption it is taken that the shape of dyed fluid region remains constant and that the growth rate of the dyed region is in step with the rate of increase of the pair separation. Thus the planform area of the dyed fluid can be related to an area equivalent to a circle of diameter, b_c. This enables the experimentally determined separation of the centres of rotation to be used as the prime variable in the analysis. Constant, C_3, can then be found knowing the ratio of the cap width, b_{CAP}, to the pair separation, b_c and the shape factor, α. It is also assumed that, in general, the overall shape is nearly circular and thus C_3 is given by:

$$C_3 = \alpha \left(\frac{b_{CAP}}{b_c}\right)^2 \qquad (5.25)$$

The overall average for all tests was found to be 2.61 ± 0.40. There was no systematic variation in this constant. An alternative method of experimentally determining C_3, is to directly measure from the photographs the dyed area at each time. This method will only be accurate for the forward portion of the cap; the shape of which is unaffected by the dye trapped in the bottom boundary layer. This was done for a number of experiments as a check on the validity of assuming a near-circular planform. On average the area of the front half of the cap, defined by $A_{1/2} = \frac{\pi}{4}(x_{LE} - x_c)(b_{CAP})$, is 104 % of half the area of the dyed fluid representing the cap.

A sample reduction of the experimental data is given in Appendix 3, and shows the variation in C_3, α and the dyed area for various times. Also included in Appendix 3, is a summary of the average values of these constants for each test.

Pierrehumbert (1980) has presented values of a similar constant for a uniformly distributed vorticity region, which is defined as the area of the flow contained within the dividing streamline divided by twice the area of the vortex core. The value corresponding to $R/y_c = 0.93$ (see previous discussion for C_1) is 2.53. An equivalent value of C_3 (using Equations (5.9) and (5.25)) will then be 1.81. This implies that the dyed fluid has a larger area than the vorticity containing region. Inspection of the steady flow patterns (Figure 5.6) would also suggest this is the case.

C_4: This constant was used in the continuity of mass relationship, and as for C_3, relates the actual circumference of the dyed fluid to the circumference of a circle of diameter, b_c.

For an elliptical section the constant C_4 evaluated along a closed surface is given by:

$$C_4 = \frac{1.5}{b_c} [((x_{LE}-x_C) + (b_{CAP}/2)) - \sqrt{((x_{LE}-x_C)(b_{CAP}/2))}] \qquad (5.26)$$

The variation of C_4 for one experiment and between different experiments is shown in Appendix 3. The overall average value of C_4 is 1.62 ± 0.10.

5.3 Summary of Similarity Constants

The constants $C_1 - C_4$ have been determined for each experiment and as there was no systematic variation it is proposed to use an overall average value of each in the analytical solutions obtained in Chapter 3. These constants are indications of the validity of the self-preservation assumption for each experiment. Also, the lack of any

correlation with the inlet entrance parameters would also indicate that a similarity formulation is applicable. The values to be used in analysis are then:

$$C_1 = 6.98$$
$$C_2 = 0.64$$
$$C_3 = 2.61$$
$$C_4 = 1.62$$

6. EXPERIMENTALLY DETERMINED GROSS BEHAVIOUR OF A PERIODIC STARTING JET

In this chapter the data obtained from the experiments described in Chapter 4 will be analysed to provide quantitative support for the qualitative observations made in Chapter 2; verification of the theoretical model describing the gross behaviour of the flow and to establish the dependence of the motion on the inlet parameters, ℓ/h_o and ℓ/b_o.

The experimental programme was divided into four main areas. The hydrogen bubble technique was used to quantify the velocity distribution in the unsteady jet tail. Confetti tracings were used to estimate the velocity distribution in the vortex pair cap. Confetti and dye tracings were used to determine the gross features of the flow behaviour of a periodic starting jet issuing into a basin of fluid initially at rest. And finally, similar tracing techniques were used for a periodic jet subject to a crossflow.

The results of this experimental programme will now be presented. Comparisons with the results of relevant previous investigations will also be made where appropriate. The results of the crossflow experiments will be discussed in a later chapter.

6.1 The Unsteady Jet Tail

The case of a two-dimensional unsteady jet with a source mass flux varying sinusoidally has been considered in Section 3.3. The results of the numerical simulation of the flow are shown in Figures 3.3 to 3.6. In an attempt to verify this predicted behaviour the velocity distribution in the jet tail of a vortex pair cap has been

experimentally determined.

6.1.1 Data Reduction

The hydrogen bubble technique was used to determine the velocity distribution in the unsteady jet tail over a time when a well defined jet-like structure was evident. This technique has been shown to provide accurate results for steady state velocities in the range $10\,\mathrm{mms}^{-1}$ to $100\,\mathrm{mms}^{-1}$. The accuracy is dependent on a number of factors including the wire diameter, the surface current density, the pulse length and interval, and the bubble size. Bubbles generated at the wire move away from the wire at a velocity less than the free stream velocity due to the presence of a wake behind the wire. The distance downstream to where the bubbles reach the free stream velocity will depend on the orientation of the wire. Wilkinson and Willoughby (1981) have investigated this and the factors influencing the bubble generation and motion for a vertical wire. For a horizontal wire Schraub et al. (1965) have shown that the bubbles will rise out of the wire wake at 70 wire diameters downstream, limiting accurate bubble trace measurements to bubbles visible beyond this distance.

The technique has been used by other investigators in boundary layer studies where the flow is turbulent and unsteady. Analysis of the data to provide accurate quantitative information is, however, very time consuming. For this reason, and because of the difficulties in applying suitable wake corrections, a complete reduction of the data obtained in this study was not undertaken.

The velocity profiles presented in this thesis were obtained by determining the distance between successive bubble traces, and, knowing the pulse interval, calculating the velocity. Traces further than 70 wire diameters from the wire were used where possible and therefore it was not necessary to apply a wake correction to the data. The results obtained can be considered to give good qualitative information on the transverse velocity distribution, and a good estimate of the mean axial velocities of each profile.

Because of the limitation of the hydrogen bubble technique in this application, velocity profile data were only obtained for one set of flow parameters. The entrance conditions were as follows:

Inlet width, b_o = 60mm

Inlet depth, d_o = 25mm

Period, T = 60 sec

Characteristic length, ℓ = 906mm

Maximum entrance velocity, U_o = 59mm s^{-1}

The basin depth was uniform and there was no crossflow. Flows with smaller characteristic lengths were not representative of the overall experimental programme, although better suited to the hydrogen bubble technique. Flows with larger characteristic lengths were at the limit of applicability of the technique, because of the higher velocities and turbulence levels.

The experimental set-up described in Chapter 4 provided velocity profiles at each fixed wire location for regular time intervals from the time the vortex pair cap passed the wire, until the flow reversal at the wire. From these profiles it is possible to determine the

temporal and spatial velocity distributions within the jet tail. Of particular interest is the jet velocity at the join between the jet `tail´ and the vortex pair cap. This location was estimated from the results of the other experiments with these initial conditions, although it could not be obtained directly from the photographic record because of the entrapment of dyed fluid in the bottom boundary layer obscuring the shape of the rear of the cap. The join was taken to be the imaginary trailing edge of the vortex pair cap and was determined by knowing the location of the leading edge, centreline and maximum width of the vortex pair cap. Assuming a symmetrical planform of the cap, the trailing edge is then the same distance from the centreline as the leading edge. Figure 6.1 shows the distance travelled by the leading edge, centreline and the estimated location of the trailing edge of the vortex pair cap with time. Also shown are the location of the hydrogen bubble wires. A composite of the velocity profiles at the trailing edge of the vortex pair cap can then be obtained from the data.

6.1.2 Velocity Distribution

The variation in the velocity with time is shown typically in Figure 6.2 for a wire location a distance $X = x/\lambda = 0.333$ from the origin. The difficulties encountered in using the hydrogen bubble technique have been detailed in Chapter 4 and the data obtained reflect these problems in that there is considerable non-uniformity in the velocity profiles.

With reference to Figure 6.1 it can be seen that the profile shown in Figure 6.2a ($\tau = 0.37$) represents the velocity within the vortex pair cap. As the cap passes the wire the shape of the profile changes.
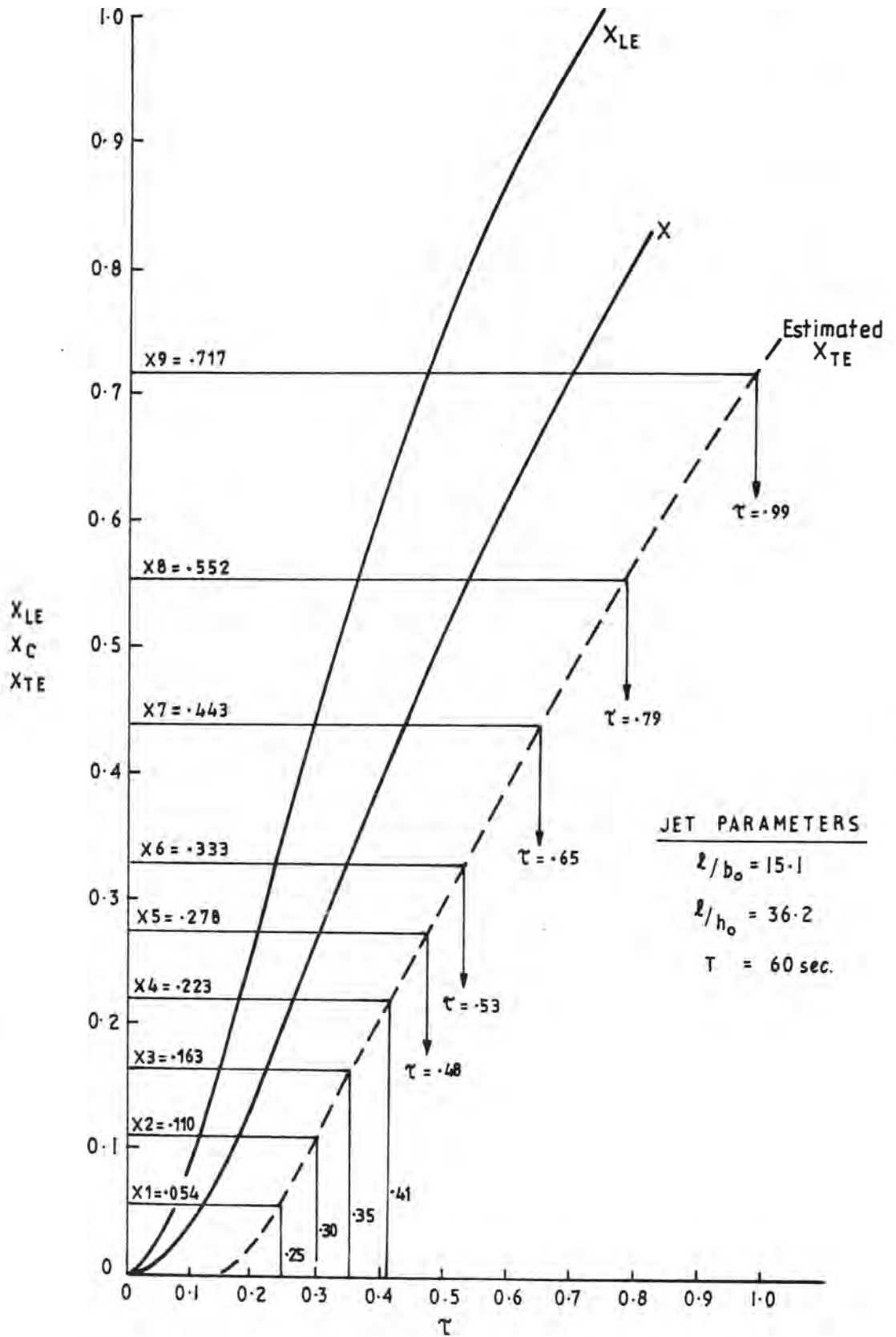
VORTEX PAIR CAP ADVANCE SHOWING THE LOCATION
OF THE HYDROGEN BUBBLE WIRES
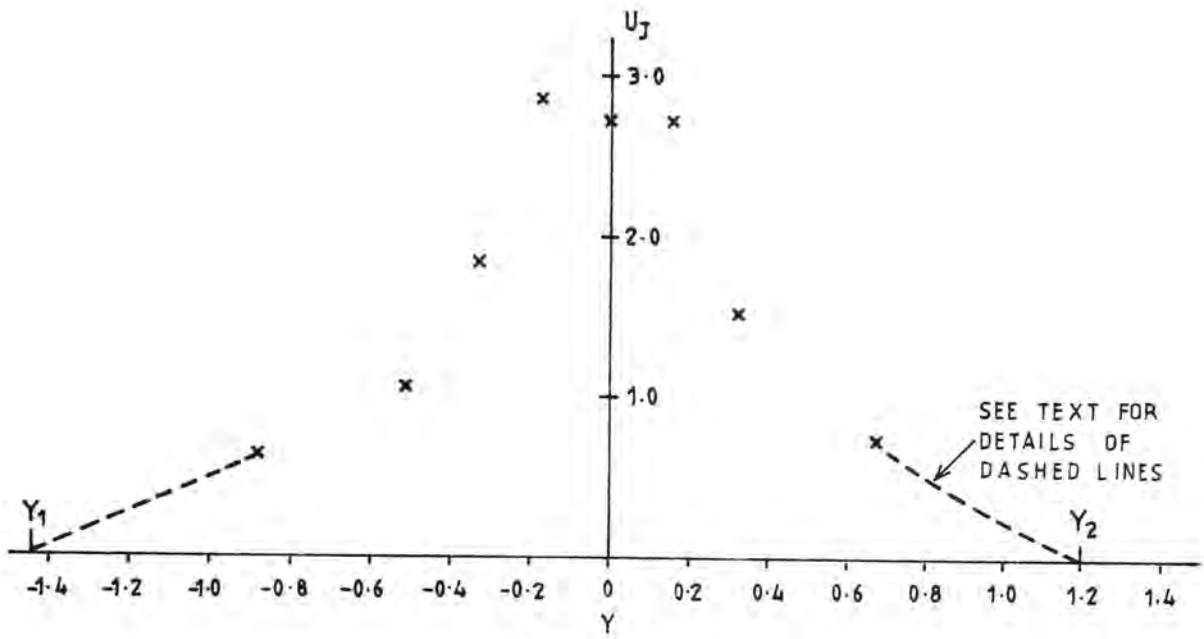
FIGURE 6·1

b) $\tau = 0.50$
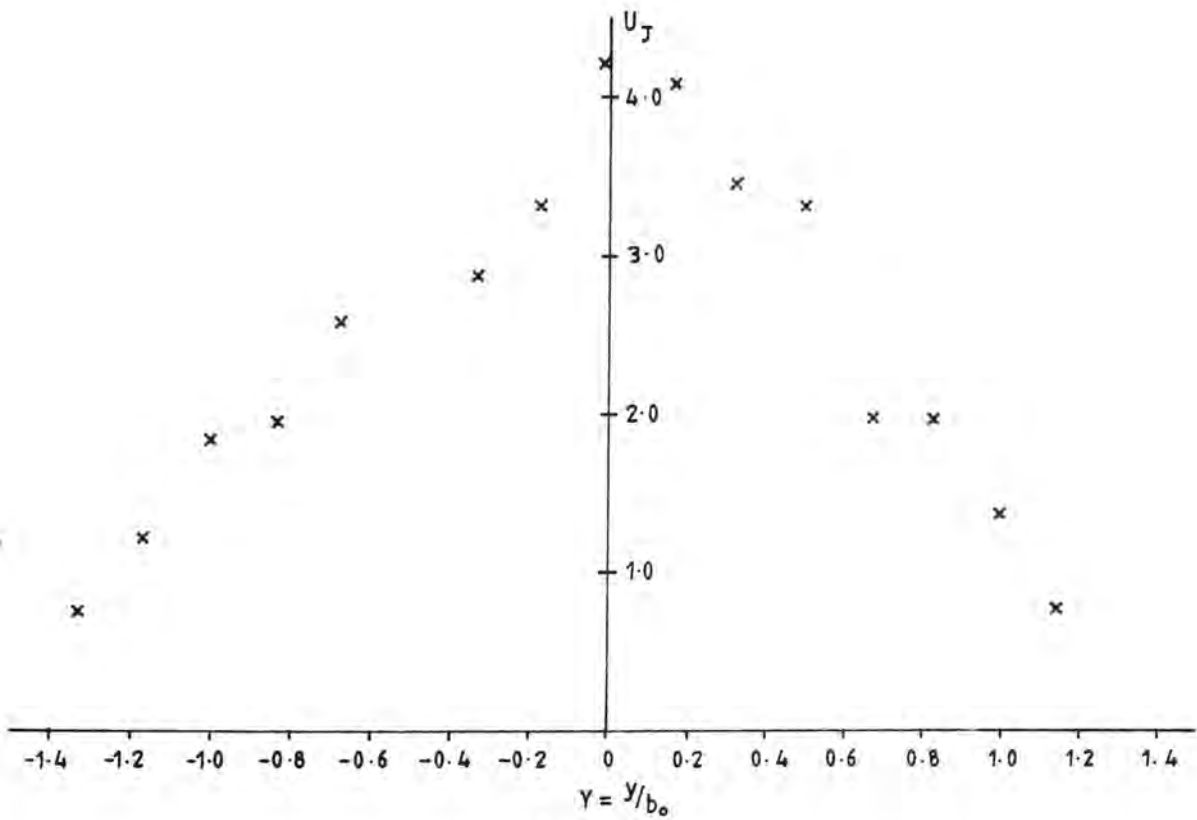
a) $\tau = 0.37$

UNSTEADY JET DIMENSIONLESS LATERAL VELOCITY
PROFILES AT LOCATION X6=0·333 FOR VARIOUS TIMES

FIGURE 6·2

d) $\tau = 0.80$

c) $\tau = 0.64$
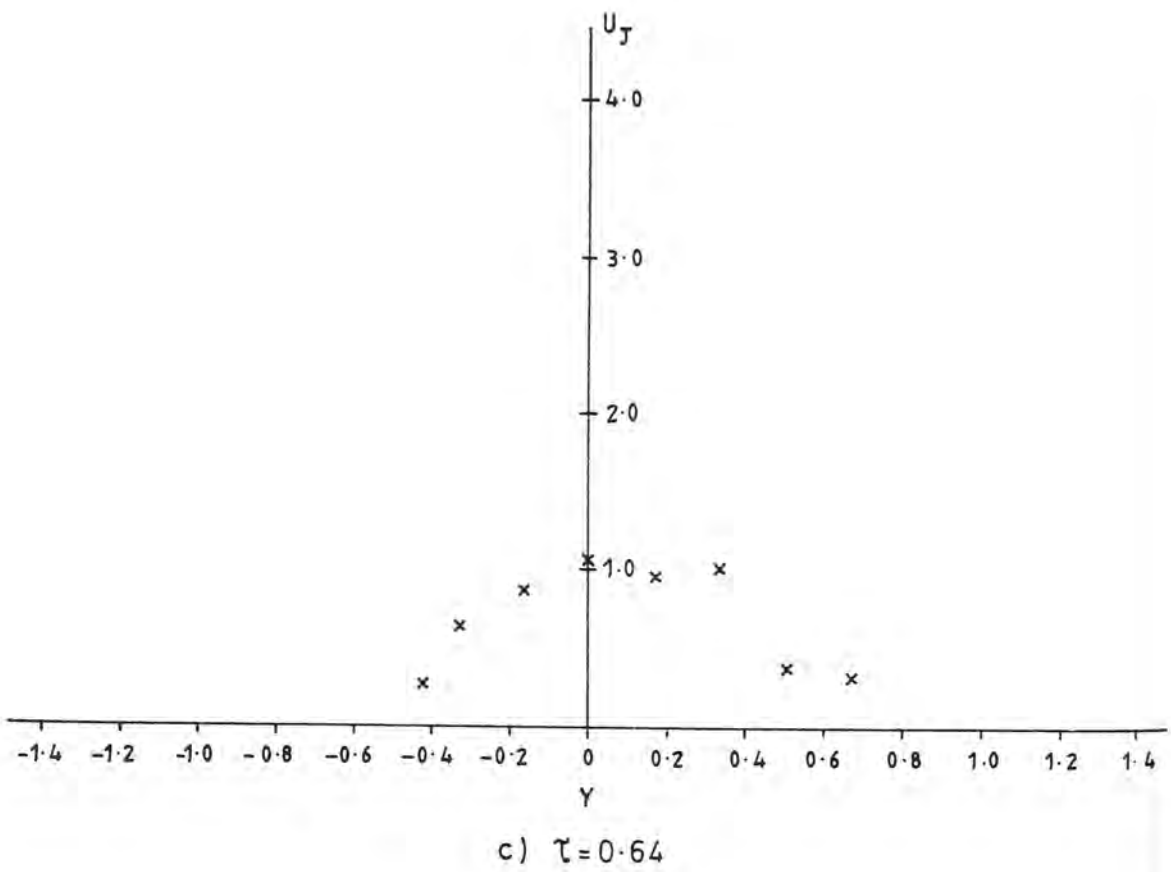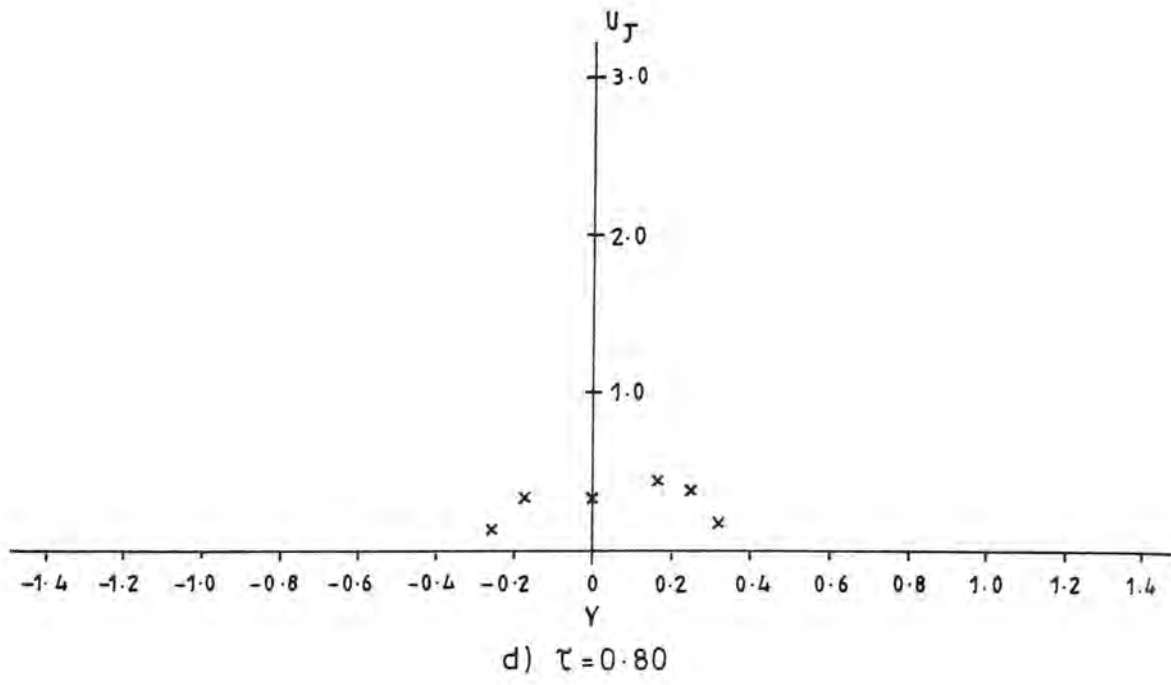
FIGURE 6.2 (Cont.)

A more typical jet-like profile is indicated for times greater than $\tau =$ 0.50. This wire location is outside the extent of influence of the flow reversal and hence it can be taken that the contraction of the jet after $\tau = 0.50$ is a feature of the jet behaviour.

An estimation was made of the dimensionless momentum and mass fluxes by assuming a shape for the tail of the profile as shown in Figure 6.2b. Thus, the momentum flux, M_J, is determined as:

$$M_J = \int_{Y_1}^{Y_2} U_J^2 (X, Y, \tau) \, dY \qquad (6.1)$$

and the mass flux, Q_J, as:

$$Q_J = \int_{Y_1}^{Y_2} U_J (X, Y, \tau) \, dY \qquad (6.2)$$

where Y_1 and Y_2 are the assumed limits ($U = 0$) of the velocity profile. This approach is justified as the theoretical analysis with which these results are to be compared was developed for an assumed uniform velocity distribution of finite width.

A nominal jet velocity and width can now be defined as:

$$U_N = \frac{M_J}{Q_J} \qquad (6.3)$$

and

$$B_N = \frac{Q_J}{U_N} \qquad (6.4)$$

These values are taken as representative of the average jet velocity and width. The discussion of the unsteady jet tail that follows will be in terms of U_N and B_N, as the prime variables for the vortex pair cap analysis are the pair separation and the translation velocity. The variation of B_N and U_N with time, τ, is shown in Figures 6.3 and 6.4 respectively for each wire location shown in Figure 6.1.

6.1.3 Discussion

The author has been unable to find any experimental data on unsteady two-dimensional jets of this type in the literature, and hence confirmation of the validity of these limited results is difficult. Comparison with the theoretical predictions of Section 3.3 is facilitated by re-plotting the experimentally determined nominal velocity, U_N, and the nominal width, B_N, as a function of X from various times, τ, as shown in Figures 6.5 and 6.6. Examination of Figure 6.1 shows that jet-like behaviour is not likely to occur at each wire location until the assumed location of the trailing edge of the vortex pair cap has passed the wire. These limits are marked on Figure 6.5. The experimental results are shown for times up to $\tau = 1.01$. After $\tau = 0.50$, the numerical solutions are no longer applicable as the flow has reversed. Examination of the experimental results after $\tau = 0.50$ show a decay of velocity with time at any location.

The numerical results that have been presented here are somewhat arbitrary in that their validity is dependent on a number of factors. Firstly, the shock location for any given time will vary depending on the chosen initial steady jet starting conditions. The greater the initial source momentum flux, the greater the distance from the origin to the shock location (see Appendix 1). The observed behaviour of the
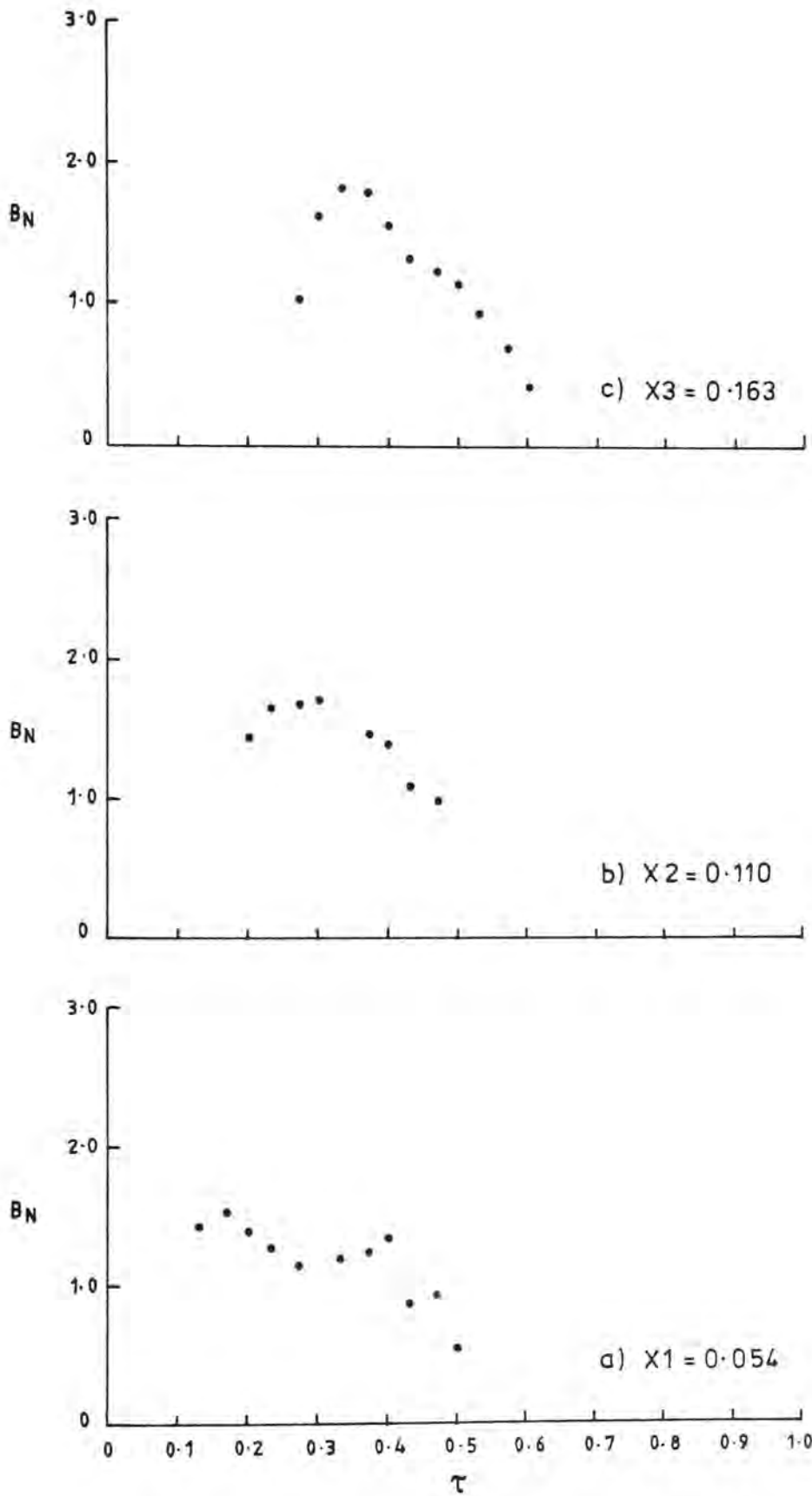
NOMINAL JET WIDTH VARIATION
WITH TIME AT EACH WIRE LOCATION

FIGURE 6·3

f) X6 = 0·333

e) X5 = 0·278

d) X4 = 0·223

FIGURE 6·3 (Cont.)

i) X9 = 0·717

h) X8 = 0·552

g) X7 = 0·443
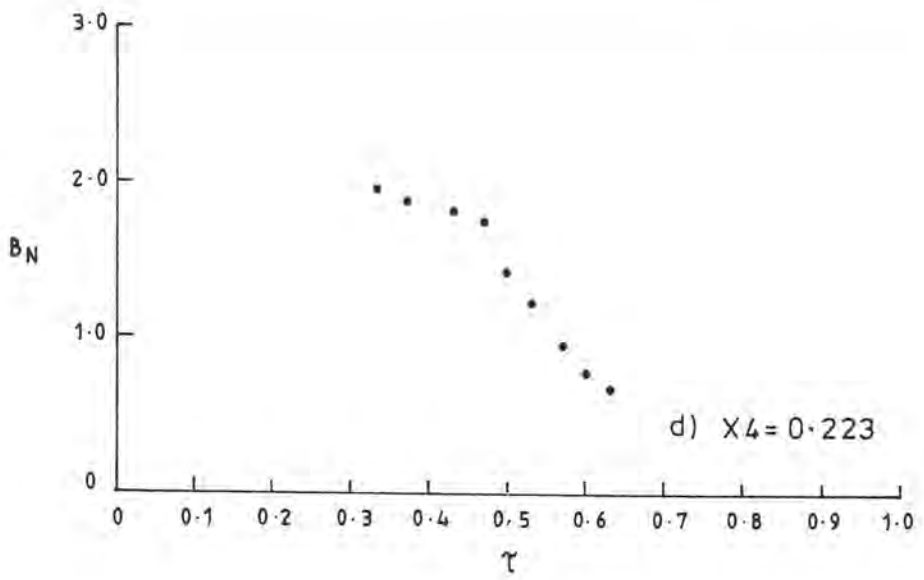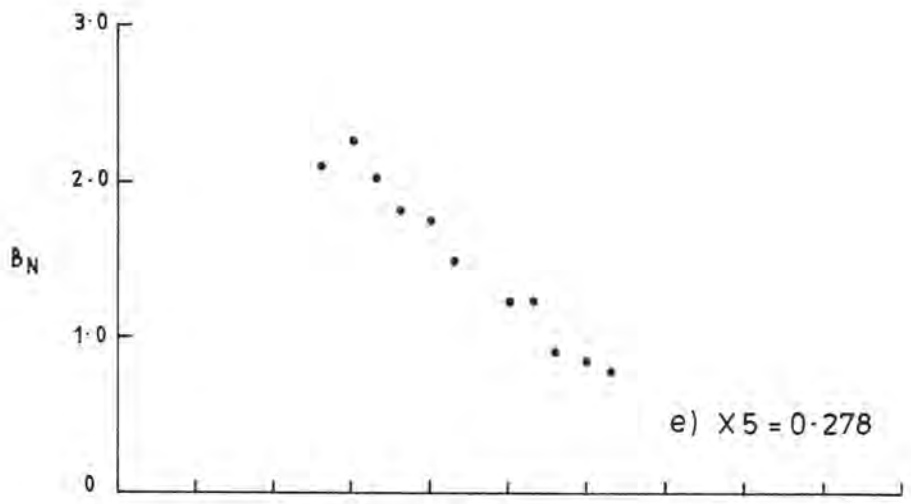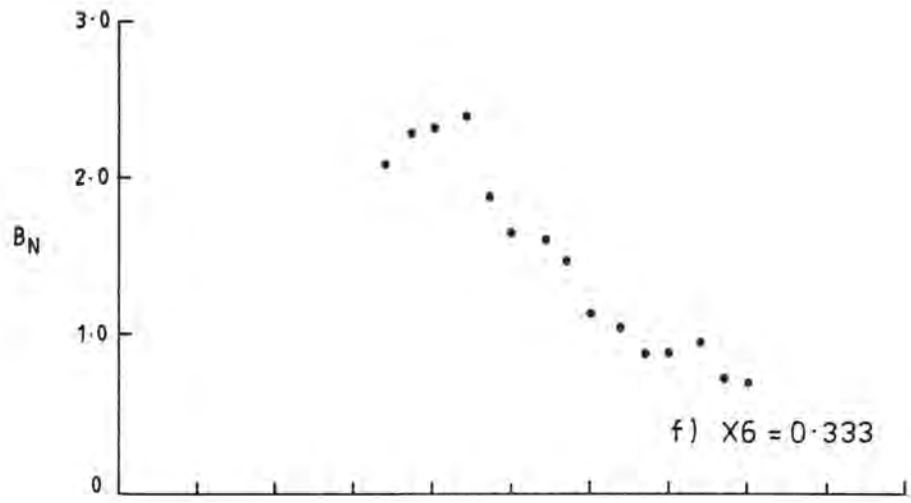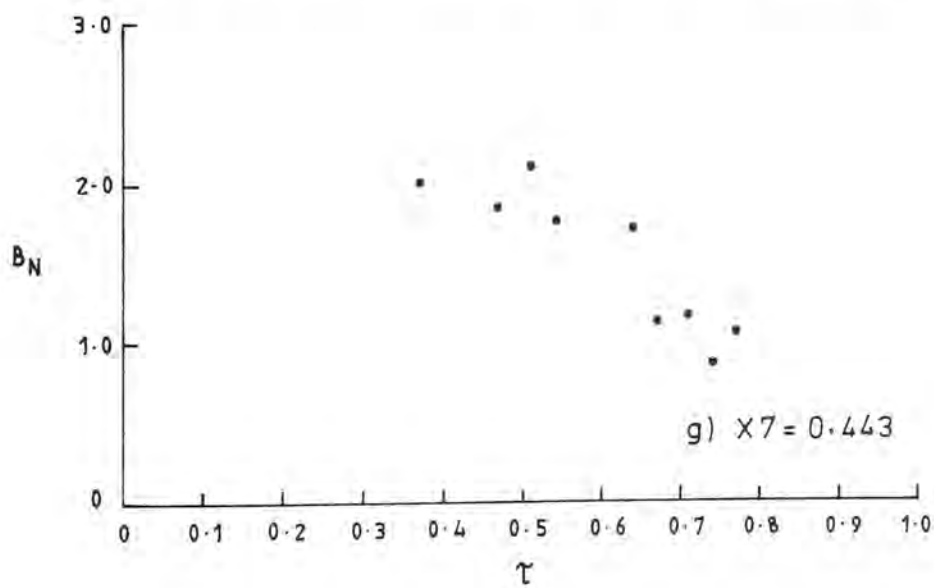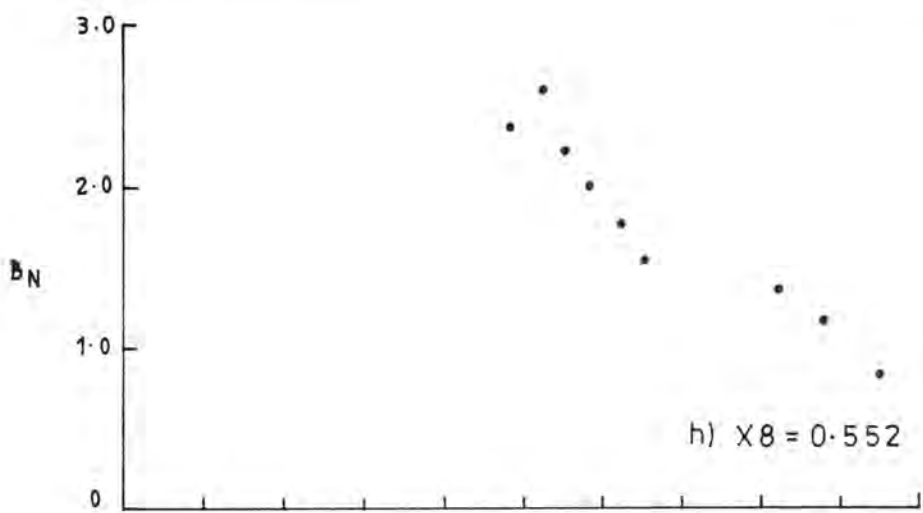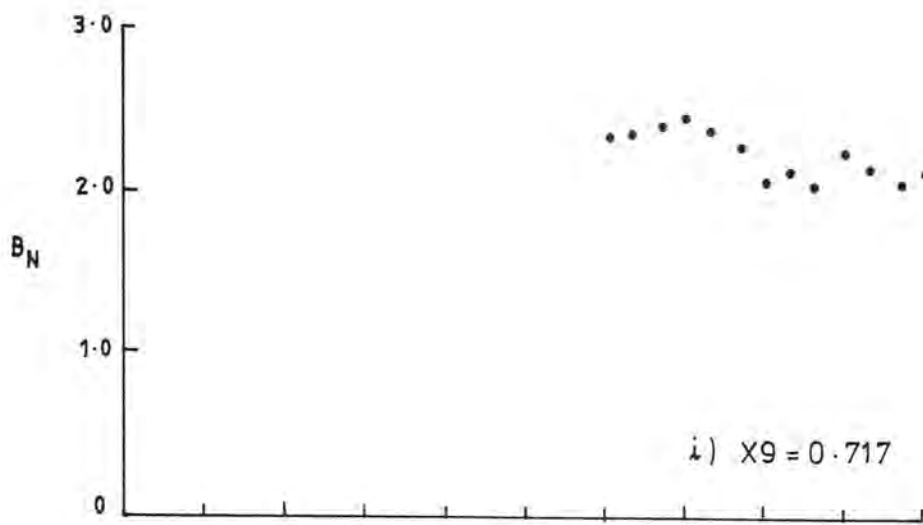
FIGURE 6·3 (Cont.)
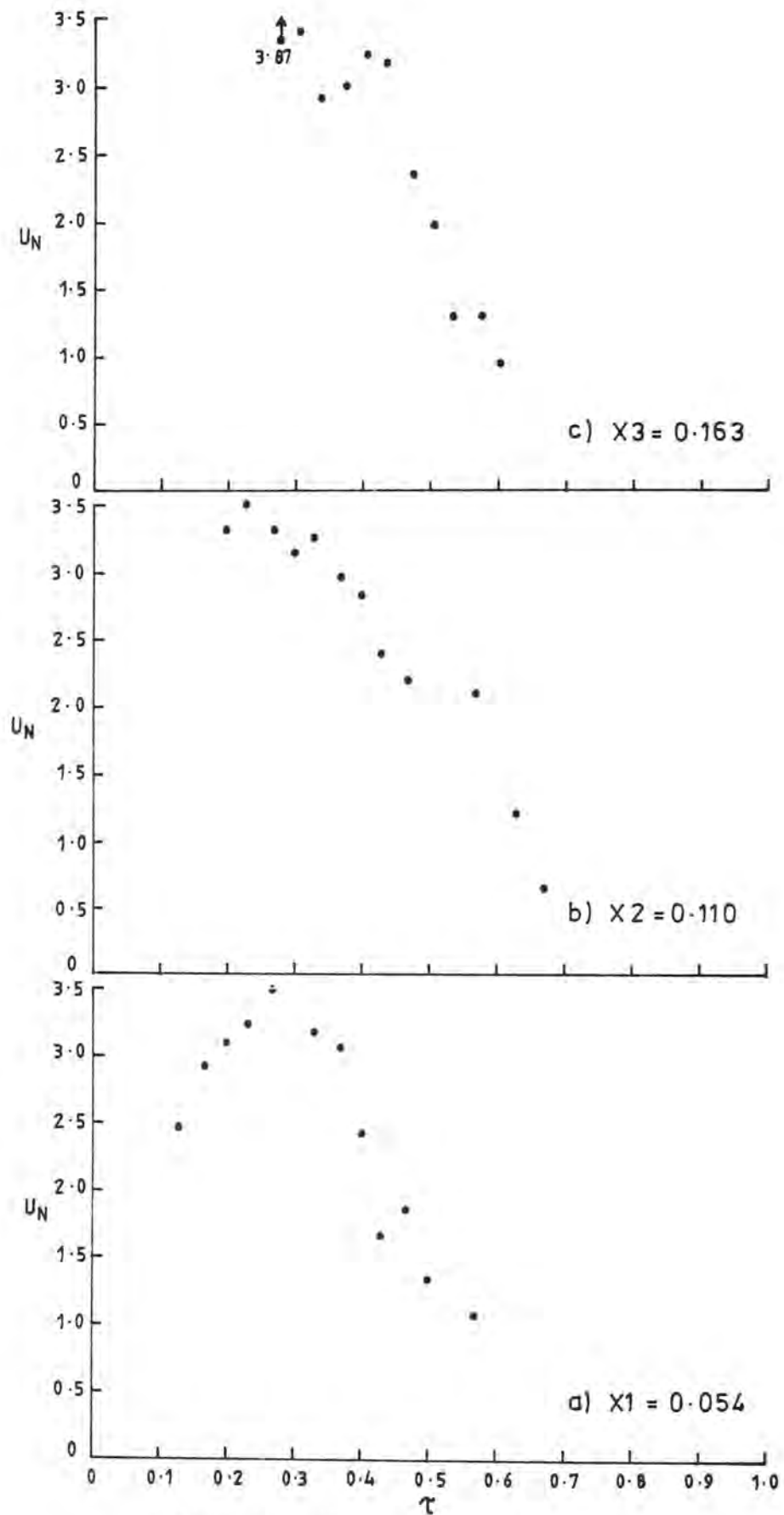
NOMINAL JET VELOCITY VARIATION
WITH TIME AT EACH WIRE LOCATION

FIGURE 6·4

f) X6 = 0·333

e) X5 = 0·278

d) X4 = 0·223

FIGURE 6·4 (Cont.)

i) X9 = 0·717

h) X8 = 0·552

g) X7 = 0·443
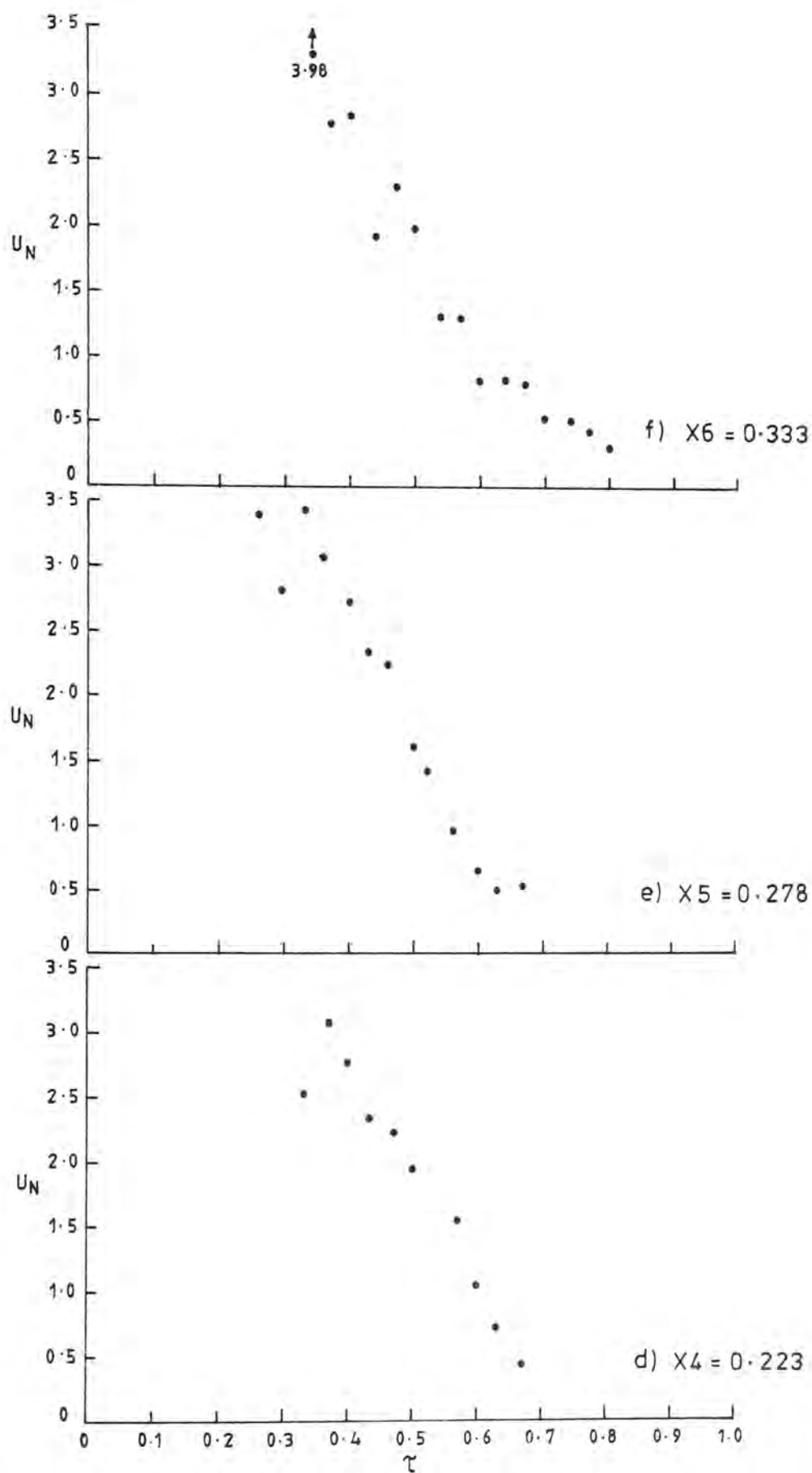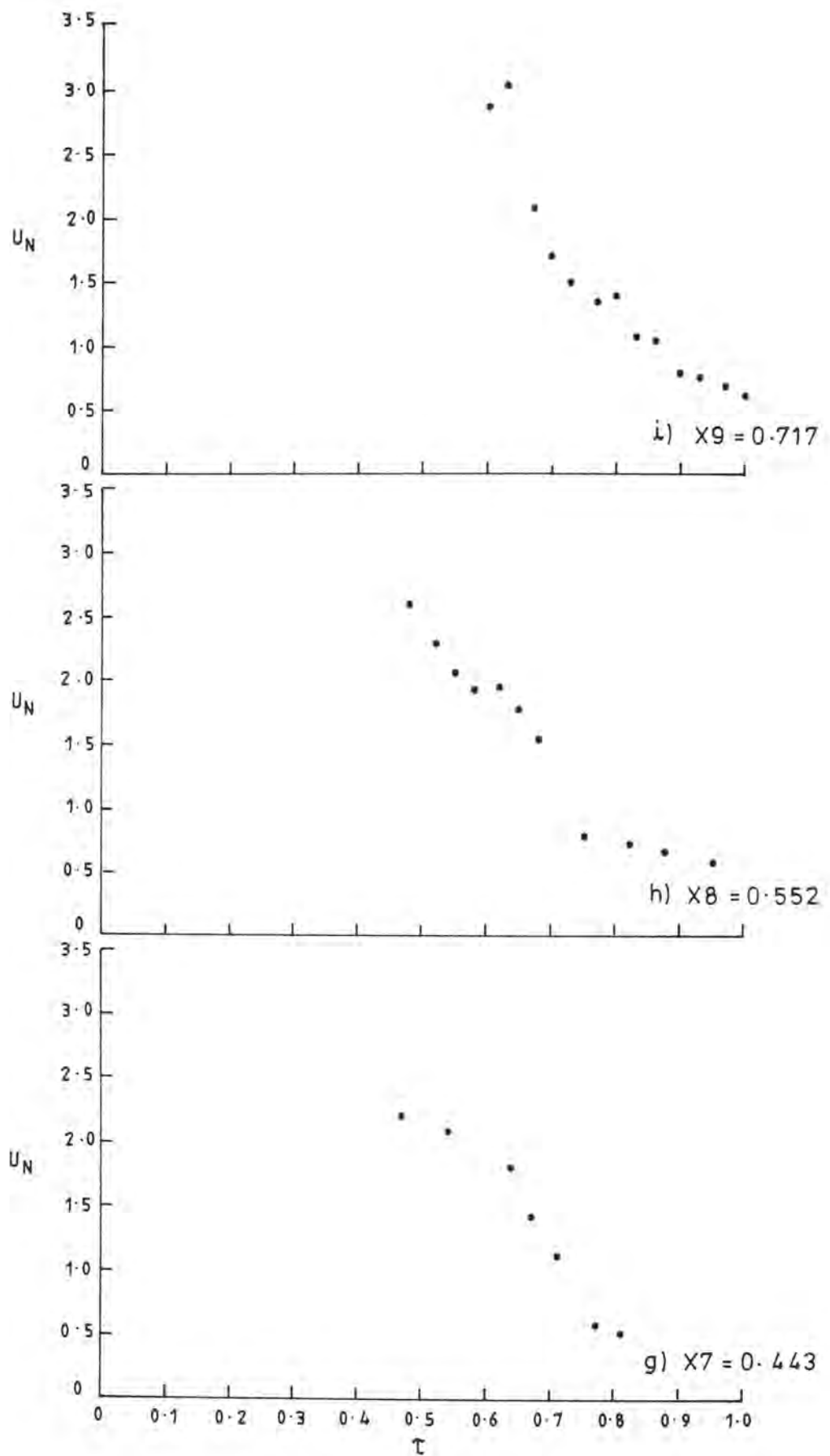
FIGURE 6·4 (Cont.)
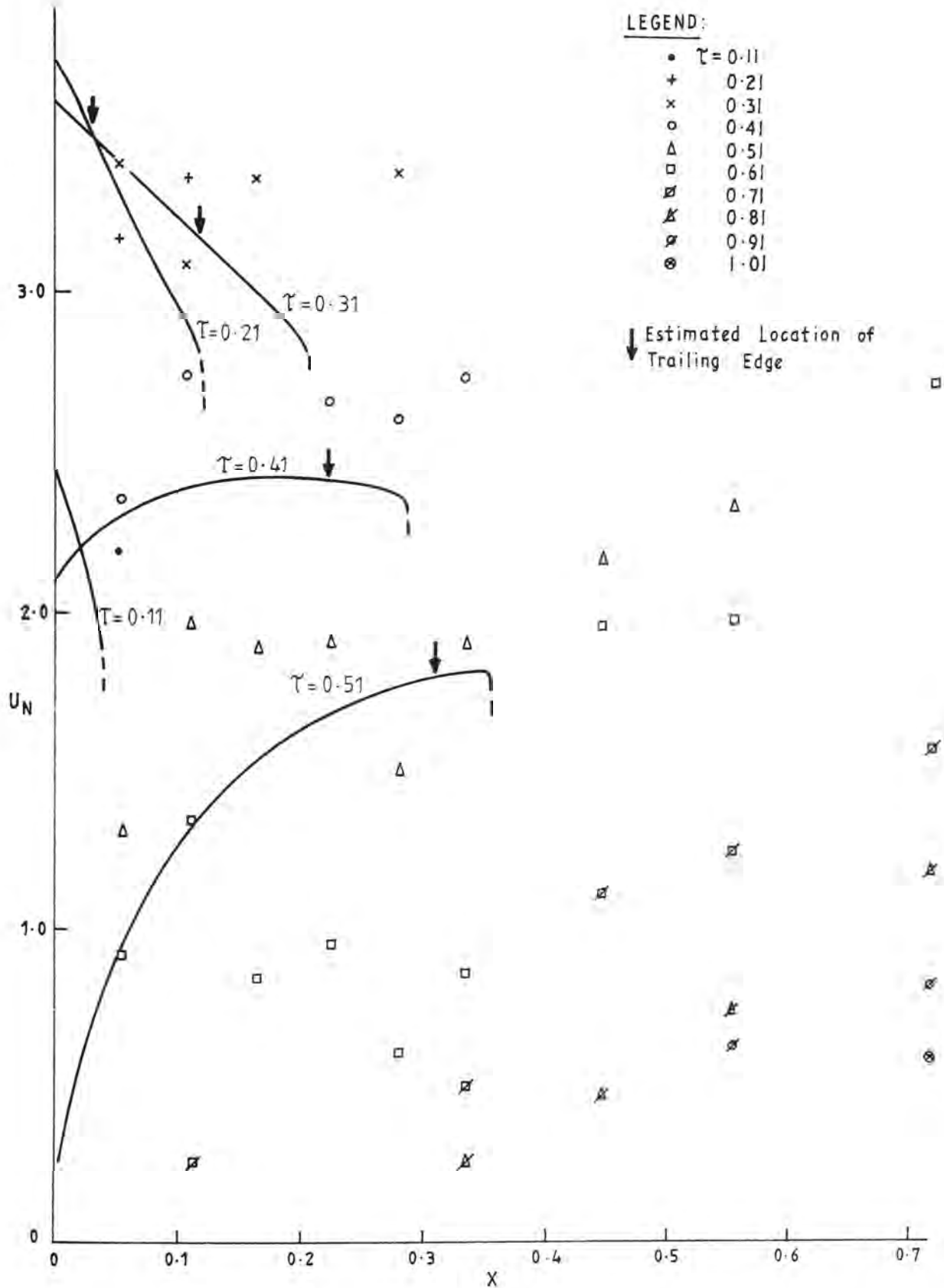
EXPERIMENTAL RESULTS FOR THE NOMINAL JET
AXIAL VELOCITY AT VARIOUS TIMES. ALSO SHOWN
ARE THE NUMERICAL SOLUTIONS

FIGURE 6·5
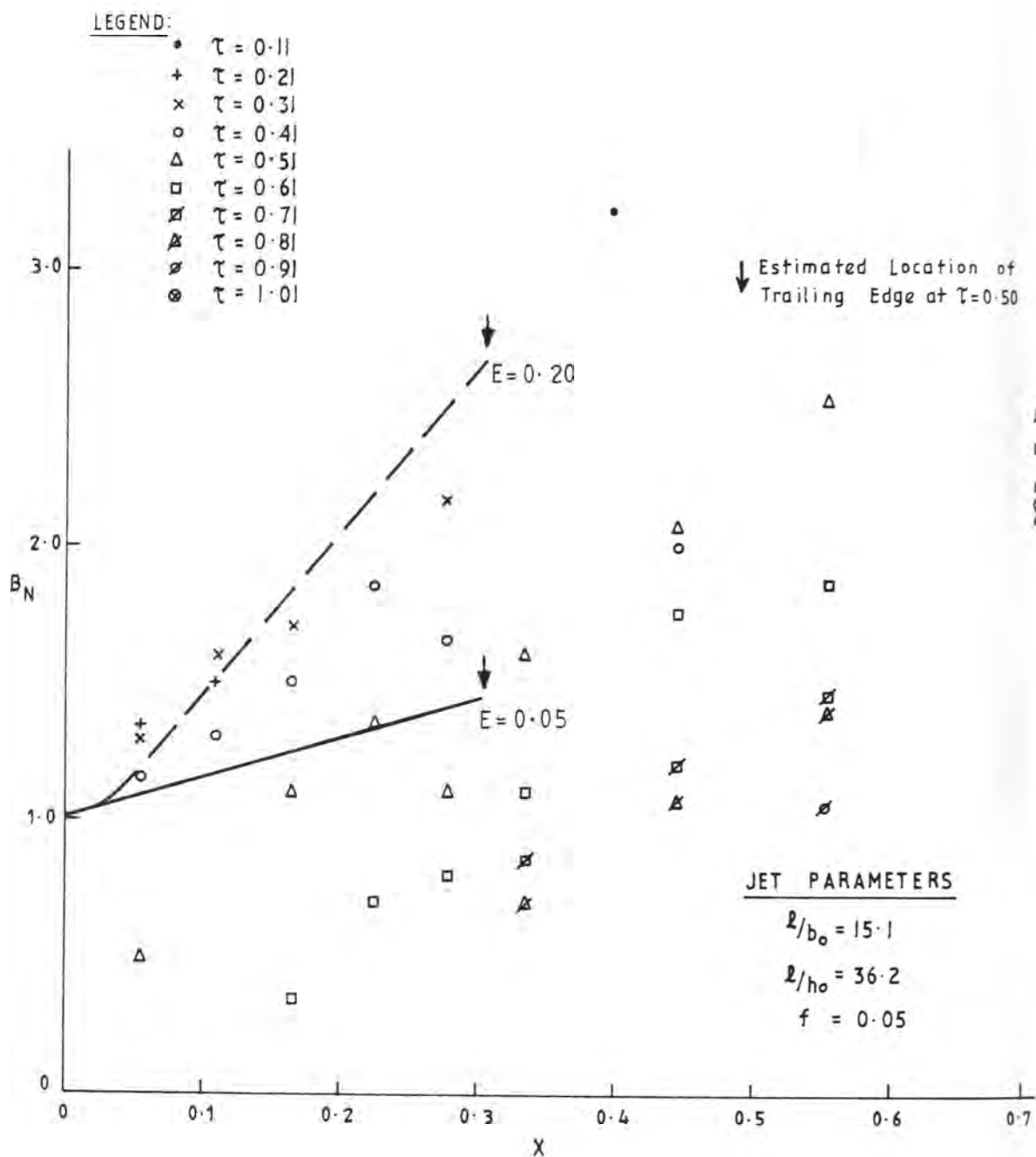
EXPERIMENTAL RESULTS FOR NOMINAL JET WIDTH
AT VARIOUS TIMES - ALSO SHOWN ARE THE
NUMERICAL SOLUTIONS FOR E = 0·05 AND 0·20

FIGURE 6·6

starting jet (see Chapter 2) indicated that there is a finite time during which the vortex pair cap is spun up and established. During this time the cap remains trapped near the inlet and hence the initial starting conditions for the numerical solution should vary depending on this time. For the experiment being discussed in this section a more appropriate initial condition may have been a jet with source conditions defined for $\tau \sim 0.1$, as this is when the trailing edge of the cap was estimated to leave the boundary. Such a change in the starting time for the solution does not change the form of the axial velocity distribution however.

The main failure of the numerical solution to reproduce the observed behaviour of the jet is shown in Figure 6.6. After the flow reversal, the jet tail progressively contracts towards the cap. The numerical solutions cannot predict this behaviour as a final steady state condition was necessary for the computations. However, at a location near the cap, and distant from the origin, it is considered that the predictions are valid.

Figures 6.7 and 6.8 show the predicted behaviour of an unsteady jet at the join between the jet and the cap. The numerical solutions were obtained by using the estimated location of the trailing edge of the cap shown in Figure 6.1 as a computational marker. As discussed earlier, the use of this location as a computational marker gives results which have the same form as those presented in Chapter 3 and Appendix 1 using the shock location as a marker. As data were obtained at various times for each wire location, the experimental jet behaviour at the join can be obtained by interpolation. These experimental results are also shown in Figures 6.7 and 6.8, and are in good agreement, particularly those for the nominal jet velocity (Figure 6.7). As
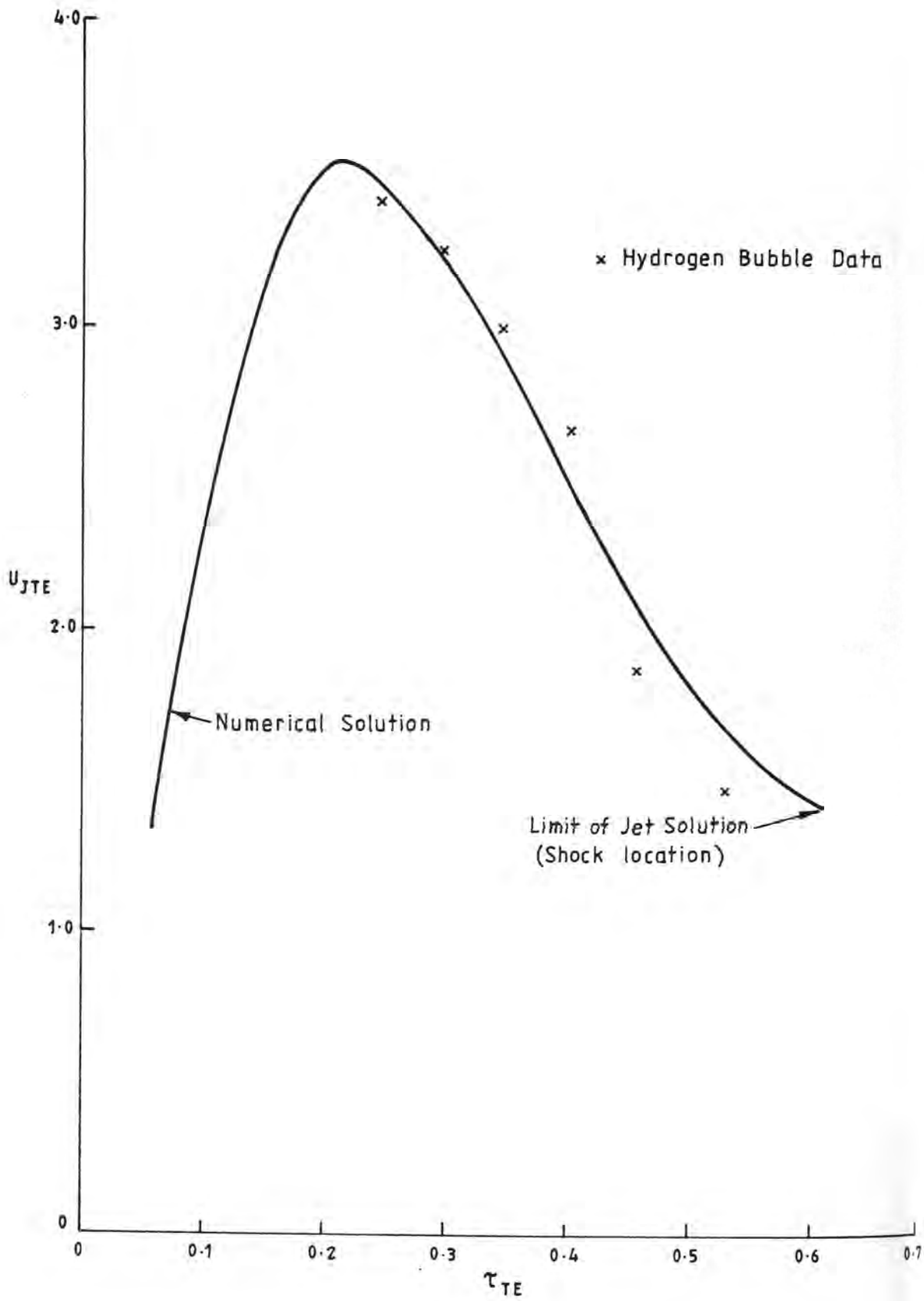
NOMINAL JET VELOCITY AT THE
TRAILING EDGE OF THE CAP

FIGURE 6·7
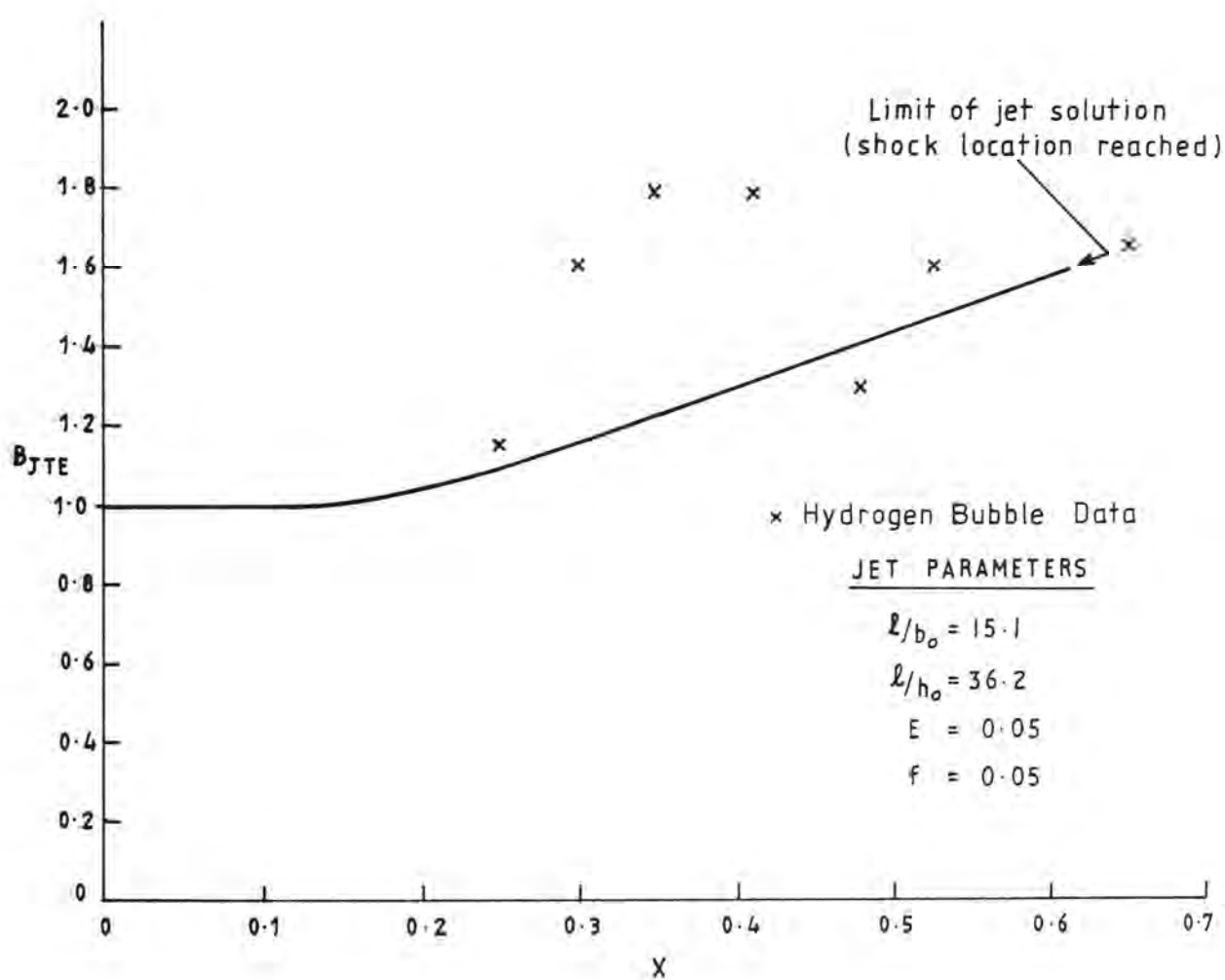
NOMINAL JET WIDTH AT THE TRAILING EDGE
OF THE CAP

FIGURE 6·8

discussed above, the growth of the jet does not follow the predicted behaviour as closely as the velocity distribution. Because of the difficulties defining the location of the trailing edge, it is possible that some of the data presented represent the cap behaviour.

An important feature of the real jet behaviour which has not been accounted for in the numerical model is the possible variation in the entrainment coefficient along the axis of the jet. The induced flow around the vortex pair cap will enhance the entrainment rate near the cap, resulting in a non-linear growth of the jet.

In general the hydrogen bubble technique can only be used to obtain qualitative information on the jet variables. Apart from the limited range of source conditions for which the technique is applicable, the main problem is that data can only be obtained at one wire location at any given time. The procedure adopted in this study was such that it was unavoidable for there to be a number of flow cycles between the photographs of the pulse trace at one wire location and at the next. This would inevitably result in varying ambient conditions for each wire and consequently may explain the variability in the results obtained.

6.2 Periodic Starting Jet

In this section the results obtained using confetti and dye tracing will be presented. The majority of experiments were performed in a basin of constant depth, h_o, with zero crossflow. The inlet parameters and characteristic scales for these experiments are presented in Table 6.1. The characteristic scales have been defined in Chapter 2. The range of ℓ/b_o and ℓ/h_o tested values was limited by the experimental

TABLE NO. 6.1:	INLET PARAMETERS AND CHARACTERISTIC SCALES FOR THE CONSTANT DEPTH EXPERIMENTS							
Expt No.	h_o mm	b_o mm	T sec	ℓ mm	ℓ/h_o	ℓ/b_o	U* mms^{-1}	K* mm^{2}s^{-1}
4	25	25	63	925	37.0	37.0	14.7	368
5	50	25	63	925	18.5	37.0	14.7	368
6	100	25	63	925	9.25	37.0	14.7	368
7	100	50	64	740	7.4	15.1	11.6	568
8	50	50	64	740	14.8	15.1	11.6	568
9	25	50	64	740	29.6	15.1	11.6	568
10	25	75	64	645	25.8	8.5	10.1	768
11	50	75	64	645	12.9	8.5	10.1	768
12	100	75	64	645	6.4	8.5	10.1	768
14	25	40	62.5	1480	59.2	37.0	23.7	948
15	12.5	40	62.5	1480	118.4	37.0	23.7	948
16	12.5	60	62.5	906	72.5	15.1	14.5	870
17	25	60	62.5	906	36.2	15.1	14.5	870
25	25	60	60	906	36.2	15.1	15.1	906
26	25	60	60	1310	52.40	21.8	21.8	1308
27	25	60	60	740	29.6	12.3	12.3	738
28	25	60	60	645	25.8	10.8	10.8	648
29	25	40	60	1310	52.4	32.8	21.8	872
30	12.5	40	60	1480	118.4	37.0	24.7	988
31	12.5	100	60	1480	118.4	14.8	24.7	2470
32	12.5	60	60	1480	118.4	24.7	24.7	1482
34	25	40	150	1310	53.8	33.7	8.7	348
35	25	40	60	1310	52.4	32.8	21.8	872
36	20	40	250	4738	236.9	118.5	18.9	756
37	25	60	60	906	36.2	15.1	15.1	906
38	25	60	120	1440	57.6	24.0	12.0	720
39	25	60	200	2020	80.8	33.7	10.1	606
43	25	60	60	906	36.2	15.1	15.1	906
44	25	60	60	906	36.2	15.1	15.1	906
46	25	60	60	792	32.8	13.2	13.2	792
47	25	160	60	1129	45.1	7.1	18.8	3008
48	25	100	60	706	28.2	7.1	11.8	1180
49	25	100	60	1321	52.8	13.2	22.0	2200
50	25	40	60	528	21.2	13.2	8.8	352
51	25	40	60	1596	63.8	39.9	26.6	1064
52	100	40	60	665	6.6	16.6	11.1	444
53	50	40	60	355	7.1	8.9	5.9	236
54	25	20	60	798	31.9	39.9	13.3	266
62	25	80	60	1510	60.4	18.9	25.2	2013
63	25	60	60	1510	60.4	25.2	25.2	1510
64	25	40	60	1510	60.4	37.8	25.2	1007

apparatus. As discussed in Chapter 5, the velocity distribution in and around the vortex pair cap is taken to be self-preserving.

6.2.1 Gross Features Of A Starting Jet

The methods used to measure the gross features of the starting jet were described in Chapter 4. The results obtained for the growth rate and translation of the cap will now be discussed.

6.2.1.1 Cap Growth Rate

The shape and size of the growing dyed fluid region was indicated on each photographic image. For each photograph, measurements were taken of the location of the leading edge of the dye, x_{LE}, the location of the centre of rotation of the vortices, x_c, the width of the cap at the centre location, b_{CAP}, and the distance between the apparent centres of rotation, b_c, as shown in Figure 6.9. An estimate was also made of the location of the trailing edge of the cap, x_{TE}. The centre of rotation of the vortices was estimated by visual inspection of the unsteady surface velocity traces. The reduction of a typical data set is given in Appendix 3.

Past investigations of turbulent vortex flows (Richards (1963), Wood (1965), Tsang (1970$_1$) and Wu (1977)) have expressed the growth of the vortex pair cap as the increase in the maximum width of the dyed fluid, b_{CAP}, with the distance to the leading edge, x_{LE}. The use of surface particle traces in the present study has enabled the growth to be expressed in terms of the increase in the separation of centres of rotation, b_c and the distance to the centreline, x_c. Both measurements of width are subject to experimental difficulties. The boundary of the
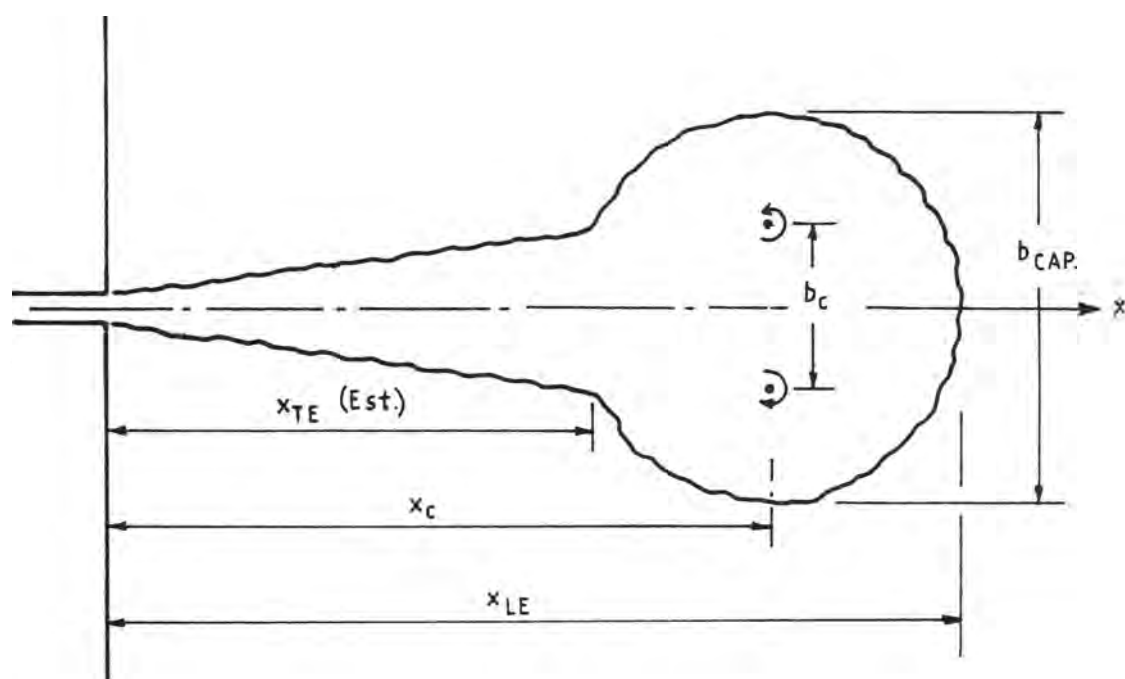
$$\alpha = \frac{2(x_{LE} - x_c)}{b_{CAP}}$$

DEFINITION SKETCH FOR MEASUREMENTS OF

THE STARTING FLOW

FIGURE 6.9

dyed fluid is irregular due to its turbulent nature, and although time exposure photography smooths the small scale fluctuations it does not eliminate the large scale billows.

The growth of a typical vortex pair cap is seen in Figure 6.10. The lateral dimension, b_c, is normalised with respect to the inlet width, b_o, and the location of the centreline of the cap, x_c, is normalised with respect to the characteristic length, ℓ. Also shown in Figure 6.10 is the variation in the dimensionless width of the dyed cap fluid, B_{CAP}. The behaviour of a starting flow released into a basin not initially at rest, is seen for the fifth cycle data in Figure 6.10. For most experiments the data for the first and fifth cycles were recorded and were found to be coincident until instabilities generated by the residual turbulence from previous cycles destroyed the vortex structure.

The dependence of the growth of the cap on the inlet parameter ℓ/b_o was examined to determine whether the flows can be considered similar for different inlet conditions. The dimensionless growth rate for all of the experiments with a given ℓ/b_o are shown in Appendix 3, Figure A3.6. Representative plots are shown as Figures 6.11 and 6.12. The dependence on ℓ/b_o is shown in Figure 6.11 for ℓ/b_o = 7.1, 16.6, 39.9, and 118.4. Also shown are the ℓ/h_o values for each experiment. Despite considerable scatter in some cases it a can be seen that the parameter ℓ/b_o can be indeed be used to group the experimental data obtained for tests with various initial characteristic lengths and inlet widths. Figure 6.12 shows the typical variation in vortex pair separation over a range of ℓ/h_o values for ℓ/b_o.
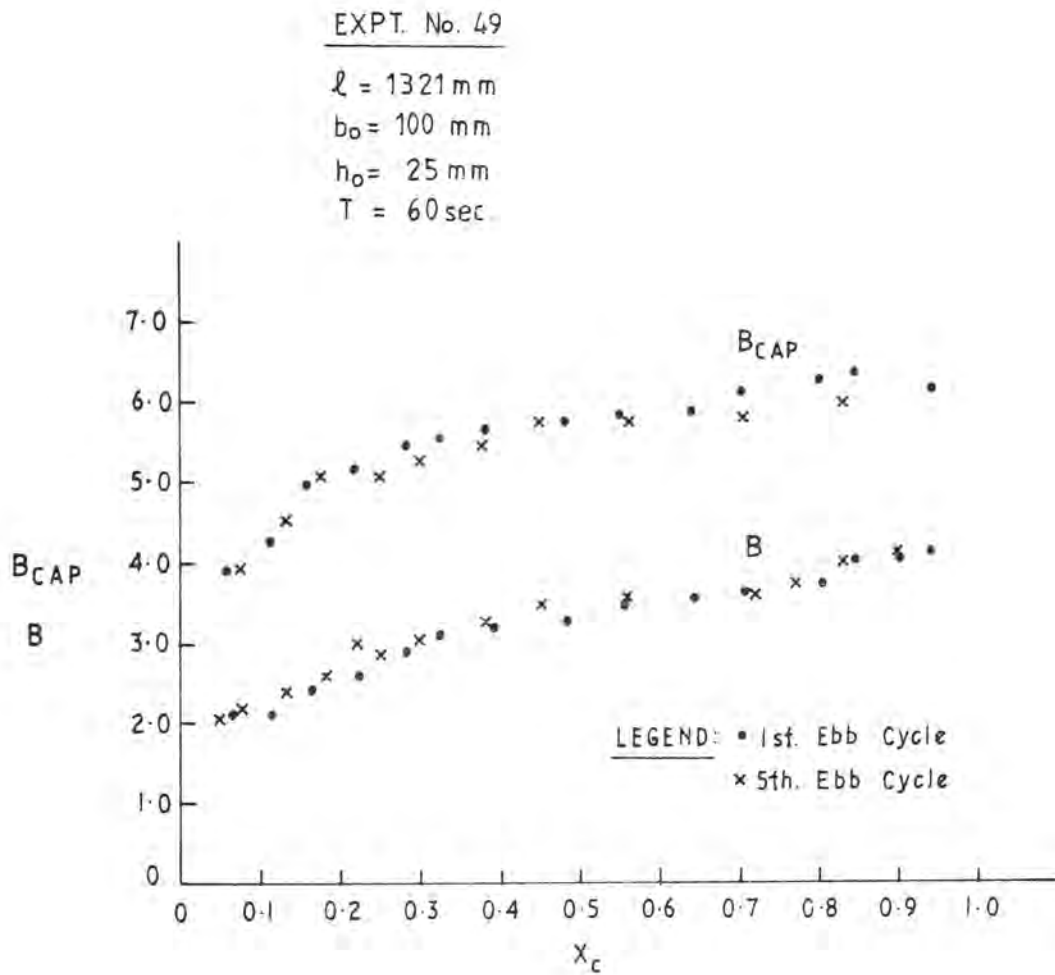
TYPICAL DIMENSIONLESS CAP WIDTH, B_{CAP},
AND VORTEX PAIR SEPARATION, B,
VERSUS DIMENSIONLESS DISTANCE X_C,
FROM THE INLET
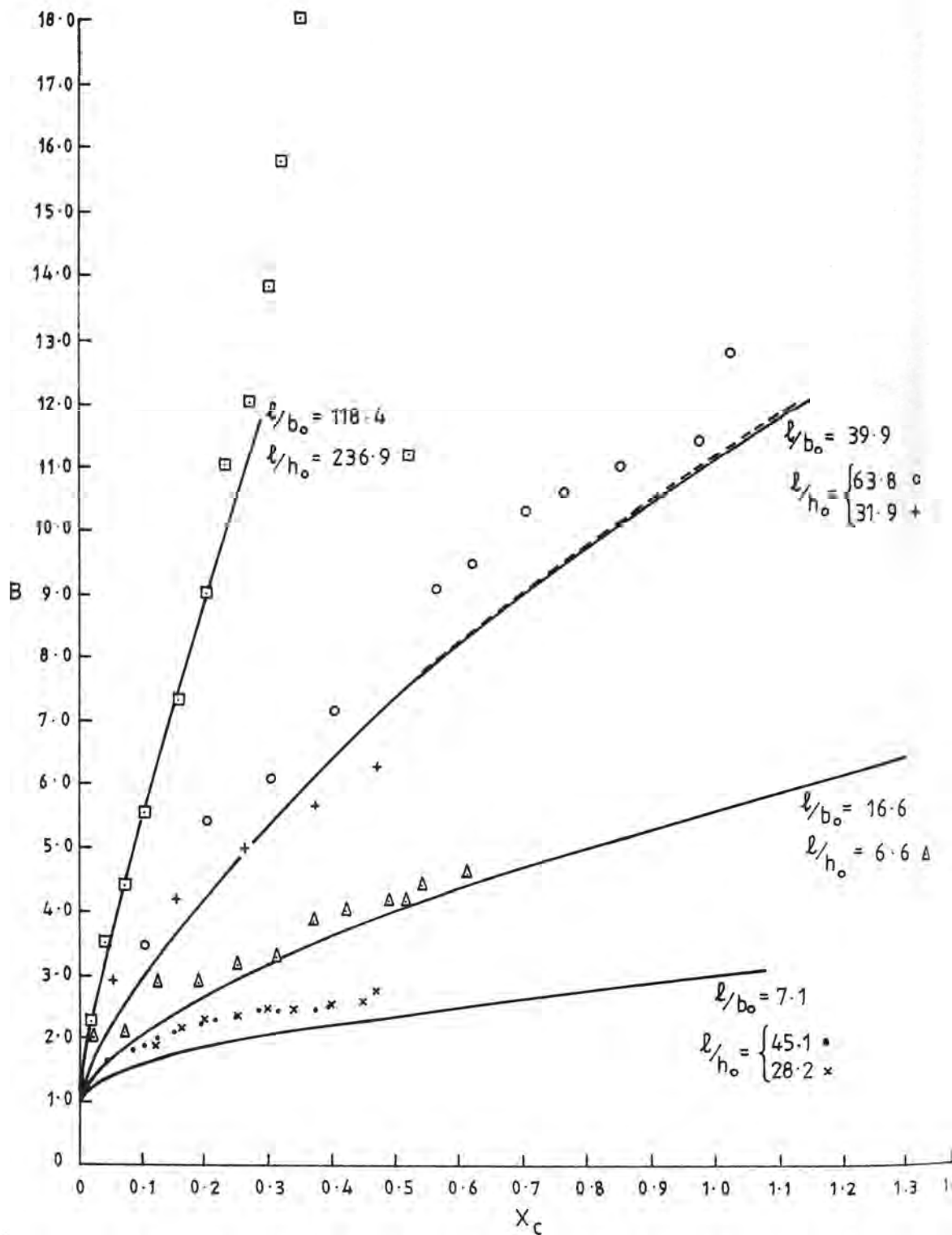
FIGURE 6·10

TYPICAL EXPERIMENTAL RESULTS SHOWING THE
DEPENDENCE OF THE VORTEX PAIR SEPARATION, B,
ON THE INLET WIDTH RATIO — ALSO SHOWN ARE
THE NUMERICAL SOLUTIONS

FIGURE 6·11
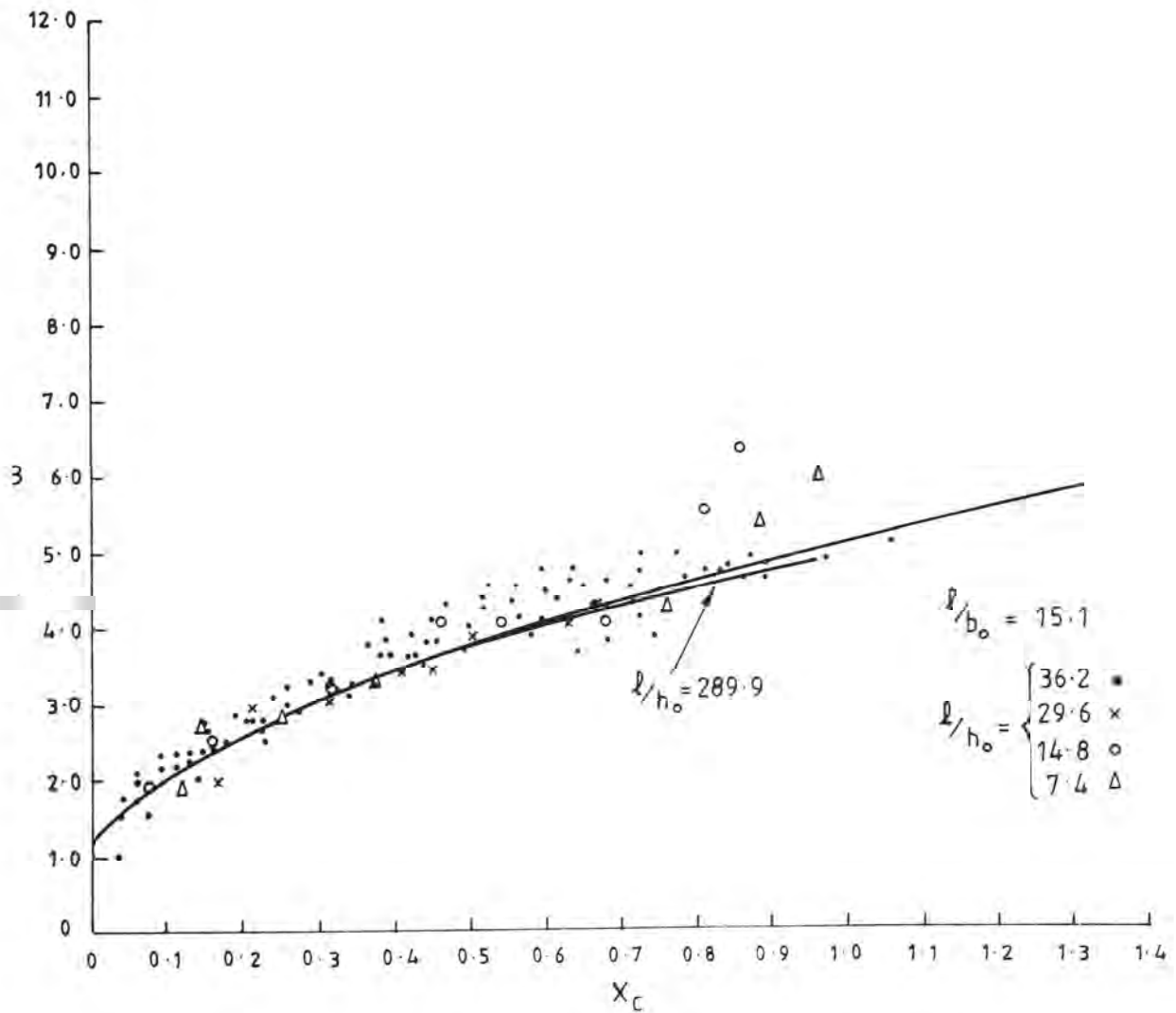
TYPICAL EXPERIMENTAL RESULTS SHOWING THE
DEPENDENCE OF THE VORTEX PAIR SEPARATION, B, ON
THE INLET DEPTH RATIO - ALSO SHOWN ARE THE
NUMERICAL SOLUTIONS

FIGURE 6·12

The line drawn through each set of data is the numerically predicted behaviour of the cap using the similarity constants determined in Chapter 5. In most cases the agreement is good. The initial rapid growth rate occurs during the increasing mass flux stage of the flow, and is dependent on the rate of increase of the mass flux. This in turn is a function of $(\ell/b_o)^{1/2}$. As the rate of supply of mass from the jet decreases, the growth rate asymptotes to that for an isolated vortex pair. The numerical predictions indicate that for most values of ℓ/b_o this state is not reached before loss of coherency in the vortex pair makes measurements impractical. The rate of increase in mass flux is greater for decreasing values of ℓ/b_o as the vortex pair remains near the source. Thus, decoupling of the vortex pair will occur sooner for these flows.

A summary of the growth rates for the later stages of the flow is given in Appendix 3, Table A3.2. In determining these values, a line of best fit was drawn through the later stages of each data set. An average entrainment coefficient, e = 0.07 ± 0.03 was determined for those experiments in which the vortex pair remained coherent. This value has been used to obtain the numerical solution shown in Figure A3.6. As expected, there is no dependence on ℓ/b_o in the variation in e.

Shown in Figure 6.12 is the ℓ/h_o dependence along with the predicted behaviour for ℓ/h_o = 289.9. There are no experimental data for this value. This ℓ/h_o dependence is only evident in the numerical solutions for very large values and during the later stages of the flow. There does, however, appear to be a weak dependence of the entrainment coefficient on the initial depth ratio ℓ/h_o. As seen in Figure 6.13, the entrainment coefficient decreases as the inlet depth

ratio increases. This trend can be explained by considering the shape of the vortex pair cap described by the shape factor α. As seen in Figure 6.14 there is a weak dependence of α on the inlet depth ratio indicating a progressive elongation of the cap in the direction of propogation as ℓ/h_o increases. Bottom friction introduces three-dimensional instabilities into the vorticity distribution, breaking down the organised structure of the vortex core. Vorticity is dispersed in the direction of travel reducing the width of the vorticity containing region. Allowance for this can be made by considering an effective entrainment coefficient equal to αe. This also has an average value of 0.07 ± 0.03, suggesting that the limitations in the method for determining e is countered by the depth effect. The entrainment coefficient can thus be considered a universal constant for the range of inlet conditions tested.

Comparison with growth rates determined by previous investigators is facilitated by estimating the growth rate of half of the maximum width of the dyed fluid, $b_{CAP}/2$, in relation to the distance to the leading edge of the cap, x_{LE}. By definition this growth rate, N, is given by:

$$N = \frac{e'}{(1+\alpha e')} = 0.10 \qquad (6.5)$$

where $e' = e\,\dfrac{C_3}{C_4} = 0.11$ and $\alpha = 0.98$.

This value is somewhat smaller than those previously reported for buoyant and non-buoyant puffs generated by an instantaneous release of fluid. Typical of the values of N for non-buoyant puffs is that obtained by Wu (1977). The average entrainment coefficient for a well
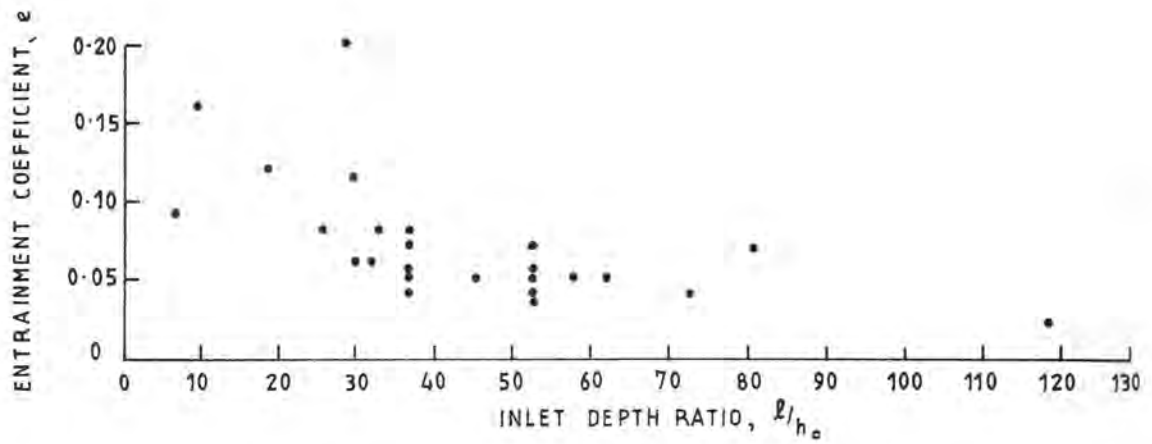
VARIATION IN THE VORTEX PAIR CAP
ENTRAINMENT COEFFICIENT WITH THE
INLET DEPTH RATIO

FIGURE 6·13
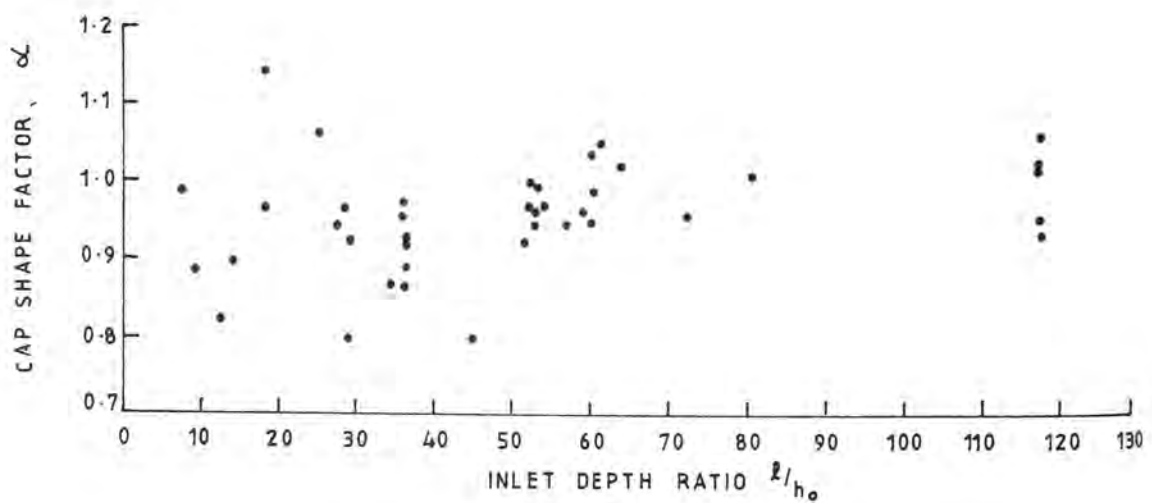
VARIATION IN THE VORTEX PAIR CAP
SHAPE FACTOR WITH THE
INLET DEPTH RATIO

FIGURE 6·14

controlled set of experiments was N = 0.26. The Reynolds Number, Re, ranged from 5,000 to 18,500, where Re is defined in terms of the source width and the initial velocity. In the present study the characteristic Reynolds Number, Re*, ranges from 400 to 3,000.

Maxworthy (1974) has suggested that the growth rate of a vortex ring (and a vortex pair) is dependent on the organisation of vorticity in the core. For a vortex ring with vorticity confined to a small turbulent core (a core radius about 0.10 times the ring radius), he obtained an entrainment coefficient e′ = 0.017, for Reynolds Numbers in the range of 14,000 to 30,000.

An impulsively generated turbulent puff has vorticity distributed throughout the puff. The scale of the turbulent fluctuations are also greater than for a vortex ring, and hence more ambient fluid will be engulfed at the cap - ambient fluid interface. The gradual spin-up process in the present case is responsible for a more organised vorticity distribution and smaller turbulent fluctuations than for a turbulent puff, and consequently a smaller growth rate.

The numerical predictions for the growth of the vortex pair cap are, in general, close to the experimentally determined behaviour (Figure 6.11). Insufficient experimental data is available on the later stages of the flow and consequently determination of the point where the vortex pair cap becomes decoupled is not possible. The theoretical solutions do not predict decoupling until well into the cycle. However, this will be an overestimate due to the inadequacies of the theoretical model in accounting for the real jet tail behaviour after τ = 0.50.

After the initial period of rapid growth of the cap, the growth rate asymptotes to that for a decoupled cap. Thus locating the exact decoupling point is not critical to the flow development.

The initial rapid growth rate corresponds to the stage of the flow where the mass flux in the jet at the trailing edge of the cap is increasing nearly linearly with time. It is interesting to note that if this linear increase in driving force was continued indefinitely, it is expected that a similarity state would be reached. The behaviour of such a starting jet would be similar to a two-dimensional starting plume which also has a linearly increasing force.

6.2.1.2 The Motion Of The Vortex Pair Cap.

The advance of the cap away from the inlet is represented by the location, x_c, of a line drawn between the apparent vortex centres. This is shown for all experiments in normalised form in Figure A3.7 in Appendix 3, plotted against time after the commencement of the ebb discharge, for various ℓ/b_o ratios. Representative plots are shown as Figures 6.15 and 6.16 indicating the ℓ/b_o and ℓ/h_o dependence respectively. In general, data are not available for times less than $\tau = 0.05$, as the vortices were too small for the velocity patterns to be recognised. For times greater than $\tau = 1.00$, the velocity pattern became incoherent due to pair instabilities. This made the determination of the location of the centreline somewhat arbitrary at these later stages of flow development.

The agreement of the predicted behaviour with that observed experimentally is not as good as it was for the cap growth. Generally, the predictions overestimate the advance of the cap for low ℓ/b_o values,
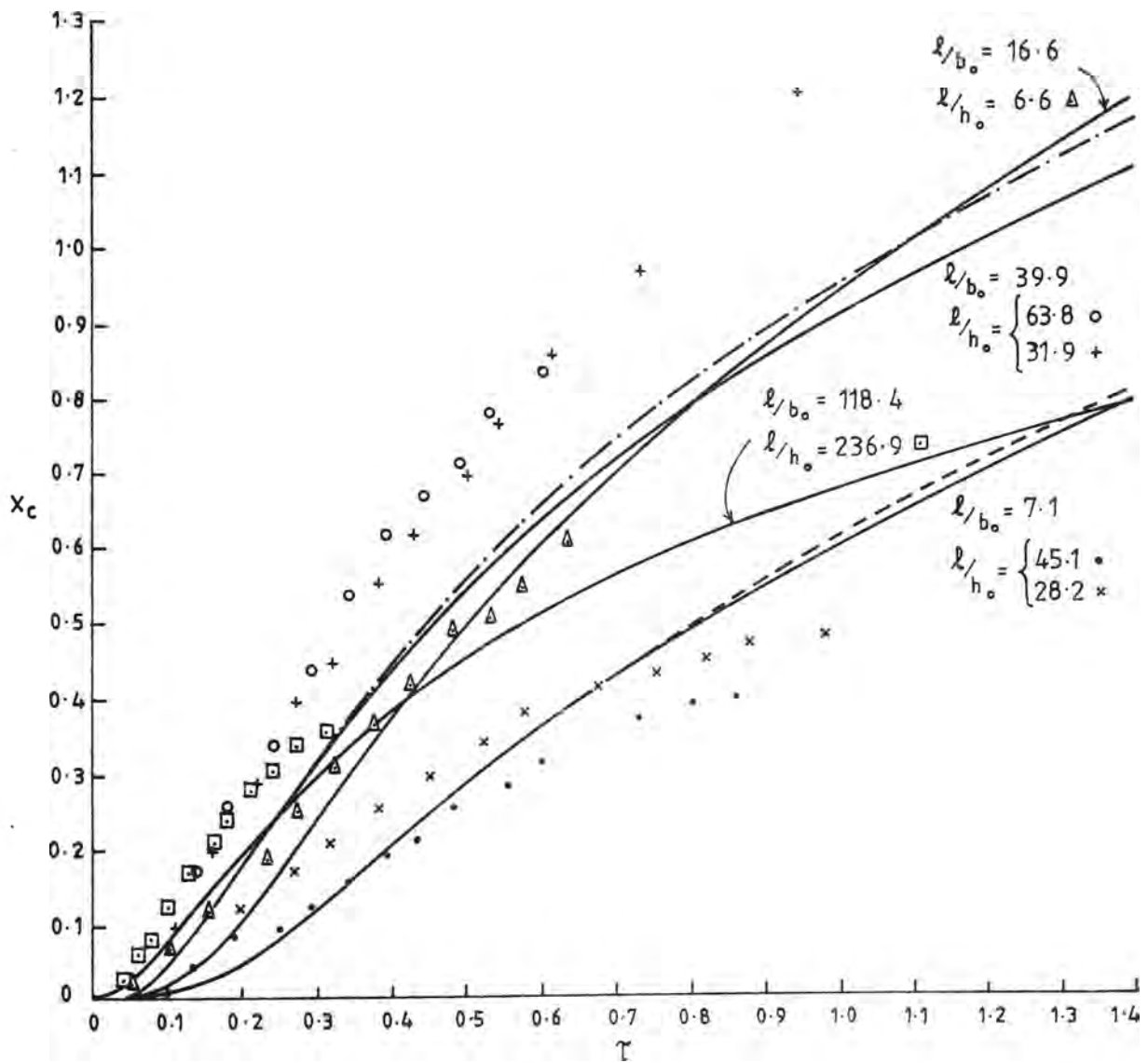
TYPICAL EXPERIMENTAL RESULTS SHOWING THE
DEPENDENCE OF THE VORTEX PAIR CAP ADVANCE
ON THE INLET WIDTH RATIO — ALSO SHOWN ARE
THE NUMERICAL SOLUTIONS

FIGURE 6·15
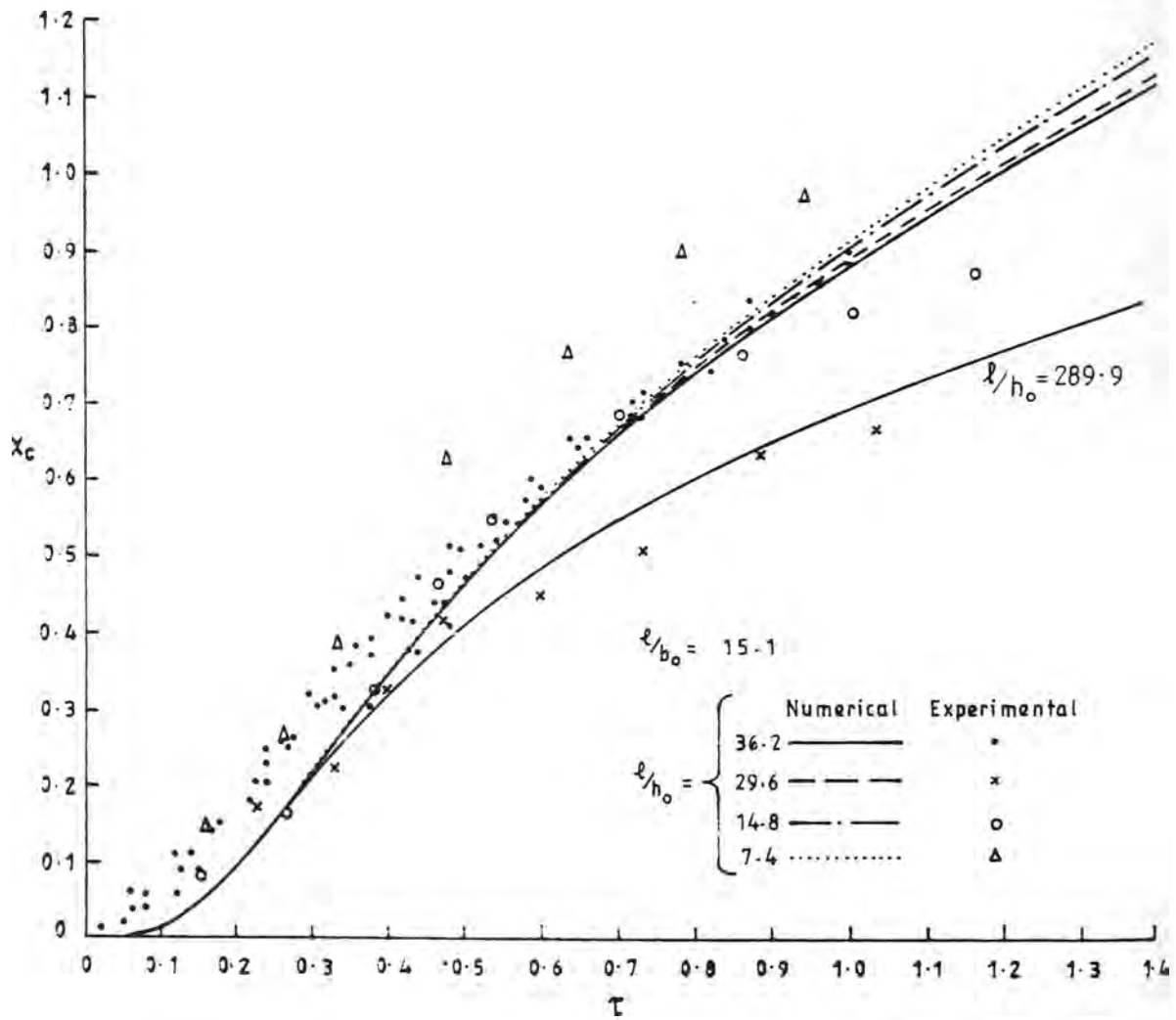
TYPICAL EXPERIMENTAL RESULTS SHOWING THE
DEPENDENCE OF THE VORTEX PAIR CAP ADVANCE ON THE
INLET DEPTH RATIO — ALSO SHOWN ARE THE
NUMERICAL SOLUTIONS

FIGURE 6·16

and underestimate the advance for high ℓ/b_o values. Possible reasons for this discrepancy will be discussed later. The shape of the advance curve does not change with variation in ℓ/b_o.

There is little variation in the advance of the cap with variation in ℓ/h_o. It must be noted, however, that the range of ℓ/h_o values was limited by the experimental facilities. A more realistic value of this parameter would be around $\ell/h_o = 200$ (See Chapter 10 for a discussion on the modelling of tidal flows). The predicted behaviour for $\ell/h_o = 289.9$ is shown on Figure 6.16. An indication of the cap behaviour at large ℓ/h_o values can be seen in the apparent inconsistency in Figure 6.15 for the predicted advance of the $\ell/b_o = 118.4$, $\ell/h_o = 236.9$ experiment and to a lesser extent the $\ell/b_o = 39.9$ experiments. Cap advance has been slowed considerably at the higher ℓ/h_o values, reversing the trend of cap advance becoming faster with increasing ℓ/hb_o values.

The discrepancy between the predicted and experimental results can be attributed to the somewhat imprecise method of experimentally determining the commencement of the ebb discharge ($\tau = 0$). There is a short time between flow commencement and the development of a clearly definable circulation. In addition, the mathematical model does not adequately describe the initial state of the starting jet. It has been assumed that the jet and cap are fully developed at the flow commencement. In reality there is an initial spin up period for the vortices before the similarity state assumed in the model is reached. Also flow must commence at a non-zero time to avoid a computational singularity. The influence of the initial conditions on the solutions is discussed in Appendix 2. An alternative description of cap translation could be obtained using the location of the leading edge of the cap, x_{LE}, was used as the prime variable. The computational method can be readily

modified for this using the assumption of cap shape similarity.

6.2.2 Gross Features of a Staring Jet in a Basin with Linearly Varying Depth

The inlet parameters and characteristic scales for those experiments in which the depth was increasing linearly with distance from the inlet are given in Table 6.2. Experiments were conducted with bed slopes of 1, 2 and 5 per cent. The numerical predictions and the experimental results are shown in Figures 6.17 and 6.18 for the variation with dimensionless distance, X_c, of the apparent vortex pair separation, B, and the variation with dimensionless time, τ, of X_c respectively. The main feature of these results is the suppression of the steady jet expansion with increasing bed slope. After the initial growth up to $\tau = 0.25$, the pair separation remains nearly constant for $\varepsilon = 0.02$ and contracts for slopes greater than 0.02. For comparison, the predictions for a horizontal bed are shown on Figure 6.17b. The experimental data matches the predictions reasonably well. However, the data is limited for the $\varepsilon = 0.05$ slopes because of the incoherency of the vortex structure caused by instabilities in the vortex core as the depth increases. As with the constant depth experiments, the predictions do not match the experimental results as well for the cap advance, Figure 6.18.

6.2.3 General Discusion

It is difficult to predict the behaviour of a periodic starting jet using a gross feature similarity model because of the numerous dynamic factors which influence the vorticity distribution. During the initial spin-up for instance, a number of influences can be identified.

TABLE 6.2	INLET PARAMETERS AND CHARACTERISTIC SCALES FOR THE LINEARLY VARYING DEPTH EXPERIMENTS							
Expt No.	h_o mm	b_o mm	T sec	ℓ mm	ℓ/h_o	ℓ/b_o	U^* mms^{-1}	Bed Slope ε,%
18	125	40	60	1480	59.2	37.0	24.7	1
21	25	40	60	1480	59.2	37.0	24.7	2
40	25	60	60	906	36.2	15.1	15.1	2
41	25	60	60	645	25.8	10.8	10.8	2
42	25	60	60	1480	59.2	24.7	24.7	2
65	25	60	60	906	36.2	15.1	15.1	5
66	25	60	60	1480	59.2	24.7	24.7	5
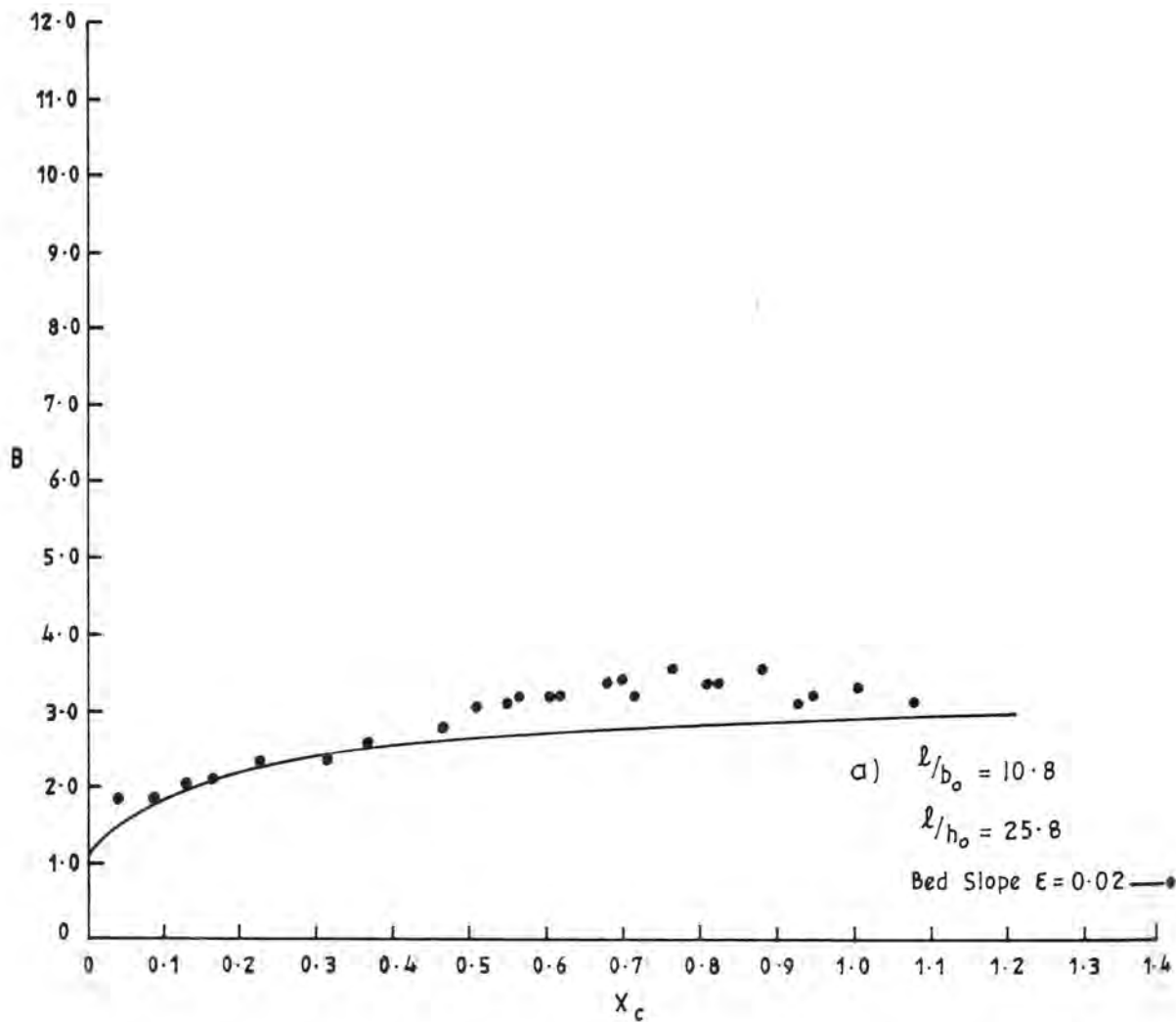
DIMENSIONLESS VORTEX SEPARATION, B, VERSUS
DIMENSIONLESS DISTANCE, X_c, FOR EXPERIMENTS
IN A BASIN WITH LINEARLY INCREASING DEPTH
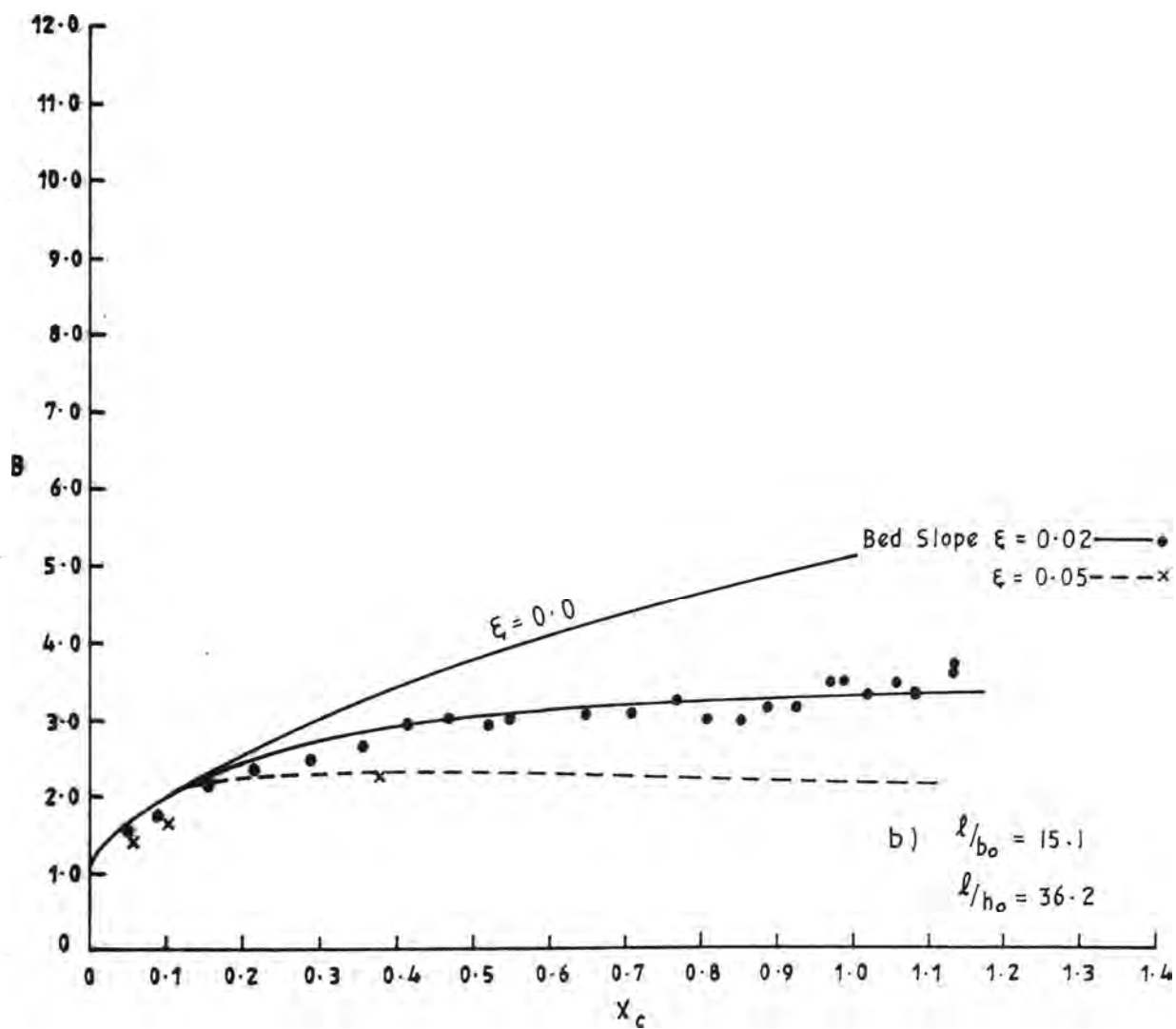
FIGURE 6·17
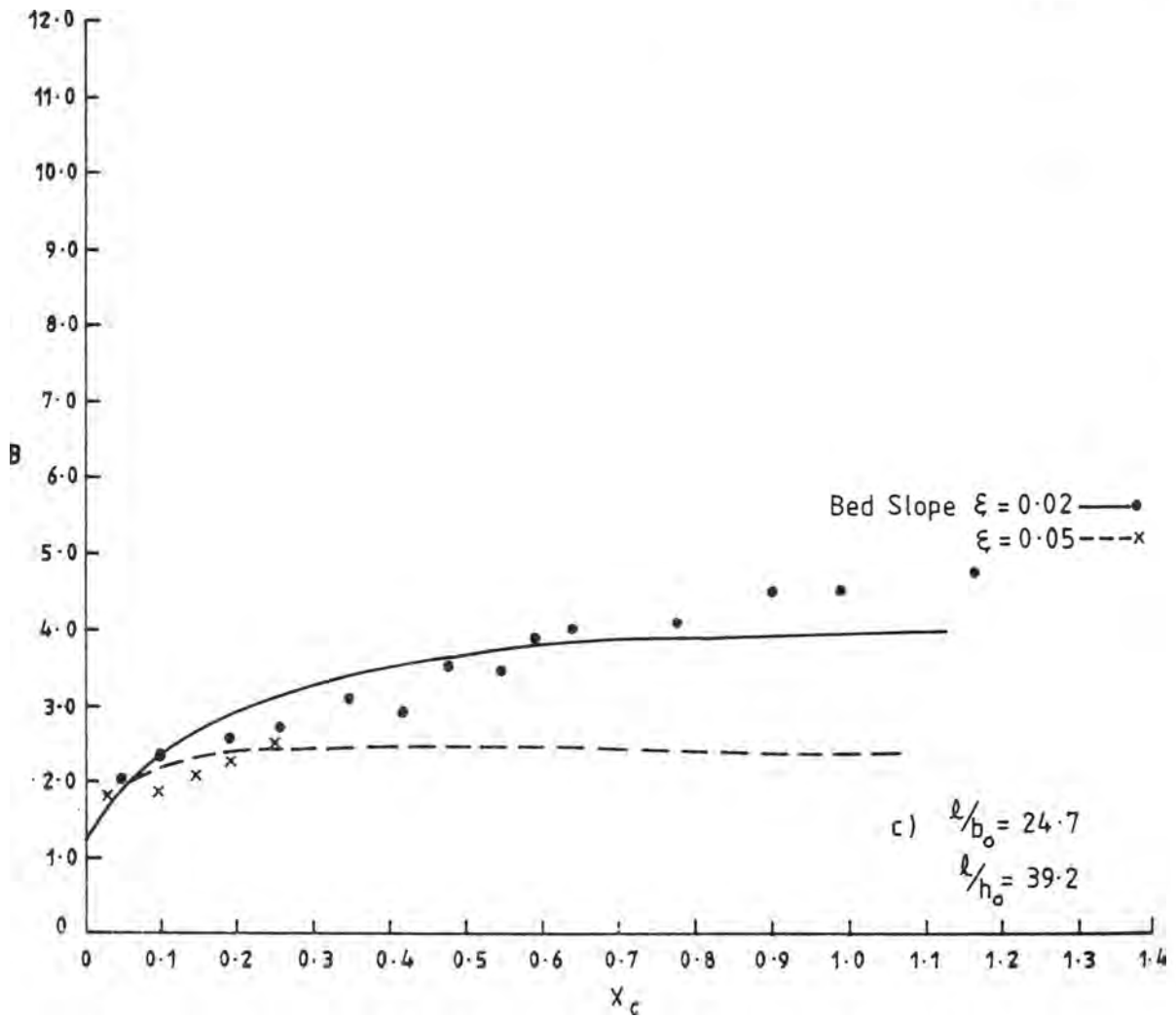
FIGURE 6·17 (Cont.)
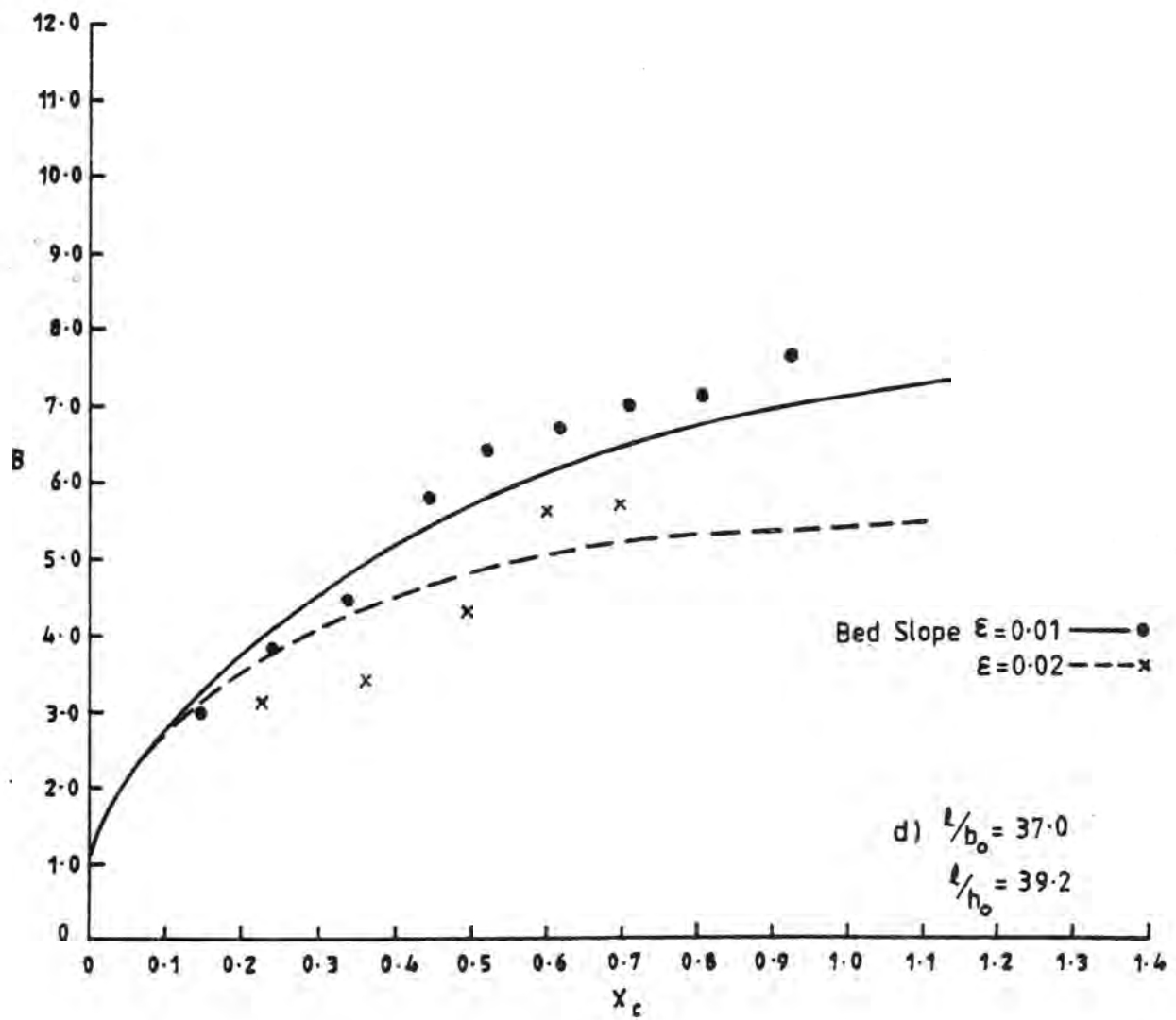
FIGURE 6·17 (Cont.)

FIGURE 6·17 (Cont.)
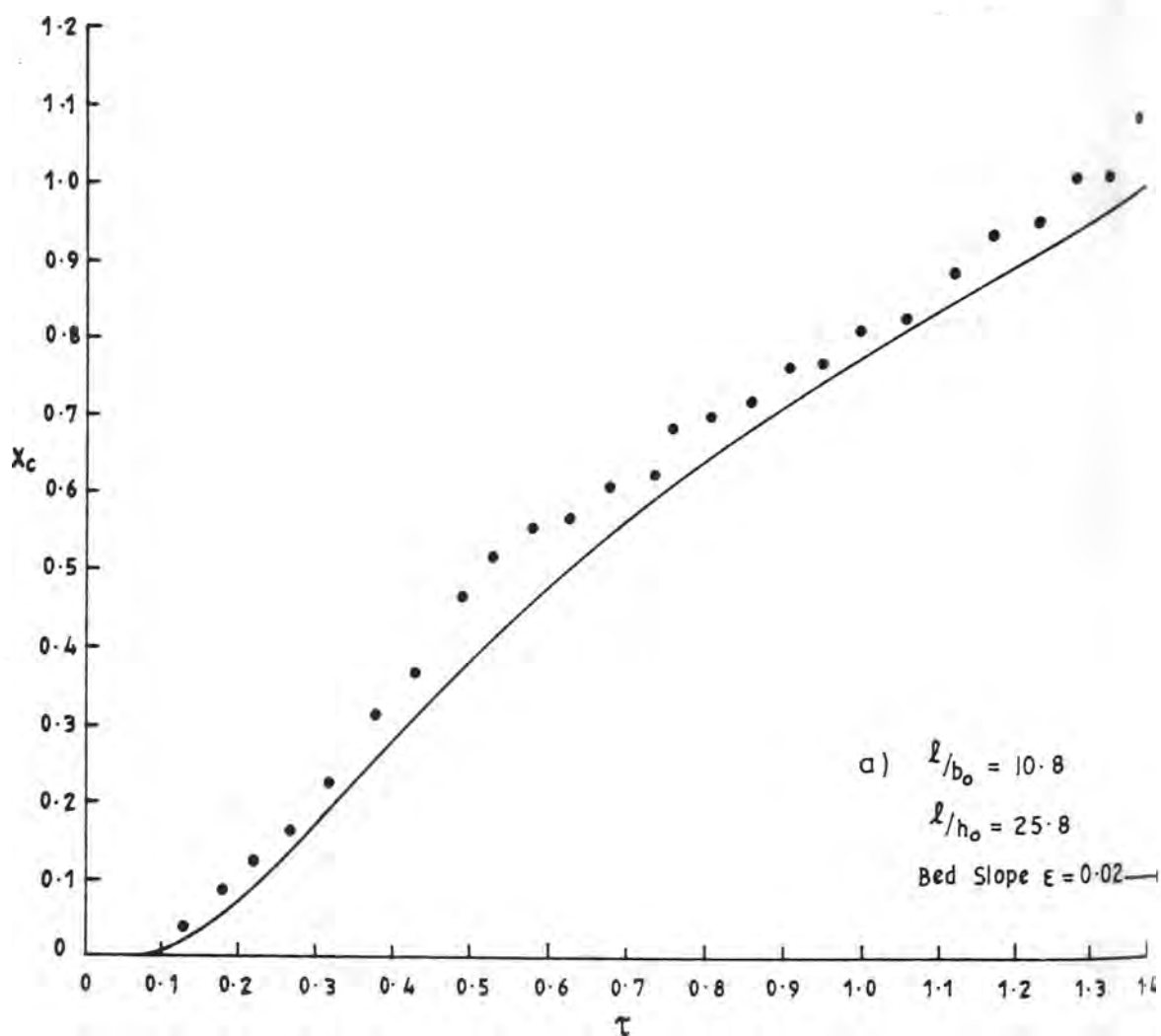
DIMENSIONLESS DISTANCE FROM THE INLET TO THE
VORTEX CENTRELINE, X_C, VERSUS DIMENSIONLESS
TIME, τ, FOR EXPERIMENTS IN A BASIN WITH
LINEARLY INCREASING DEPTH

FIGURE 6·18

b) $\ell/b_o = 15 \cdot 1$

$\ell/h_o = 36 \cdot 2$
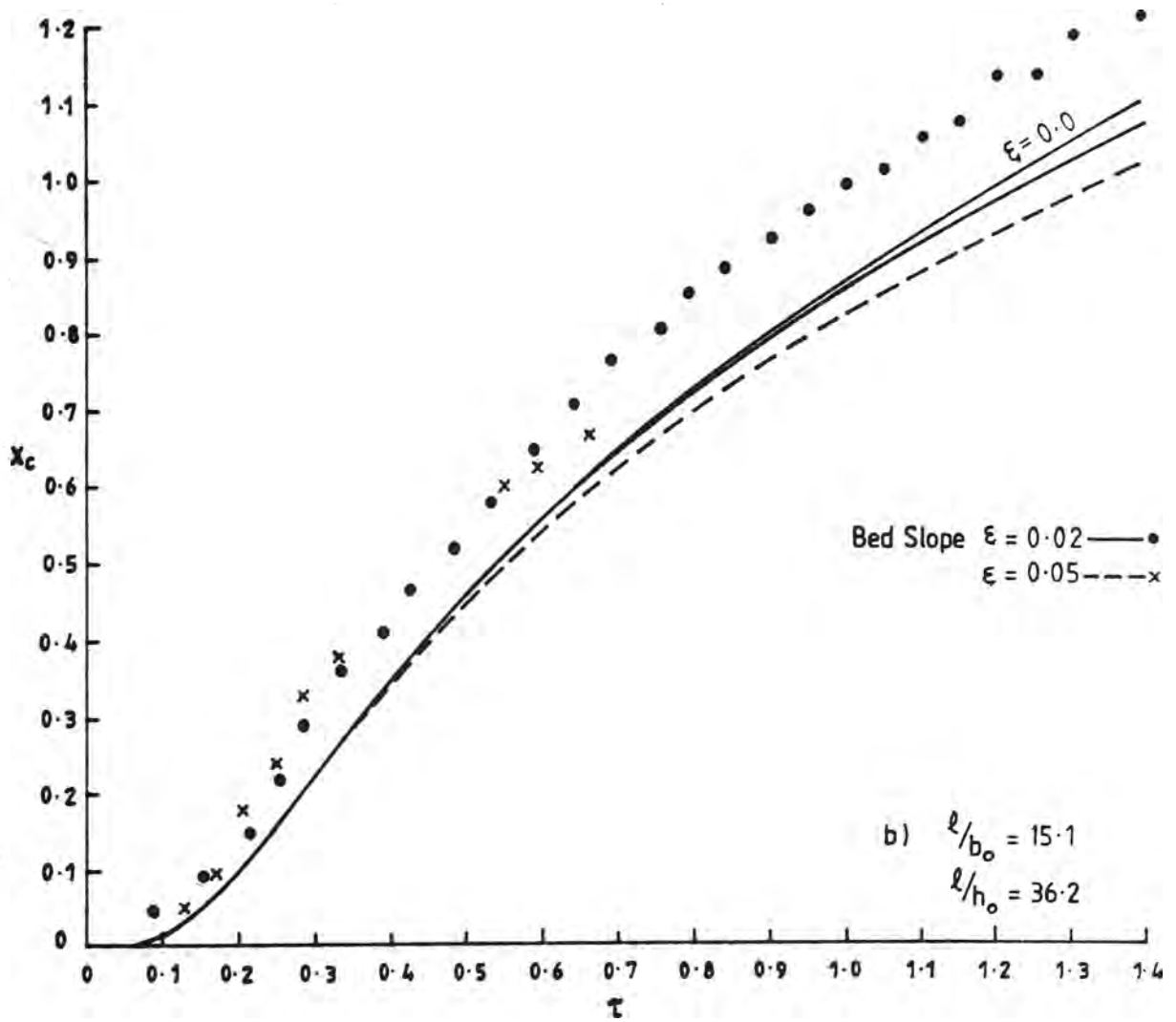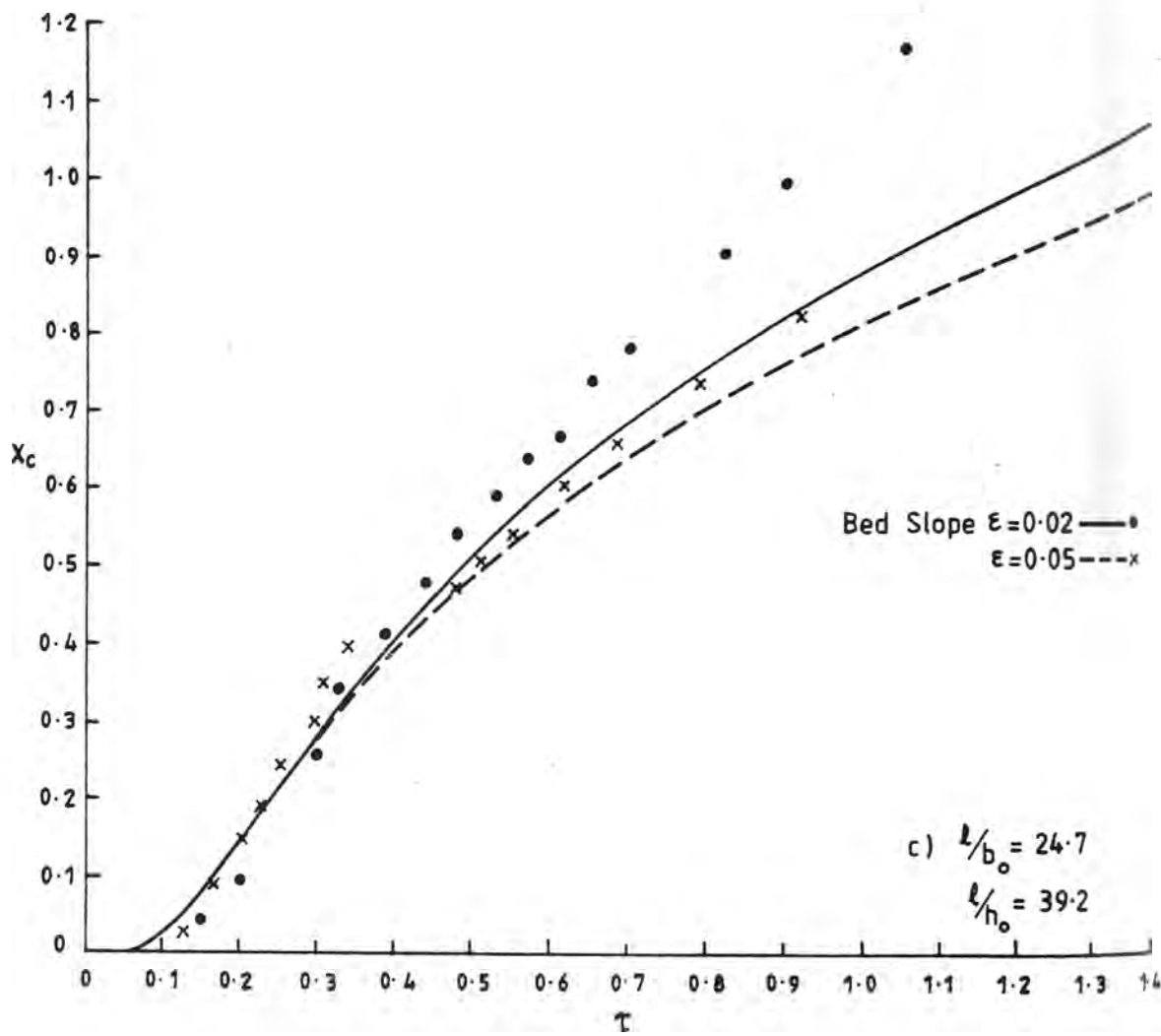
FIGURE 6·18 (Cont.)

FIGURE 6·18 (Cont.)

d) $\ell/b_o = 37.0$

$\ell/h_o = 39.2$

Bed Slope $\varepsilon = 0.01$ ———•

$\varepsilon = 0.02$ ———×
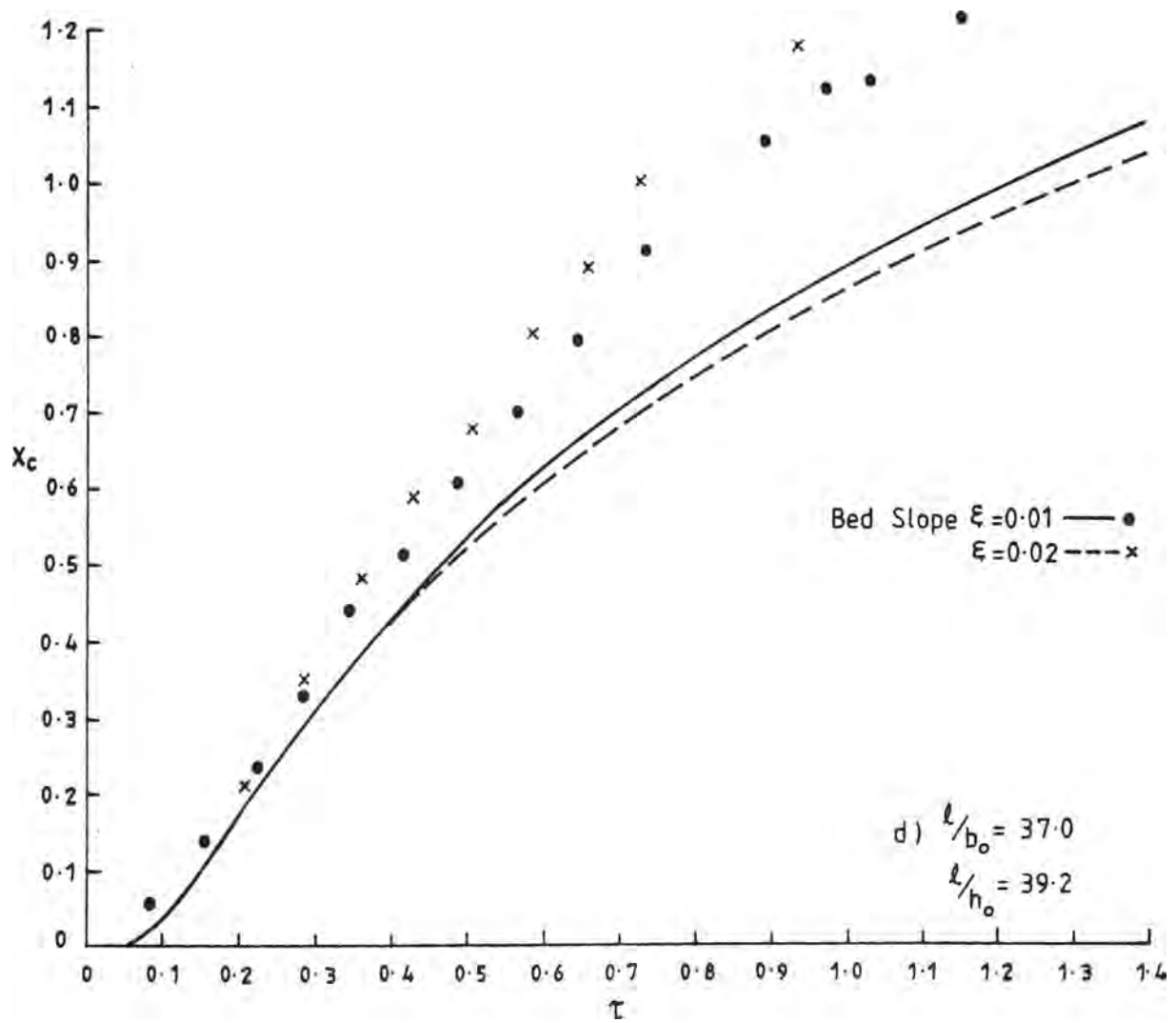
FIGURE 6·18(Cont.)

Vorticity of opposite sign to that of each vortex will be generated along the model basin boundary by the induced flow around the vortex. This is of particular importance for flows with small ℓ/b_o value, which remain near the boundary for longer periods. This negative vorticity is advected into the cap and cancels some of the cap vorticity. For flows with large ℓ/b_o, the cap quickly migrates away from the boundary and hence the induced flow is only that due to the local jet entrainment. Cancellation of vorticity reduces the impulse associated with the vortex pair and this may explain the overestimated predicted cap advance. The presence of image vortices across the boundary will also act to reduce the initial cap speed for small ℓ/b_o.

The significance of the ℓ/b_o parameter can be demonstrated by considering the strength of each vortex in the vortex pair cap. Although the data presented in Chapter 5 are not detailed enough to determine this by intergration of the vorticity distribution, an estimate can be obtained using the similarity relationship given by Equation (5.13). The dimensionless vortex circulation, K', is then given by:

$$K' = C_1 C_2 UB \qquad (6.6)$$

where C_1 and C_2 are constants defined in Chapter 5. The numerical predictions and the experimentally determined values are shown on Figure 6.19 for two experiments. Also shown is a refernce value for the vortex strength defined by Maxworthy (1977) as the slug circulation, K_o, generated at an orifice. This is given by:

$$K_o = \frac{1}{2} \int_0^t u_o(t)^2 \, dt \qquad (6.7)$$
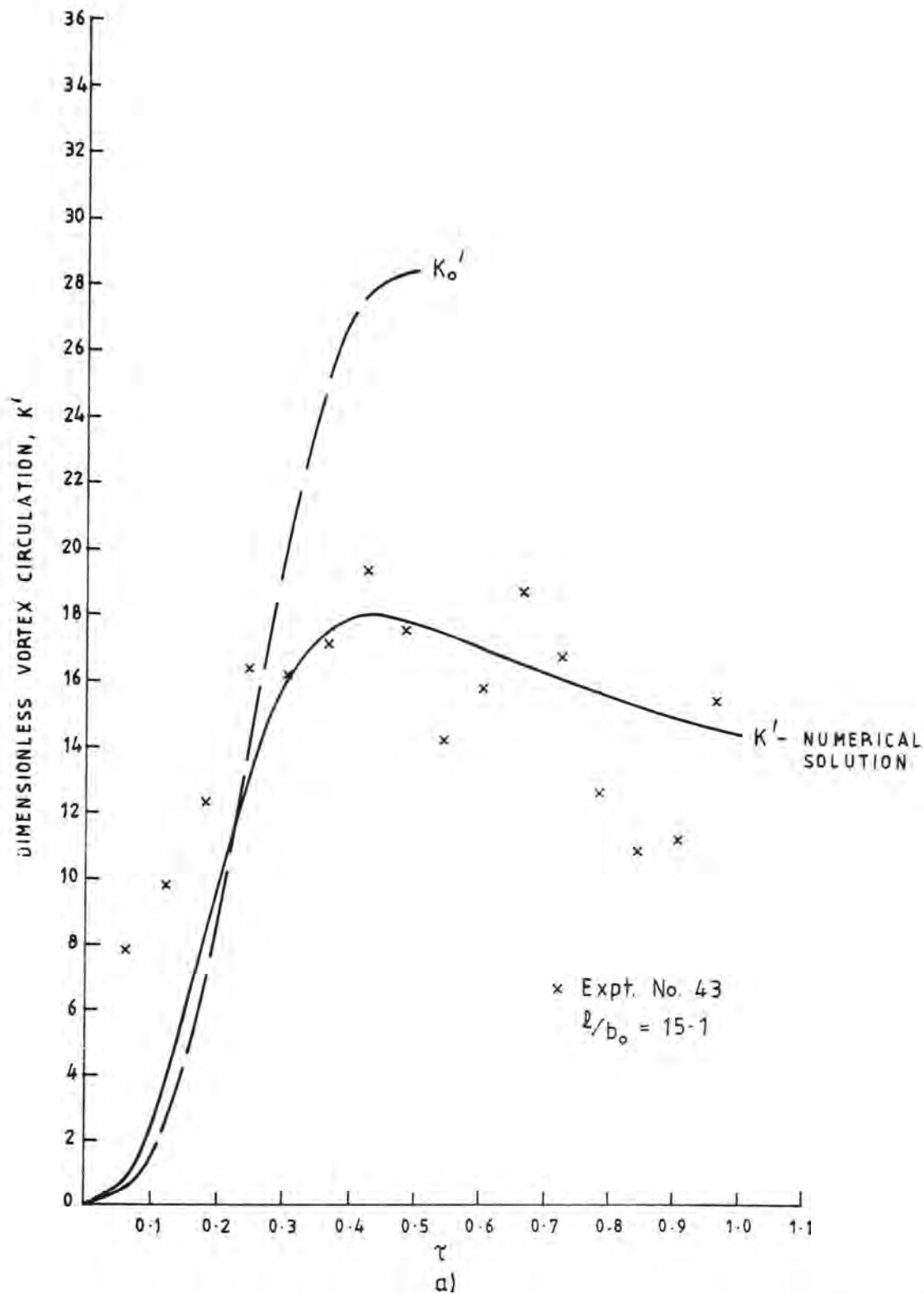
DIMENSIONLESS VORTEX CIRCULATION, $K' = K/K^*$ VERSUS
DIMENSIONLESS TIME, τ, FOR INLET WIDTH RATIOS
$\ell/b_o = 15 \cdot 1$ and $118 \cdot 4$

FIGURE 6·19
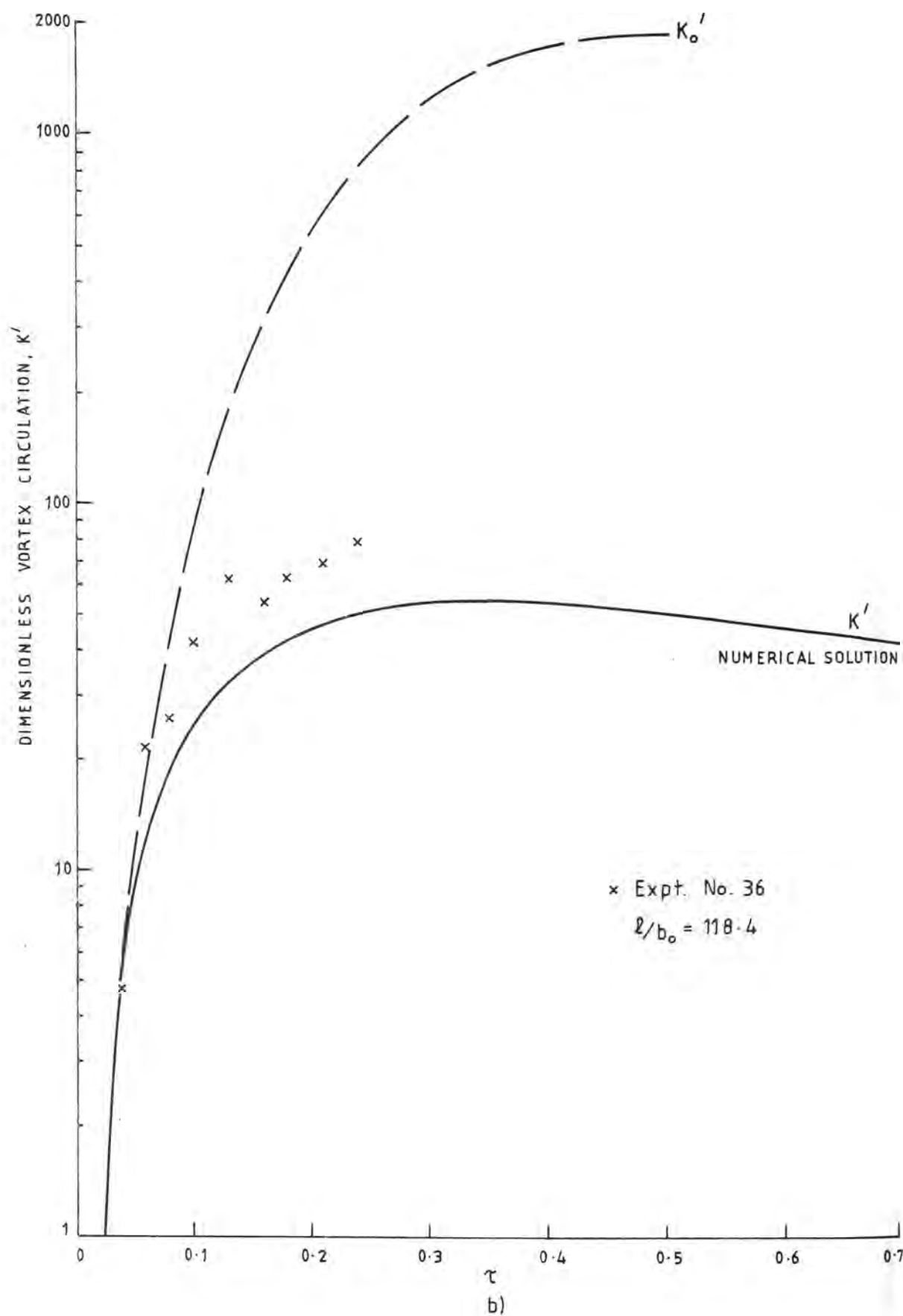
FIGURE 6·19 (Cont.)

Normalized with respect to the characteristic circulation, K^*, as defined in Chapter 2 this becomes:

$$K'_o = \frac{1}{2}(\frac{\ell}{b_o})^2 \int_0^\tau \sin^2(2\pi\tau)d\tau \qquad (6.8)$$

The variation in this reference value with time up to $\tau = 0.50$ is also shown on Figure 6.19. It can be seen from Figure 6.19a that for an inlet width ratio, $\ell/b_o = 15.1$, approximately 60% of the vorticity generated at the inlet is contributing to cap motion at $\tau = 0.50$. For the higher inlet width ratio, $\ell/b_o = 118.4$, shown on Figure 6.19b as a semi-log plot, only 5% of the generated vorticity is contributing to cap motion.

The breakdown of the clearly defined vortex structure results from instabilities induced by ambient turbulence and other mechanisms discussed in Chapter 7. It should be noted that these instabilities make the determination of the apparent centres of rotation in some cases somewhat arbitrary. The apparent erratic behaviour in the later stages of these experiments can be attributed to the difficulties in obtaining measurements.

After the initial spin-up phase the flow development appears similar to a steady starting jet or plume. However, examination of the results show that the requirements for a similarity model are not met. The cap does not travel at a constant fraction of the jet axial velocity and does not grow linearly with distance. The flow asymptotes to such a condition as the mass and momentum contribution from the jet reduces after $\tau = 0.25$. The initial rapid growth rate parallels the reported behaviour of turbulent puffs generated impulsively

(Richards,1963). The present case can be considered a ´slow motion´ impulsive generation of a vortex pair.

In Chapter 2 it was proposed that the characteristic length , ℓ, can be used to scale the translation of the vortex pair cap after one flow cycle. As a way of confirming this, the average translation speed, $U = X_c /\tau$, has been determined at $\tau = 0.25$, 0.50 and 1.00 for a range of ℓ/b_o and ℓ/h_o values. These are shown as Figure 6.20 along with a limited set of experimental results for $\dfrac{\ell}{h_o} \sim 50$. In the early stages of the flow the translation of the cap is a function of the inlet width ratio up to $\dfrac{\ell}{b_o} \sim 50$, with a weak dependence on the depth ratio. For times greater than $\tau = 0.50$ the cap translation is approximately independent of the inlet width ratio for ℓ/b_o values greater than 20. This demonstrates the influence of bottom friction on the development of an isolated vortex pair and also indicates the possibility of obtaining an approximate depth independent solution for the early flow stage when the source mass flux in increasing nearly linearly with time.
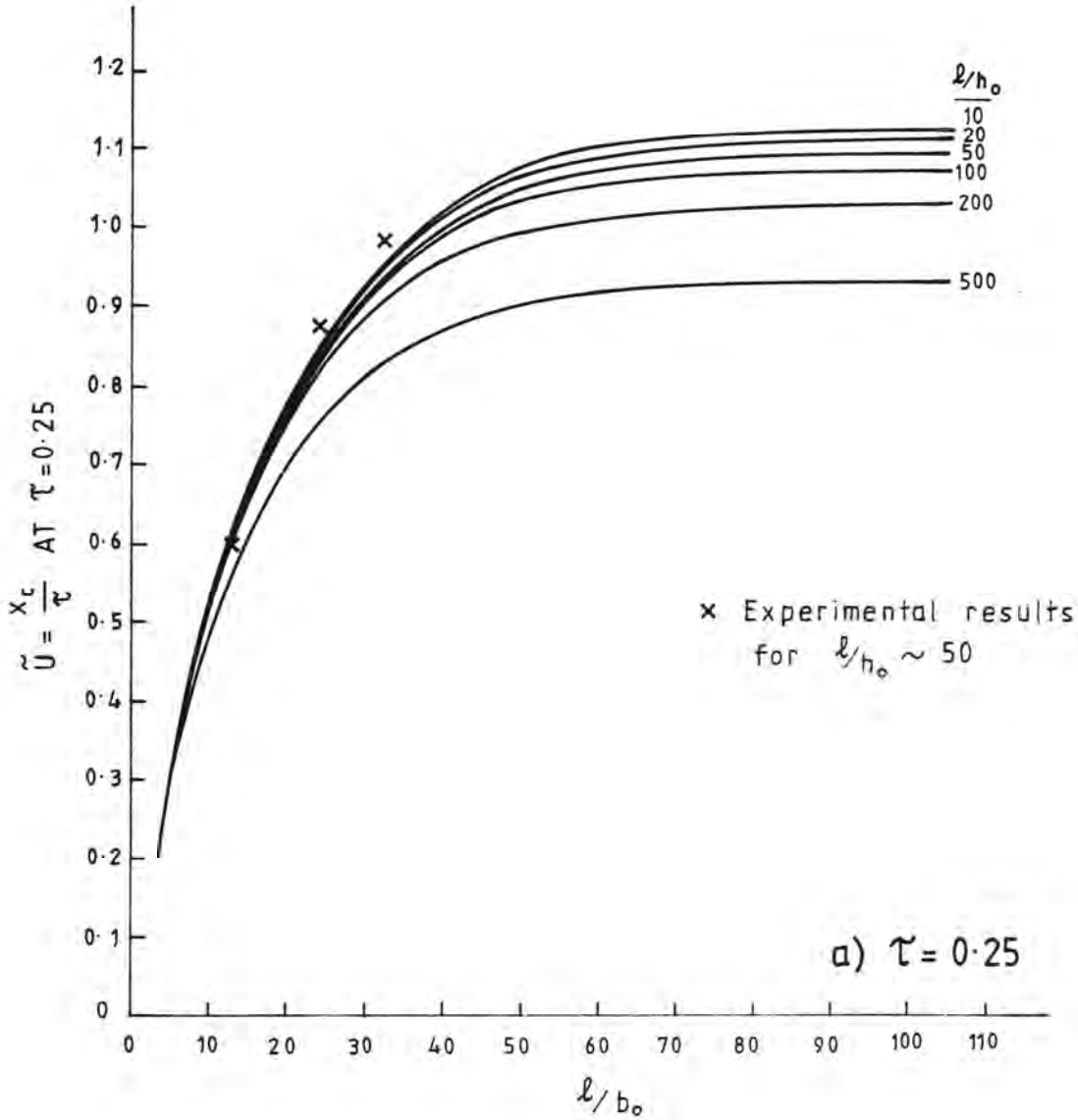
AVERAGE TRANSLATION SPEED, $\tilde{U}$, AT VARIOUS TIMES
AS A FUNCTION OF THE INLET WIDTH AND DEPTH RATIOS.
NUMERICAL SOLUTIONS OBTAINED FOR $f = 0.05$, $E = 0.05$,
$e = 0.07$ AND CONSTANT DEPTH

FIGURE 6·20

b) $\tau = 0 \cdot 50$

c) $\tau = 1 \cdot 00$
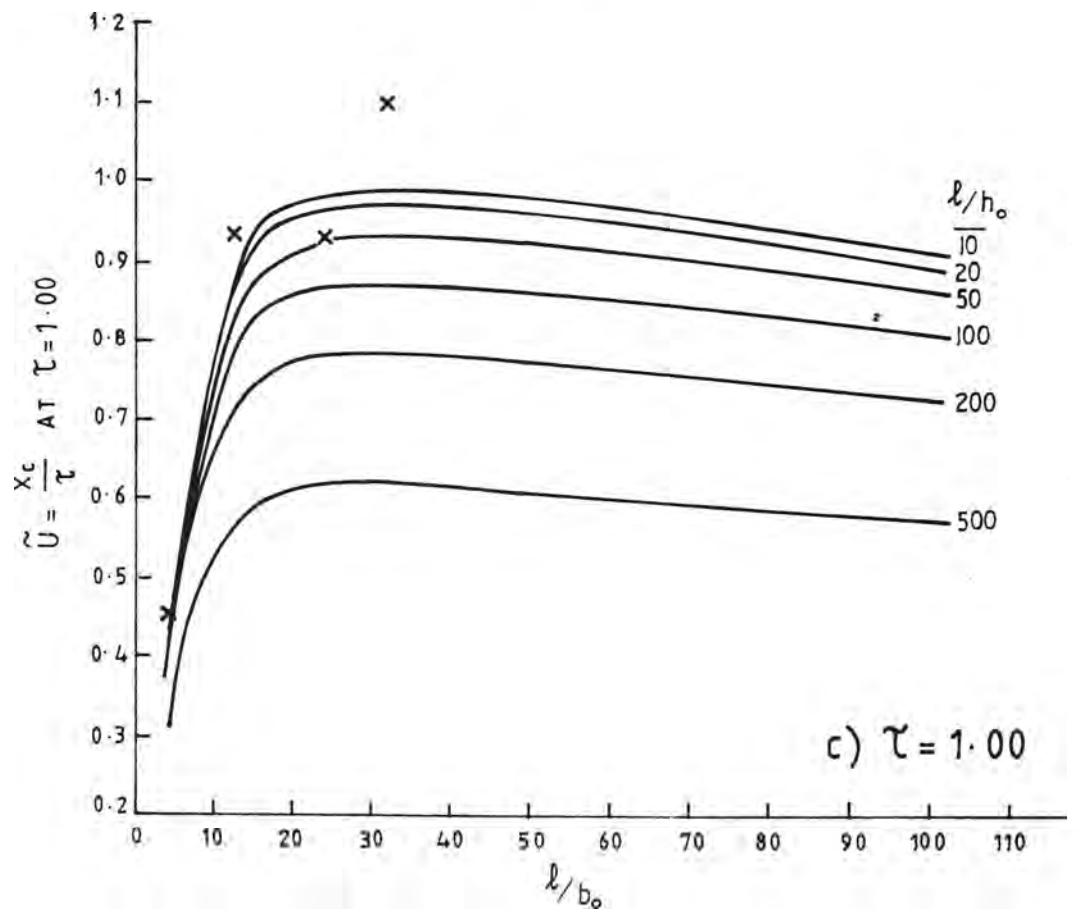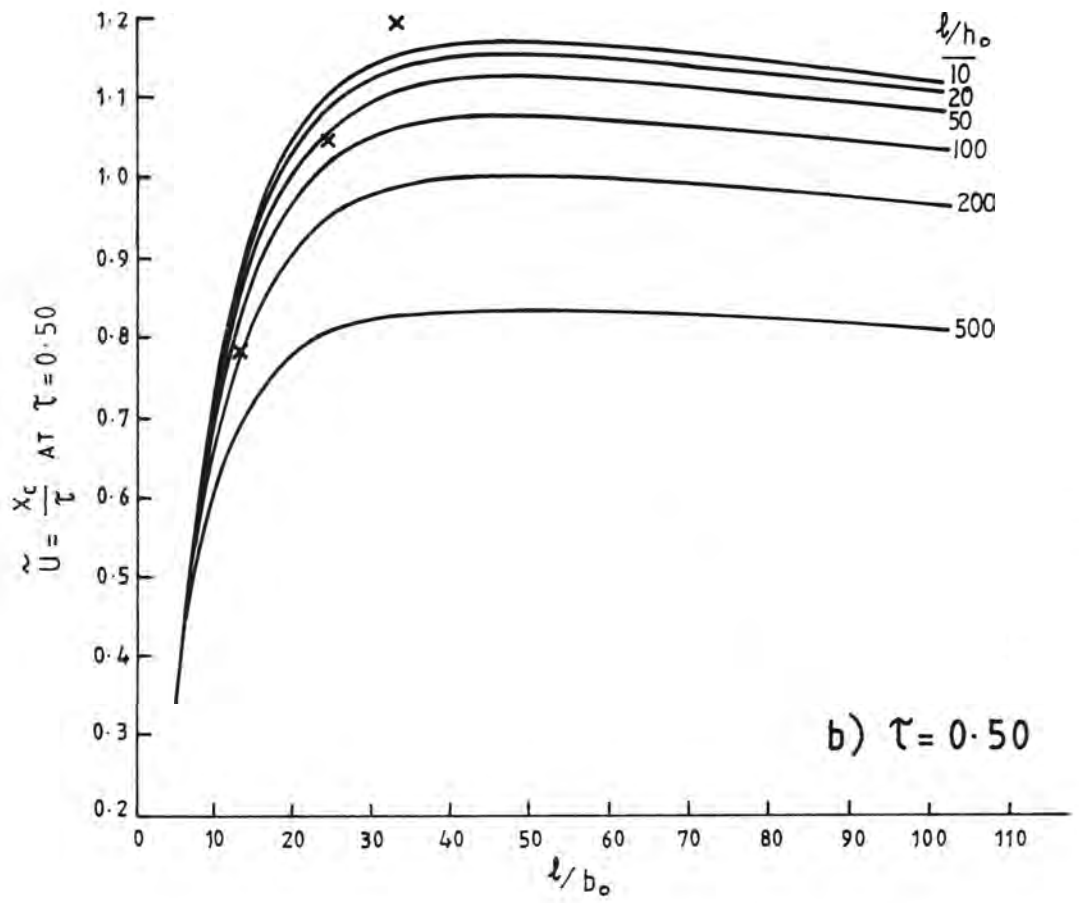
FIGURE 6·20 (Cont.)

7. <u>INSTABILITY OF THE VORTEX PAIR CAP</u>

The development of a periodic starting jet has been described in Chapter 2. In that ideal case a symmetrical vortex pair was spun up and migrated into a still basin along a path normal to the boundary. This situation was achieved in the majority of experiments with the flow remaining symmetrical for approximately one flow period. For various reasons - see Chapters 4 and 6 - the development of the vortex pair was only traced for about one period in most experiments. This, however, was long enough for the starting flow phase to be completed and the cap to become decoupled from the jet tail.

In 28% of the experiments a markedly asymmetrical velocity distribution was evident from the surface particle traces. This apparent lack of coherency resulted in two main types of flow development.

i.A pair of unequal strength vortices or one strong vortex as shown in Figure 7.1a occured in 21% of the experiments.
ii.The "rolling" of one vortex about the other resulting in a change of direction of propagation as shown in Figure 7.1b occured in 9% of the experiments.

In addition, of those experiments considered to exhibit an ideal vortex pair development, five experiments developed a pronounced meander-like structure in the jet tail.

Mechanisms which would cause this apparent loss of coherency are not available for an inviscid vortex pair in which vorticity is concentrated along line singularities. The vortex pair under consideration in this study has vorticity distributed over finite sized cores. The
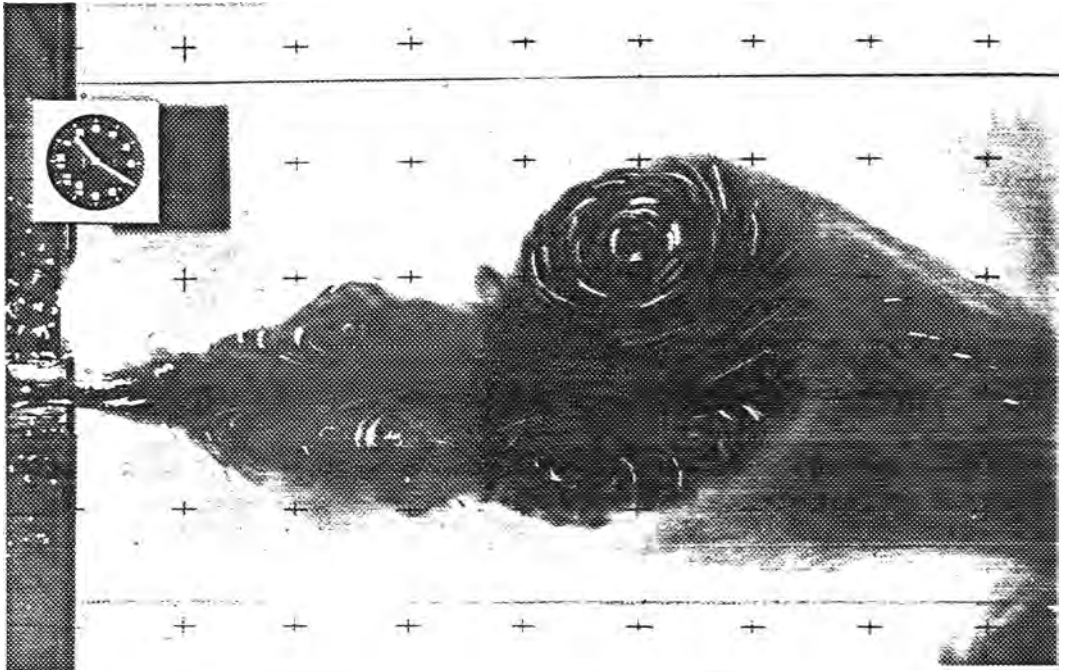
a) Unequal Strength Vorticies

b) Vortex 'Rolling"

FLOW INSTABILITIES

FIGURE 7·1

core length is also finite and is bounded by horizontal surfaces which introduce boundary layer effects. In addition they are coupled to an unsteady turbulent jet during the starting jet phase. The influence of these aspects of the vortex flow on the stability of the cap will now be considered.

7.1 Vortex Structures in the Jet Mixing Layer

During the course of an experiment (see Chapter 4), great care was taken to ensure that any residual motion in the tank was suppressed prior to the commencement of a test. The initial discharge can be considered to be issuing into a fluid at rest. The intrusion of the jet, however, sets up a large scale circulation and turbulence in the tank which will act to destabilize subsequent discharges. The scale of this turbulence is such that it is most likely to affect the gross behaviour of subsequent discharge cycles and not the coherency of the vortex pair cap.

The most probable mechanism causing the initiation of the vortex destabilization is the development of coherent vortex structures in the mixing layer of the jet tail. It has been well established (Davies and Yule, 1975) that the transition to fully turbulent flow near the source of the jet is accompanied by the presence of coherent structures in the mixing layer. The interface between the jet and the ambient fluid is initially a plane vortex sheet which rolls up due to a Kelvin-Helmholtz instability into a series of coherent line vortices (Figure 7.2). Subsequent growth of the mixing layer occurs owing to interaction of the small line vortices in the mixing layer. The vorticity is then dispersed throughout the mixing layer.
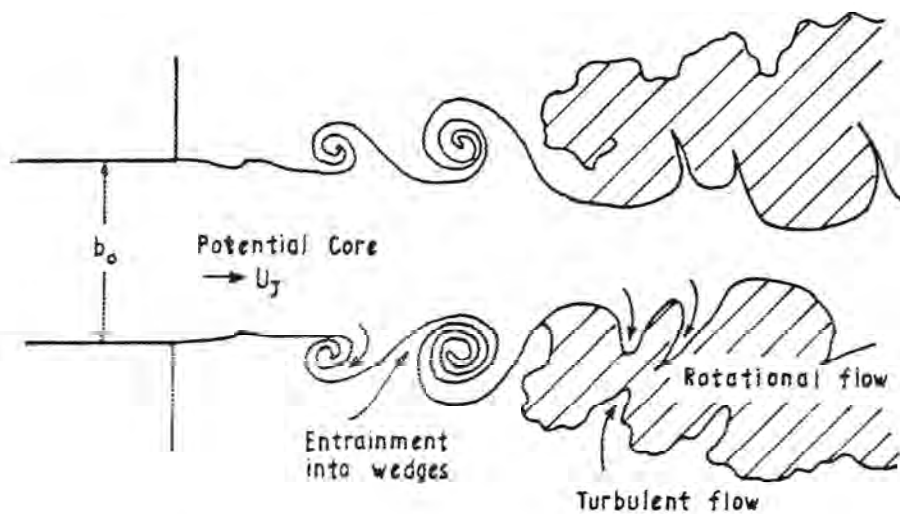
TRANSITION TO TURBULENCE IN THE
NEAR FIELD OF A JET
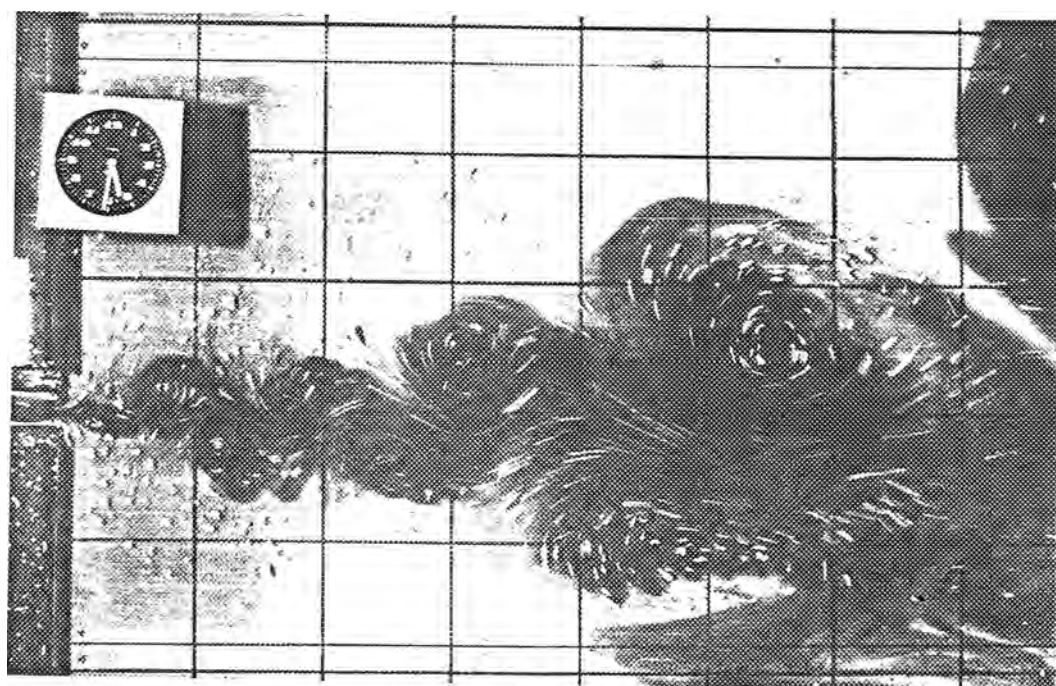
LARGE SCALE VORTEX STRUCTURES
IN THE JET TAIL $(\tau = 0.58)$

FIGURE 7·2 & 7·

It would appear that for the case of an unsteady jet during the decreasing momentum flux phase ($\tau > 0.25$) there is a reorganisation of the vorticity in the mixing larger resulting in the formation of large vortex structures. The interaction between these will result in the characteristic waviness in the jet observed in a number of cases (Figure 7.3). It is proposed that this restructuring of coherent vortices results in an intermittent variation in the vorticity being advected into the vortex pair cap and hence producing a destabilizing effect on the vortex pair.

7.2 Vortex Pair Destabilization

Observations of aircraft wake vortices (Tombach, 1971, 1973), indicate that the coherence of eddy motions is short lived. The form of this loss of coherency of wake vortices is similar to that observed experimentally as outlined earlier. For the purposes of the following discussion it is assumed that the vortex tubes are displaced slightly by some disturbance and also by the ambient turbulence level. This displacement is then amplified by the mutual interaction between the vortex pair, resulting in destabilization.

Aircraft wake vortices have been observed to distort into a pair of sinusoidal vortex tubes that eventually link and break down. A linear stability theory for a pair of trailing vortices in an inviscid fluid was developed by Crow (1970). He assumed the vortex wake to consist of an idealised pair of nearly parallel line vortices. His model agreed well with known solutions for displacement waves on a columnar vortex. He showed that there are strong and weak interaction modes with wavelengths of 8.6 b_c and 0.37 b_c, respectively. In this case the pair separation, b_c, is taken to be the real separation, $b_c = 2y_c$ (see

Section 5.2.2). In the atmosphere (aircraft wake) and the oceans (tidal flow), turbulence will tend to favour the instabilities with longer wavelengths which are propagated more energetically than the shorter waves, but do not amplify as quickly.

Widnall et al (1971) developed a more general solution of the flow field within or near a curved vortex tube. Figure 7.4a is part of the stability diagram Widnall et al presented for the most unstable (corresponding to the maximum amplification rate) short and long waves of wavelength, λ, as a function of core radius. These are presented as dimensionles wavelength λ/b_c and core radius R/b_c. Figure 7.4b shows the corresponding dimensionless maximum amplification rate, a', for a given vortex core size. This is defined in terms of the amplification rate, a, as:

$$a = \frac{K}{2\pi b_c^2} a' \qquad (7.1)$$

where K the circulation and b_c the pair separation.

For a long wave instability to occur in the experiments the depth would have to be greater than the wavelength shown in Figure 7.4a. The range of inlet entrance widths used (and hence the minimum value of b_c possible) was 20 - 160 mm resulting in a minimum wavelength of 344 mm. As the maximum water depth used was 100 mm, the greatest value of ratio of depth to width (h_o/b_o) is 5. The core radius to separation ratio has been found to be typically, R/b_c 0.5. This will correspond to a most unstable long wave of wavelength, $\lambda/b_c \sim 5.0$. Thus for the range of experimental conditions under consideration, the long wave instability has been suppressed. The symmetric short wave instability
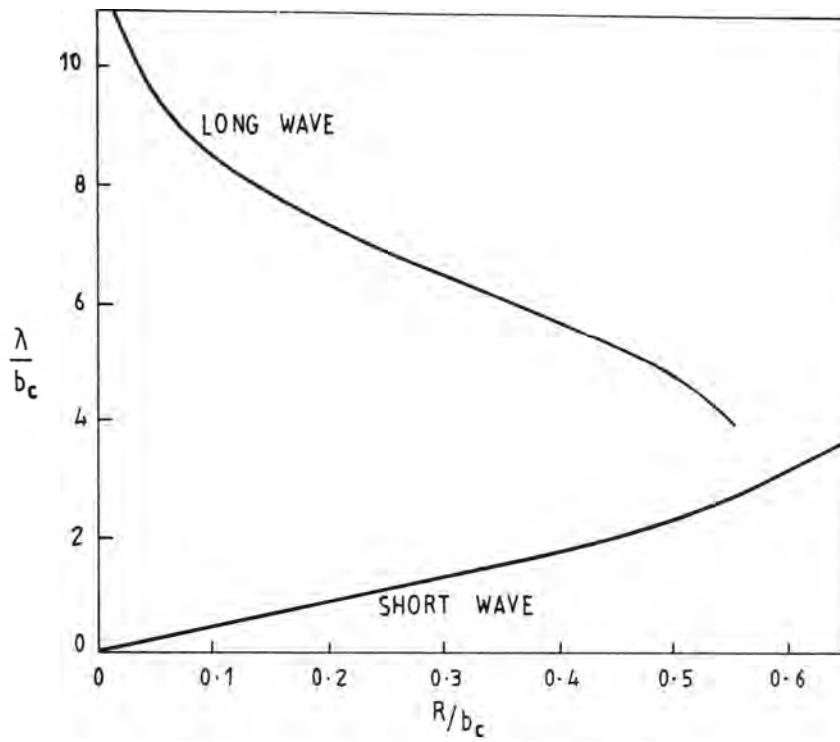
Most unstable wave length
versus vortex core size

(a)
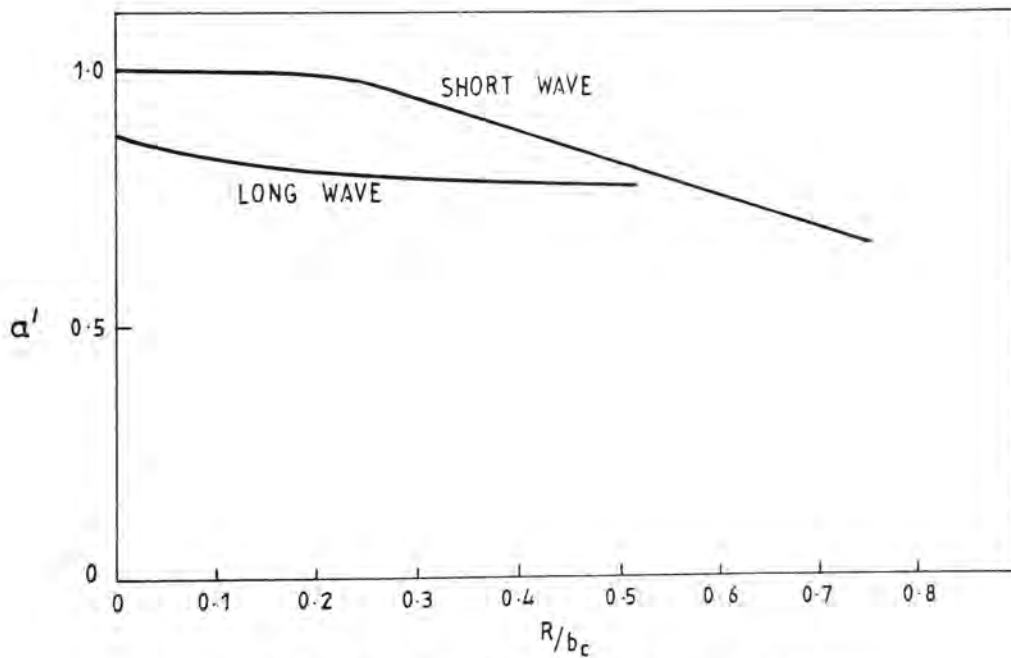
Maximum amplification rate
versus vortex core size
(After Widnall et al 1971)

(b)

FIGURE 7·4

corresponding to a core ratio, $R/b_c \sim 0.5$, has a wavelength, $\lambda/b_c \sim$ 2.3. This type of instability is clearly possible under the experimental conditions. Amplification of this short wave instability will occur at a rate, $a' \sim 0.8$. For typical experimental values, the amplitude of a short wave disturbance will double in approximately 20 seconds. Moore and Saffman (1971) have shown that a line vortex in the irrotational flow field of another will have a plane strain applied to it which elongates the vortex core. The equilibrium shape for a finite sized core has been discussed in Chapter 5. The dispersal of vorticity along the axis of symmetry enhances the diffusion and cancellation processes which reduces the impulse of the vortex pair. This may be the reason for the apparent loss of coherency as indicated by the distortion of the velocity trace patterns in the later stages of the flow.

7.3 Influence of Bottom Boundary

As discussed in an earlier chapter, the presence of a solid boundary perpendicular to the axis of a line vortex will result in the formation of an Ekman type boundary layer. A similar layer will also form on the free surface. The lower layer pumps fluid into the low pressure centre of the vortex from below, while the upper layer will pump fluid downward. The combined effect is to compress the vortex tube and thus reduce the interior vorticity.

The axial flow produced by this mechanism may enhance the instability mechanism described in Section 7.2. To estimate the significance of the bottom boundary layer and its possible effect on the stability, the Ekman number and corresponding boundary layer thickness will be determined.

For a rotating fluid the Ekman number is:

$$E_k = \frac{\nu}{\Omega L'^2} \tag{7.2}$$

and the thickness scales as:

$$\delta' \sim \left(\frac{\nu}{\Omega}\right)^{1/2} \tag{7.3}$$

where ν is the kinematic viscosity, Ω is the angular velocity of the rotating fluid and L' is a radial length scale. Expressed in terms of the flow variables u_v and b_c as in Chapter 2,

$$E_k \quad \frac{\nu}{u_v b_c} = \frac{1}{Re} \tag{7.4}$$

and

$$\delta' \sim \frac{R}{R_e^{1/2}} \tag{7.5}$$

where R is the radius of the vortex core.

A typical value of the Reynolds Number from the experiments is of the order 10^4 and the radius, R, of the order 10^{-2} m.

Thus

$$E_k \quad 10^{-4} \tag{7.6}$$

and

$$\delta' \sim 10^{-4} \text{ m} \tag{7.7}$$

These values would indicate that the Ekman layer effect is small.

Observations of the dye trace in an experiment further supports this view as dye is being left behind on the bottom after the vortex cap has passed. Thus the boundary layer produced by the translation of the pair dominates the Ekman boundary layer. The relative magnitude of these two layers can be obtained by comparing δ' with the boundary layer thickness, δ, developed over a length b_c,

$$\delta \sim b_c \, (Re)^{-0.2} \tag{7.8}$$

$$\sim 10^{-2} \, m \tag{7.9}$$

Because of the vorticity generated at the bed due to the translation of the pair, the axis of the line vortices will become three-dimensional. This will lead to the amplification of the kind of instability discussed in the previous section.

7.4 General Comments

In general, the symmetric vortex structure remains coherent during the ebb discharge phase. During most of this time, the cap is being driven by a jet with an increasing momentum flux at the trailing edge of the cap. This positive force flux dominates the dynamics of the vortex cap. The deceleration of the jet flow at the trailing edge probably initiates the destabilisation of the cap, which may occur as early as $\tau = 0.2$, but in most cases around $\tau = 0.8$.

In all of the constant depth experiments, some remnant of the vortex pair was visible up to the time of interference by the experimental tank boundaries. Except for some tests conducted with a large value of ℓ/b_o, the vortex pair became unstable in the field of view of the

stationary camera, and hence the recorded data on the development of the pair covered the coherent phase. Although this study was not primarily concerned with the interaction between successive vortex pairs, it was observed that only during a few tests did the vortices remain coherent long enough for there to be mutual interaction with the previously generated pair (Figure 7.5).

The predominance of the meander-like structure in the jet tail is a function of the relative dimensions of the vortex cap and the jet tail. For tests with small ℓ/b_o, the migration away from the entrance is retarded by the image vortices and the flow structure is confined to the near field. Successive ebb discharges interact to prevent the typical pair development. For ebb discharges with large ℓ/b_o the jet Reynolds number will be large. The characteristic Reynolds Number can be defined in terms of the maximum jet velocity and the entrance width as:

$$Re = (\frac{\ell}{b_o})^{1/2} \; \frac{\ell}{T} \; \frac{b_o}{\nu} \qquad\qquad (7.10)$$

The free shear layers of a large Re jet are long, relative to the width of the cap. In this case there is sufficient time for the reorganisation of the vorticity in the mixing layer to result in the formation of larger vortex structures (Figure 7.3). This mechanism appears to control the collapse of the unsteady jet tail during the flow reversal and subsequent time. The tail is seen to develop into discrete flow cells corresponding to the pairing of the vortex structures. In experiments where this was evident, the following ebb vortex pair cap was destabilized in that it followed the meandering path of the previous ebb.
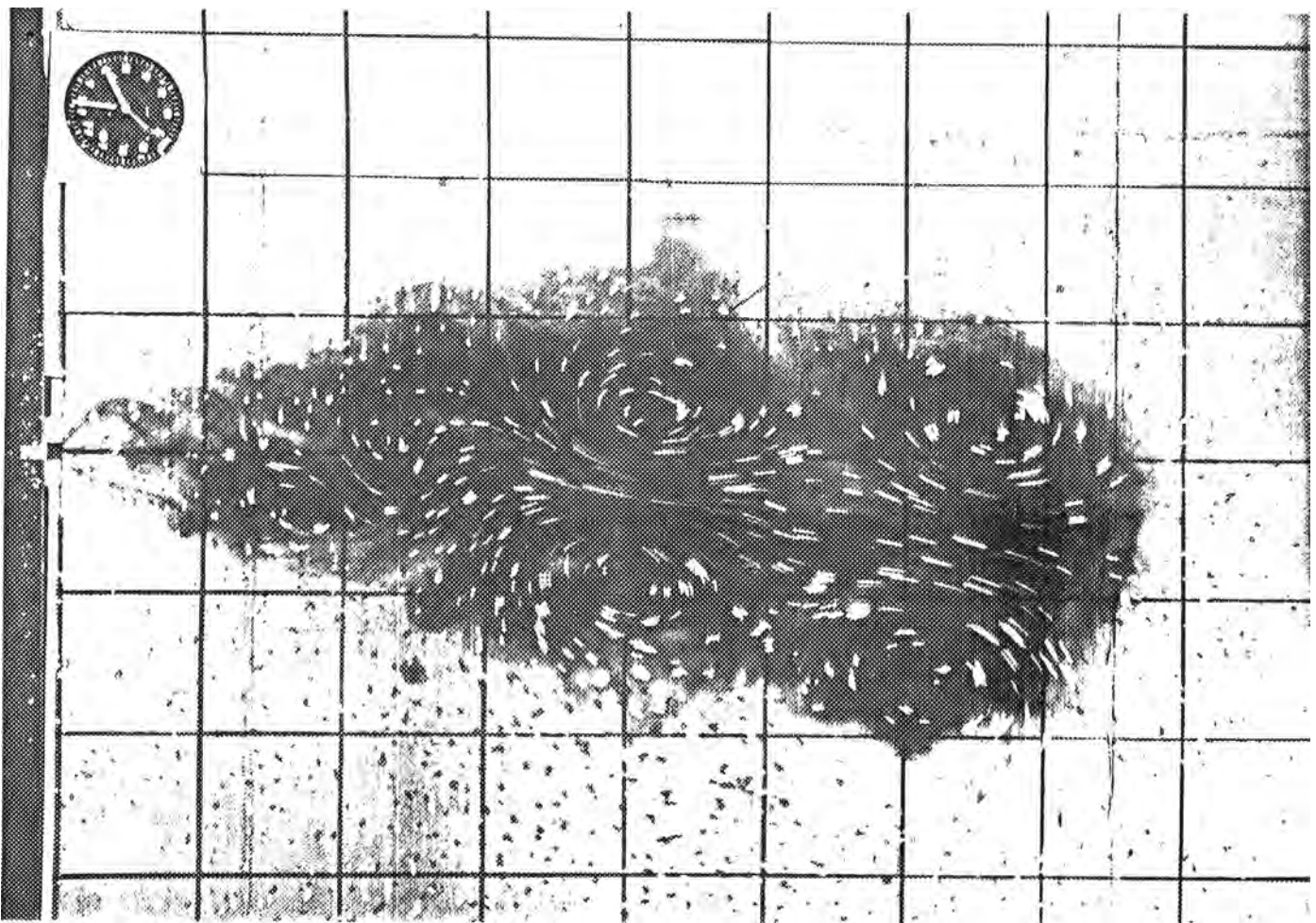
MUTUAL INTERACTION BETWEEN

SUCCESSIVE VORTEX PAIRS

FIGURE 7·5

8. FLOW REVERSAL

Consideration of a periodic jet flow would not be complete without an analysis of the flow induced in the basin by the reversal of flow at the inlet. It has been shown that for the range of flows being considered, this reversal does not influence the development of the ebb discharge vortex pair to any significant extent. For completeness, however, the flood flow will be analysed with regard to possible limit conditions where the residual velocity distribution at the commencement of the ebb would influence the pair formation.

In the case of real tidal flows, the flood flow is as relevant as the ebb flow when considering the dynamics of sediment transport near the inlet entrance, for example. The radial flow into the inlet combined with the entrained flow into the ebb discharge jet result in a continual longshore flow toward the inlet. As tidal inlets act as interfaces between the ocean and a bay or coastal lake, they control the exchange and mixing of waters from the inlet and the ocean. Water discharged during the ebb phase will be mixed with the ocean water by a number of processes. The fraction of ebb water which is returned to the inlet during the flood flow will affect the flushing efficiency of the inlet.

An estimate of the extent of the withdrawal during a flow reversal can be obtained by considering the velocity distribution in the near-field of the inlet. The flow towards the entrance over regular topography can be considered to radially converge on the entrance. The velocity at any point well removed from the entrance will change very slowly with time. Near the entrance, the velocity can be considered time dependent, particularly if confined to some flood channel as is

usual in the real case. For the purposes of determining the extent of the flood withdrawal it is assumed that the velocity distribution is quasi-steady.

Making the further assumption of inviscid flow, the potential theory can be used to provide an approximate velocity distribution. In its simplest form, the flow can be considered a radial point sink of constant strength. French (1960) has considered potential flow into two different types of tidal entrances; a channel cut perpendicular to the boundary, and a channel entrance corresponding to two parallel jetties extending into the ocean. Özsoy (1977) and others have presented an approximate analysis including a linear variation in basin depth. Taking the far field flow to be similar to a point sink flow (neglecting the influence of a finite inlet width), Özsoy has determined the extent of withdrawal from the ocean during the flood phase. Using this, he has established exchange and mixing criteria.

Consider flow, which is varying slowly with time, entering a channel of width b_o. As with the analysis of the ebb flow the variation in the free surface elevation is neglected. Variation in surface elevation with velocity changes along a streamline are also neglected, and for the case of a constant depth basin, the flow can be considered two-dimensional. The model therefore is only applicable to flows in which the local Froude Number is of the order 10^{-1} or less. The method of conformal transformations can be used to determine the velocity distribution. For irrotational, two-dimensional, steady flow it is necessary that only Laplace's equation and the appropriate boundary conditions be satisfied.

For the flow as shown in Figure 8.1, Vallentine (1967) gives the transformation from the physical $Z = x + iy$ plane to the complex potential $\Phi = \phi + i\beta$ as:

$$Z = i \frac{b_o}{\pi} [(e^{-(2/k)\Phi} -1)^{1/2} - \sec^{-1} e^{-(1/k)\Phi}] \tag{8.1}$$

where ϕ is the velocity potential, ψ is the streamfunction and k is the strength of the sink.

The conservation of mass for shallow water flow is defined by Equation (3.7) as:

$$\frac{\partial hu}{\partial x} + \frac{\partial hv}{\partial y} = 0 \tag{8.2}$$

Özsoy (1977) has proposed that a velocity potential can be defined for the variable (hu) and (hv) if the depth varies gradually. The potential ϕ can be defined as:

$$hu = \frac{\partial \phi}{\partial x} \quad , \quad hv = \frac{\partial \phi}{\partial y} \tag{8.3}$$

The irrotationality condition will be approximately satisfied if:

$$\frac{\partial hv}{\partial x} - \frac{\partial hu}{\partial y} = 0 \tag{8.4}$$

or, by combining with Equation (8.2),

$$v \frac{\partial h}{\partial x} - u \frac{\partial h}{\partial y} = 0 \tag{8.5}$$

Thus, if $\frac{\partial h}{\partial x}$ and $\frac{\partial h}{\partial y}$ are small such that:

Sink strength $k = \frac{1}{\pi} (u\, b_o\, h_o)_{x=o}$

SCHEMATIC REPRESENTATION OF FLOW INTO ENTRANCE
DURING FLOW REVERSAL

FIGURE 8·1

$$\frac{\partial h}{\partial x} \, , \quad \frac{\partial h}{\partial y} \ll \frac{h_o}{b_o} \tag{8.6}$$

then Equation (8.5) is approximately satisfied. Substituting Equation (8.3) into Equation (8.2) gives the Laplace equation:

$$\frac{\partial^2 \phi}{\partial x^2} + \frac{\partial^2 \phi}{\partial y^2} = 0 \tag{8.7}$$

The flow pattern described by Equation (8.1) has been determined numerically for a range of ℓ/b_o using the complex arithmetic facility of FORTRAN. Figure 8.2 shows the flow net for an inlet width ratio $\ell/b_o = 37$. The sink strength, k, is given by:

$$k = \frac{1}{\pi} (u \, b_o \, h_o) \tag{8.8}$$

For the average velocity into the entrance, the strength is given by:

$$k = \frac{2}{\pi^2} \, q_o \, h_o \tag{8.9}$$

Expressing in terms of the characteristic length and period gives:

$$k = \frac{2}{\pi^2} \, [\frac{b_o \, \ell^3}{T^2}]^{1/2} \, h_o$$

$$= \frac{2}{\pi^2} \, [\frac{b_o \, \ell^3 \, h_o^2}{T^2}]^{1/2} \tag{8.10}$$

Also shown on Figure 8.2 is the ´radius´ of withdrawal of the sink of strength k. This is defined as the outer boundary of the fluid volume drawn into the inlet during the flood phase. The time, t, taken
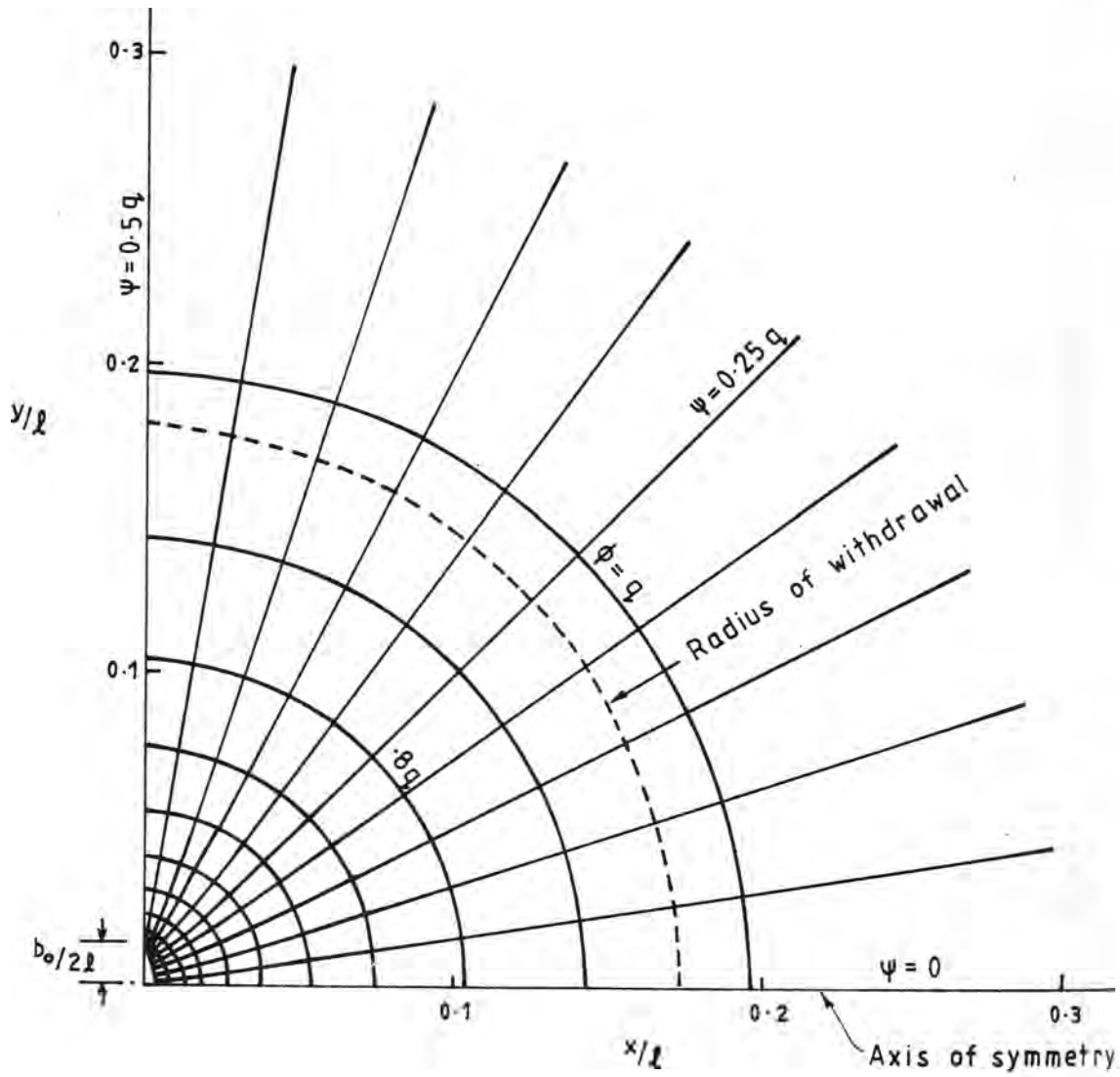
FLOW PATTERN DURING FLOW REVERSAL

$\ell/b_o = 37.0$, Bed slope = 0.0

FIGURE 8·2

for a particle initially a distance, s, from the inlet to reach the inlet is given by:

$$t = \int_0^s \frac{1}{V} \, ds \qquad (8.11)$$

where V is the velocity along a streamline towards the inlet. Expressed in terms of the depth dependent variables being used:

$$t = \int_0^s \frac{h(x)}{((hu)^2 + (hv)^2)^{1/2}} \, ds \qquad (8.12)$$

The value of $((hu)^2+(hv)^2)^{1/2}$ can be determined by considering the derivative, of the complex potential $\Phi = \phi + i\psi$. It can be shown that $\frac{d\Phi}{dZ}$ represents the complex velocity variable (hu-ihv) at any point in the flow. The absolute value of $\frac{d\Phi}{dZ}$ can then be expressed as:

$$\frac{d\Phi}{dZ} = ((hu)^2 + (hv)^2)^{1/2} \qquad (8.13)$$

The shape of the outer boundary of the fluid withdrawn during the flood has been determined for various sink strengths and inlet widths. Before discussing these and their relevance to the overall flow behaviour, it would be helpful to consider the inlet as a point sink of strength k. In this case the streamlines are radials from the sink. Expressed in cylindrical co-ordinates (r,θ), the complex velocity potential is given by:

$$\Phi = k \ln (r \, e^{i\theta}) \qquad (8.14)$$

The velocity potential ϕ is given by the real part of the complex potential Φ as:

$$\phi = k \ln r \tag{8.15}$$

The radial velocity, u_r, is given by:

$$u_r = \frac{1}{k} \frac{\partial \phi}{\partial r} = \frac{k}{hr} \tag{8.16}$$

For the case of constant depth, the outer boundary of the withdrawn fluid is given by Equation (8.11) as:

$$t = \frac{T}{2} = \int_0^s \frac{1}{k/hr} dr$$

$$= \frac{h}{k} [\frac{s^2}{2}] \tag{8.17}$$

Therefore

$$s^2 = T \frac{k}{h} \tag{8.18}$$

or, expressing in terms of characteristic parameters.

$$\frac{s}{\ell} = (\frac{2}{\pi^2})^{1/2} (\frac{bo}{\ell})^{1/4} \tag{8.19}$$

Thus for constant depth, the outer boundary of the flow reversal influence is a semi-circle, with radius proportional to the inlet width. Özsoy (1977) has also given a solution for the case of a linearly varying depth of small slope which expressed in characteristic terms is:

$$\frac{\pi^2}{2} (\frac{\ell}{b_o})^{1/2} (\frac{s}{\ell})^2 + \frac{\pi^2 \alpha_1}{3} \cos\theta (\frac{\ell}{b_o})^{1/2} (\frac{s}{\ell})^3 = 1 \tag{8.20}$$

where α_1 is the slope parameter given by:

$$\alpha_1 = \frac{\partial h(x)}{\partial x} \frac{\ell}{h_o} \tag{8.21}$$

The radius of withdrawal associated with flow into a finite sized entrance has been calculated for various inlet characteristics, and bed slopes. An example of these are shown as Figures 8.3 and 8.4. Figure 8.3 shows the comparison between the present approach and that of Özsoy (1977) for various bed slopes. It can be seen from these figures that the extent of the withdrawal zone increases with decreasing inlet width ratios.

The influence of residual velocity distribution in the basin on the behaviour of the next ebb discharge is not considered significant. Towards the end of the flood phase, these velocities will be relatively small compared to the velocity of propagation of the ebb discharge even near the inlet. However, the flood flow may exert an influence on the preceding ebb discharge. If as an approximation, the ebb vortex pair is taken to move away from the inlet at an average velocity proportional to ℓ/T, then the limiting condition for a flood withdrawal to influence its motion would be when the radius of withdrawal given by Equation (8.19) or Equation (8.20) is greater than the distance travelled by the pair at time $T/2$. The limiting condition for a constant depth flow can be obtained by using the point sink approximation, Equation (8.19) as:

$$s \geqslant C \frac{\ell}{T} \frac{T}{2}$$

or

$$\frac{s}{\ell} \geqslant 0.5 \ C \tag{8.22}$$

where C is a constant of proportionality.
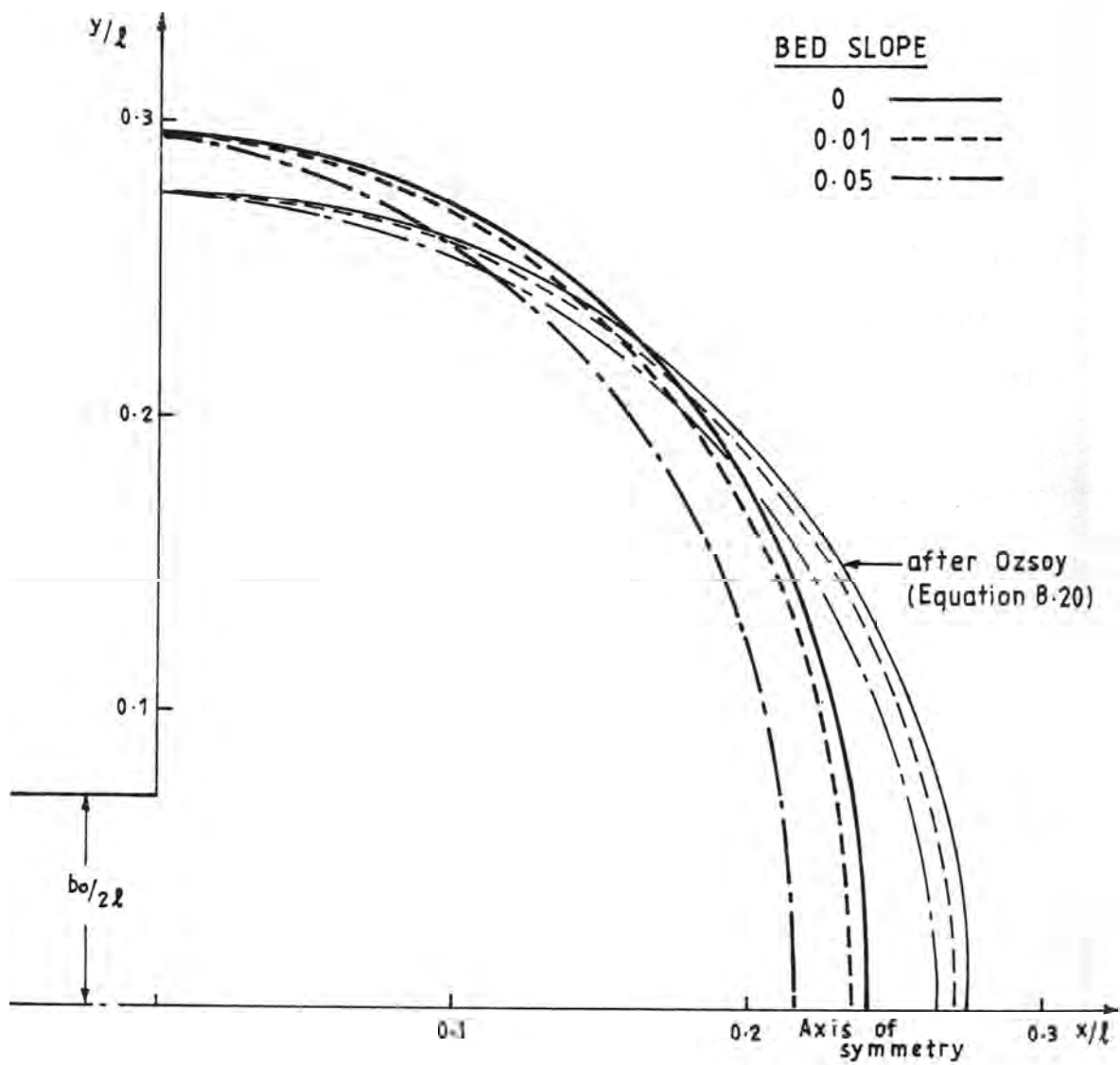
RADIUS OF WITHDRAWAL

DURING FLOW REVERSAL. $\ell/b_o = 7\cdot1$

FIGURE 8·3

b) $\ell/b_o = 118 \cdot 5$

a) $\ell/b_o = 37 \cdot 0$
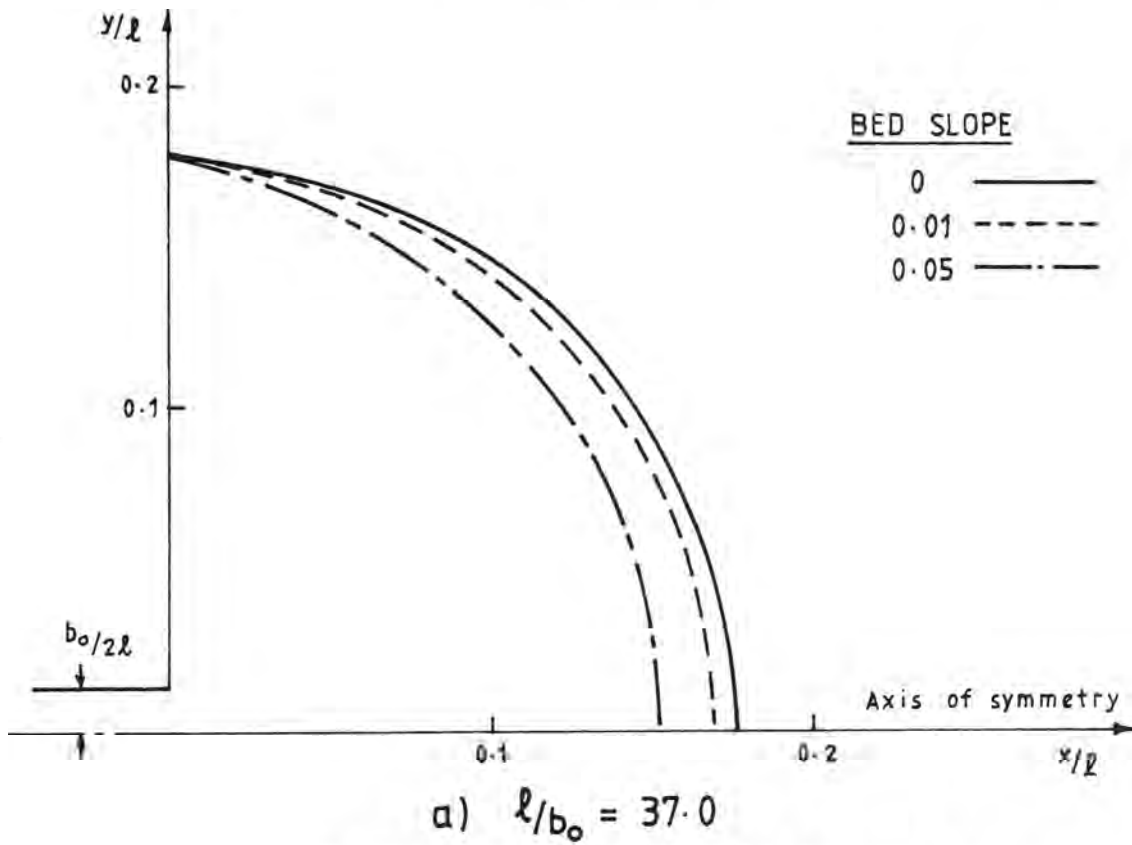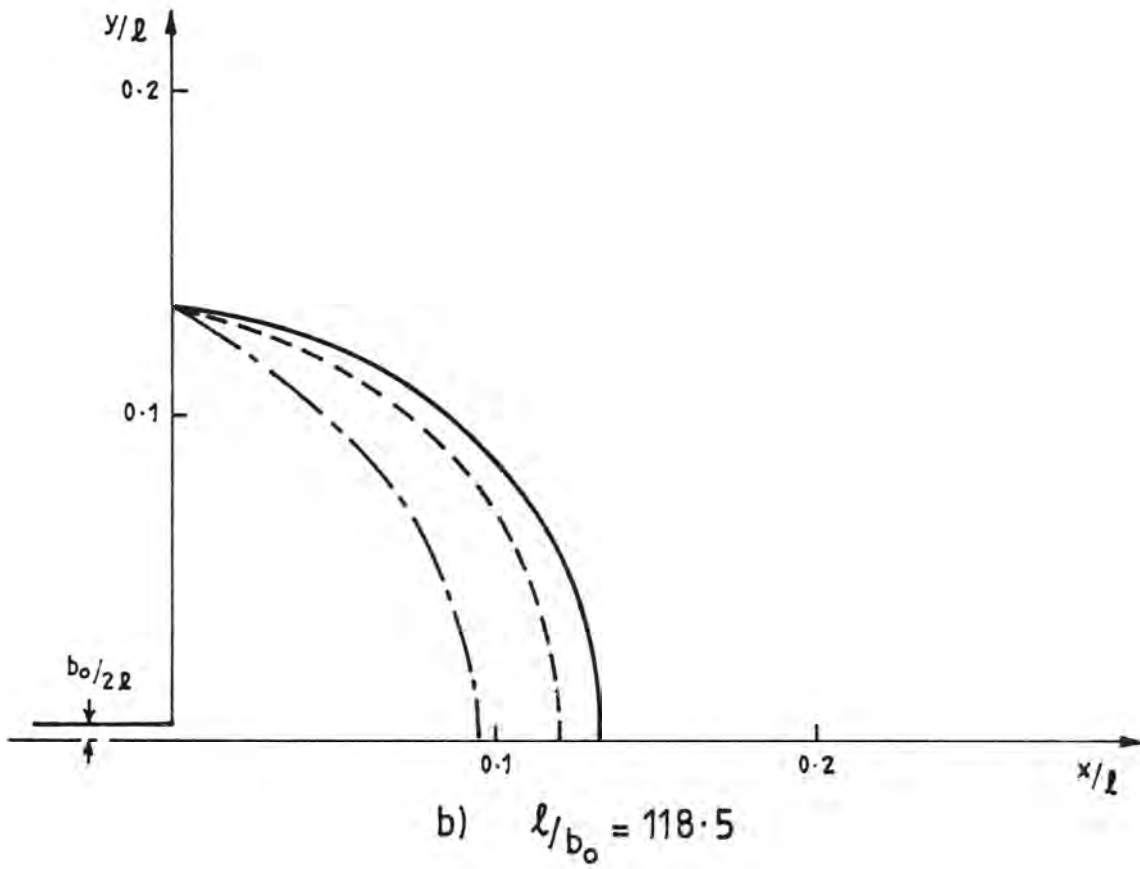
RADIUS OF WITHDRAWAL DURING
FLOW REVERSAL

FIGURE 8·4

As can be seen from Figure 6.18, the average translation velocity at $\tau = 0.50$ is approximately ℓ/b_o dependent for low ℓ/b_o values and ℓ/h_o dependent for ℓ/b_o greater than 20. As the flow reversal is most likely to influence low ℓ/b_o flows, an approximate relationship for C as a function of ℓ/b_o only is obtained as follows:

$$U = C \sim 0.12 \left(\frac{\ell}{b_o}\right)^{3/4} \tag{8.23}$$

Substituting Equations (8.22) and (8.23) into Equation (8.19) gives:

$$0.5 \left(0.12 \left(\frac{\ell}{b_o}\right)^{3/4}\right) \leqslant \left(\frac{2}{n^2}\right)^{1/2} \left(\frac{\ell}{b_o}\right)^{-1/4}$$

or
$$\frac{\ell}{b_o} \leqslant 13.3 \tag{8.24}$$

This shows that for constant depth flows, the vortex pair cap will be outside the radius of withdrawal of the next flood flow for $\ell/b_o > 13$.

Clearly, a more sophisticated analysis of the flow reversal could be carried out. However, the simple approach presented here provides a useful indication of the influence of the cap parameters on the possibility of fluid discharged on one ebb returning to the inlet on the following flood.

On the natural scale, the returning flow has importance in relation to pollutant dispersal at tidal inlets. In an attempt to quantify the amount of flow returning, dye concentration measurements were taken as outlined in Chapter 4. The fraction returning was obtained by means of conductivity probes located at the inlet channel which detected the concentration of electrolyte labled fluid in the flood phase flow (see

Figure 4.10). The total fraction of fluid re-entering the inlet was calculated by intergrating the product of the fraction returning and the total inflow over the flood phase of the cycle. This total is shown on Figure 8.5 as a function of the inlet width ratio. As predicted above, a large fraction of the ebb discharge returns to the inlet at low ℓ/b_o values. The considerable scatter in the data for experiments with similar ℓ/b_o values has masked any ℓ/h_o dependence.
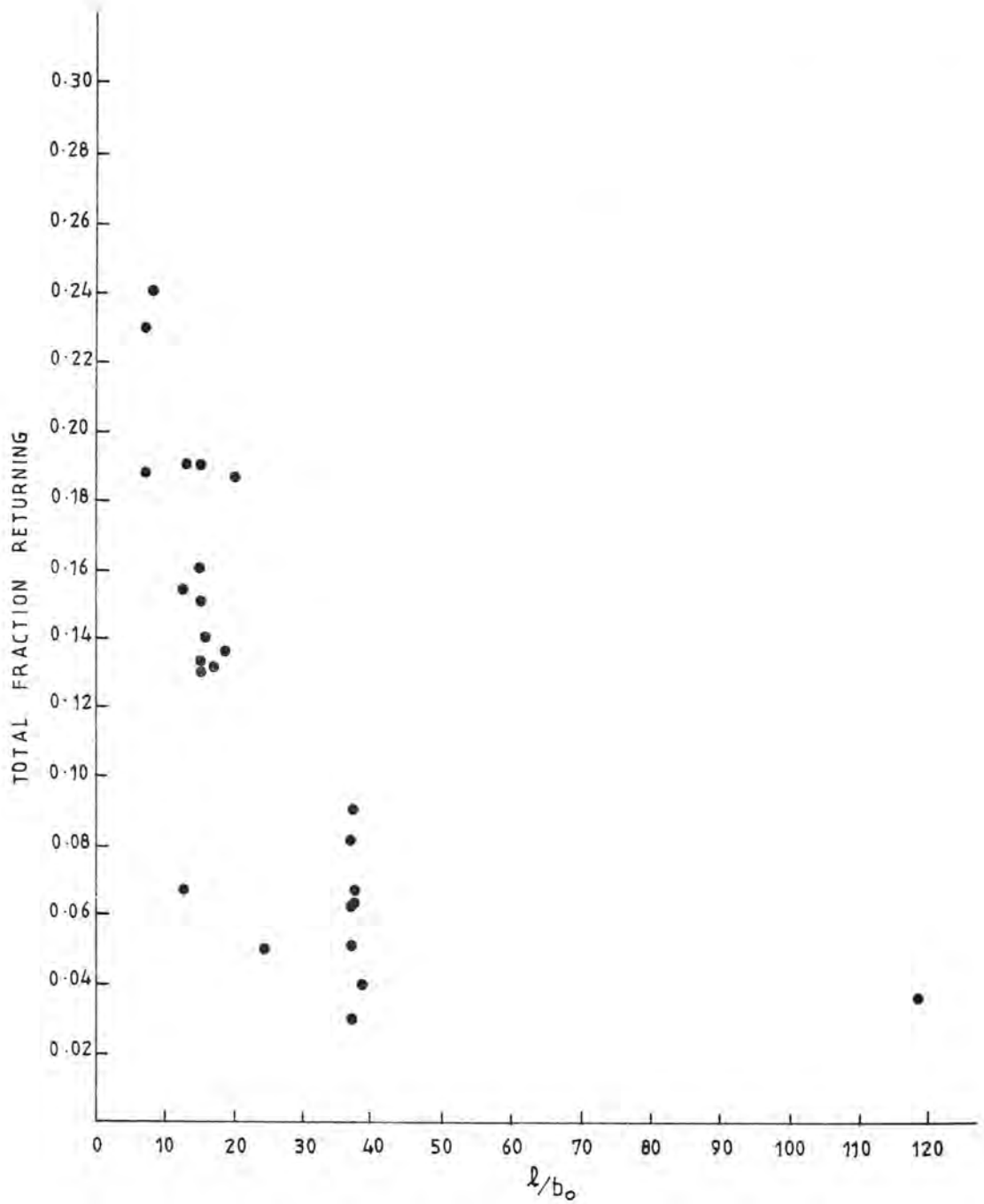
TOTAL FRACTION OF PRECEDING EBB FLOW RETURNING
TO THE INLET DURING THE FLOOD PHASE AS A
FUNCTION OF THE INLET WIDTH RATIO

FIGURE 8·5

9. PERIODIC JETS IN THE PRESENCE OF A CROSS-FLOW

The behaviour of a periodic jet issuing into a uniformly flowing cross-current will now be considered. A general review of deflected steady jets and in particular two-dimensional jets will first be given to provide a background for the later unsteady case.

Most studies on deflected jets (for example, Fearn and Weston (1974)) have been concerned with the trajectory and dilution of a round turbulent buoyant jet as would be encountered with a chimney plume or submerged sewage discharge. The deflection of these jets is taken to be due to the entrainment of the cross-flow momentum and the pressure drag force resulting from the wake formed in the lee of the jet. The dynamics of the flow are complicated further by the presence of internal circulations consisting of two counter-rotating vortices. An analysis by Jirka and Fong (1981) has included these features and also refers to a great number of previous studies.

Studies of two-dimensional jets or plumes subject to a cross-flow are not as common. Discharge of a fluid with less density than the ambient fluid cannot be considered two-dimensional because the buoyancy effects result in surface spreading of the jet (Stolzenbach and Harleman (1971)). Wolanski and Banner (1978) have considered a buoyant surface jet subject to a periodically reversing cross-flow as would be encountered when a pollutant is discharged into a tidal river.

For a two-dimensional jet of neutral buoyancy the dynamics of flow are somewhat simpler than for the flows described above. Stolzenbach and Harleman (1971) and Özsoy (1977) have presented analyses for a gradually bent jet in which the interactions between the jet and the

cross-flow are weak. Özsoy's analysis is limited to the nearfield of the entrance and no account is made for the presence of a boundary on the downstream side or the development of a separation eddy on that side. The ebb discharge from a tidal inlet subject to a longshore current and a discharge through a side channel into a river are both examples of this type of flow.

It has been shown by Taylor (1954) and others that a steady jet will attach to the boundary and form a recirculation cell in the lee of the jet as shown in Figure 9.1. In the case of a steady jet the recirculation is initiated by the lateral inflow into the jet being confined between the jet and the boundary. This reduces the pressure, causing the jet to bend and eventually attach to the boundary. The significance of this in coastal discharges is that any pollutant load in the jet will become trapped near the discharge point.

The re-circulation cell which forms in the lee of a periodic jet is fundamentally different in both its generation and its behaviour during the flood phase. Before discussing this in detail it will be useful to consider the parameters which affect the steady jet case.

9.1 Boundary Attachment Of A Steady Jet Subject To A Cross-flow

The case of a steady two-dimensional jet issuing into a shallow basin with a frictionless bottom will now be considered.

Assuming that the eddy is large compared with the side channel width and the Reynolds Number is large, the relevant variables are the jet momentum flux per unit density per unit depth, m_o, the jet exit velocity, u_o, the inlet channel width, b_o, the cross-flow velocity, v_c,
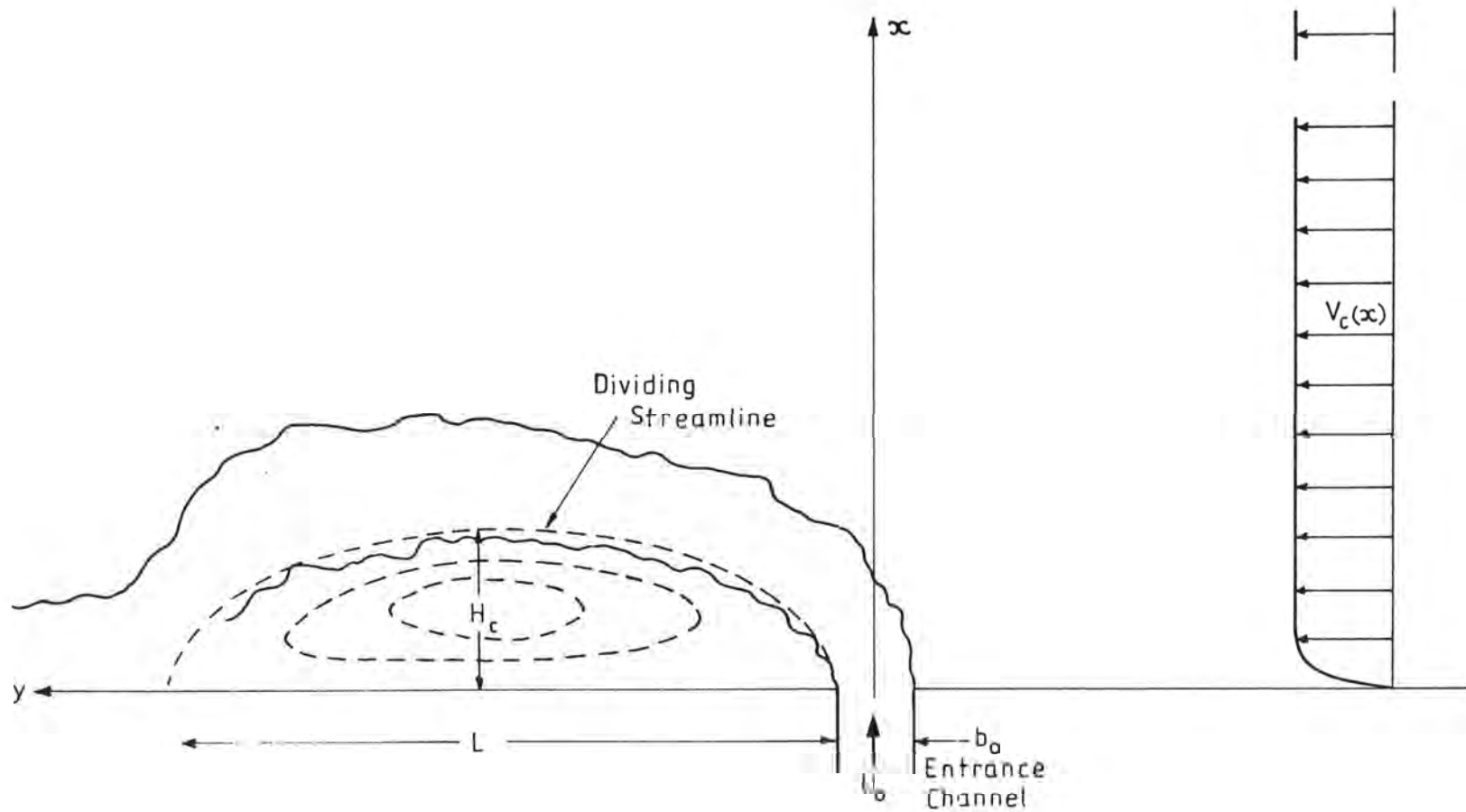
DEFINITION SKETCH OF A STEADY JET
SUBJECT TO A CROSS-FLOW

FIGURE 9·1

and the height and length of the recirculation cell, H_c and L. Dimensional analysis yields the following relationships if similarity exists:

$$\frac{m_o}{H_c v_c^2} = \text{constant} \tag{9.1}$$

$$\frac{m_o}{L v_c^2} = \text{constant} \tag{9.2}$$

$$\frac{H_c}{L} = \text{constant} \tag{9.3}$$

where

$$m_o = u_o^2 b_o \tag{9.4}$$

and hence

$$\frac{L}{b_o} \propto \frac{u_o^2}{v_c^2} \tag{9.5}$$

Rouse (1957) obtained an empirical relationship with the velocity ratio u_o/v_c to the power 1.5. An analysis by Wygnanski and Newman (1968) assuming a circular dividing streamline enclosing the recirculation eddy, predicted the length to be proportional to the velocity ratio to the power 1.8. More recent experimental work by Mikhail et al. (1975) and numerical predictions by McQuirk and Rodi (1978) support the relationship previously derived on dimensional grounds.

Of importance to side discharges into rivers is the influence of the far bank. Mikhail et al. (1975) have shown that the size and shape of the re-circulation eddy in a confined flow will be a function of the

ratio of jet to cross-flow momentum flux, $\dfrac{u_o^2 b_o}{v_c^2 b_{cc}}$, where b_{cc} is the

width of the confining channel. The results of Mikhail et al. indicate

that the shape of the eddy remains similar over a wide range of test

conditions and is unaffected by the presence of confining walls. The

size of the eddy was found to depend solely on the momentum flux ratio

$\dfrac{u_o^2 b_o}{v_c^2 b_{cc}}$.

The shape of the jet trajectory up to the point of maximum pene-

tration into the cross-flow has been found experimentally by Kamotani

and Greber (1974) to be of the form:

$$\frac{x}{b_o} = f[\frac{u_o^2 b_c}{v_c^2 b_{cc}} , \frac{b_{cc}}{b_c}] \ (\frac{y}{b_o})^{0.5} \tag{9.6}$$

The parabolic trajectory is a consequence of the deflection being

caused by a force proportional to the cross-flow dynamic pressure.

One major influence not considered in the above referenced work is

that of bottom friction on both the initial trajectory, and on the size

and shape of the re-circulation eddy. As the ratio of the impulse

applied to the flow due to bottom frictional stresses and the jet

momentum decreases, the jet will penetrate further, and hence the

recirculation cell size would be expected to increase. McQuirk and

Rodi (1978) have presented both data and predictions showing the above

stated effect. Rodi (1982) has considered the significance of the

friction coefficient on the recirculation eddy parameters using a tur-

bulence transport model. His limited results suggest that the height

and length of the eddy are changed little by a substantial change in

friction coefficient. This result is not very suprising as the vorticity associated with the eddy is orthogonal to that produced in the bottom boundary layer.

9.2 Two-Dimensional Constant-Depth Periodic Jets Subject To A Cross-flow

The behaviour of a periodic starting jet as observed in experiments in a constant depth basin and subject to a cross-flow will now be described with reference to Figure 9.2.

During the initial stage of roll-up a pair of vortices can be seen to form near the entrance. The upstream vortex does not remain coherent for long, however. By the time the jet has become established only a strong downstream circulation is evident (Figure 9.2a). The jet stream deflects under the influence of the cross-flow dynamic pressure. Depending on the magnitude of cross-flow velocity, the jet will attach to the downstream boundary, Figure 9.2b. During the flood phase, Figure 9.2c, the vortex will move downstream under the influence of the cross-flow dynamic pressure and the induced velocity due to the image vortex across the boundary. In all of the observed cases, the vortex continued to translate downstream, Figure 9.2d.

The main feature of the behaviour in the presence of the cross-flow is the apparent elimination of the upstream vortex early in the flow development. It is proposed that this represents the dispersal of the upstream vorticity by the action of a cross-flow shear.
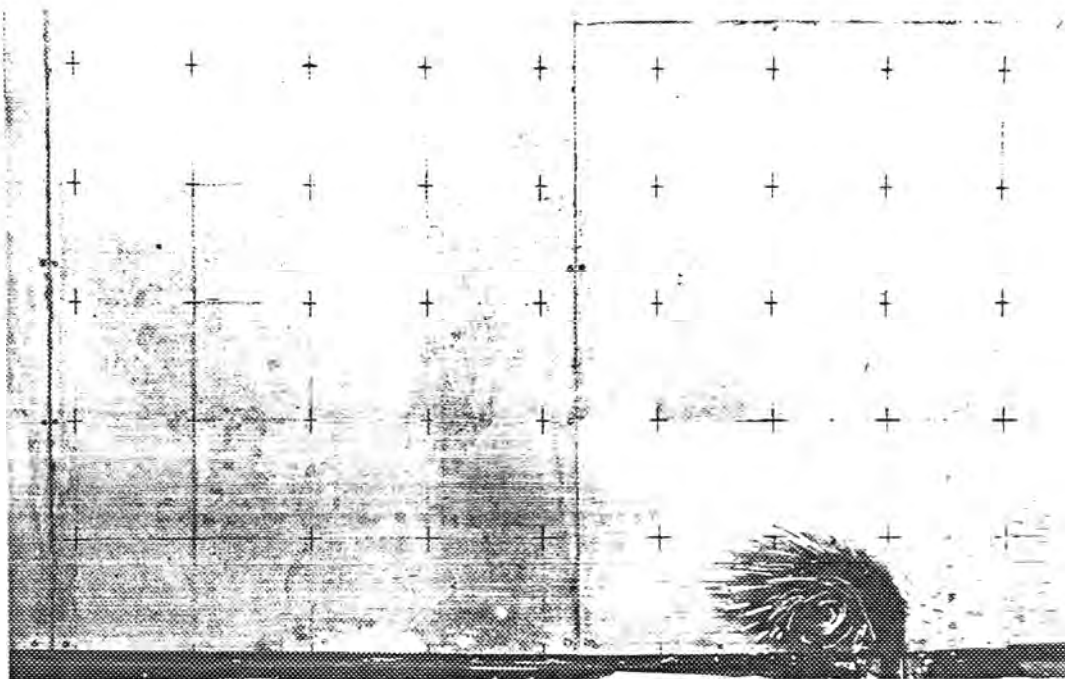
a) t = 0·11 T
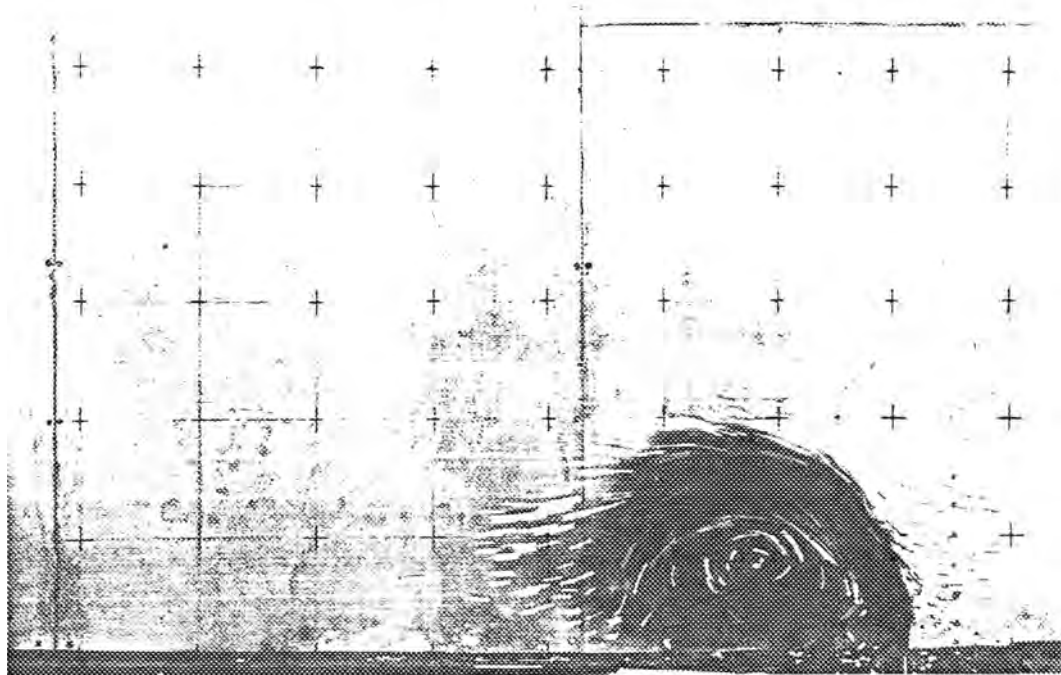
b) t = 0·25 T

EXPT. No. CF 31
See Table 9·1 for
details

PERIODIC JET SUBJECT TO A CROSS-FLOW

FLOW STRUCTURE AT TIME, t, AFTER COMMENCEMENT OF
THE EBB DISTANCE. FLOW RELATIVE TO A STATIONARY OBSERVER

FIGURE 9·2
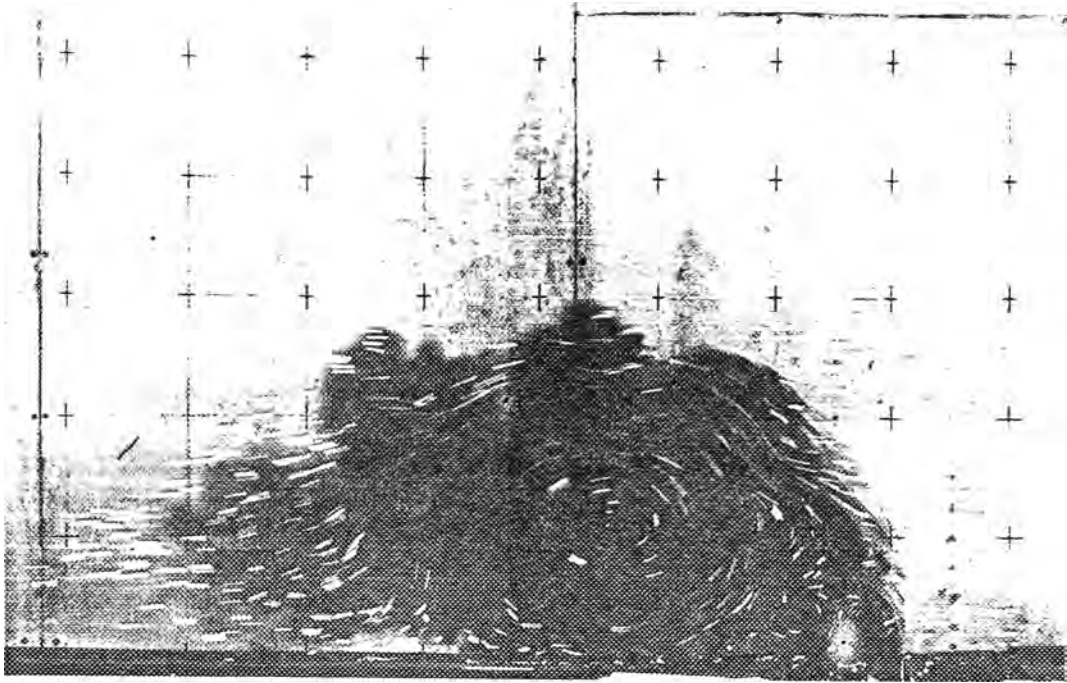
c)   t = 0·57 T
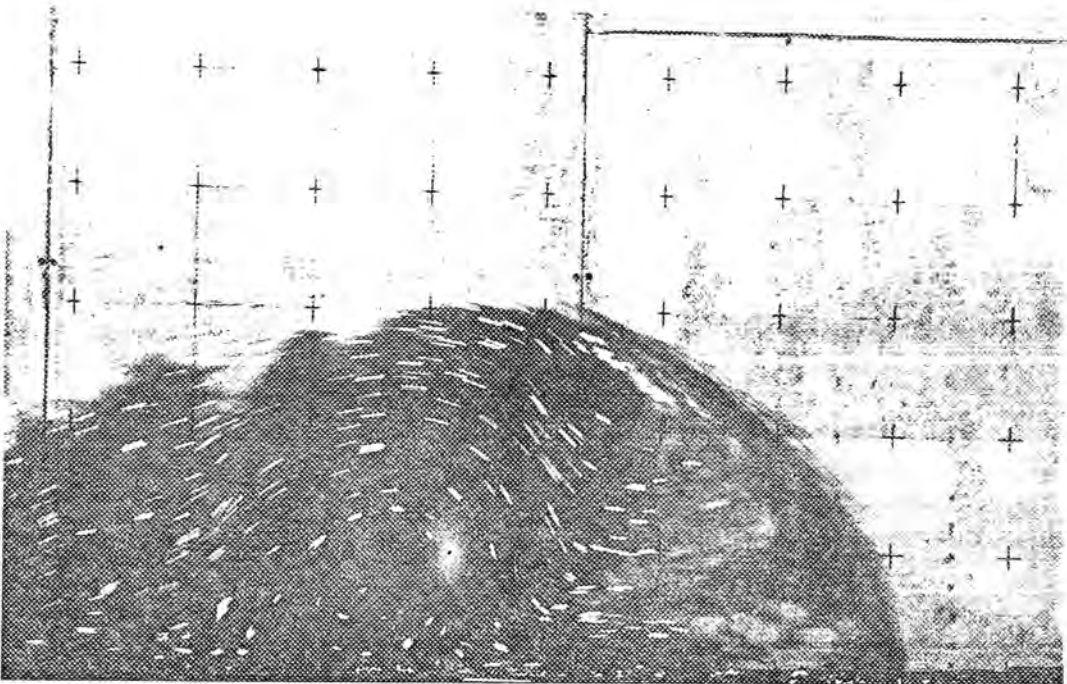
d)   t = 1·02 T

FIGURE 9·2 (Cont.)

Near the boundary, the cross-flow will not be uniform, due to the no slip condition at the wall. Vorticity is associated with the cross-flow for linear or higher order cross-flow velocity profiles. In the present case this will be of opposite sign to that of the upstream vortex. Rossow (1976) has shown numerically that for a vortex pair in the presence of a linear cross-flow velocity profile, the vortex with the opposite vorticity to the cross-flow will disperse and the other with vorticity of the same sign will concentrate. This behaviour has been observed for aircraft wake vortices by Tombach (1973). Brashears et al. (1975) have analysed the effect of a ground plane as well as cross-flow on aircraft wake vortices using a potential flow model. They have also shown a reduction in the vortex core size for the vortex of opposite sign to the cross-flow shear. This redistribution of the vorticity has also been confirmed by Bilanin et al. (1978) using a numerical turbulence model.

Experimental observations show that the apparent elimination of the upstream vortex is a function of the magnitude of the cross-flow velocity. For low velocities some form of upstream vortex remains visible throughout the cycle. Rossow (1976) has quantified this in terms of a cross-flow shear parameter, V_{sh}, which can be defined for a linear cross-flow velocity profile in a frame of reference with its origin at the vortex centre ($x' = y' = 0$) as:

$$v_c(x') = \frac{2x'}{d_c} \frac{K}{\pi d_c} V_{sh} \qquad (9.7)$$

where K is the circulation associated with a circular vortex of diameter, d_c. For $V_{sh} = 1$, the circulation velocity at a distance $d_c/2$ from the vortex center, $x' = 0$, is equal but opposite to the cross-flow velocity at that distance. Rossow's results show that for a Rankine

vortex, the minimum cross-flow shear required to eliminate the coherent vortex structure is $V_{sh} = 0.2$.

9.3 Discussion Of The Observed Behaviour

The results of the constant depth cross-flow experiments will now be discussed. The number of experiments was limited by the size of the experimental tank and the capacity of the cross-flow generating mechanism. Three sets of experiments were conducted, each with the same set of characteristic scales and parameters, but with varying cross-flow magnitude. The details of each experiment are listed in Table 9.1. The cross-flow velocity profile was determined by scattering confetti and photographically tracing its movement.

With reference to Figure 9.3, the flow can be idealised in three stages. In the first stage ($t < 0.25T$), the downstream vortex rolls up near the inlet entrance. In the second stage ($0 < t < 0.5T$) this vortex grows and translates depending on the deflection of the jet by the cross-flow. In the final stage ($t > 0.5$), the vortex translates parallel to the boundary under the influence of the cross-flow dynamic pressure and the image vortex induced motion. The profile was found to be nearly uniform except for the initial boundary region. The cross-flow velocity is normalised with respect to the characteristic velocity ℓ/T.

The experimental observations indicate that ebb discharges into a uniform cross-flow behave differently depending on whether or not the downstream vortex attaches to the boundary. The experimental data obtained are limited and consequently the discussion which follows deals mainly with attached flows.

Expt No	h_o mm	b_o mm	T sec	ℓ mm	ℓ/h_o	ℓ/b_o	U* mms^{-1}	K* mm^{2}s^{-1}	V_c
CF31	25	40	60	1480	59.2	37.0	24.7	986	0.52
CF32	25	40	60	1480	59.2	37.0	24.7	986	1.40
CF33	25	40	60	1480	59.2	37.0	24.7	986	2.49
CF41	25	100	60	1320	52.8	13.2	22.0	2200	0.69
CF42	25	100	60	1320	52.8	13.2	22.0	2200	1.31
CF43	25	100	60	1320	52.8	13.2	22.0	2200	2.21
CF51	25	60	60	906	36.2	15.1	15.1	906	1.24
CF52	25	60	60	906	36.2	15.1	15.1	906	2.33
CF53	25	60	128	1500	60.0	25.0	11.7	1500	1.80

TABLE NO. 9.1: INLET PARAMETERS AND CHARACTERISTIC SCALES FOR THE CROSS-FLOW EXPERIMENTS

a) ROLL-UP STAGE $t < 0.25\,T$

b) JET DEFLECTION STAGE $0 < t < 0.5\,T$

c) VORTEX TRANSLATION STAGE $t > 0.5\,T$
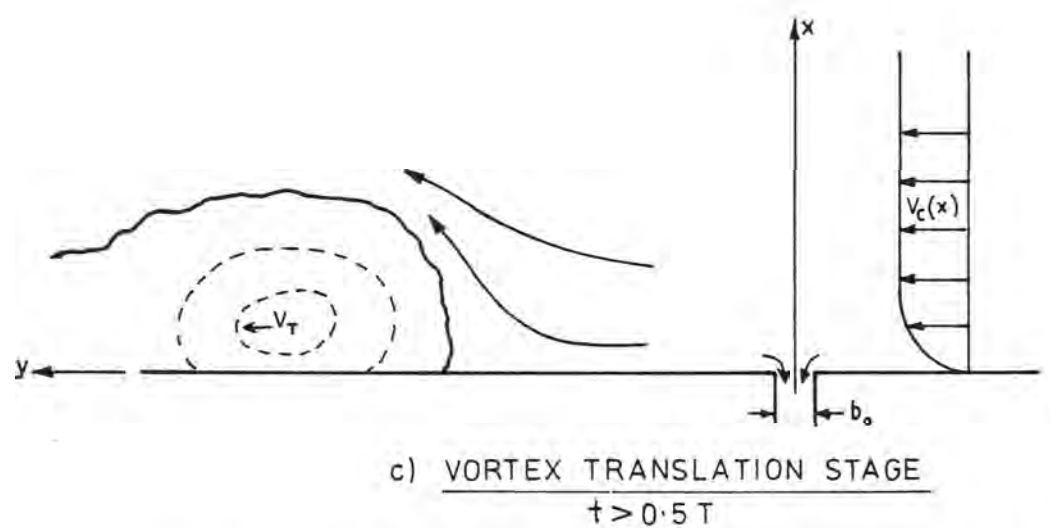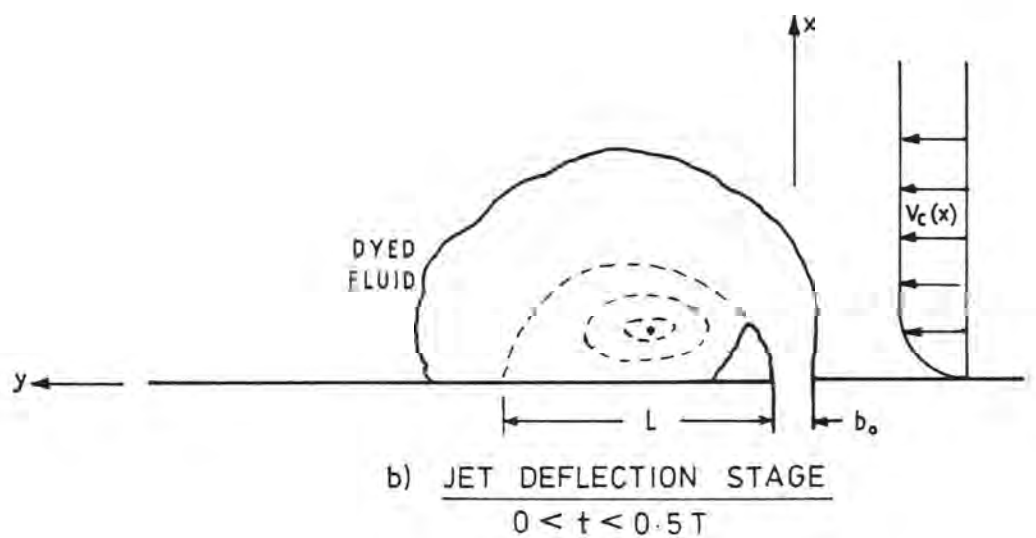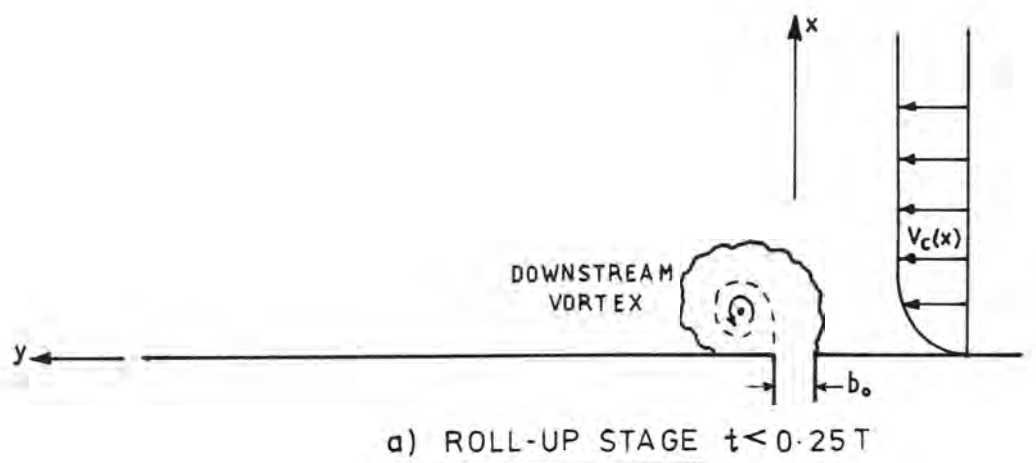
DEVELOPMENT OF PERIODIC STARTING JET FLOW
SUBJECT TO A CROSS-FLOW

FIGURE 9·3

9.3.1 Criteria For Vortex Attachment To The Boundary

From the experimental results it is taken that the downstream vortex will attach to the boundary for a dimensionless cross-flow velocity greater than $V_c = v_c/(\ell/T) \simeq 0.6$. For an ebb discharge into a cross-flow of smaller magnitude, the deflection of the jet by the end of the ebb cycle is insufficient to confine the downstream vortex near the boundary. During the flow reversal the vortex is no longer in the lee of the jet and is advected with the cross-flow. By physical reasoning, attachment of the flow will also be dependent on the inlet width ratio, ℓ/b_o, as this is a dimensionless measure of the jet momentum flux. The discussion which follows will be for an attached flow.

9.3.2 Initial Roll Up Stage

The main feature of the development of the flow was the apparent elimination of the upstream vortex. The criteria for this appears to be linked to those for attachment, in that a flow which does not attach has a well defined though less coherent upstream vortex structure. If the cross-flow velocity has sufficient magnitude to cause attachment of the downstream vortex, then the cross-flow shear associated with the boundary region is sufficient to redistribute the upstream vorticity.

This dispersal of upstream vorticity is due to the vorticity of opposite sign associated with the cross-flow. A first order estimate of this vorticity can be obtained from Equation (9.7) using Rossow's linear shear expression. The cross-flow vorticity is defined as:

$$\omega_c = \frac{\partial v_c(x')}{\partial x'}$$

$$= \frac{2K}{\pi d_c^2} V_{sh} \tag{9.8}$$

An estimate of the circulation, K, of the downstream vortex is taken from the similarity solution developed by Pullin (1978) as outlined in Appendix 2. The functional dependence of the circulation and core diameter on time are given by Equations (A2.2) and (A2.3). The functional dependence of K/d_c^2 is thus taken to be:

$$\frac{K}{d_c^2} = \beta_3 t_f^{-1} \tag{9.9}$$

where β_3 is a constant to be determined experimentally or from Pullin's numerical solution, and t_f is the spin-up time. Thus, Equation (9.8) becomes:

$$\omega_c = \frac{2}{\pi}\beta_3 t_f^{-1} V_{sh} \tag{9.10}$$

The implications of this are seen if the centre of rotation of the vortex, x_c, is assumed to move away from the edge of the inlet channel as the radius $d_c/2$. That is from Equation (A2.3):

$$x_c \approx \ell^{3/8} b_o^{5/8} T^{-3/2} t_f^{3/2} \tag{9.11}$$

Using this transformation Equation (9.10) becomes:

$$\omega_c = \beta_4 \ell^{1/4} b_o^{5/12} T^{-1} x_c^{-2/3} V_{sh} \tag{9.12}$$

For some appropriate value of V_{sh} and β_4, Equation (9.12) represents

the limiting cross-flow vorticity for which dispersal of the upstream vortex will occur. Expressed in dimensionless form and integrated from 0 to X_c, Equation (9.12) becomes:

$$V_{c\ LIM} = 3\beta_4(\frac{\ell}{b_o})^{-5/12}X_c^{1/3}V_{sh} \qquad (9.13)$$

This equation does not represent a cross-flow velocity profile. It defines the limiting dispersal velocity at each location, X_c, for a family of linear velocity profiles. Any profile which falls outside this limit can be expected to disperse the upstream vortex. Figure 9.4 shows the measured profiles near the boundary for all experiments. From visual observation it was found that the upstream vortex disperses for all velocity profiles other than profiles CF31 and CF41. The values of the constant β_4 can be determined for $V_{sh} = 0.2$ by fitting a curve of the form of Equation (9.13) through profile CF51, which is the experimental limit for complete dispersal. A good fit is obtained for $\beta_4 = 12.5$ and this curve is also plotted on Figure 9.4. (This compares with a value of $\beta_4 = 47$ from Pullin's numerical solutions). Clearly, these constants are somewhat arbitrary, being derived either from a numerical simulation which has not been experimentally verified or by a visual inspection of a limited set of experimental results.

The cross-flow shear parameter, V_{sh}, depends on the vorticity distribution within the vortex. The value, $V_{sh} = 0.2$, was chosen from Rossow's (1976) numerical results for a Rankine vortex. The vorticity distribution of the vortex pair resembles that of a pair of Rankine vortices where diffusion of vorticity has smoothed out the transition from the rotational core to the potential flow around it. Thus in this case, a value of V_{sh} somewhat lower than 0.2 would be expected.
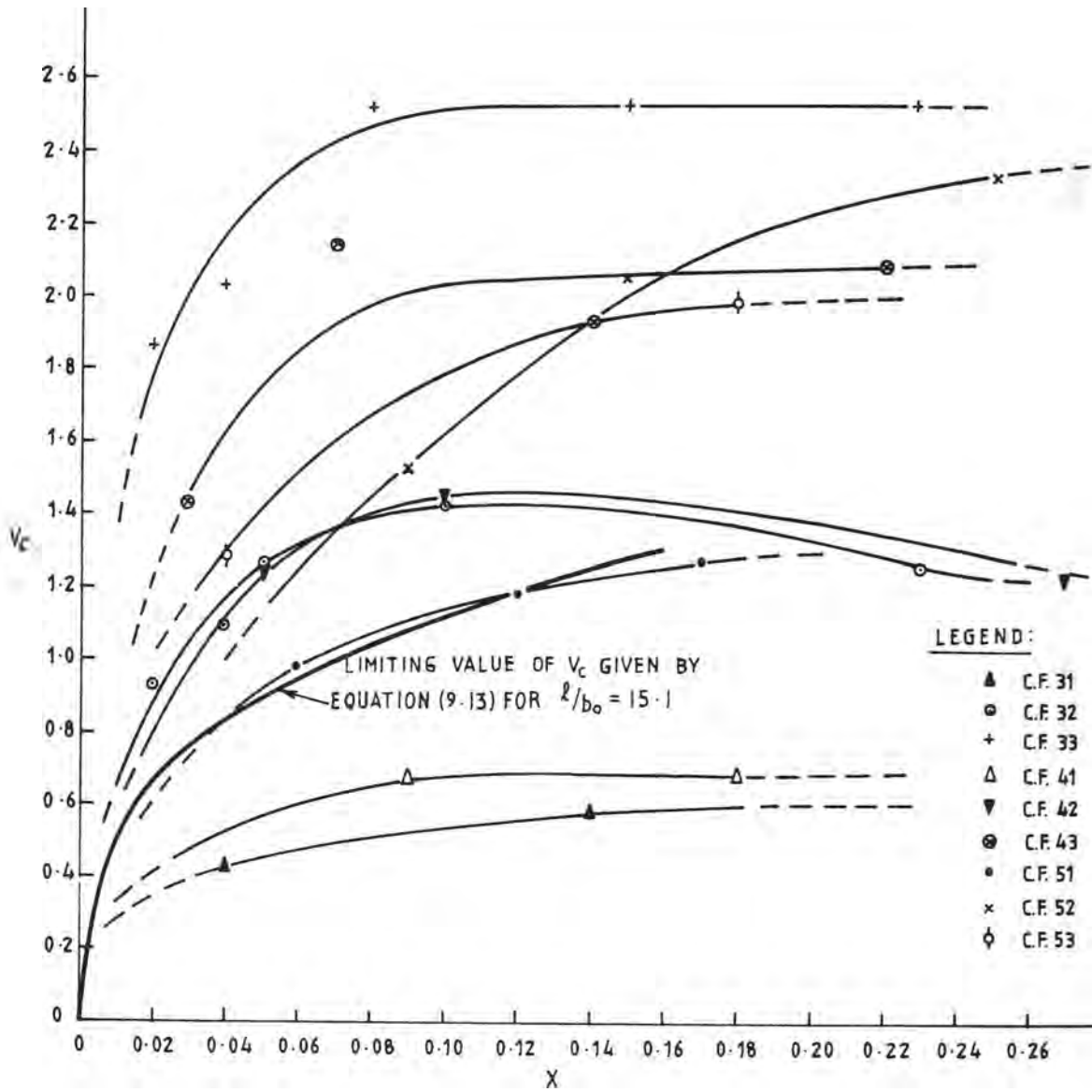
MEASURED DIMENSIONLESS CROSS-FLOW VELOCITY PROFILES

NEAR THE BOUNDARY

FIGURE 9·4

9.3.3 Jet Deflection Stage

During the ebb cycle the starting jet is deflected by the cross-flow. The redistribution of the upstream vorticity results in an upstream boundary of the jet which resembles that of a steady jet. It would be expected that the jet tail trajectory would be similar to that predicted for a starting jet. A parabolic trajectory of the form:

$$X = f[\ V_c, \tau, \frac{\ell}{b_o}]\ Y^{0.5} \tag{9.14}$$

would be expected on this basis. Insufficient data is available to formalize this relationship. The presence of a circulation in the lee of the jet — the downstream vortex and the induced circulation — will add to the imbalance in pressure force either side of the jet and deflect the jet further.

9.3.4 Vortex Translation Stage

The vortex which has spun up in the lee of the deflected jet will become attached to the boundary and will move with a velocity dependent on the velocity, v_i, due to the mutual interaction with the image vortex and the cross-flow velocity, v_c. Expressed mathematically the translation velocity, v_T, is given by:

$$v_T = v_c - v_i \tag{9.15}$$

The translation velocity and the rate of growth of the vortex can be obtained by considering the location of the apparent centre of rotation of the downstream vortex. This is shown in Figure 9.5 as distance versus time relationships for the dimensionless x and y co-ordinates of

the centre. The two main features of the behaviour of the vortex are as follows.

Firstly, the propagation away from the boundary (Figure 9.5a) is shown to be a function only of $\overline{V}_c$, the average dimensionless cross-flow velocity. The longshore movement of the vortex (Figure 9.5b) revealed a surprising feature of the flow. For the limited range of experimental data it is shown that the vortex translates downstream at a nearly constant velocity which is apparently independent of the magnitude of the cross-flow velocity. This feature is evident up until the vortex development is influenced by the downstream experimental boundary (gutter, Figure 4.8) of the flow. The implications of this will now be discussed.

A periodic jet discharging into a relatively low magnitude cross-flow will develop in a similar fashion to the no cross-flow case except that the upstream vorticity is dispersed. The downstream vortex is spun up and attains some value of circulation, K. The deflection of the jet is small and hence the downstream vortex migrates clear of the boundary. The induced image velocity is small, being dependent on the distance of the vortex from the boundary. Thus the translation velocity downstream alongshore after the peak discharge has been reached will be approximately equal to the cross-flow velocity.

Consider now the same jet discharging into a cross-flow of much greater magnitude. During the spin up stage the greater deflection of the jet restricts the downstream vortex to the region near the inlet. The amount of vorticity amalgamated into the vortex from the separation at the inlet will be greater than for the low cross-flow case. The strength of the vortex is also enhanced by the induced circulation in
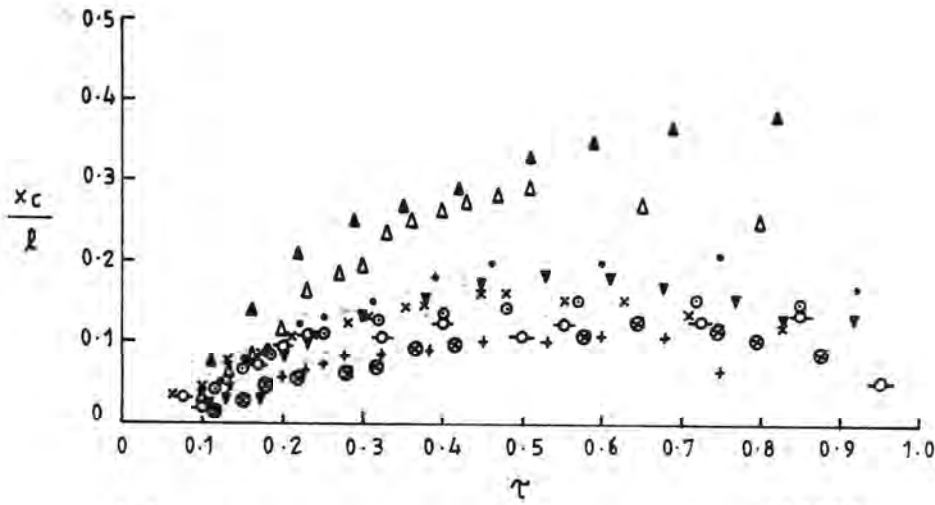
LEGEND:		
Expt. No.	ℓ/b_o	$\overline{V_c}$
▲ C.F. 31	37·0	0·55
⊙ C.F. 32	37·0	1·40
+ C.F. 33	37·0	2·49
△ C.F. 41	13·2	0·69
▼ C.F. 42	13·2	1·31
⊗ C.F. 43	13·2	2·21
• C.F. 51	15·1	1·24
× C.F. 52	15·1	1·80
⊖ C.F. 53	15·1	2·33
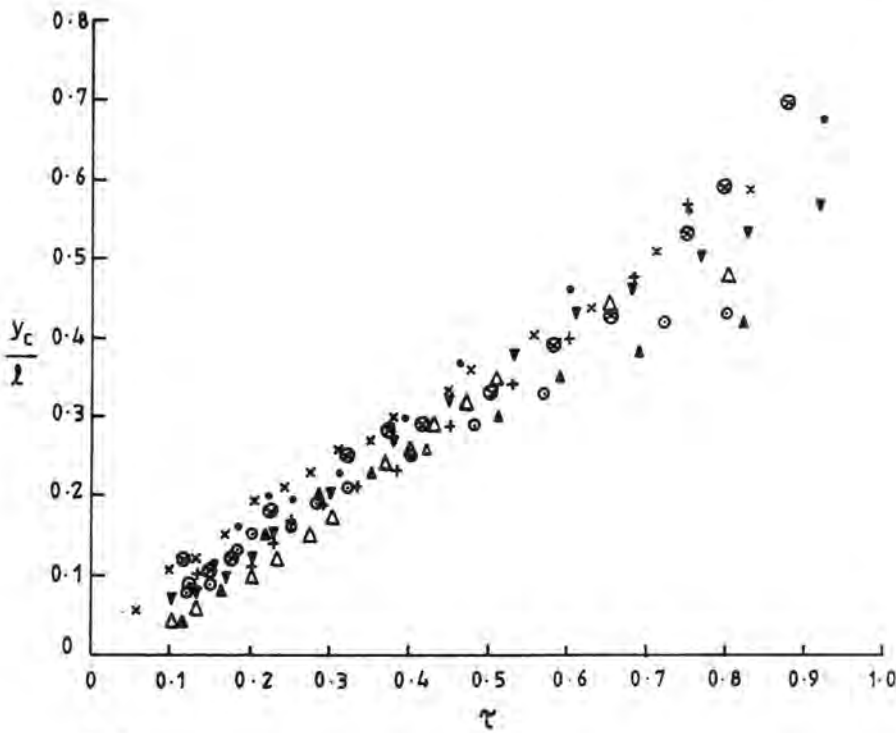
LOCATION OF DOWNSTREAM VORTEX CENTRE

FIGURE 9·5

the lee of the deflected jet. As the vortex is confined near the boundary as it develops, the induced velocity due to the image vortex will be greater than before. From the experimental results it can be inferred for the range of initial conditions tested, that any increase in the cross-flow velocity is countered by an increase in the self-induced velocity of the vortex back towards the inlet.

An estimate of the penetration of the downstream vortex, and hence its centre location, x_c, can be obtained by considering the relative magnitudes of the cross-flow velocity and the characteristic velocity. The characteristic velocity has been shown in previous chapters to be a reasonable measure of the average propagation speed of the starting jet front. The maximum dimensionless penetration of the downstream vortex, X_{cmax}, can then be taken to be inversely proportional to the dimensionless cross-flow velocity $V_c = v_c/(\ell/T)$. From the results shown in Figure 9.5a, good agreement is obtained for a relationship of the form:

$$X_{cmax} = 0.18 \ V_c^{-1} \tag{9.16}$$

The dimensionless translation velocity, $V_T = \dfrac{dy_c}{dt}/(\ell/T)$, can then be expressed as:

$$V_T = V_c - V_i$$

$$= V_c - \frac{b_o K'}{\ell \ 4\pi X_c} \tag{9.17}$$

where $K' = K/(b_o \frac{\ell}{T})$ is the dimensionless circulation.

Using X_{cmax} as a measure of the half spacing of vortex and its image, this equation becomes:

$$V_T = V_c - C(\frac{\ell}{b_o})^{-1} K \, V_c \qquad (9.18)$$

where C is a constant.

The implication of the apparent constancy of the translation velocity is that the circulation possessed by the downstream vortex must also be a function of the cross-flow velocity. It is interesting to note that Equation (9.18) is only valid for $V_c \geqslant V_T$. From the results shown in Figure 9.5b the average translation velocity is $V_T \simeq 0.66$. This is close to the limiting cross-flow velocity required for attachment of the downstream vortex to the boundary, $V_c \simeq 0.6$.

9.4 General Comments

The behaviour of a periodic jet subject to a cross-flow cannot be considered the same as that of a steady jet. There are, however, a number of similarities. A two-dimensional steady jet, like the periodic jet, may or may not attach to the boundary, depending on the relative magnitude of the cross-flow velocity compared to the jet source velocity. Steady jets that do attach form a re-circulation cell downstream of the source, the size and shape of which can be predicted. This eddy remains stationary for all time. A similar vortex-like structure develops in the lee of a periodic jet, but this is a transient feature, being swept along by the cross-flow during the flow reversal.

The experimental facilities were inadequate to provide a comprehensive data set for the influence of a cross-flow. In particular, there was insufficient capacity in the cross-flow generating system and the model length downstream of the inlet was too short for the vortex to be traced for any length of time. As a consequence the vortex interacted with the downstream boundary (gutter, Figure 4.8) while the vortex was still coherent.

The development of the flow during this vortex translation stage, Figure 9.3, would be described more completely using a conservation of angular momentum relationship including circulation losses due to the frictional torque on the boundary and entrainment of the ambient flow.

10. PERIODIC FLOWS IN NATURE

In the introduction to this thesis reference was made to a number of studies of periodic flows on a natural scale. These were mainly due to tidal action at a coastal inlet or through a strait. In this chapter it is proposed to discuss these flows in greater detail in relation to the present work. At the onset of this study, the emphasis was placed on tidal flows at coastal inlets, and, despite the more general description of a periodic starting flow presented in this thesis, it is considered that the flow mechanisms described herein have particular significance to the mass transport at tidal inlets.

10.1 Tidal Flows At Coastal Inlets

A tidal inlet can be defined as an enclosed body of water such as a coastal lagoon or lake which is connected by a narrow channel to the ocean. The dynamics of the flow (with no fresh water inflow) through this channel are usually taken to be controlled by the relative elevation of the ocean and inlet waters and the flow resistance of the channel. The dynamics and stability of the entrance channel have been investigated extensively by coastal engineers concerned with the problems of navigation and sediment movement. In more recent years, studies by Özsoy (1977), Mehta and Zeh (1980) and others have examined the nearshore hydrodynamics of the flow. These studies have considered the ebb discharge to be a quasi-steady turbulent jet. Analyses of this type predict the flow behaviour near the entrance and give a good estimate of the velocity distribution, sediment movement and induced flow.

The significance of the present study is that it gives a better understanding of the long term fate of the ebb discharge (including any

pollutant load). It will be assumed for the present that the complexities that arise due to the presence of cross-winds, ambient currents, and density stratification will not prevent the formation of the vortex like cap of the periodic starting jet. The obvious question to ask in establishing the validity of an unsteady formulation for a tidal flow is whether the flow will scale from the model to the prototype. Evidence for the existence of large scale vortices offshore is difficult to obtain and the available field data will be discussed later.

The flow characteristics at a tidal entrance can be expressed in terms of the characteristic scales and parameters defined in Chapter 2. In terms of the tidal prism, P_T, the mean cross-sectional area of the channel, A_C, and the mean depth of flow in the channel, h_o, the characteristic length scale, ℓ, is given by:

$$\ell = [\frac{\pi^2 P_T^2}{A_C h_o}]^{1/3} \tag{10.1}$$

Typical values of this length scale for tidal inlets range from 7 km - 19 km (U.S. data, Per Bruun (1978)). The corresponding inlet depth ratio, ℓ/h_o, ranges from 10^3 to 6×10^3, and the inlet width ratio, ℓ/b_o, from 8 to 77.

10.1.1 Model Case Study - Nerang River Entrance

A detailed description will now be given of an attempt to realistically model a tidal ebb discharge, outlining the scaling difficulties encountered. The inlet studied was the Nerang River entrance in Queensland (Wilkinson et al.,1979). This river discharges into a large intra-coastal waterway which is connected to the ocean by a short

channel. The average river discharge is less than 2% of the total discharge through the channel and was ignored. It was proposed to train the inlet to provide safer navigation and a stable inlet location. The characteristic length scale and inlet parameters for this proposed entrance were estimated as:

$$\ell = 7,960 \, m$$
$$\ell/b_o = 33.7$$
$$\ell/h_o = 1,090$$

An idealised physical model of the inlet and nearshore region was constructed in the same test facility as described in Chapter 4. An undistorted scale model should ideally be used to correctly scale the lateral mixing of the jet. However, the important role played by bottom friction requires the correct scaling of bottom shear. Due to unavoidably low Reynolds Numbers in a model, this requirement necessitates distortion of the vertical model scale. A compromise between these two requirements was adopted in which water depths everywhere were increased by a fixed amount while bottom slopes were undistorted and were the same as in the prototype. This meant that momentum and lateral mixing were correctly scaled but that friction effects would only be correctly scaled at one particular depth contour. The flow at the inlet channel was considered two-dimensional.

Similarity of frictional and inertial forces can only be achieved if the ratio of these two forces is the same for both model and prototype. In Chapter 2 it was shown that this ratio is given in terms of the characteristic scale as:

$$\frac{I_F}{M} = \frac{f}{8} \frac{\ell}{h_o} \qquad (10.2)$$

Similarity between model and prototype requires that:

$$(\frac{f}{8} \frac{\ell}{h_o})_m = (\frac{f}{8} \frac{\ell}{h_o})_p \qquad (10.3)$$

or,

$$(\frac{\ell}{h_o})_r = (f_r)^{-1} \qquad (10.4)$$

This states that the ratio of the prototype inlet depth parameter to the model parameter is equal to the inverse of the prototype to model friction factor ratio. This ratio was determined as follows.

In the model the bed was formed of asbestos cement sheeting. Reynolds Numbers based on the flow depth were in the range of 2000 to 800 in the area of interest. A mean friction factor of $f = 0.04$ was adopted for the smooth turbulent flow.

In the prototype, the median diameter of bottom sediments is approximately 0.25 mm for a distance of 3 km offshore from the Nerang entrance channel. Swart (1974) has found that the mean ripple height in such material would be approximately 20 mm. Taking a mean depth of 25 m, and a typical velocity of $0.3 \, \mathrm{ms}^{-1}$ in the jet, the relative roughness of the sea bed is 800 and the Reynolds Number of the order 10^6 to 10^7. Under these conditions the bottom would be hydraulically rough and the friction factor would have a value of 0.014 (Henderson, 1966).

The ratio of friction factor in prototype and model is therefore taken as:

$$f_r = 0.35$$

Thus from Equation (10.4)

$$(\frac{\ell}{h_o})_R = 2.87 \tag{10.5}$$

The horizontal length scale was fixed by the dimensions of the experimental tank. A section of the nearshore region 14 km alongshore and 12 km offshore was modelled at a scale of 4170:1. The depth scale from Equation (10.5) was therefore 1500:1. The time scale is fixed by the model periodic flow generating mechanism and scaled a 12.6 hour tidal cycle at 720:1. These scaling requirements resulted in a depth of flow in the model at the inlet of 10 mm. The entrance channel was 55 mm wide. The offshore slope was modelled in two linear stages.

This case study differed from the main experimental program in that the model inlet depth ratio is larger ($\ell/h_o = 380$) compared with a typical experimental value in the range $\ell/h_o = 36-118$. Large ℓ/h_o experiments were not conducted in the main experimental program as bed irregularities become a significant feature in a shallow depth, and would make comparative studies difficult. The exception to this was Expt. No. 36, where a $\ell/h_o = 236$ was acheived by increasing the period, T, to 250 seconds. The inlet width parameter value for the Nerang Study was typical of the range covered in the program. The characteristic Reynolds Number was 1,515. The results of the testing of this configuration can be summarised as follows.

In general the flow pattern was similar to that described in Chapter 2. However, a number of factors acted to destabilize the vortex pair more quickly. Frictional effects dominated this flow and

would also dominate most coastal flow situations. The bottom boundary layer acts to introduce three-dimensionality into the vorticity distribution. For shallow depth flows this distortion of the line vortices is large, leading to the instabilities described in the earlier chapters.

The predicted behaviour of the periodic jet is shown in Figure 10.1. The width variation indicated clearly the influence of bed slope. Near the inlet where the slope is quite steep, the flow expands at a slower rate than in the far-field where the slope is shallower. The model test results are plotted up to the time the vortex pair cap became incoherent. Verification of these predicted results with field data has not been possible.

10.2 Factors Influencing The Vortex Pair Dynamics

The application of the present theory to real flows at coastal inlets in general is limited in that no allowance has been made in the theory for factors such as wave activity, wind driven currents, irregular bottom topography and density stratification. The anticipated effect of these influences on the development and migration of a vortex pair will now be discussed.

It has been shown in steady jet analyses that the bottom topography greatly influences the growth of the jet. For a linearly increasing depth away from the inlet, a steady jet will expand exponentially at a rate dependent on the bed slope. For a slope greater than $0.1\dfrac{h_o}{b_o}$ Özsoy (1977) has shown that the jet will contract.
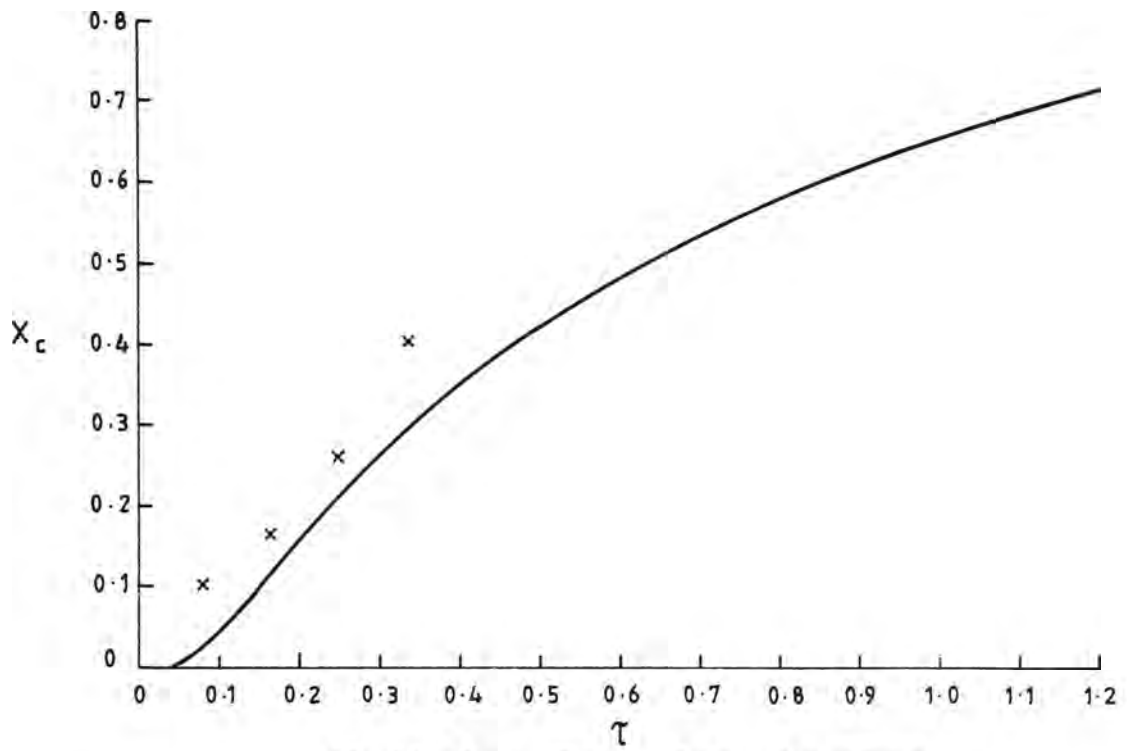
b) Vortex Pair Cap Advance
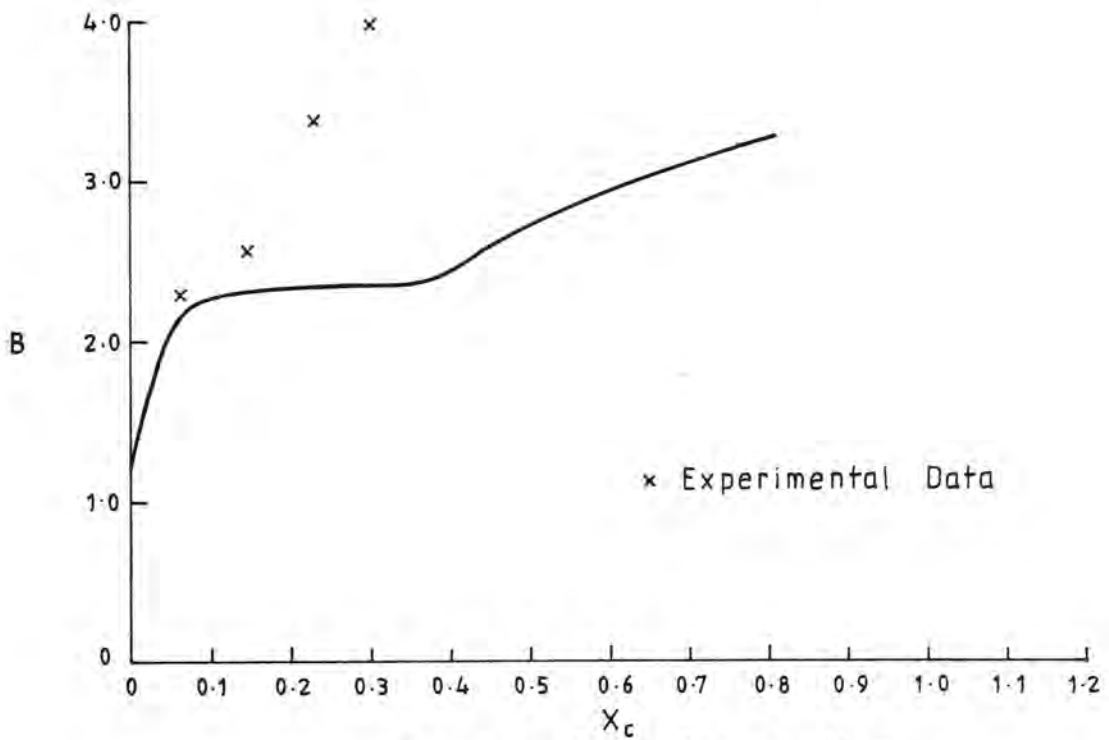
a) Vortex Pair Separation

PREDICTED BEHAVIOUR OF THE NERANG RIVER

ENTRANCE EBB DISCHARGE

FIGURE 10·1

The influence on the dynamics of the vortex pair is twofold. An increase in depth results in the vortex tube stretching and consequently a re-organisation of the vorticity in the core. A highly organised core of small cross-section will entrain less ambient fluid and will remain coherent for a longer period. This stabilizing feature is countered by the three-dimensioal instability of the vortex tube induced by the bottom boundary layer. The amplification of this instability will be enhanced by the axial flow in the vortex core produced by the vortex tube stretching.

Other features which influence the vortex behaviour include local variations in the bottom topography which act to change the vorticity balance of the flow. Zimmerman (1978) has shown that depth variation in combination with bottom friction is both a source and a a sink of vorticity. Onishi et al. (1981) have shown that a local concavity acts to trap a large scale vortex pair (see Section 10.3).

The rotation of the earth has been shown to only significantly influence steady jets in deep water where they cannot support rotational pressure gradients. Density differences between the jet and the ambient flow will enhance this effect as the jet may become detached from the bed. An estimate of the relative importance of the earth's rotation on the vorticity distribution of the vortex pair can be found by an order of magnitude analysis of the expected vorticity in a typical tidally produced pair. Using the estimates obtained experimentally for the vorticity associated with an elliptical core with uniformily distributed vorticity (Chapter 5) and the data presented by Onishi and Nishimura (1980_2), the vorticity in the core is $\omega \simeq 0[\ 10^{-3}s^{-1}\ ]$. The coriolis parameter is of the order $10^{-5}s^{-1}$. The vortex pair generated at a typical inlet such as the Nerang Entrance, would propagate at

about the characteristic velocity $U* = 0.2 \text{ ms}^{-1}$. The pair separation after one half cycle would be of the order of 1 km. Thus, the vorticity associated with such a pair would be of the order of $\omega \simeq 10^{-3}\text{s}^{-1}$. Generally speaking for a large inlet the vorticity is an order of magntidue larger than that due to the earth's rotation.

Flierl et al (1980) have reported on the existence of solitary oceanic vortex pair-like eddies which move in the opposite direction to the planetary rotational effects. The vortex pair self-induced motion in balance with the planetary effect, provides an explanation for this observed behaviour.

It has been seen from the experiments that ambient turbulence and motion can greatly reduce the coherent duration of a vortex pair. In a real flow situation (particularly at a coastal inlet) wave activity, wind shear, and longshore drift are present at varying magnitudes throughout the flow cycle and would greatly influence the spin-up of vorticity. As has already been shown, the presence of a cross-current of relatively low magnitude can greatly change the vorticity distribution even in the ideal case.

The theoretical model assumes a sinusoidal discharge variation. Real flow variations tend to be irregular and asymmetrical for the flood and ebb tides. This would not prevent vortex pair formation, as the vortex pair are the result of a viscous induced instability in a starting flow and hence their existence is not dependent on the ebb duration. However, a relatively long flow reversal may be more likely to influence the previous ebb flow. The characteristic scales are still relevant parameters describing the flow although the approximate relationships determined for the ideal flow case would not be relevant.

It is apparent that a more useful time scale would be the duration of flow during the ebb phase. (The characteristic velocity being a good measure of the cap speed during the first half of the cycle). Thus the length scale could be defined in terms of the ebb period without loss of generality. The nearly constant velocity of propagation in the first half cycle of the experiments has been shown to be attributable to the nearly constant inlet flow acceleration. A more irregular discharge variation would result in a less predictable flow behaviour. The unsteady jet-vortex pair model developed in this thesis is capable of handling such an initial boundary condition, as well as any one-dimensional depth variation.

10.3 Field Studies and Remote Sensing

The collection of field data pertaining to the mass transport in the vicinity of tidal inlets has mainly been limited to cases where there is a significant constant freshwater outflow. River effluents have been studied extensively as referred to in Chapter 1. These studies usually are concerned with the deposits of delta forming sediments and the long term fate of suspended sediments and pollutants. Only a few studies have considerd the nearshore velocity distribution in an ebb discharge at a tidal inlet and even fewer have considered the long term dynamics of the flow.

Mehta and Zeh (1980) presented data from a field study of flow through Sikes Cut, Florida. Lateral velocity distribution, entrainment velocity, jet width and jet axial velocity were determined in the jet tail section of the starting jet. The velocity measurements were taken just prior to the peak discharge ($\tau \sim 0.25$). The agreement of their data with the steady jet analysis is consistent with the quasi-steady

behaviour exhibited in the early stages of the flow by the unsteady formulation presented in this thesis. An entrainment coefficient, E = 0.21, was determined. However, the measurement was taken just after the vortex pair cap had passed and was consequently enhanced by the induced flow around the vortex pair cap. The results presented show good agreement with the steady jet analysis, but also suggest the presence of the unsteady features of a starting flow. An estimate of the characteristic parameters for Sikes Cut are:

$$\ell = 7290 \text{ m}$$

$$\ell/b_o = 21.7$$

$$\ell/h_o = 2,080$$

The large scale unsteady circulations predicted by the vortex pair analysis and the case study for the Nerang Entrance, have not been detected by conventional field data collection techniques. The difficulties inherent with such an exercise are apparent. There are some data available showing a circulation which is stationary or has been measured at one instant in time. Harrison et al (1964), for example, present data on the circulation resulting from the interaction between the ebb discharge from Chesapeake Bay, Virginia and the Gulf Stream. The circulation pattern inferred from their data is shown as Figure 10.2. As predicted in Chapter 9, a cross-current results in a dominant down current vortex which may remain stationary near the inlet or move alongshore due to the cross-current (Figure 9.2).

A number of studies in recent years have employed the earth resources satellites remote sensing imagery. In particular the LANDSAT satellites have proven to be useful tools for coastal studies. Multispectral scanning data from LANDSAT can be analysed to detect changes
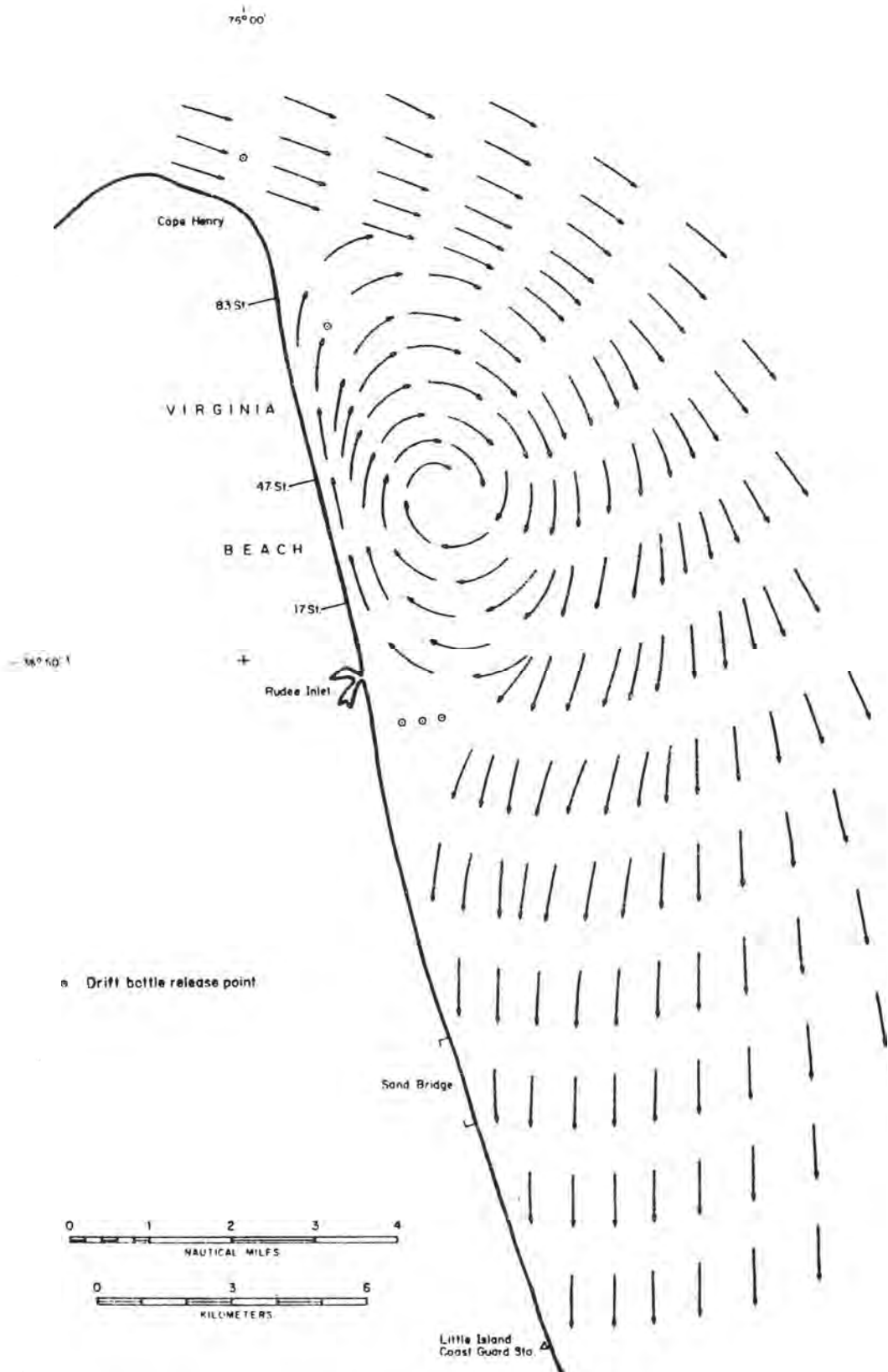
CIRCULATION PATTERN NEAR CHESAPEAKE BAY, VIRGINIA

(After Harrison et al., 1964)

FIGURE 10·2

in turbidity in the upper surface layer of the ocean. This is particularly useful for detecting river plumes. Tidal discharges with a small suspended load have also been detected. Finley and Baumgardner (1980) qualitatively examined the ebb discharge at Aransas Pass, Texas. The influence of cross-current due to wind shear was evident as well as a clearly defined circulation.

The most extensive use of LANDSAT has been by Onishi and Nishimura $(1980_1,_2)$ as has been referred to in Chapter 1. Their study was of the vortex pairs produced by the tidal flow through the straits connecting the Island Sea of Japan and the Pacific Ocean. Onishi and Nishimura have analysed the LANDSAT data as well as aerial infra red photographic data and have satisfactorily described the tidal exchange mechanism in terms of the vortex pair behaviour. Estimates of the characteristic scales of this motion are as follows:

$$\ell \quad = \quad 25,870 \, m$$
$$\ell/b_o = \quad 74$$
$$\ell/h_o = \quad 430$$
$$\ell/T = \quad 0.5 \, m\,s^{-1}$$

From a composite of satellite images and other data, the self-induced velocity of the pair was determined by Onishi and Nishimura as $0.4 \, m\,s^{-1}$. The vortex pair separation was estimated as 4km. From this they have estimated that about 10% of the vorticity generated at the strait is present in the vortex pair after the flow reversal. The mechanism proposed by Onishi and Nishimura for the spin up of the vortex pair is the amalgamation of the smaller coherent vortices present in the free shear mixing layer of the tidal jet. Extensive measurements of the dynamics of these smaller vortices was undertaken.

The vortex pair remains trapped near the straits for some time. This would appear to be due to the image vortices and the bottom irregularities in the vicinity of the straits. Image vortex effects would be significant in this case as the neighbouring coastline has a V shape in planform with the strait at the apex. Onishi, et al. (1981) have considered the influence of the bottom topography on the small scale line vortices and they propose that local bottom topography concavity acts to trap the large scale vortex pair. Also evident from their LANDSAT and aerial photography studies is the upwelling of colder water due to the Ekman pumping in the vortex core.

Satellite detection is limited by the orbit and sensitivity of the individual satellite. For example, LANDSAT passes one location every 18 days and has a ground resolution of 79 m. The resolution of LANDSAT 4 has been increased to 30 m and other satellites such as SEASAT also provide greater detail more regularly. Despite these limitations, satellite remote sensing provides useful information on the gross behaviour of the ebb discharge vortex pair and is considered by the author to be the simplest way to establish the validity of the vortex pair model for more typical tidal inlet flows.

Recent analysis of LANDSAT imagery of the Great Barrier Reef by Wolanski (1983) has revealed the existence of vortex pair-like structures being generated by tidal flow through gaps in the outer reef. An enhanced spectral image is shown in Figure 10.3. The dark areas in the centre are the reef, with the gaps and channels clearly indicated. A number of vortex like structures are indicated as less distinct dark areas. Two successive vortex pairs have been generated from the large gap. Data are not available on the scale of these flows, the dimensions of the channels or the bottom topography. The size of the largest of

LANDSAT IMAGE OF VORTEX PAIR FLOWS BEING GENERATED BY
TIDAL ACTION AT OPENINGS ALONG THE GREAT BARRIER REEF

FIGURE 10·3

the vortices is estimated of the order of 10 km, being of similar scale to those reported by Onishi and Nishimura. Although these flows would have been turbulent at generation, an organised structure is evident in the vortices distant from their source. This apparent re-organisation of the vorticity distribution has been demonstrated recently by Flierl et al (1983). They conducted laboratory experiments where a three-dimensional starting jet issued into a rotating basin. The inflow was stopped and a vortex pair was seen to form and migrate away from the source in a circular path. The turbulent motions of the jet gave way to more ordered two-dimensional motions according to the Taylor-Proudman theory (Pedlosky, 1979). It is possible that a similar adjustment is made during the life of a tidally produced vortex pair migrating in deep water.

The results of the present experimental study would indicate that flows of the type described by Onishi and Nishimura (1980_1) and Wolanski (1983) should not remain coherent due to the destabilising effect of the bottom frictional stress. Both flows are estimated to have large ℓ/h_o values, suggesting large frictional damping. However, it would seem that there is a negligible destabilising effect in these cases. This suggests that a more relevant measure of the influence of bottom friction on the vortex pair may be the ratio of the Ekman boundary layer thickness to the flow depth, δ'/h_o.

The significance of this can be seen by comparing the Nerang Inlet and Naruto Strait flows. These flows have similar ℓ/h_o values. The equation for the boundary layer thickness given in Section 7.3 based on the characteristic Reynolds Number Re* and taking the inlet width as the radial length scale, gives $\delta' \sim 0.04$ and 0.03 for Nerang and Naruto respectively. The corresponding δ'/h_o ratios are 0.005 and 0.0004. It

can be seen that the bottom frictional influence is greater for the coastal inlet flow and would be expected to be so for all similar flows. This, combined with other ambient conditions in the coastal zone, will act to rapidly destabilise the vortex pair cap.

11. CONCLUDING REMARKS

The investigation described in the preceding chapters has shown that a periodically reversing flow through an orifice issuing into a shallow basin can be modelled as a series of impulsively generated two-dimensional starting flows.

The behaviour of the starting flow has been examined using an idealised physical model which has demonstrated the features of the flow. At the commencement of each flow cycle a two-dimensional starting jet develops which has a pronounced head or cap. It has been shown that this cap behaves like a vortex pair. The vortex pair cap is growing due to turbulent entrainment of fluid into the vorticity containing region and the advection of mass from the unsteady jet tail up until such time that the cap and jet decouple. The hydrodynamic impulse of the vortex pair cap is not constant, but changes with time due to the influence of the advection of momentum from the unsteady jet tail during the coupled flow stage and due to the retarding force of bottom frictional resistance. The experimental results have shown that it is reasonable to take the patch of dyed fluid which traces the ebb discharge as representing the vorticity contining region.

Solutions to the intergral equations of mass and momentum for the general case of a two-dimensional shallow water unsteady jet have been obtained. Despite the simplifying assumptions, it has been shown that the generalised unsteady jet solutions predict the behaviour of the jet reasonably well in the near-field of the inlet during the ebb phase and in the far-field near the vortex pair cap during subsequent stages of the flow development. The self-preservation of flow in and around the cap which is nearly circular in shape has enabled empirical

relationships to be derived for the conservation of cap mass and momentum. Thus, these equations have been coupled to the jet equations to give the overall periodic jet behavior. The cap behaviour has been expressed in terms of the translation velocity of the cap centreline and apparent separation of the vortex centres of rotation. The form of the relationships obtained have been verified for a two-dimensional periodic jet over a range of initial boundary conditions.

The flow has been described in terms of dimensionless parameters and characteristic flow variables which incorporate characteristic length and time scales. For a sinusoidal mass flux variation the relevant time scale is the cycle period, T. It has been shown that the the motion of the flow in the direction of propogation is dependent on the ratio of the characteristic length scale, ℓ to the inlet width, b_o. The length scale, ℓ, has been derived by dimensional reasoning and is a function of the fluid density, the cycle period and the peak inlet momentum flux per unit depth. Where bottom frictional resistance is to considered, the ratio of the characteristic length, ℓ, to inlet depth, h_o, is the appropriate parameter. The velocity, ℓ/T, characterises the dynamics of the flow.

The idealised case of a symmetrical vortex pair migrating away from the source along a path normal to the boundary was approximated in 72% of the experiments. Asymmetrical flow patterns were evident in the remaining experiments. Generally, at times greater than one period the vortex pair becomes incoherent due to three-dimensional instabilities which are amplified by the turbulence level of the ambient fluid and the residual motion of the preceding flow cycles.

The experiments in which the periodic jet was subject to a cross-flow indicated that the clearly defined vortex pair structure is reorganised by the cross-flow. For uniform cross-flows with low velocity relative to the jet exit velocity, the vortex pair is deflected downstream and migrates away from the inlet and the boundary. For larger values of cross-flow the vorticity associated with the upstream vortex is dispersed by the cross-flow shear and the downstream vortex is spun up near the boundary. This vortex then migrates away from the inlet along the boundary under the influence of the cross-flow and the self-induced motion of the image vortex across the boundary. A complete data set describing the influence of the cross-flow was not obtained because of the the inadequacies of the experimental apparatus. Hence the cross-flow results presented in this thesis can only be taken as preliminary.

The studies undertaken elsewhere as described in Chapters 1 and 10 have shown that a vortex pair model provides an adequate description of tidal exchange flows. Many aspects of the theoretical analysis presented in Chapters 3 and 9 have involved simplifying assumptions which limit the application of the solutions to more general flow cases such as tidal inlet ebb jets. Field studies are required to verify the suitability of this model in tidal inlet flows particularly in locations where there is an active wave climate.

12. REFERENCES

[1] Abramovich, G.N. (1963). The theory of turbulent jets. The M.I.T. Press,Cambridge,Mass.

[2] Barker, S.J. and Crow, S.C. (1977). The motion of two-dimensional vortex pairs in a ground effect. J. Fluid Mech., Vol. 82, pp. 659-671.

[3] Batchelor, G.K. (1967). An introduction to fluid dynamics. Cambridge University Press, Reprint 1979.

[4] Beardsley, R.C. and Hart, J. (1978). A simple theoretical model for the flow of an estuary onto a continental shelf. J. Geophys. Res., Vol. 83, No. C2, pp.873-883.

[5] Beghin, P., Hopfinger, E.J. and Britter, R.E. (1981). Gravitational convection from instantaneous sources on inclined boundaries. J. Fluid Mech., Vol. 107, pp. 407-422.

[6] Bilanin, A.J., Teske, M.E. and Hirsch, J.E. (1978). Neutral atmospheric effects on the dissipation of aircraft vortex wakes. A.I.A.A.J., Vol. 16, pp.956-961.

[7] Brashears, M.R., Logan, N.A. and Hallock, J.N. (1975). Effect of wind shear and ground plane on aircraft wake vortices. A.I.A.A.J. Aircraft, Vol. 12, No. 10, pp.830-833.

[8] Cantwell, B.J. (1981). Transition in the axisymmetric jet. J. Fluid Mech. Vol. 104, pp. 369-386.

[9] Chow, C-Y (1979). An introduction to computational fluid mechanics. John Wiley and Sons, New York.

[10] Crow, S.C. (1970). Stability theory for a pair of trailing vortices. A.I.A.A.J., Vol. 8, p.2172.

[11] Csanady, G.T. (1965). The buoyant motion within a hot gas plume in a horizontal wind. J. Fluid Mech., Vol. 22, pp. 225-239.

[12] Davies, P.O.A.L. and Hardin, J.C. (1973). Potential flow modelling of unsteady flow. Proc. Int. Numerical Methods in Fluid Dynamics, pp.42-64.

[13] Davies, P.O.A.L. and Yule, A.J. (1975). Coherent structures in turbulence. J. Fluid Mech., Vol 69, pp.513-537.

[14] Dean, R.G. and Walton, T.L. (1974). Sediment transport processes in the vicinity of inlets with special reference to sand trapping. Estuarine Research, Vol. 2, pp.129-149.

[15] Delichatsios, M.A. (1979). Time similarity analysis of unsteady buoyant plumes in neutral surroundings. J. Fluid Mech., Vol. 93, pp.241-250.

[16] Demetriou, J.D. (1983). Experiments on starting homogeneous jets. Proc. ASCE Hyd. Div., Vol. 109, No. 7, pp.1039-1044.

[17] Fearn, R. and Weston, R.P. (1974). Vorticity associated with a jet in a cross flow. A.I.A.A.J., Vol 12, No. 12, pp.1666-1671.

[18] Finley, R.J. and Baumgardner, R.W. (1980). Interpretation of surface water circulation Aransas Pass, Texas, using Landsat imagery. Remote Sensing of Environment, Vol. 10, pp.3-22.

[19] Flierl, G.R., Larichev, V.D., McWilliams, J.C. and Reznik, G.M. (1980). The dynamics of baroclinic and barotropic solitary eddies. Dyn. Atmos. Oceans, Vol. 5, pp.1-41.

[20] Flierl, G.R., Stern, M.E. and Whitehead, J.A. (1983). The physical significance of Modons: laboratory experiments and general intergral constraints. Dyn. Atmos. Oceans, Vol. 7, pp.233-263.

[21] French, J.L. (1960). Tidal flow in entrances. Corps of Engineers, U.S. Army Committee on Tidal Hydraulics, Tech. Bull. No. 3, 49pp.

[22] Gadgil, S. (1971). Structure of jets in rotating systems. J. Fluid Mech., Vol. 47, pp.417-436.

[23] Garvine, R.W. (1977). Observations of the motion field of the Connecticut river plume. J. Geophys. Res., Vol. 82, No. 3, pp.441-454.

[24] Groen, P. and Groves, G.W. (1962). "Surges" in The Sea (Ed. M.N.Hill), Vol. 1, pp.611-646. Interscience Pub. N.Y.

[25] Harrison, W., Brehmer, M.L., and Stone, R.B. (1964). Nearshore tidal and non tidal currents, Virginia Beach, Virginia. U.S. Army Coastal Engineering Research Centre, Tech. Mem. No. 5, 20 pp.

[26] Henderson, F.M. (1966). Open channel flow. Macmillan, New York.

[27] Ikeda, M. (1977). Finite disturbances and growing vortices in a two-dimensional jet. J. Fluid Mech., Vol. 80, pp. 401-421.

[28] Jeffrey,A. and Taniuti,T. (1964). Non-linear wave propogation. Ist.Edn., Academic Press, New York, pp.3-64.

[29] Jirka, G.H. and Fong, L.M. (1981). Vortex dynamics and bifurcation of buoyant jets in crossflow. Proc. ASCE Eng. Mech. Div., EM 3, pp.479-499.

[30] Joshi,P.B. (1982). Hydromechanics of tidal jets. Proc. ASCE Wat.,Port,Coast. and Ocean Div., WW 3, pp.239-253.

[31] Kamotani, Y. and Greber, I. (1974). Experiments on confined turbulent jets in cross flow. NASA REP. CR - 2392, 75 pp.

[32] Keller, H.B. and Thomee, V. (1962). Unconditionally stable difference methods for mixed problems for quasi-linear hyperbolic systems in two dimensions. Comm. Pure Appl. Maths., Vol. 15, pp. 63-73.

[33] Kent, J.C. (1973). Unsteady viscous jet flow into stationary surroundings. Computers and Fluids, Vol. 1, pp.101-117.

[34] Killworth, P.D. and Turner, J.S. (1982). Plumes with time-varying buoyancy in a confined region. Geophys. Astrophys. Fluid Dyn., Vol. 20, pp.265-291.

[35] Kotsovinos, N.E. (1976). A note on the spreading rate and virtual origin of a plane turbulent jet. J. Fluid Mech., Vol. 77, pp.305-311.

[36] Lai, J.C.S. and Simmons, J.M. (1980). Instantaneous velocity measurements in a periodically pulsed plane turbulent jet. A.I.A.A.J., Vol. 18, No. 12, pp. 1532-1534.

[37] Lamb, H. (1952). Hydrodynamics.

[38] McGuirk, J.J. and Rodi, W. (1978). A depth-averaged mathematical model for the rear field of side discharges into open-channel flow. J. Fluid Mech., Vol. 86, pp.761-781.

[39] Maxworthy, T. (1972). The structure and stability of vortex rings. J. Fluid Mech., Vol. 51, pp.15-32.

[40] Maxworthy, T. (1974). Turbulent vortex rings. J. Fluid Mech., Vol. 64, pp.227-239.

[41] Maxworthy, T. (1977). Some experimental studies of vortex rings. J. Fluid Mech., Vol. 81, pp.465-495.

[42] Mehta, A.J. and Zeh, T.A. (1980). Influence of a small inlet in a large bay. Coastal Engineering, Vol. 4, p. 157-176.

[43] Middleton, J.H. (1975). The asymptotic behaviour of a starting plume. J. Fluid Mech., Vol. 72, pp.753-771.

[44] Mikhail, R., Chu, V.H. and Savage, S.B. (1975). The re-attachment of a two-dimensional turbulent jet in a confined cross flow. Proc. 16th I.A.H.R. Cong., Vol. 3, pp.414-419.

[45] Moore, D.W. and Saffman, P.G. (1971). Structure of a line vortex in an imposed strain. Proc. Symp. Aircraft wake turbulence and its detection, Ed. by Olsen, Goldberg and Rogers. Plenum Press, pp.339-354.

[46] Morton, B.R., Taylor, G. and Turner, J.S. (1956). Turbulent gravitational convection from maintained and instantaneous sources. Proc. Roy. Soc. Lond., Vol. A234, pp.1-23.

[47] Oertel, G.F. (1974). Ebb-tidal deltas of Georgian estuaries. Estuarine Research, Vol. 2, pp.267-276.

[48] Onishi, S. and Nishimura, T. (1980_1). Study of vortex current in strait with remote-sensing. Proc. 17th Coastal Eng. Conf. Sydney, pp.2655-2670.

[49] Onishi, S. and Nishimura, T. (1980_2). Field observation of tidal-exchange through straits from deterministic view points and consideration of methods to control the process. Coastal Eng. in Japan, Vol. 23, pp.251-261.

[50] Onishi, S., Tanaka, S., and Nishimura, T. (1981). Influence of the sea bottom topography on the large scale tidal vortices at the straits .... its field observation through remote sensing .... Coastal Eng. in Japan, Vol. 24, pp.215-228.

[51] Özsoy, E. (1977). Flow and mass transport in the vicinity of tidal inlets. Coastal and Oceanographic Eng. Dept., College of Eng., Univ. of Florida, Tech. Rep. UFL/COEL/TR-036, 196 pp.

[52] Özsoy, E. and Ünlüata, Ü. (1982). Ebb-tidal flow characteristics near inlets. Estuarine, Coastal and Shelf Science, Vol. 14, pp.251-263.

[53] Pedlosky, J. (1979). Geophysical fluid dynamics. Springer-Verlag, N.Y.

[54] Per Bruun (1978). Stability of tidal inlets. Elsevier, Amsterdam.

[55] Pierrehumbert, R.T. (1980). A family of steady translating vortex pairs with distributed vorticity. J. Fluid Mech., Vol. 99, pp. 129-144.

[56] Pullin, D.I. (1978). The large scale structure of unsteady self-similar rolled up vortex sheets. J. Fluid Mech., Vol. 88, pp.401-430.

[57] Pullin, D.I. (1979). Vortex ring formation at tube and orifice openings. Phys. Fluids, Vol. 22, pp. 401-403.

[58] Richards, J.M. (1963). Experiments on the motions of isolated cylindrical thermals through unstratified surroundings. Int. J. Air. Wat. Poll., Vol. 7, pp.17-34.

[59] Richards, J.M. (1965). Puff motions in unstratified surroundings. J. Fluid Mech., Vol. 21, pp.97-106.

[60] Rodi, W. (1982). Testing and calibration of turbulence models for transport and mixing. Proc. Conf. Applying Research to Hydraulic Practice, ASCE., pp.584-593.

[61] Roman, I. and Bühler, J. (1979). Starting plane jets. Proc. 18th. I.A.H.R., Cong., Vols. 4-5, pp.205-213.

[62] Rossow, V.J. (1976). Convective merging of vortex cores in lift generated wakes. A.I.A.A. Paper 76-415, San Diego, Calif., July 14-16.

[63] Rouse, H., Yih, C.S. and Humphreys, H.W. (1952). Gravitational convection from a boundary source. Tellus, Vol. 4, pp.201-210.

[64] Rouse, H. (1957). Diffusion in the lee of a two-dimensional jet. Proc. 9th Congr. Int. Mec. Appl. , Univ. Bruxelles.

[65] Saffman, P.G. (1972). The motion of a vortex pair in a stratified atmosphere. Studs. in App. Maths., Vol. L1, No. 2, pp.107-119.

[66] Saffman, P.G. (1979). The approach of a vortex pair to a plane surface in inviscid fluid. J. Fluid Mech., Vol. 92, pp.497-503.

[67] Savage, S.B. and Sobey, R.J. (1975). Horizontal momentum jets in rotating basins. J. Fluid Mech., Vol. 71, pp. 755-768.

[68] Schlichting, H. (1968). Boundary layer theory. 6th Ed. McGraw-Hill, New York.

[69] Schmidt,W. (1941). Turbulente Ausbreitung eines Stromes erhitzter Luft. Zeitschr. Angew. Math. und Mech., Vol.21, pp.265-278, 351-363.

[70] Schraub, F.A., Kline, S.J., Henry, J., Runstadler, P.W. and Littell, A. (1964). Use of hydrogen bubbles for quantitative determination of time-dependent velocity fields in low speed water flows. Themosciences Div., Dept.Mech.Eng., Standford Uni.,Rep. MD-10.

[71] Scorer, R.S. (1958). Natural Aerodynamics. Pergamon Press, London.

[72] Sheffield, J.S. (1977). Trajectories of an ideal vortex pair near an orifice. Phys. Fluids, Vol. 20, No. 4, pp.543-545.

[73] Sonu, C.J. and Wright, L.D. (1975). Mass transport and dispersion off a tidal inlet. Proc. 7th Offshore Tech. Conf., Vol. 3, pp.489-498.

[74] Spreiter, J.R. and Sacks, A.H. (1951). The rolling up of the trailing vortex sheet and its effect on the downwash behind wings. Aeronautical Sciences, Vol. 18, pp.21-32.

[75] Stolzenbach, K.D. and Harleman, D.R.F. (1971). An analytical and experimental investigation of surface discharges of heated water. Ralph M. Parsons Lab., M.I.T., Rep. No. 135, 207 pp.

[76] Swart, D.H. (1974). Offshore sediment transport and equilibrium beach profiles. Delft Hyd. Lab. Publ. No. 131.

[77] Takano, K. (1954). On the salinity and the velocity distributions off the mouth of a river. J. Oceanogr. Soc. Japan, Vol. 10, No. 3.

[78] Takano, K. (1955). A complementary note on the diffusion of the seaward river flow off the mouth. J. Oceanogr. Soc. Japan, Vol. 11, No. 4.

[79] Taylor, G.I. (1954). The use of a vertical air jet as a windscreen. Memoires sur la Mecanique des Fluids, Ministere de l'air, pp. 537-540.

[80] Taylor, R.B. and Dean, R.G. (1974). Exchange characteristics of tidal inlets. Proc. 14th Coastal Eng. Conf. ASCE, pp.2268-2289.

[81] Tollmein, W. (1926). Strahl verbreiterung. Zeitschr. Angew. Math. und Mech., pp.468-478.

[82] Tomassian, J.D. (1979). The motion of a vortex pair in a strati-
fied medium. Ph.D. Thesis, University of California.

[83] Tombach, I.H. (1971). Transport of a vortex wake in a stably
stratified atmosphere. Proc. Symp. Aircraft wake turbulence and
its detection, Ed. Olsen, Goldberg and Rogers. Plenum Press,
pp.41-55.

[84] Tombach, I.H. (1973). Observations of atmospheric effects on
vortex wake behaviour. A.I.A.A.J. Aircraft, Vol. 10, No. 11,
pp.641-647.

[85] Townsend, A.A. (1976). The structure of turbulent shear flow.
Cambridge University Press.

[86] Tsang, G. (1970$_1$). Laboratory study of two-dimensional starting
plumes. Atmospheric Environment, Vol. 4, pp.519-544.

[87] Tsang, G. (1970$_2$). Laboratory study of line thermals. Atmos-
pheric Environment, Vol. 5, pp.445-471.

[88] Tsang, G. and Wood, I.R. (1968). Motion of two-dimensional
starting plume. Proc. ASCE. Eng. Mech. Div., EM 6, pp.1547-1561.

[89] Turner, J.S. (1960). A comparison between buoyant vortex rings
and vortex pairs. J. Fluid Mech. Vol. 7, pp.419-432.

[90] Turner, J.S. (1962). The 'starting plume' in neutral surround-
ings. J. Fluid Mech., Vol. 13, pp.356-368.

[91] Turner, J.S. (1964_1). The flow into an expanding spherical vortex. J. Fluid Mech., Vol. 18, pp.195-208.

[92] Turner, J.S. (1964_2). The dynamics of spheriodal masses of buoyant fluid. J. Fluid Mech., Vol. 19, pp.481-496.

[93] Ünlüata, U. and Özsoy E. (1977). Tidal jet flows near inlets. Proc. Spec. Conf. Hydraulics in the Coastal Zone, ASCE, Texas, pp.90-98.

[94] Vallentine, H.R. (1967). Applied Hydrodynamics. 6th. Ed. Butterworths.

[95] Waldrop, W.R. and Farmer, R.C. (1974). Three-dimensional computation of buoyant plumes. J. Geophys. Res., Vol. 79, No. 9, pp.1269-1276.

[96] Widnall, S.E., Bliss, D. and Zalay, A. (1971). Theoretical and experimental study of the stability of a vortex pair. Proc. Symp. Aircraft wake turbulence and its detection, Ed. Olsen, Goldberg and Rogers, Plenum Press. pp. 305-337.

[97] Wilkinson, D.L. (1978). Periodic flows from tidal inlets. Proc. 16th Coastal Eng. Conf., Hamburg, pp. 1336-1346.

[98] Wilkinson, D.L., Tomlinson, R.B., Willoughby, M.A., and Foster, D.N. (1979). Gold coast sewerage outfall study. Vol. I: Characteristics of the tidal jet at the Nerang river entrance. Tech. Rep. No. 79/5, Water Res. Lab., Univ. of N.S.W., 13 pp.

[99] Wilkinson, D.L. and Willoughby, M.A. (1981). Velocity measurement with hydrogen bubbles - the wake correction. J. Hyd. Res., Vol. 19, No. 2 pp. 141-153.

[100] Winant, C.D. and Browand, F.K. (1974). Vortex pairing: the mechanism of turbulent mixing-layer growth at moderate Reynolds number. J. Fluid Mech., Vol. 63, pp.237-255.

[101] Wolanski, E.J. (1983). Personal Communication.

[102] Wolanski, E.J. and Banner, M.L. (1978). Buoyant surface jets in tidal longshore current. Proc. ASCE. J. Hyd. Div., HY 11, pp.1505-1519.

[103] Wood, I.R. (1965$_1$). The two-dimensional starting plume. 2nd Aust. Conf. on Hyd. and Fluid Mech., pp.C31-C44.

[104] Wood, I.R. (1965$_2$). Studies in unsteady self preserving turbulent flows. WRL Report No. 81, Wat. Res. Lab., Univ. of N.S.W.

[105] Woodward, B. (1959). The motion in and around isolated thermals. Quart. J. Roy. Met. Soc., Vol. 85, pp.144-151.

[106] Wright, L.D. and Coleman, J.M. (1974). Mississippi river mouth processes: effluent dynamics and morphologic development. J. Geology, Vol. 82, pp.751-778.

[107] Wu, J. (1977). Turbulent vortex pairs in neutral surroundings. Phys. Fluids, Vol. 20, No. 12, pp.1967-1974.

[108] Wygnanski, I and Newman, B.G. (1968). The reattachment of an inclined two-dimensional jet to a flat surface in streaming flow. Trans. Canadian Aero. Space Inst. Vol. 1, No. 1, pp.3-8.

[109] Zimmerman, J.T.F. (1978). Topographic generation of residual circulation by oscillatory (tidal) currents). Geophys. Astrophys. Fluid Dyn., Vol. 11, pp.35-47.

APPENDIX 1 - NUMERICAL SOLUTION TO THE UNSTEADY JET EQUATIONS

1. Introduction

In this appendix the development of the difference form of the Equations of Motion (3.34) and (3.35) will be outlined with particular reference to the physical constants which appear in the equations.

A survey of the literature, although not extensive, showed that previous work on unsteady jet solutions has dealt mainly with the following topics. High frequency periodic fluctuations in source mass flux have been considered in studies of the growth of coherent structures in the jet shear layer at the onset of instability (Davies and Hardin, 1973 and Ikeda, 1977). Cantwell (1981) has examined the transition to turbulence of low Reynolds Number momentum jets with an increasing source momentum flux. Turbulence models have been used by Lai and Simmons (1980) in studies of entrainment enhancement in the excitation of turbulent jets by acoustic, mechanical and fluidic means. Kent (1973) examined the behaviour of an unsteady laminar round jet using an integral method. The flow conditions at an initial streamwise location were varied with time from one steady state to a final steady state. A time dependent integral method was also used by Banner & Wolanski (1978) studying the behaviour of a steady buoyant jet subject to a time varying cross-flow.

In the present case the integral method has been applied to the Navier Stokes and Continuity equations to derive time-dependent equations of motion for shallow water flows. These can be reduced to the standard steady two-dimensional jet equations by simply dropping the

time derivatives.

These equations will now be set in finite difference form and the results of the numerical computations will be presented.

2. Derivation of Unsteady Jet Finite Difference Equations

The equations of continuity and momentum of unsteady one dimensional flow are given by Equations (3.26) and (3.27) as:

$$h \frac{\partial b}{\partial t} + \frac{\partial}{\partial x} (hb F_1 u_c) = 2Ehu_c \qquad (A1.1)$$

$$h \frac{\partial}{\partial t} (b F_1 u_c) + \frac{\partial}{\partial x} (hb F_2 u_c^2) = -\frac{f}{8} b F_2 u_c^2 \qquad (A1.2)$$

where F_1 and F_2 are constants of integration of the velocity profile given by:

$$F_1 = \int_0^1 \frac{u}{u_c} \, d\xi \qquad (A1.3)$$

$$F_2 = \int_0^1 \left(\frac{u}{u_c}\right)^2 d\xi \qquad (A1.4)$$

where
$$\xi = \frac{y}{b/2} \qquad (A1.5)$$

Expressed in dimensionless terms using the parameters defined in Equations (3.29) and (3.33) the equations of motion can be written as:

$$\frac{\partial}{\partial \tau}(HB_J) + F_1 \frac{\partial}{\partial X}(HB_J U_J) = 2E(\frac{\ell}{b_o})HU_J \qquad (A1.6)$$

$$\frac{\partial}{\partial \tau}(HB_J U_J) + \frac{F_2}{F_1} \frac{\partial}{\partial X}(HB_J U_J^2) = -(\frac{f \ell}{8h_o} \frac{F_2}{F_1}) B_J U_J^2 \qquad (A1.7)$$

The depth term has been included in the time derivatives for reasons of convenience which will be explained later.

Multiplying Equation (A1.6) by U_J and combining with an expanded version of Equation (A1.7) gives:

$$HB_J \frac{\partial U_J}{\partial \tau} + [\frac{F_2}{F_1} U_J \frac{\partial(HB_J U_J)}{\partial X} - F_1 U_J \frac{\partial(HB_J U_J)}{\partial X}] + (\frac{F_2}{F_1}) HB_J U_J \frac{\partial U_J}{\partial X}$$

$$= -(\frac{f \ell}{8h_o} \frac{F_2}{F_1}) B_J U_J^2 - 2E (\frac{\ell}{b_o}) HU_J^2 \qquad (A1.8)$$

Now, this equation can be simplified if:

$$F_1^2 \sim F_2 \qquad (A1.9)$$

Condition (A1.9) is not generally satisfied with the similarity forms of the lateral velocity distribution usually applied to jets. A number of different forms of the similarity velocity profile function have been proposed, such as a Gaussian distribution, the so-called Top-Hat distribution which asssumes a uniform velocity across the jet section, or that due to Schlichting (1968):

$$\frac{u}{u_c} = (1-(2\xi)^{1.5})^2 \qquad (A1.10)$$

The condition, $F_1^2 \sim F_2$, is met for a Top-Hat profile ($F_1 = F_2 = 1$). For all other jet profiles the condition is only approximately satisfied. For example, Schlichting's profile gives $F_1^2 = 0.20$ and $F_2 = 0.316$.

Assuming that (A1.9) is approximately satisfied it is reasonable to reduce Equation (A1.8) to:

$$\frac{\partial U_J}{\partial \tau} - (\frac{F_2}{F_1}U_J)\frac{\partial U_J}{\partial X} = -(\frac{f_1}{H} + \frac{E_1}{B_J})U_J^2 \qquad (A1.11)$$

where $\qquad f_1 = \frac{f\ell}{8h_o}\frac{F_2}{F_1} \qquad$ and $\qquad E_1 = 2E\frac{\ell}{b_o} \qquad (A1.12)$

Keller and Thomee (1962) have presented a finite difference form of this quasi-linear hyperbolic equation, the exact formulation of which depends on the magnitude of $(\frac{F_2}{F_1}U_J)$. As will be shown in the next section a limit can be placed on the numerical value of this and hence an appropriate difference form is:

$$U_J(i,j+1) - U_J(i,j) - \frac{\Delta\tau}{\Delta X}(-\frac{F_2}{F_1}U_J(i,j))\,[U_J(i,j) - U_J(i-1,j)]$$

$$= -\Delta\tau[\frac{f_1}{H(i)} + \frac{E_1 H(i)}{A_J(i,j)}]\,U_J^2(i,j) \qquad (A1.13)$$

where a new variable $A_J(i,j) = H(i)\,B_J(i,j)$ has been introduced for convenience. In a similar way the Continuity Equation (A1.6) may be expressed as:

$$A_J(i,j+1) - A_J(i,j) - \frac{\Delta\tau}{\Delta X}(F_1 U_J(i,j+1))[A_J(i,j) - A_J(i-1,j)]$$

$$= \Delta\tau[E_1 H(i) U_J(i,j+1)] \qquad (A1.14)$$

Subscripts i,j represent the spatial and time steps respectively. The boundary conditions given by Equations (3.36) and (3.37) are expressed in difference form as:

$$U_J(1,j) = (\frac{\ell}{b_o})^{\frac{1}{2}} \sin(2\pi(j-1)\Delta\iota) \qquad (A1.15)$$

$$B_J(1,j) = 1.0 \qquad (A1.16)$$

The initial steady state jet solution is obtained by dropping the time derivatives from Equations (A1.6) and (A1.7) to give:

$$\frac{\partial Q_J}{\partial X} = (\frac{E_1}{F_1})\frac{M_J H}{Q_J} \qquad (A1.17)$$

$$\frac{\partial M_J}{\partial X} = -f_1\frac{M_J}{H} \qquad (A1.18)$$

where $Q_J = HB_J U_J$ and $M_J = HB_J U_J^2$

These equations are solved first for M_J and then Q_J using a 4th order Runge-Kutta method (Chow, 1979) and then the values of B_J and U_J are determined by the appropriate divisions.

3. Numerical Stability

Keller and Thomee (1962) define the criterion for unconditional stability of the numerical scheme as:

$$-1 < \frac{\Delta\tau}{\Delta X}\left(-\frac{F_2}{F_1} U_J(i,j)\right) < 0 \qquad (A1.19)$$

For computational economy the larger the value of $\frac{\Delta\tau}{\Delta X}$ the better. This is, however, limited by the maximum value attained by U_J, which can be taken to be the peak dimensionless source velocity, $U_0 = (\frac{\ell}{b_0})^{1/2}$. The limit of stability can then be expressed as:

$$\frac{\Delta\tau}{\Delta X} < \frac{F_1}{F_2}\left(\frac{\ell}{b_0}\right)^{-1/2} \qquad (A1.20)$$

For the chosen $\Delta X = 0.005$ and using a Top-Hat velocity distribution, then:

$$\frac{\Delta\tau}{\Delta X} \sim 0.25 \qquad \text{for } \frac{\ell}{b_0} = 15.1 \qquad (A1.21)$$

The numerical scheme proved to be stable with a time step, $\Delta\tau = 0.00125$. At the extreme of the range of inlet parameters examined, $\ell/b_0 = 118.4$, the required $\frac{\Delta\tau}{\Delta X} < 0.183$. For convenience, $\frac{\Delta\tau}{\Delta X} = 0.15$ was chosen.

4. Numerical Procedure

The initial conditions for the computations are taken as a fully established steady jet with exit velocity defined by Equation (3.36) at time $\tau = 0.01$. This is arbitrarily chosen. The initial source velocity is varied by finite timewise steps according to Equation (A1.15) until $\tau = 0.49$. The source conditions are then held constant. Performing the computations in this manner avoided numerical difficulties which result when the initial conditions approach zero in value. The numerical computations were asymptotic to some final state for times greater than $\tau = 0.49$. This procedure was followed to enable the behaviour of the jet variables to be estimated during the period of flow reversal at locations far removed from the origin. In the near-field of the inlet the results obtained in this manner are meaningless due to the flow reversal. Experimental observations show that the jet velocity will behave in a similar manner to that shown in Section 3.3, but that the nominal jet width begins to contract during the flow reversal.

The exact choice of initial starting conditions is not critical as can be shown by considering the physical development of the flow. The vortex pair cap which develops from rest initially remains near the boundary under the influence of the image vortices. During this time a jet tail is non-existent. As the pair circulation increases, it moves away from the boundary allowing the jet tail to develop. This initial spin up phase dominates the flow in most cases up until $\tau \simeq 0.05$.

The spatial extent of the computations was set to $X = 1$.

In the development of this solution, the potential core of the jet (zone of flow establishment) has been ignored. The steady solutions presented by Özsoy (1977), Mehta and Zeh (1980) and others have shown that this region is short for real flows (of the order 5 b_o). Mehta and Zeh have shown from field observations that theroretical models will exaggerate the length further, as in reality the lateral velocity distribution in the inlet is not uniform. Thus, the scheme adopted here is a reasonable one for all but an ideal frictionless jet.

5. Determination of Coefficients E and f

A search of the literature has not revealed any previous evaluation of these coefficients for unsteady jet flows. It is assumed for this analysis that appropriate steady state values can be used. The literature provides an range of values of the entrainment coefficient, E, for steady plane turbulent jets.

Kotsovinos (1976) listed previously determined spreading rates, K_1, defined as:

$$K_1 = \frac{2E}{F_1} \tag{A1.22}$$

The average of the spreading rates quoted is $K_1 = 0.103$ which corresponds to an entrainment coefficient which depends on the form of the velocity profile. As entrainment coefficients vary considerably between experiments and are determined by integration of the experimentally derived velocity profiles, the use of the values given by Kotsovinos for K_1 would provide the least inaccurate measure of the entrainment coefficient as there is little scatter in the K_1 values. The

value of E most commonly quoted is 0.056.

There is little reported data on the entrainment characteristics of unsteady jets. It has been shown by Lai and Simmons (1980) and others that the entrainment rate for a jet with a rapidly pulsing mass flow differs from that of a steady jet. In general, the rate of entrainment increases as the pulse frequency increases. In previous studies of time varying buoyancy sources (Delichatsios, 1975 and Killworth and Turner, 1982) the appropriate steady plume entrainment coefficients were used. In the present study, it is assumed that the time scale of the periodic variation in the mass flux is sufficiently long for the entrainment coefficient to be taken as constant.

Field data obtained by Mehta and Zeh (1980) for a tidal jet gave E = 0.21. This value is much higher than that normally associated with a steady plane jet. It is comparable with the estimates obtained from the surface particle trace data in the present study. By measuring directly the lateral trace velocity in the vicinity of the jet boundary and estimating the centreline velocity, a range of E = 0.05 - 0.25 is obtained. The higher values of E, as well as that of Mehta and Zeh, are obtained in the region of the jet near the trailing edge of the vortex pair cap. In this region the entrainment process is enhanced by the induced flow around the cap. Experiments with large ℓ/b_o values allow entrainment coefficients to be determined from trace measurements distant from the cap and the inlet. Values of E in the range 0.04 - 0.07 have been estimated for such an experiment. Thus a value of E = 0.05 was adopted in the analysis.

The Darcy-Weisbach friction factor, f, is also assumed constant by most investigators. Mehta and Zeh (1980) have adopted a wholly rough turbulent relationship for f given by:

$$f = \frac{0.25}{[1.1171 + \log(h(x)/k_s)]^2} \qquad (A1.23)$$

where k_s is an equivalent grain roughness.

In the experiments described here the Reynolds Number of the flow varied considerably. Defined in terms of the flow variables the entrance Reynolds Number, Re_o, is given by:

$$Re_o = (\frac{\ell}{b_o})^{1/2} \frac{\ell}{T} \frac{4h(x)}{\nu} \sin(2\pi\tau) \qquad (A1.24)$$

For example, a flow with $\frac{\ell}{b_o} = 15.1$, $\frac{\ell}{T} = 0.0151$ ms^{-1} and h(x) = constant = 0.025 m, the range of Re_o is 0 - 5,900. The roughness value, k_s, for the asbestos sheeting used as the model bed is taken as 0.015 mm, thus the relative roughness, $k_s/h(x)$ for the above example is 0.0006. The range of $k_s/h(x)$ for the experiments conducted is 0.0012 - 0.0001. Over the range of Reynolds Numbers used in the experiments the bed is hydraulically smooth and the friction factor is given by the Blaisus equation:

$$f = \frac{0.316}{Re^{0.25}} \qquad (A1.25)$$

This yields a range of values from f = 0.036 at τ = 0.25 to f = 0.072 at τ = 0.01.

In the numerical computations two approaches were tried:- setting f = constant = 0.05 and defining f by Equation (A1.25) with Re redefined as:

$$Re(x,t) \; = \; \frac{4}{\nu} \; h(x) \; u(x,t) \qquad\qquad (A1.26)$$

or,in terms of the dimensionless variables:

$$Re(X,\tau) \; = \; \frac{4}{\nu} \; (\frac{\ell}{b_o})^{1/2} \; \frac{\ell}{T} \; h_o HU_J \qquad\qquad (A1.27)$$

6. Numerical Results

The numerical solution was tested for sensitivity to changes in the various constants and parameters. The general behaviour of the flow variables has been discussed in Section 3.3. Figures 3.3 - 3.6 represent a typical Eulerian description of the flow. However, of more particular interest is the variation in the flow variables at the join between the jet `tail´ and the vortex pair cap. This location can not be determined directly. Thus, in order to gain an insight into the influence of the various parameters on the solution, an arbitrary lagrangian time history for a fluid element was chosen. The shock location discussed in Section 3.3 provides an ideal computational marker for such a specification. As shown in that section, the shock represents a computational limit for which solutions can be found for an unsteady jet and hence is also a computational limit to the location of the cap trailing edge at any given time. The real cap location would be at a location closer to origin during the phase of the flow when the cap is coupled to the jet tail. For subsequent time it is taken that the cap is decoupled from the jet and hence the jet is no

longer a contributor of mass and momentum to the cap. Using this shock location as a computational marker, the behaviour of the jet variables will now be considered for a range of boundary conditions.
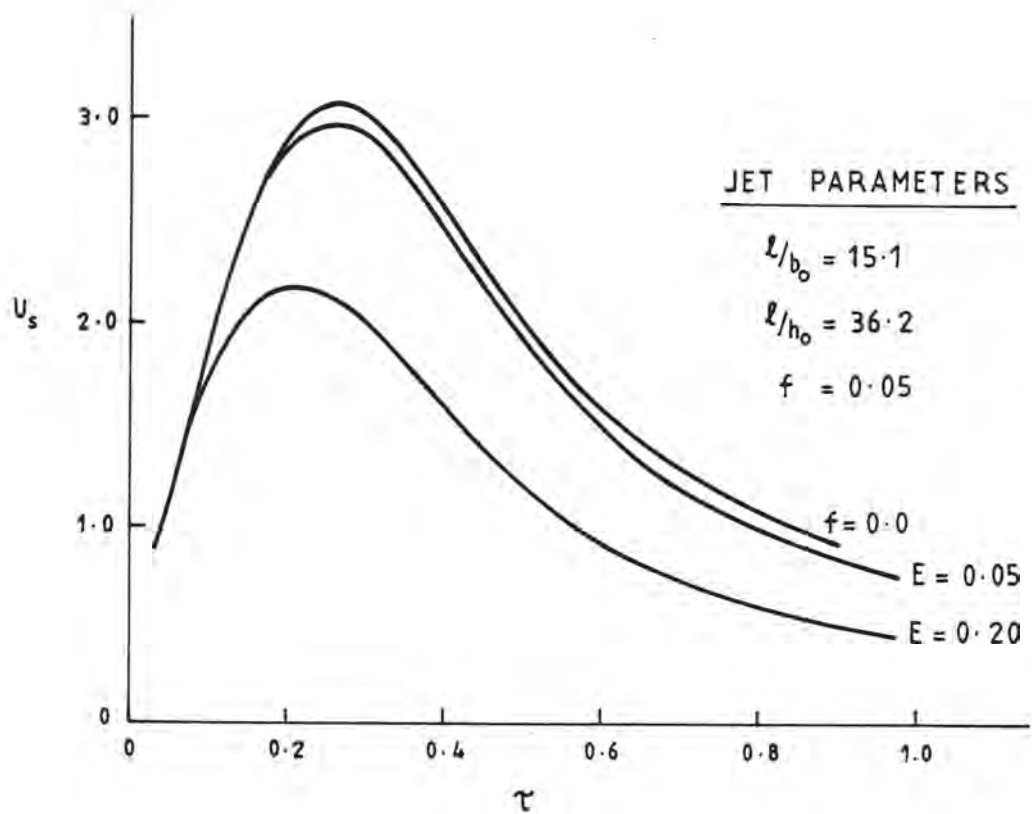
6.1 Entrainment Coefficient

As discussed earlier, a range of entrainment coefficients, E, from 0.05 to 0.25 have been reported for jets. Figure A1.1 shows the effect on shock speed of a change in entrainment coefficient from 0.05 to 0.20. The shock initially travels at the same speed but then slows markedly for the higher entrainment coefficient. The velocity in the jet behind the shock would also be expected to be slower for the higher entrainment value, as shown in Figure A1.2. Plotted on Figure A1.1 is the location of the vortex cap leading edge and an estimate of the location of the trailing edge for Experiment No. 43 which had the same inlet parameters. Matching this with the numerical solution for the shock location shows that the shock is contained within the cap until τ = 0.6 for E = 0.20 and τ = 0.8 for E = 0.05. This supports the hypothesis made in Chapter 3 that the join between the cap and the jet will be closer to the origin than the shock location. Beyond this time the cap becomes decoupled from the jet. At τ = 0.8 the dimensionless jet velocity is approximately 1.0 while the cap trailing edge velocity estimated from the experimental data is approximately 1.0. This would suggest that the lower value of the entrainment coefficient should be used.

Figure A1.3 shows the jet width, B_s, variation near the shock. Up to a location reached by τ = 0.8 (X_s = 0.52, Figure A1.3), the jet width can be said to increase linearly with the distance travelled by the shock.
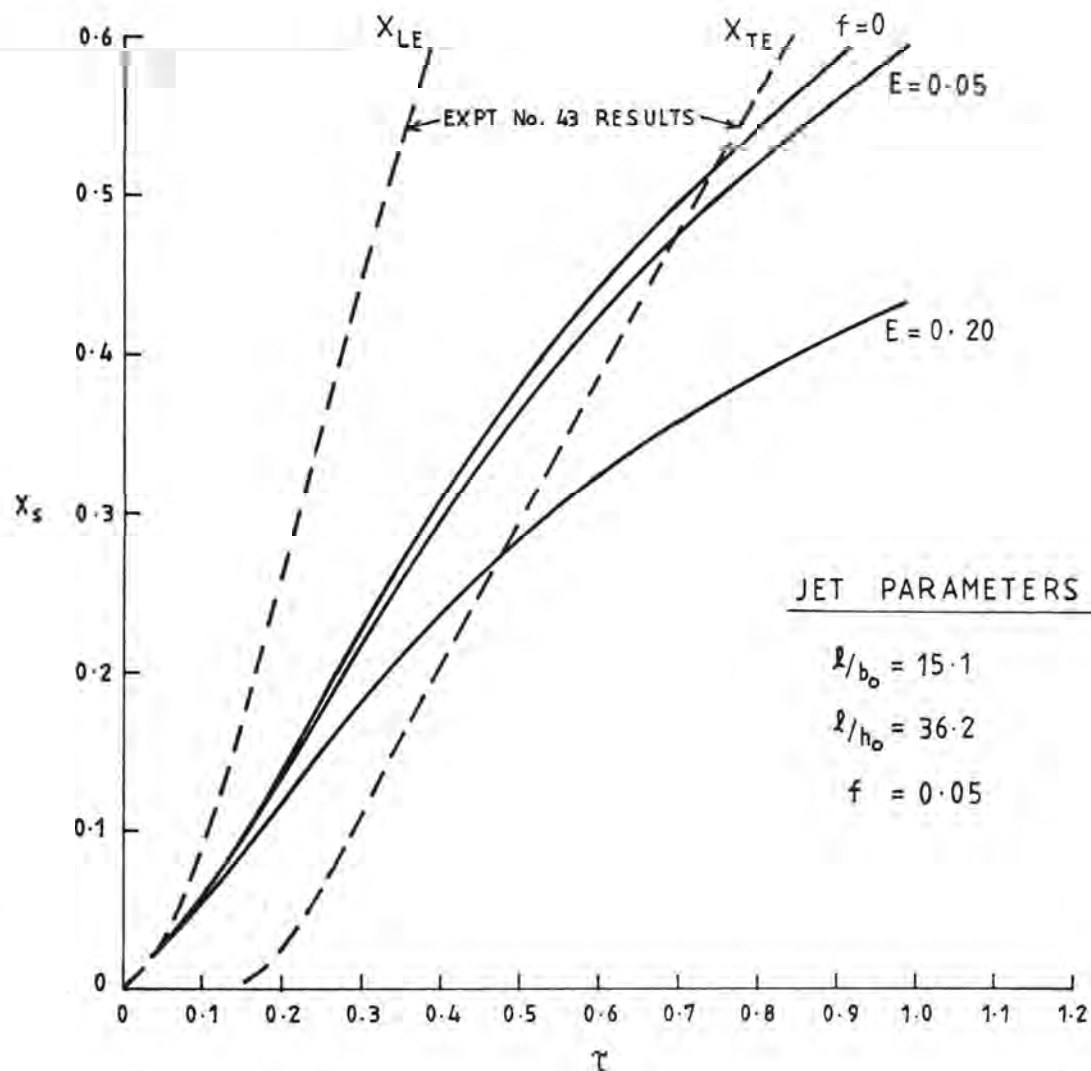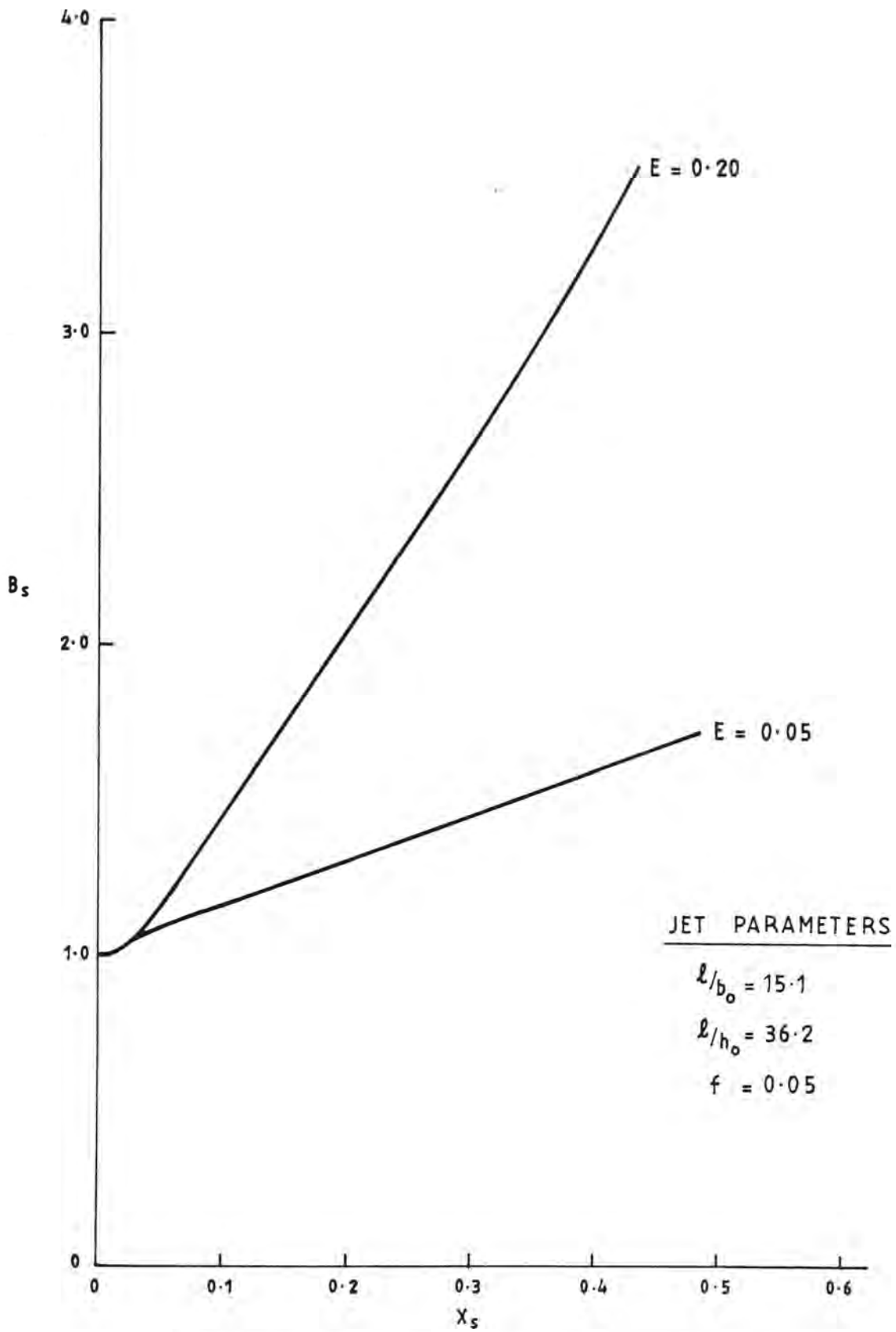
EFFECT OF ENTRAINMENT COEFFICIENT

ON SHOCK ADVANCE

FIGURE A1·1

EFFECT OF ENTRAINMENT COEFFICIENT
ON VELOCITY OF JET
NEAR THE SHOCK

FIGURE A1·2

EFFECT OF ENTRAINMENT COEFFICIENT
ON JET WIDTH AT SHOCK

FIGURE A1·3

6.2 Inlet Entrance Width Parameter, ℓ/b_o

This parameter is important as it not only controls the jet behaviour but also defines the initial spin up characteristics of the vortex pair and has consequently been investigated separately from the entrainment coefficient, E. The shock speed and velocity of the jet near the shock have already been presented in Figures 3.7 and 3.8. These indicate that the shock speed increases as the inlet width ratio increases. The jet velocity initially is less for small ℓ/b_o at any given time. After the peak jet velocity is reached the reverse is true - the jet velocity is greater for small ℓ/b_o. The peak velocity reached at around $\tau = 0.25$, is surprisingly constant, being $U_s \simeq 3.0$. The jet width variation near the shock location is plotted in Figure A1.4 for a frictionless jet. The increase in width with distance from the origin is not linear, a feature which is shown more clearly for the higher entrainment rates as seen in Figure A1.3.

6.3 Depth of Flow

The importance of the flow depth h_o for a constant depth case is gauged by the relative magnitude of the bottom frictional resistance compared to the momentum of the flow. In Chapter 2 this was expressed as being proportional to $f\dfrac{\ell}{h_o}$. For large values of this parameter the bottom friction will markedly affect the jet behaviour, causing the velocity to decay more rapidly. The jet characteristics are shown in Figures A1.5 - A1.7 for a range of $f\dfrac{\ell}{h_o} = 0.9 - 5.9$. The further the jet advances the greater the retarding impulse applied to the flow as shown in Figure A1.5. It can be taken from the results that the parameter $f\dfrac{\ell}{h_o}$ only becomes significant when its value is large, say, $f\dfrac{\ell}{h_o} > 50$. Thus, in the experiments reported in this thesis, the jet flow
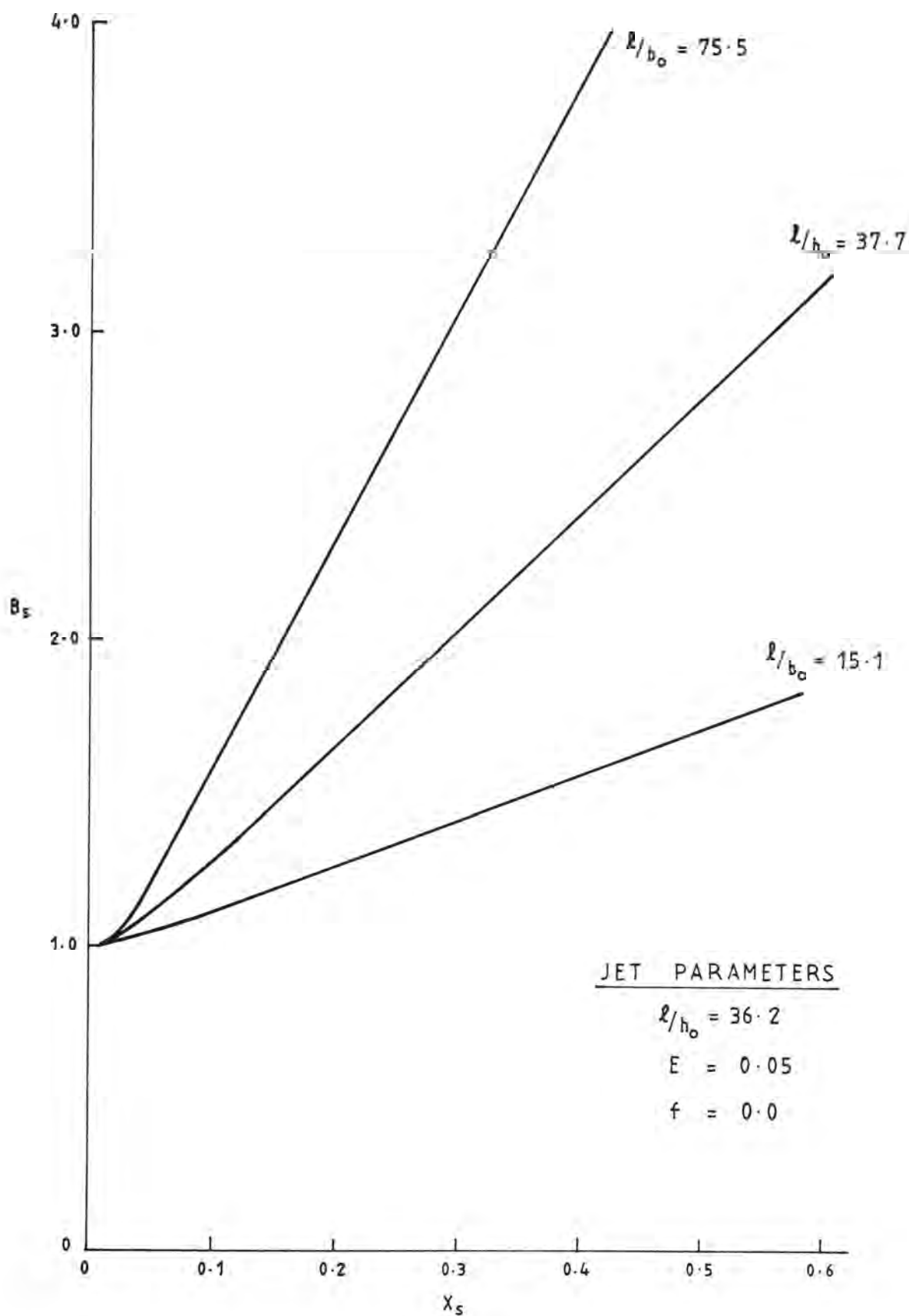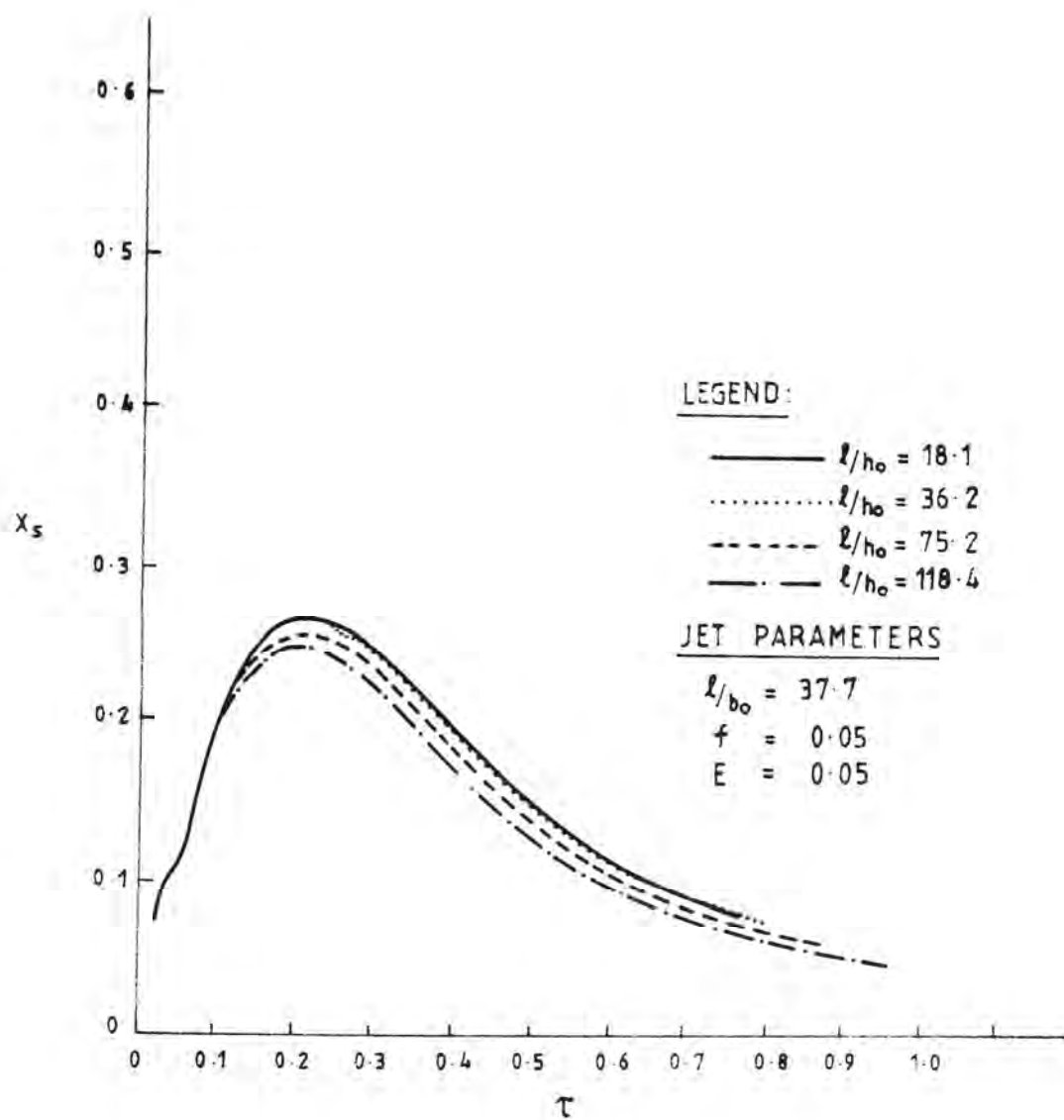
JET WIDTH AT SHOCK FOR VARIOUS
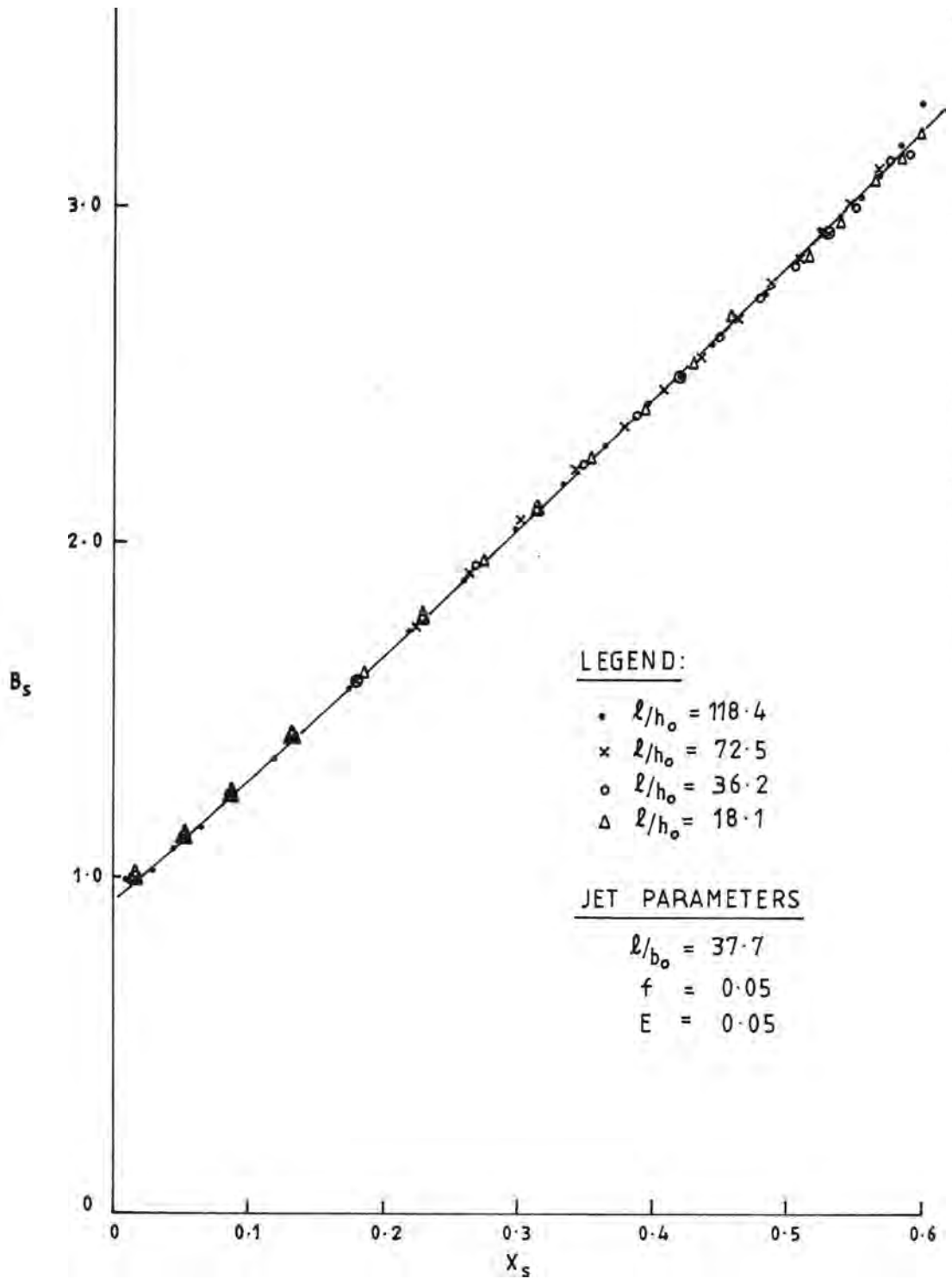
INLET WIDTH PARAMETERS

FIGURE A1·4
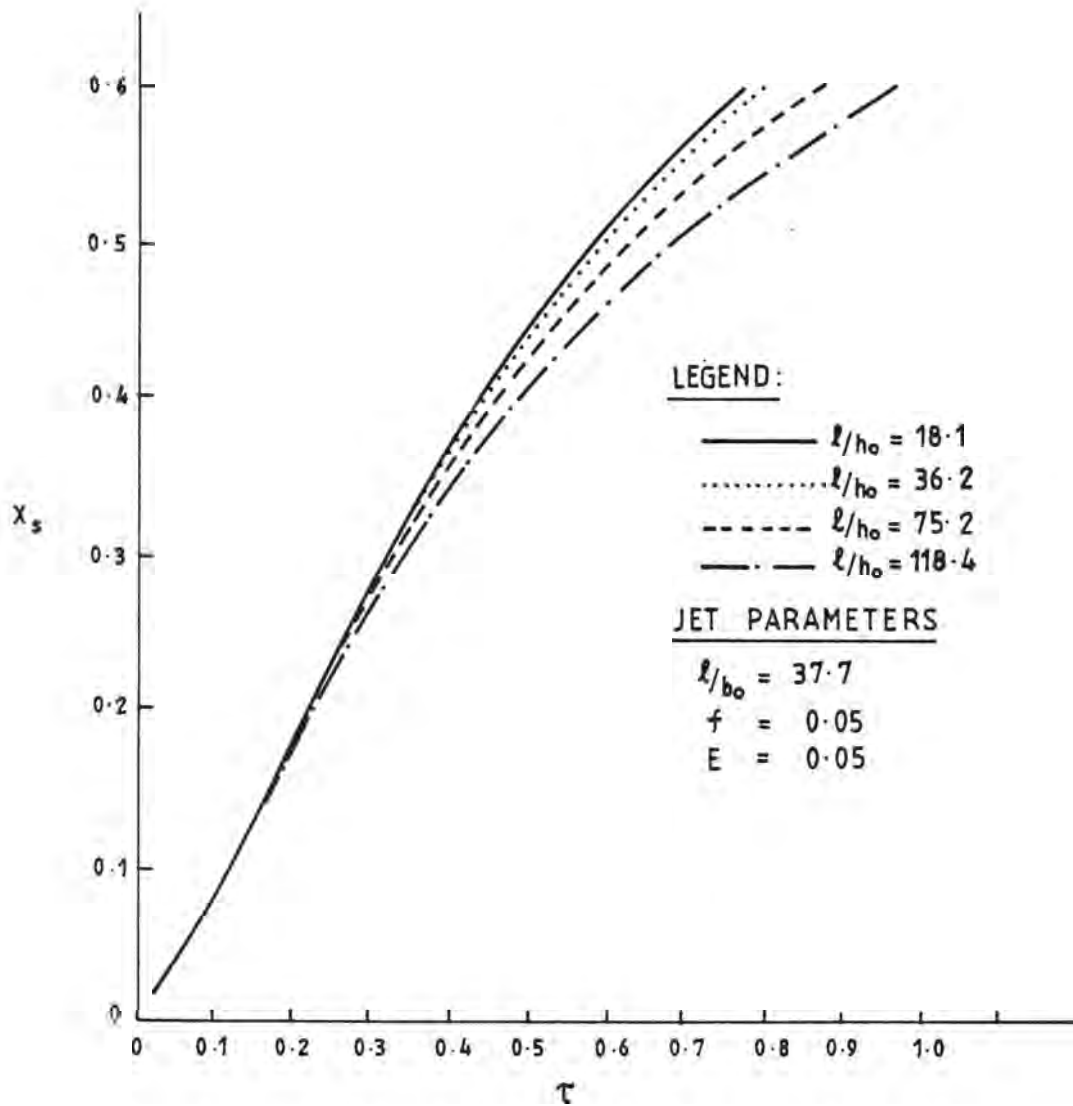
JET SHOCK ADVANCE FOR DIFFERENT VALUES
OF THE INLET DEPTH PARAMETER

FIGURE A1·5

JET VELOCITY AT SHOCK FOR DIFFERENT VALUES
OF THE INLET DEPTH PARAMETER

FIGURE A1·6

JET WIDTH AT SHOCK FOR VARIOUS
VALUES OF INLET DEPTH PARAMETER

FIGURE A1·7

will be only marginally dependent on the depth. (The behaviour of the vortex pair cap will also be depth dependent. This has been discussed in Chapters 3 and 7). In real flow cases, such as tidal inlet flows, the value of this parameter is much larger, resulting in a rapid decay of the jet velocity (see Chapter 10).

6.4 Bed Slope

Figures Al. 8 to Al. 10 show the effect of a linear variation in water depth defined by the slope parameter α_1. There is little variation in the shock characteristics for the shallower slopes, except in the jet width B_S. The width at the shock demonstrates similar features to the steady case in that for increasing bed slope the growth of the jet is reduced. Close to the origin the jet actually contracts for a short time for all slopes, before establishing a nearly linear growth. This contraction was evident in the field data obtained by Mehta and Zeh (1980).
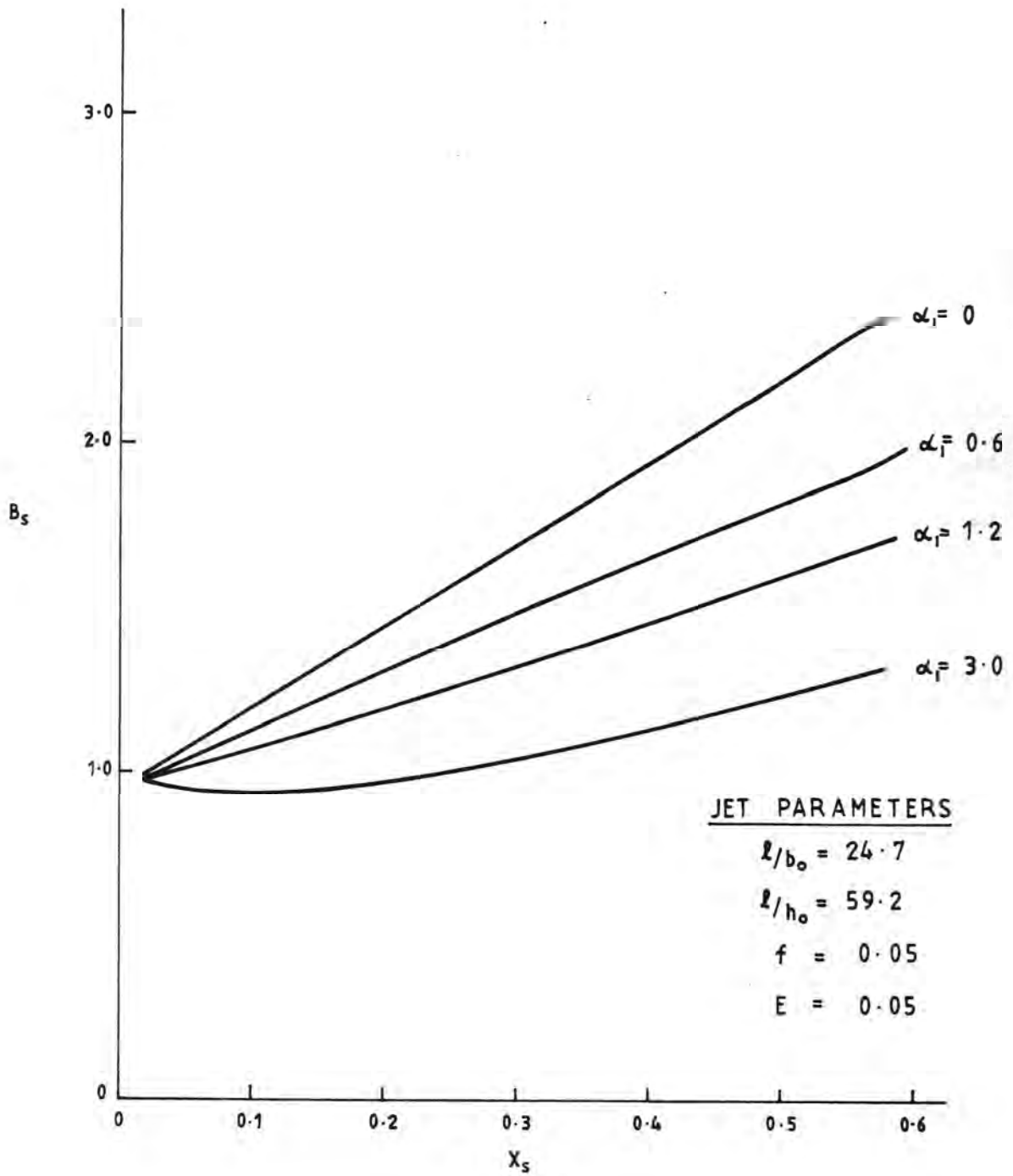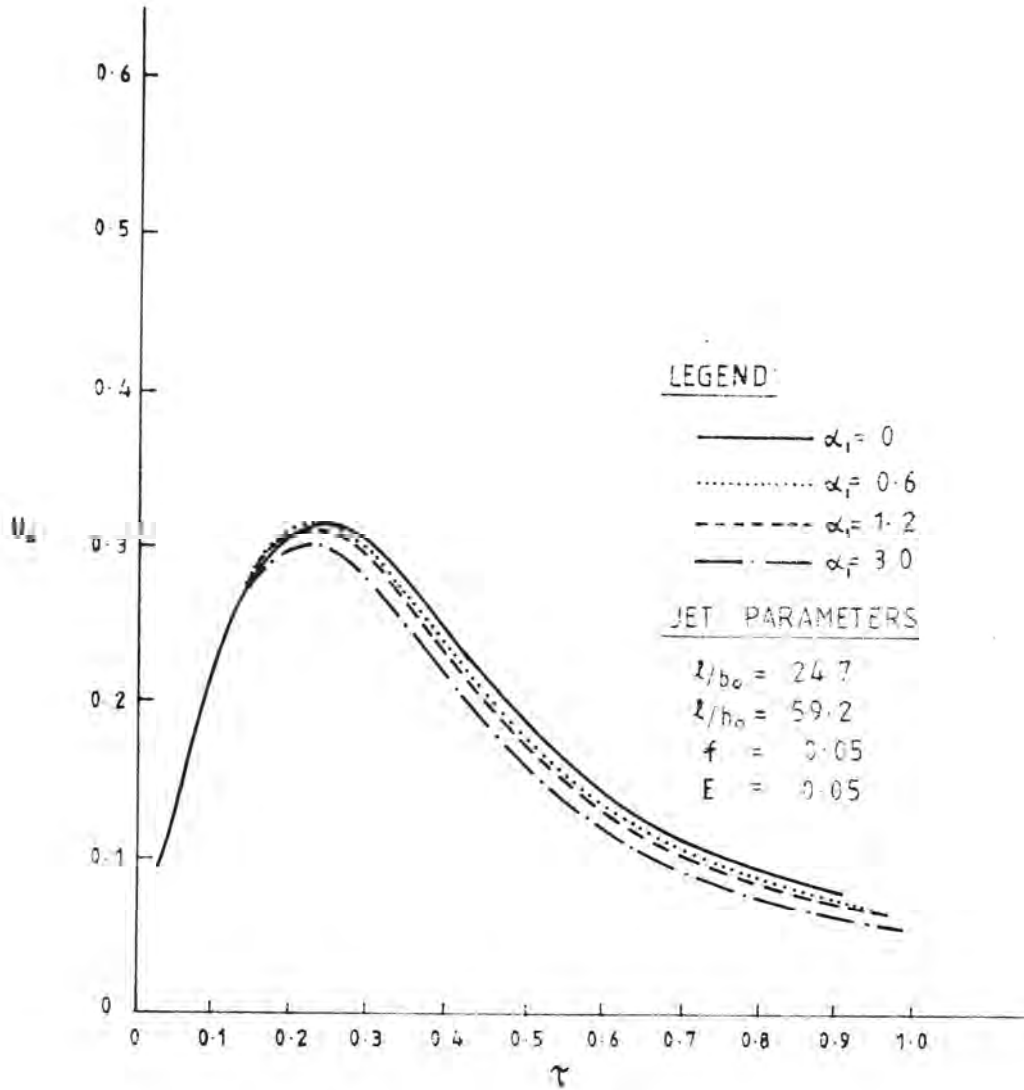
JET WIDTH AT SHOCK FOR DIFFERENT

BED SLOPES

FIGURE A1·8
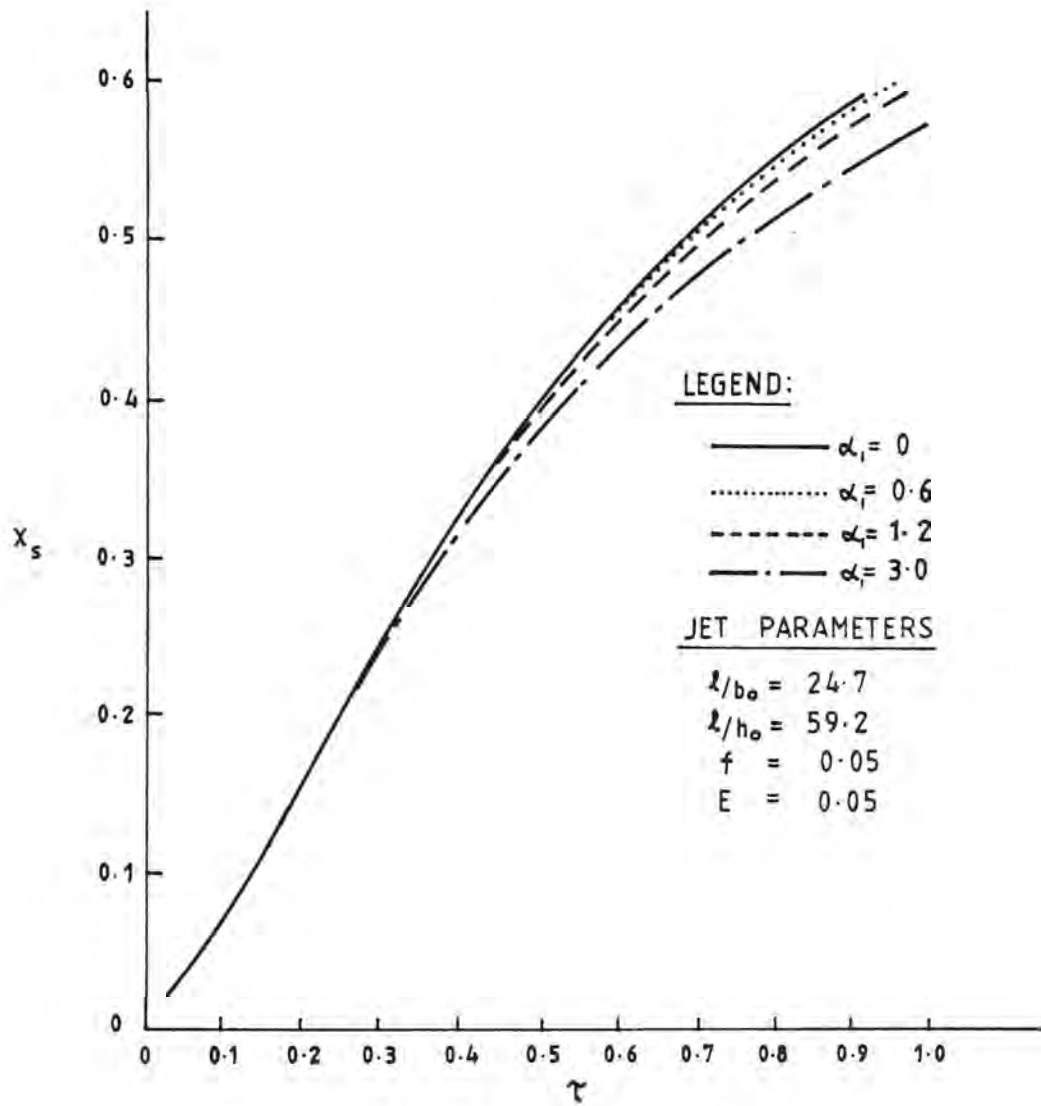
JET SHOCK ADVANCE FOR
DIFFERENT BED SLOPES

FIGURE A1·9

JET VELOCITY AT SHOCK FOR
DIFFERENT BED SLOPES

FIGURE A1·10

APPENDIX 2   INITIAL ROLL UP OF A VORTEX PAIR

In this appendix, the initial roll up of vorticity at the commencement of the ebb discharge will be considered. It is proposed to consider a time similarity formulation of the gross features of the roll up process. From this an appropriate initial state can be obtained for the vortex pair cap and for the vortex under the influence of a cross-flow.

This approach is supported in the general case of a periodic jet by examining the experimental behaviour at early times. As the slug of fluid emerges from the inlet channel, a pair of vortices is seen to spin up close to the boundary. As the velocity of the discharge increases, the circulation of the vortices increases and they move away from the boundary. In a flow subject to cross-flow, the downstream vortex is assumed to spin up in the vicinity of the inlet during a time, t_f, but remains trapped near the bounary by the cross-flow.

Pullin (1978) gives the similarity theory relationships for circulation, K, and core radius, R, of a two-dimensional vortex shed in time, t_f, at an edge of angle $\pi/2$, with a velocity varying as a function of time to the power, p, such that:

$$u_o(t) = u_1 t^p \qquad\qquad (A2.1)$$

The relationships given by Pullin (1978) are then simplified to give the circulation varying as:

$$K = 1.80 \ [3-\tfrac{4}{3}(1+p)^{-1}]^{-3/4} \ [\tfrac{\beta_1^3}{1+p}]^{1/2} \ t_f^{[3(1+p)/2]-1} \qquad (A2.2)$$

and the radius as:

$$R = 0.324\beta_2 [\frac{\beta_1}{1+p}]^{3/4} t_f^{3(1+p)/4} \qquad \text{(A2.3)}$$

where β_1 and β_2 are constants dependent on the source geometry and the form of the velocity function.

For the present case of a periodic sinusoidally varying flow at the entrance, the velocity during the early stages of the discharge can be approximated closely by a linear function of time:

$$u_o(t) = \frac{6\ell}{T^2}(\frac{\ell}{b_o})^{1/2}t$$

$$= u_1 t \qquad \text{(A2.4)}$$

which is equivalent to Equation (A2.1) for $p = 1$.

Equation (A2.2) then simplifies to:

$$K = 1.15\ \beta_1^{3/2} t_f^2 \qquad \text{(A2.5)}$$

β_1 is a constant obtained by considering the complex potential of the flow near the edge which is initially taken to be radial and is given by:

$$\Phi = \phi + i\psi = -i\beta_1 tr^{2/3} e^{i2\theta/3} \qquad \text{(A2.6)}$$

The value of β_1 can be obtained by matching to the flow far from the edge. Using numerical results obtained for the flow reversal

analysis (see Chapter 8), an approximate value of β_1 has been found.

$$\beta_1 = 5.5(\frac{b_o}{\ell})u_1 b_o^{1/3} \tag{A2.7}$$

It is important to note that the numerical constants given above are somewhat arbitrary as the numerical solutions of Pullin have not been experimentally verified in this case. However, the dependence on the characteristic scales, ℓ and b_o, is of particular relevance. Thus the circulation shed at the edge will be:

$$K = 218\ell^{3/4} b_o^{5/4} T^{-3} t_f^2 \tag{A2.8}$$

The dimensionless circulation K' is given by:

$$K' = \frac{K}{K^*} = 218(\frac{\ell}{b_o})^{-1/4} \tau_f \tag{A2.9}$$

This relationship has been used in the numerical solutions (Chapter 3) to obtain an initial circulation, and hence, velocity and separation for the vortex pair cap at $\tau = 0.01$.

Maxworthy (1977) has defined a slug circulation at the source as:

$$K_o = \frac{1}{2}\int_0^{t_f} u_o^2(t)\,dt$$

$$= \frac{6\ell^3}{T^4 b_o} t_f^3 \tag{A2.10}$$

or, $$K'_o = 6(\frac{\ell}{b_o})^2 \tau_f^3 \tag{A2.11}$$

Combining Equations (A2.9) and (A2.11) then:

$$\frac{K'}{K'_o} = 36.3(\frac{\ell}{b_o})^{-9/4}\tau_f^{-1} \tag{A2.12}$$

An estimate of the upper limit of the validity of the similarity formulation can be found by setting the radius, $R = b_o/2$. This yields from Equation (A2.3):

$$\tau_f < 0.329\beta_2^{-2/3}(\frac{\ell}{b_o})^{-1/4} \tag{A2.13}$$

which for $\beta_2 \sim 0.3$ (from Pullin, 1978) becomes:

$$\tau_f < 0.73(\frac{\ell}{b_o})^{-1/4} \tag{A2.14}$$

The upper limit for the validity of these similarity formulations occurs then at spin up times, $\tau_f = 0.37, 0.30, 0.22$ for $\ell/b_o = 15.1$, 37 and 118.5 respectively.

1. Initial Starting Condition For The Cap Model

As discussed in Chapter 3, the unsteady jet solutions require an initial steady state condition in order to avoid a computational singularity. Similarly the development of the vortex pair cap at the head of the jet requires an initial non-zero specification of the vortex circulation and radius. From this a translation speed and vortex separation can be deduced for the vortex pair at the initial time.

The initial vortex circulation and radius is taken as defined by the similarity thoery of Pullin (1978) as described above. This has been incorporated into the vortex pair numerical solutions with the similarity constants given by Pullin. The initial vortex separation is then defined as the inlet width plus twice the vortex radius. The translation speed is then calculated using the relationship of self induced motion of a vortex pair (Equation 3.1).

The use of this technique leads to a dependence on the initial time of the cap solutions. This dependence has not been examined in detail. However, it has been found that for a typical set of experimental parameters, the dependence of cap variables on the computational starting time reduces as the cap migrates away from the origin. The difference between computed cap variables for initial times of $\tau = 0.02$ and 0.05 was less than 1 percent for times greater than $\tau = 0.25$. The differnece at time $\tau = 0.1$ was about 5 percent. This reduction in dependence with time is a function of the contribution of jet fluxes to the cap, as it has been shown in Chapter 3 that within the computational range, the jet solutions are independent of the staring conditions.

A detailed description of the initial flow development is outside the scope of this study. However it can be stated that the discrepancy during the early stages of the flow outlined above is not significant when considered in relation to the difficulties encountered in experimentally describing the initial spin-up of the vortex pair.

APPENDIX 3: A SUMMARY OF EXPERIMENTAL DATA

1. Typical Reduction Of Test Data For A Single Experiment

It is impractical to include all the experimental data in full detail in this thesis. Therefore only the relevant results are quoted in the main text. However, one complete reduction is tabulated below.

EXPERIMENT NO. 43

Initial Conditions

Q_o = 8.80×10^{-5} m^3s^{-1} 　　　　Peak volumetric flow rate

T = 60 sec 　　　　Period

h_o = 0.025 m 　　　　Basin water depth

q_o = 3.52×10^{-3} m^3s^{-1}/m 　　　　Peak flow rate per unit depth

b_o = 0.060 m 　　　　Entrance channel width

ℓ = $[\dfrac{q_o^2 T^2}{b_o}]^{1/3}$ 　　　　Characteristic length scale

= 0.906 m

T_I = 26.4 deg C   Inflow temperature

T_B = 25.0 deg C   Basin temperature

$R.D_I$ = 1.0220   Inflow relative density

$R.D_B$ = 1.0221   Basin relative density

Characteristic Scales and Parameters

ℓ/b_o = 15.1   Entrance width parameter

ℓ/h_o = 36.2   Entrance depth parameter

U^* = 1.51 × 10⁻² ms⁻¹   Characteristic velocity

U^* = 1.51×10^{-2} ms⁻¹   Characteristic velocity

K^* = 9.06×10^{-4} m³s⁻¹   Characteristic circulation

Re^* = 906   Characteristic Reynolds number

Table A3.1 outlines the typical reduction for an experiment to determine dimensionless flow variables and shape factors. The variation of these variables and factors with dimensionless time or distance from the inlet are shown on Figures A3.1 to A3.5.

TABLE A3.1:   TYPICAL DATA REDUCTION FOR EXPERIMENT NO. 43

τ	x_c	x_{LE}	b_c	b_{cap}	A_{cap}	X_c	X_{LE}	U	U_{LE}	B	B_{CAP}	α	C_3	C_4
	m	m	m	m	m^2									
1ST CYCLE														
0.06	0.054	0.131	0.123	0.192	0.0161	0.060	0.145	0.861	2.384	2.05	3.200	0.80	1.95	1.41
0.12	0.100	0.200	0.131	0.230	0.0208	0.110	0.221	0.993	1.258	2.18	3.833	0.87	2.68	1.64
0.18	0.162	0.315	0.146	0.292	0.0547	0.179	0.348	1.126	2.119	2.43	4.867	1.05	4.19	2.05
0.24	0.223	0.385	0.185	0.308	0.0767	0.246	0.425	1.192	1.258	3.08	5.133	1.05	2.92	1.71
0.30	0.292	0.462	0.192	0.370	0.0916	0.322	0.510	1.126	1.391	3.20	6.167	0.92	3.41	1.85
0.36	0.346	0.531	0.231	0.384	0.1160	0.382	0.586	0.993	1.258	3.85	6.400	0.96	2.66	1.63
0.42	0.400	0.600	0.246	0.400	0.1475	0.442	0.662	1.060	1.258	4.10	6.667	1.00	2.64	1.63
0.48	0.462	0.685	0.254	0.462	0.1546	0.510	0.756	0.927	1.589	4.23	7.700	0.97	3.19	1.79
0.54	0.500	0.738	0.262	0.470	0.1564	0.552	0.815	0.728	0.993	4.37	7.833	1.01	3.26	1.81
0.60	0.538	0.769	0.269	0.438	0.1749	0.594	0.849	0.795	0.596	4.48	7.300	1.05	2.80	1.67
0.66	0.585	0.800	0.273	0.438	0.1576	0.646	0.883	0.927	0.596	4.55	7.300	0.98	2.53	1.59
0.72	0.638	0.838	0.262	0.438	0.1475	0.704	0.925	0.861	0.728	4.37	7.300	0.91	2.55	1.60
0.78	0.677	0.869	0.269	0.438	0.1517	0.747	0.959	0.662	0.596	4.48	7.300	0.88	2.32	1.53
0.84	0.708	0.900	0.277	0.438	−	0.781	0.993	0.530	0.596	4.62	7.300	0.83	2.31	1.53
0.90	0.738	0.938	0.285	0.476	0.1416	0.815	1.035	0.530	0.728	4.75	7.933	0.87	2.28	1.51
0.96	0.769	0.985	0.292	0.462	0.1576	0.849	1.087	0.728	0.861	4.87	7.700	0.91	2.41	1.56

τ	x_c m	x_{LE} m	b_c m	b_{cap} m	A_{cap} m^2	X_c	X_{LE}	U	U_{LE}	B	B_{CAP}	α	C_3	C_4
5TH CYCLE														
0.08	0.027	0.062	–	–	–	–	0.068	0.728	0.861	–	–	–	–	–
0.12	0.054	0.115	0.115	0.160	–	0.060	0.060	0.927	1.457	1.92	2.667	0.76	1.48	1.23
0.17	0.104	0.200	0.146	0.210	–	0.115	0.221	1.325	1.854	2.43	3.500	0.91	1.89	1.38
0.21	0.158	0.285	0.169	0.246	–	0.174	0.315	1.457	2.318	2.82	4.100	1.03	2.19	1.48
0.26	0.223	0.362	0.185	0.270	–	0.246	0.400	1.258	1.722	3.08	4.500	1.03	2.19	1.48
0.31	0.269	0.423	0.200	0.300	–	0.297	0.467	1.523	1.325	3.33	5.000	1.03	2.31	1.52
0.34	0.323	0.485	0.231	0.370	–	0.357	0.535	1.325	2.252	3.85	6.167	0.88	2.25	1.50
0.39	0.354	0.562	0.246	0.416	–	0.391	0.620	0.662	1.722	4.10	6.933	1.00	2.86	1.69
0.45	0.392	0.608	0.254	0.438	–	0.433	0.671	0.795	0.861	4.23	7.300	0.99	2.93	1.71
0.50	0.435	0.669	0.238	0.438	–	0.480	0.738	1.523	1.325	3.97	7.300	1.07	3.62	1.90
0.58	0.546	0.777	0.254	0.400	–	0.603	0.858	1.060	0.993	4.23	6.667	1.15	2.86	1.70
0.63	0.585	0.808	0.238	0.392	–	0.646	0.892	1.126	0.662	3.97	6.533	1.14	3.09	1.76
0.68	0.646	0.854	0.246	0.354	–	0.713	0.943	0.927	0.993	4.10	5.900	1.18	2.43	1.57
0.74	0.677	0.900	0.254	0.376	–	0.747	0.993	0.927	0.861	4.23	6.267	1.19	2.60	1.62
0.78	0.723	0.931	0.262	0.384	–	0.798	1.028	1.258	0.861	4.37	6.400	1.08	2.33	1.53
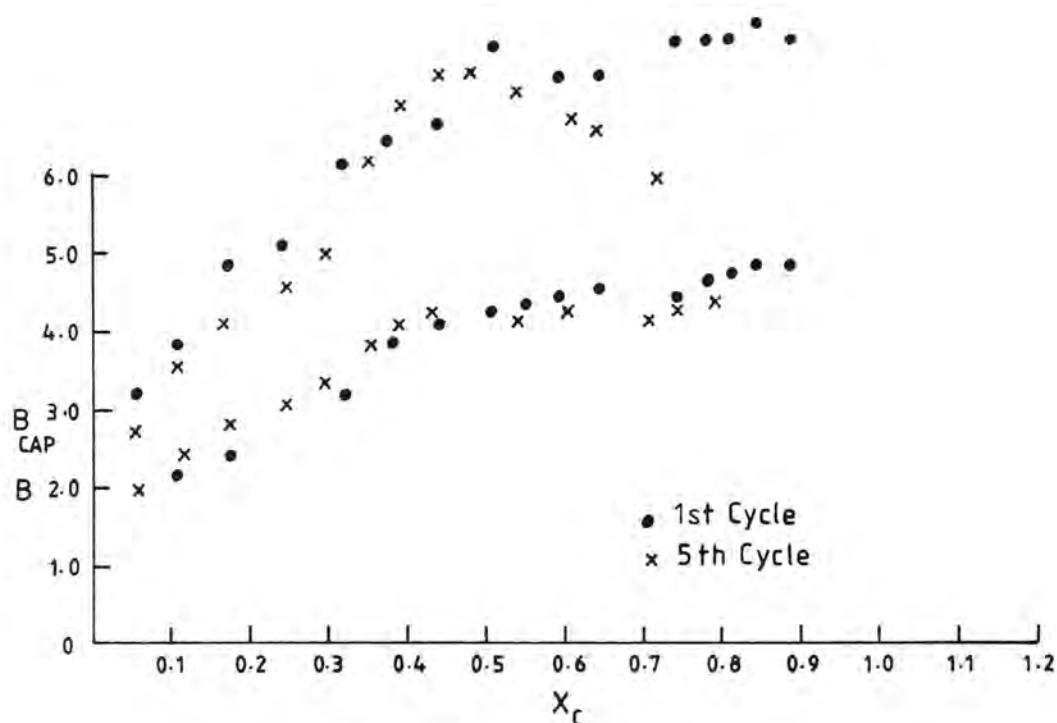
DIMENSIONLESS CAP WIDTH B_{CAP} AND VORTEX PAIR
SEPARATION, B, VERSUS DIMENSIONLESS DISTANCE
X_c FROM THE INLET
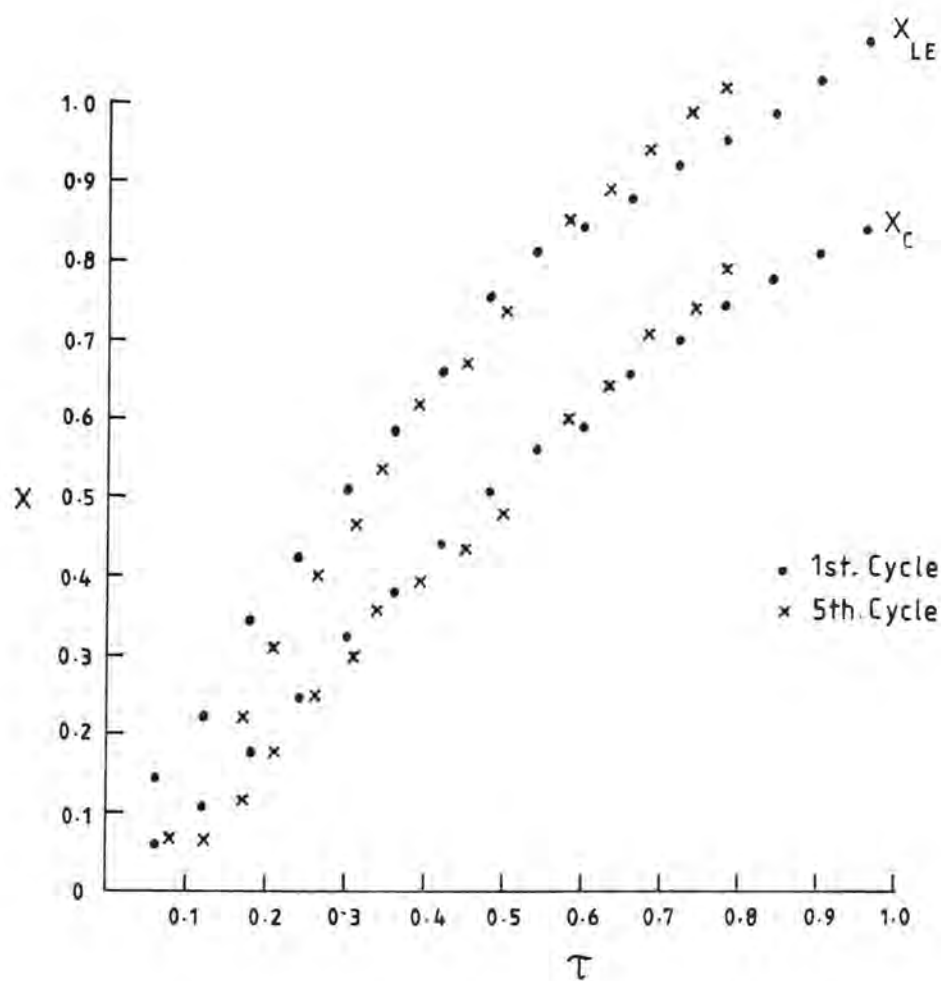
FIGURE A3·1

DIMENSIONLESS ADVANCE OF THE LEADING EDGE
OF THE CAP, X_{LE} AND THE CAP CENTRELINE, X_C
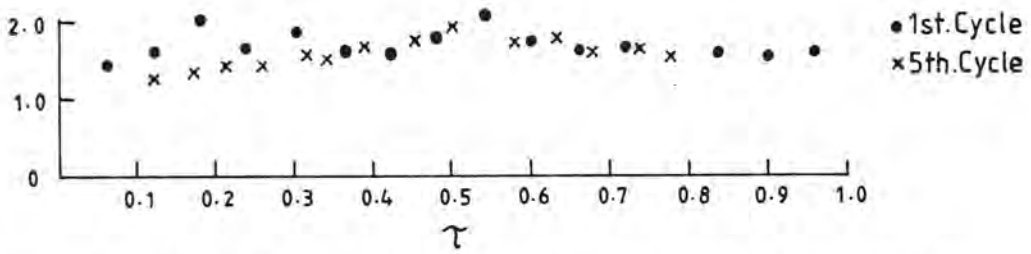
VARIATION IN CAP SIMILARITY CONSTANT, C_4, WITH TIME

FIGURE A3·4
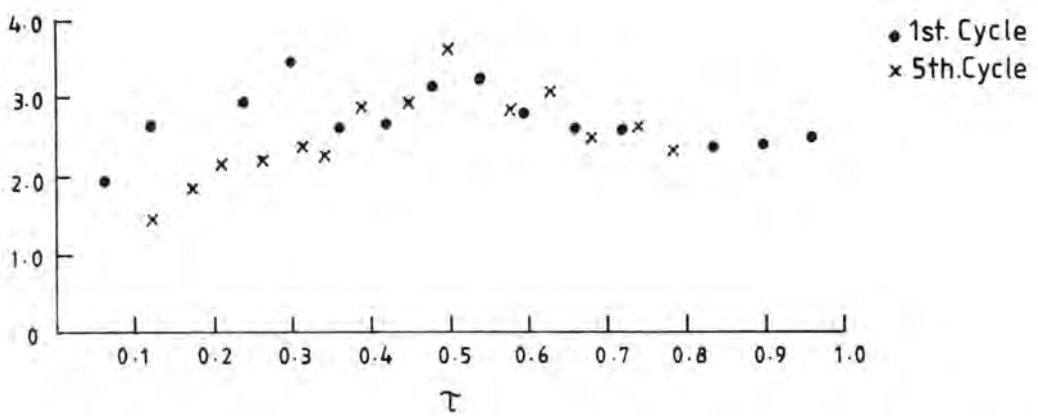
VARIATION IN CAP SIMILARITY CONSTANT, C_3, WITH TIME

FIGURE A3·3
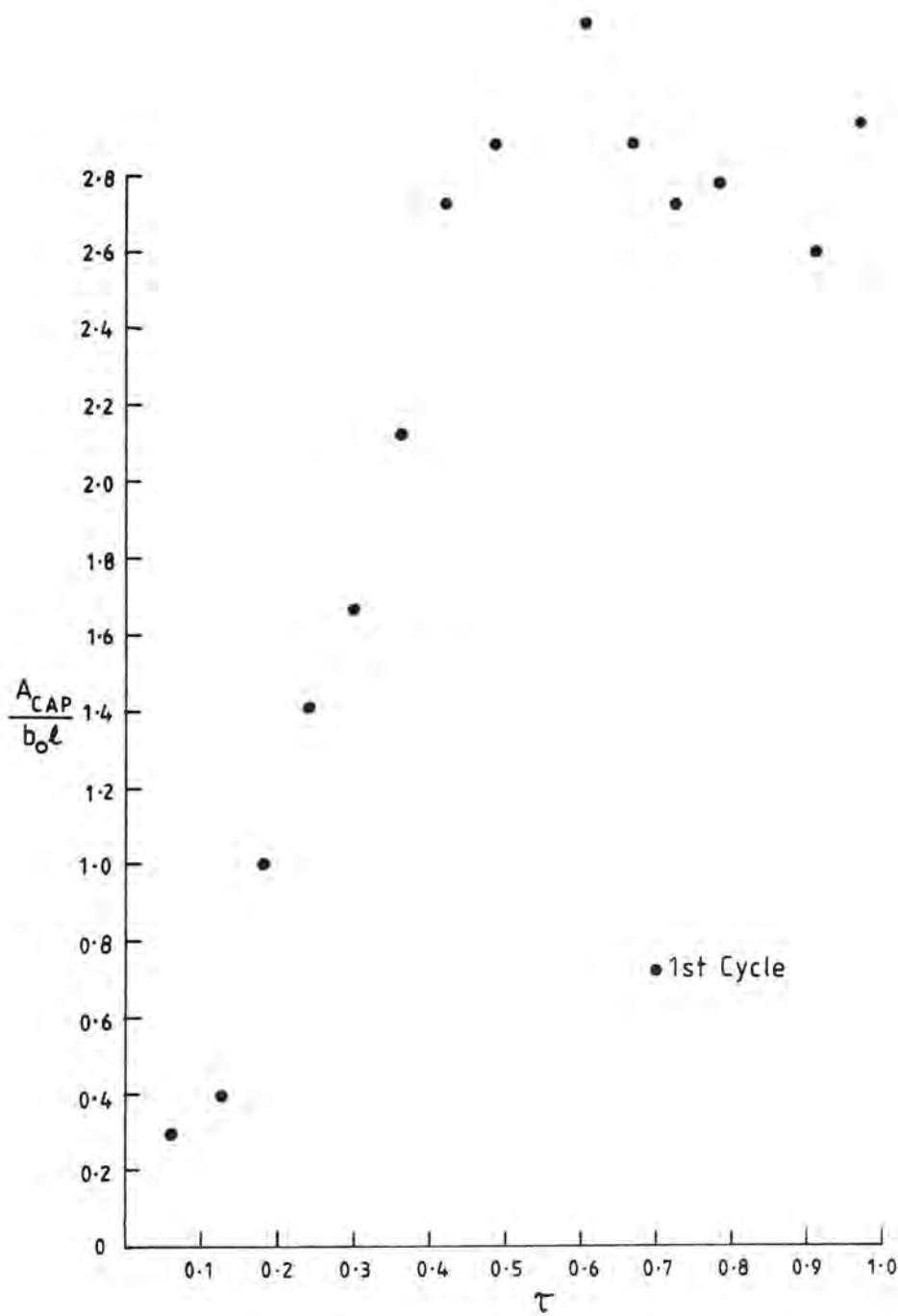
DIMENSIONLESS AREA ^{A}CAP$/$b$_o\ell$, OF THE DYED
CAP FLUID VERSUS DIMENSIONLESS TIME τ

2. Constants Determined For Each Experiment

Table A3.2 below lists for each experiment (constant depth basin) aver-age values of the various experimentally determined constants and parameters which describe the flow. These are:

α - the cap shape factor (Chapter 5)

C_3 - the cap area similarity constant (Chapter 5)

C_4 - the cap circumference similarity constant (Chapter 5)

n_2 - the decoupled vortex pair growth rate proportionality constant (Chapter 5)

$$= 2e(\frac{\ell}{bo})$$

τ_1 - the experimentally determined time for the decoupling of the jet and the cap

$\tilde{U}$ - the average translation speed up to $\tau = 0.50$

$\tilde{U}_{LE}$ - average translation speed of the leading edge of the vortex pair cap up to $\tau = 0.50$

TABLE A3.2	SUMMARY OF EXPERIMENTAL RESULTS FOR CONSTANT DEPTH EXPERIMENTS					
Expt No.	α	C_3	C_4	n_2	τ_1	$\tilde{U}$	$\tilde{U}_{LE}$
4	1.095	3.255	1.804	–	0.54	1.036	1.475
5	1.140	3.309	1.867	8.87	0.55	1.303	1.767
6	.88	2.114	1.429	11.75	0.49	1.632	2.045
7	.98	2.909	1.696	–	0.54	1.511	1.946
8	.885	2.359	1.561	–	0.52	1.552	1.616
9	.79	2.089	1.453	3.45	0.49	.577	1.267
10	.63	2.758	1.730	–	0.38	.445	0.908
11	.82	6.459	2.466	–	0.44	.727	1.572
12	.56	4.309	2.073	1.55	0.52	.488	1.211
14	1.13	2.007	1.413	–	0.46	1.130	1.821
15	1.05	2.515	1.578	–	0.42	1.235	1.541
16	.95	2.078	1.454	0.98	0.60	1.257	1.575
17	.97	2.552	1.604	2.15	0.60	1.200	1.447
25	.88	2.891	1.714	2.85	0.53	1.036	1.311
26	.91	2.431	1.566	1.67	0.47	1.351	1.650
27	.96	2.908	1.707	1.46	0.40	1.000	1.395
28	1.055	3.656	1.906	1.00	0.38	0.869	1.560
29	.955	2.490	1.576	2.23	0.42	1.613	1.876
30	1.015	2.520	1.582	–	0.39	1.455	1.825
31	.92	2.468	1.682	0.96	0.70	–	–
32	.94	2.517	1.597	–	0.40	1.732	1.812
34	.935	2.838	2.695	5.43	0.54	1.428	1.842
35	.955	2.602	2.612	3.75	0.48	1.494	2.193
36	1.01	2.554	1.595	–	–	1.333	1.862
37	.86	3.068	1.748	3.85	0.48	1.089	1.357
38	.94	3.091	1.766	2.37	0.52	1.126	1.473
39	1.00	2.919	1.705	4.77	0.54	1.208	1.527
43	0.95	2.653	1.624	1.17	0.38	1.107	1.517
44	0.95	2.890	1.698	2.47	0.44	1.289	2.062
46	1.05	2.960	1.722	1.63	0.45	1.154	1.037
47	0.78	2.784	1.690	0.78	0.55	0.576	1.104
48	0.94	2.595	1.609	2.74	0.45	0.687	1.876
49	0.99	2.938	1.720	1.75	0.47	1.327	1.471
50	–	2.208	1.486	–	0.43	1.770	2.024
51	1.02	2.689	1.625	–	0.34	1.798	2.000
52	1.28	6.676	2.646	–	0.42	1.121	–
53	–	–	–	–	–	–	1.812
54	1.06	2.242	1.514	4.68	0.43	1.585	1.792
62	1.03	3.230	1.826	1.19	0.50	1.548	1.945
63	0.98	2.868	1.742	3.11	0.65	1.349	1.726
64	0.94	2.440	1.564	4.57	–	1.742	1.915

3. <u>Numerical Predictions and Experimental Results</u>

Dimensionless plots have been made of the vortex pair separation and the translation of the cap centreline and are shown as Figures A3.6 and A3.7 respectively. All constant depth experimental data are shown on these figures. Also shown are the numerical predictions. These results have been discussed in Chapter 6. The linearly varying depth results are presented separately in Chapter 6.
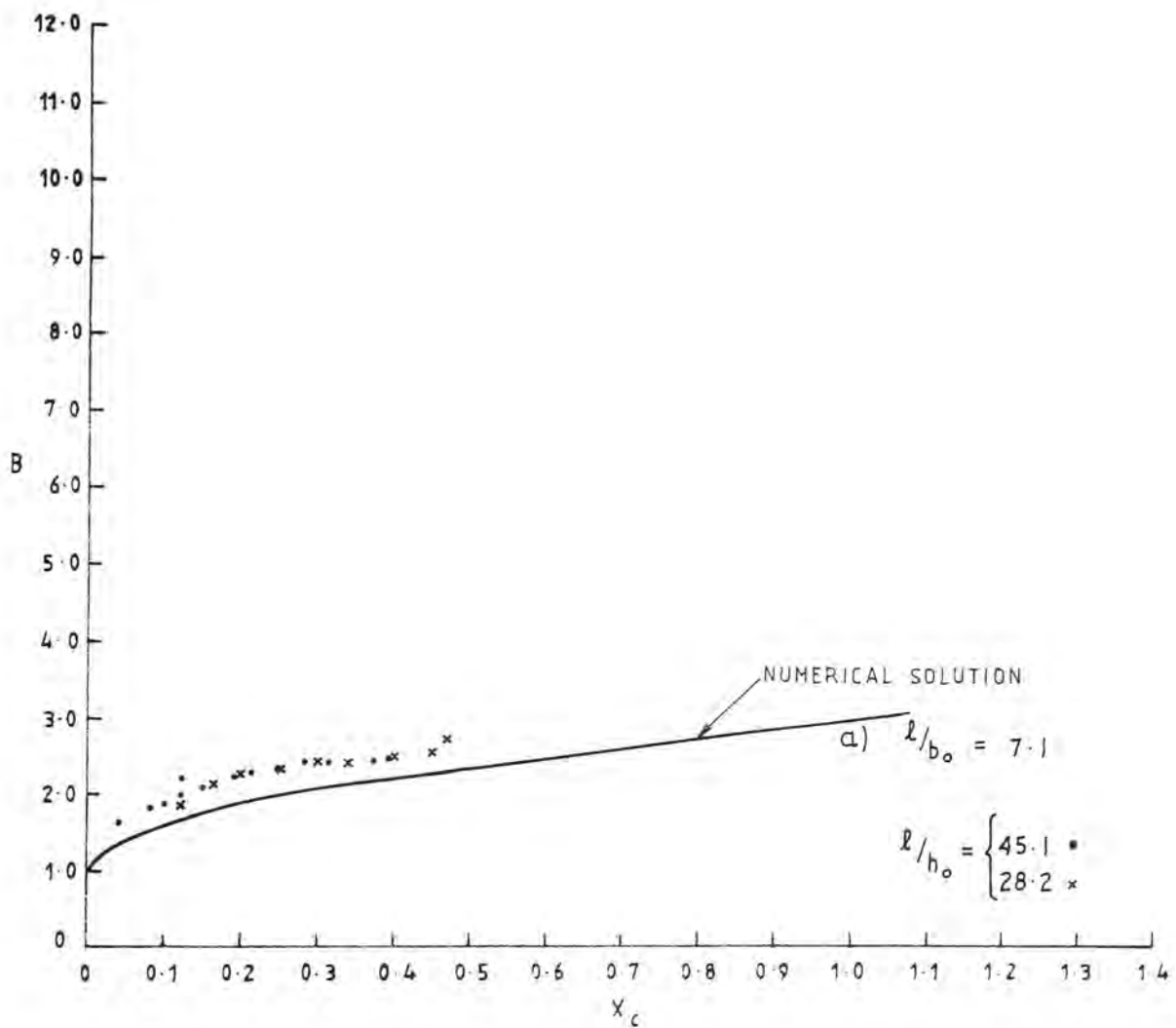
DIMENSIONLESS VORTEX PAIR SEPARATION, B, VERSUS
DIMENSIONLESS DISTANCE FROM THE INLET, X_c FOR
VARIOUS INLET WIDTH RATIOS

FIGURE A3·6
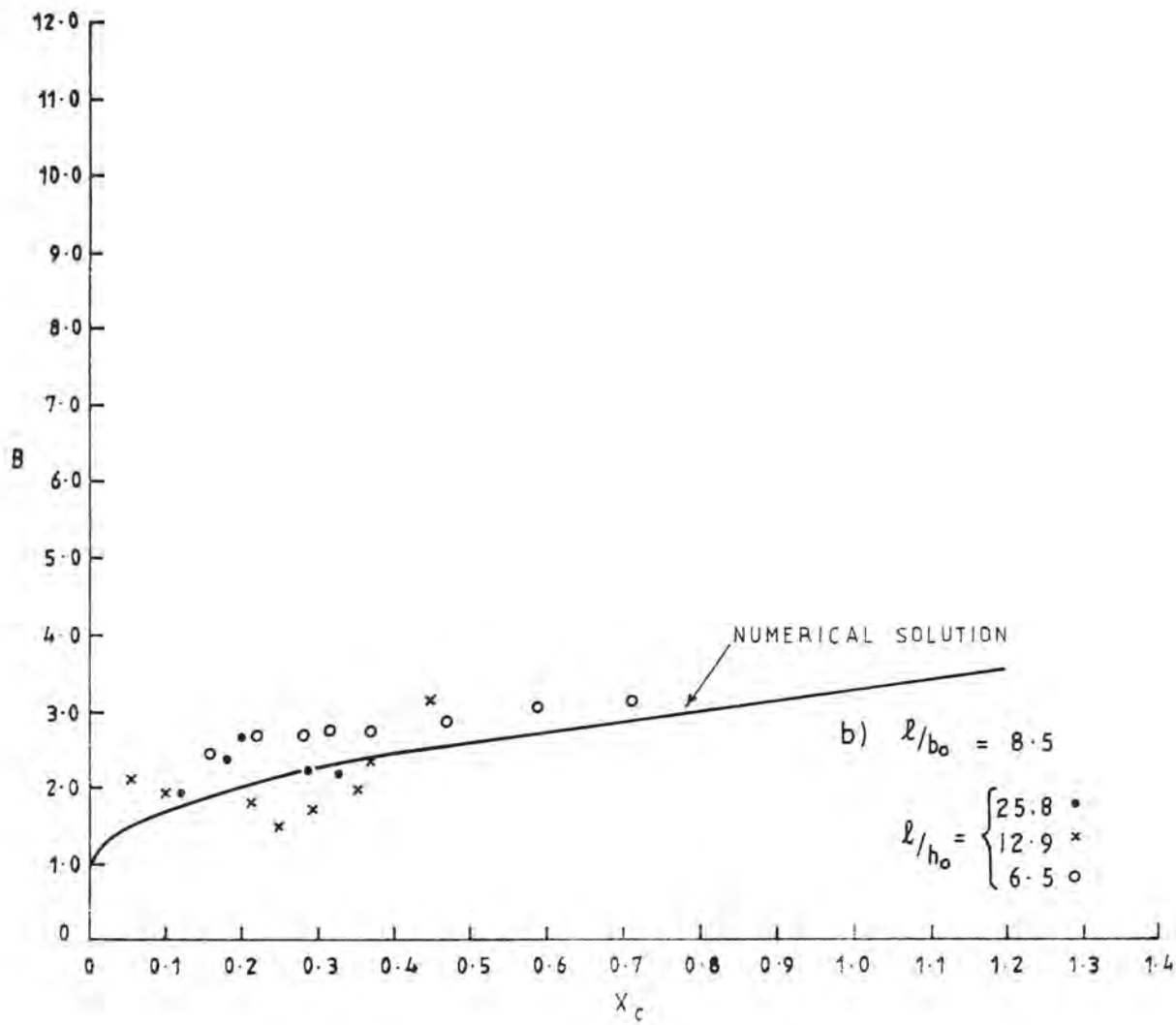
FIGURE A3·6(Cont.)
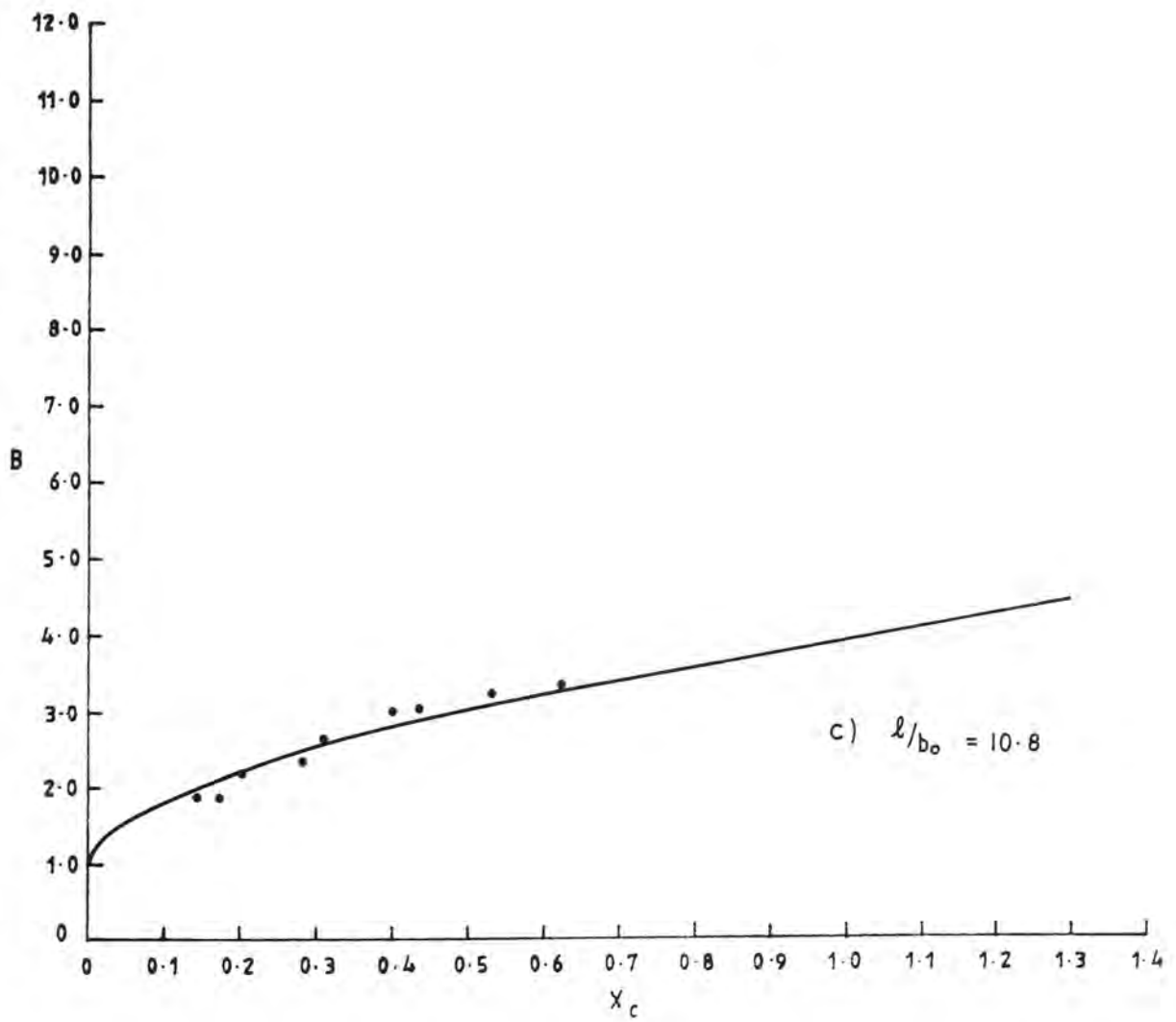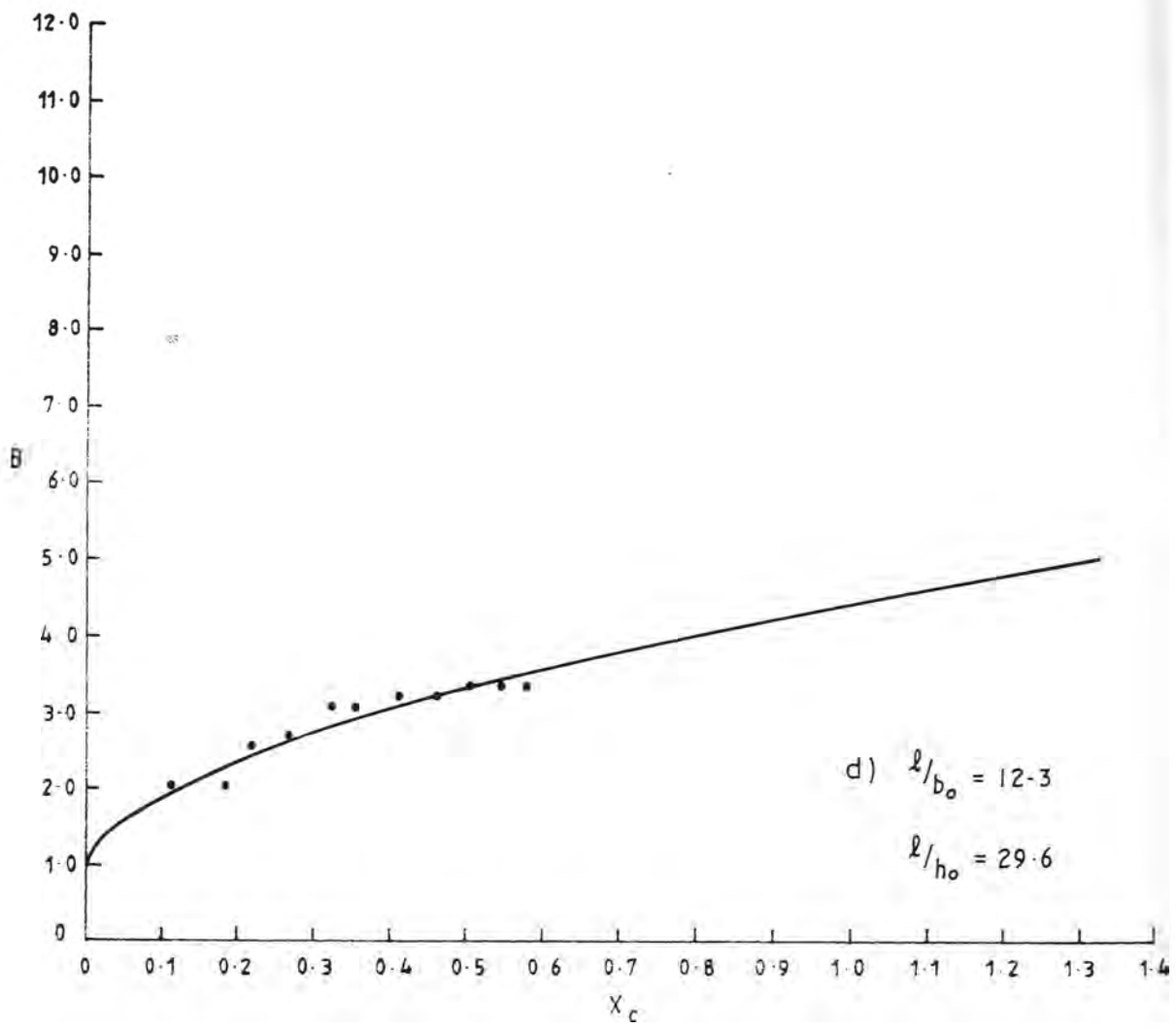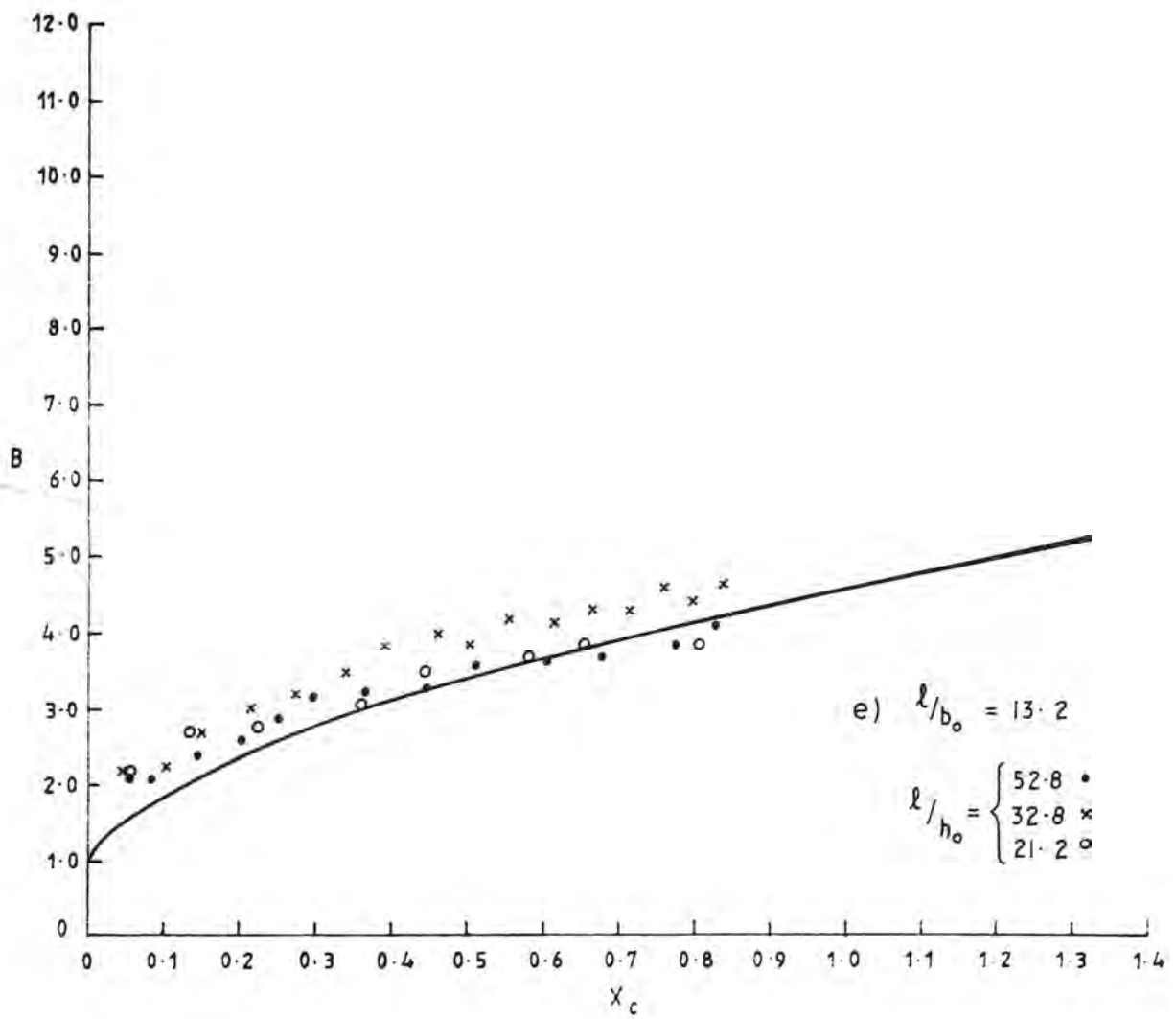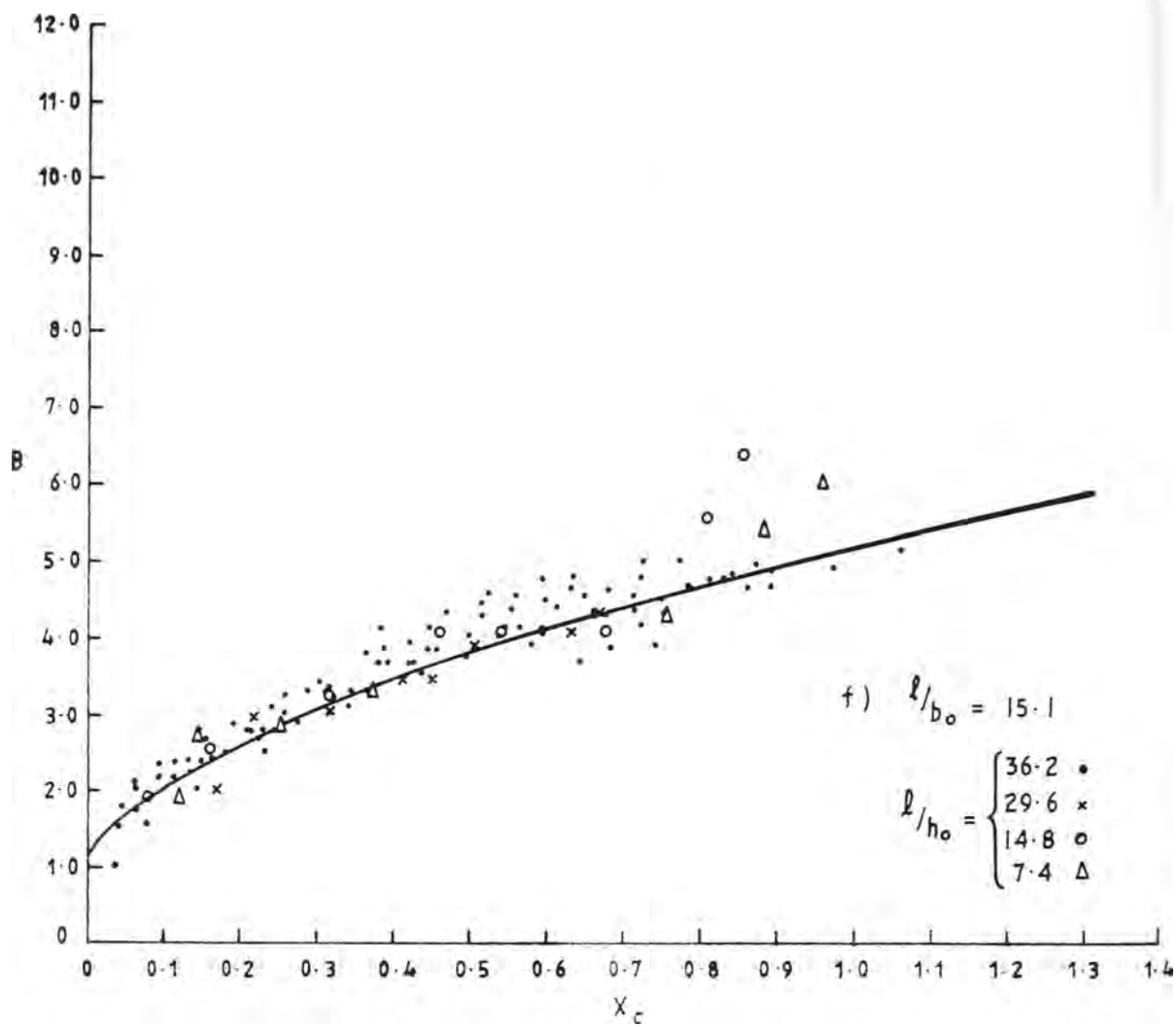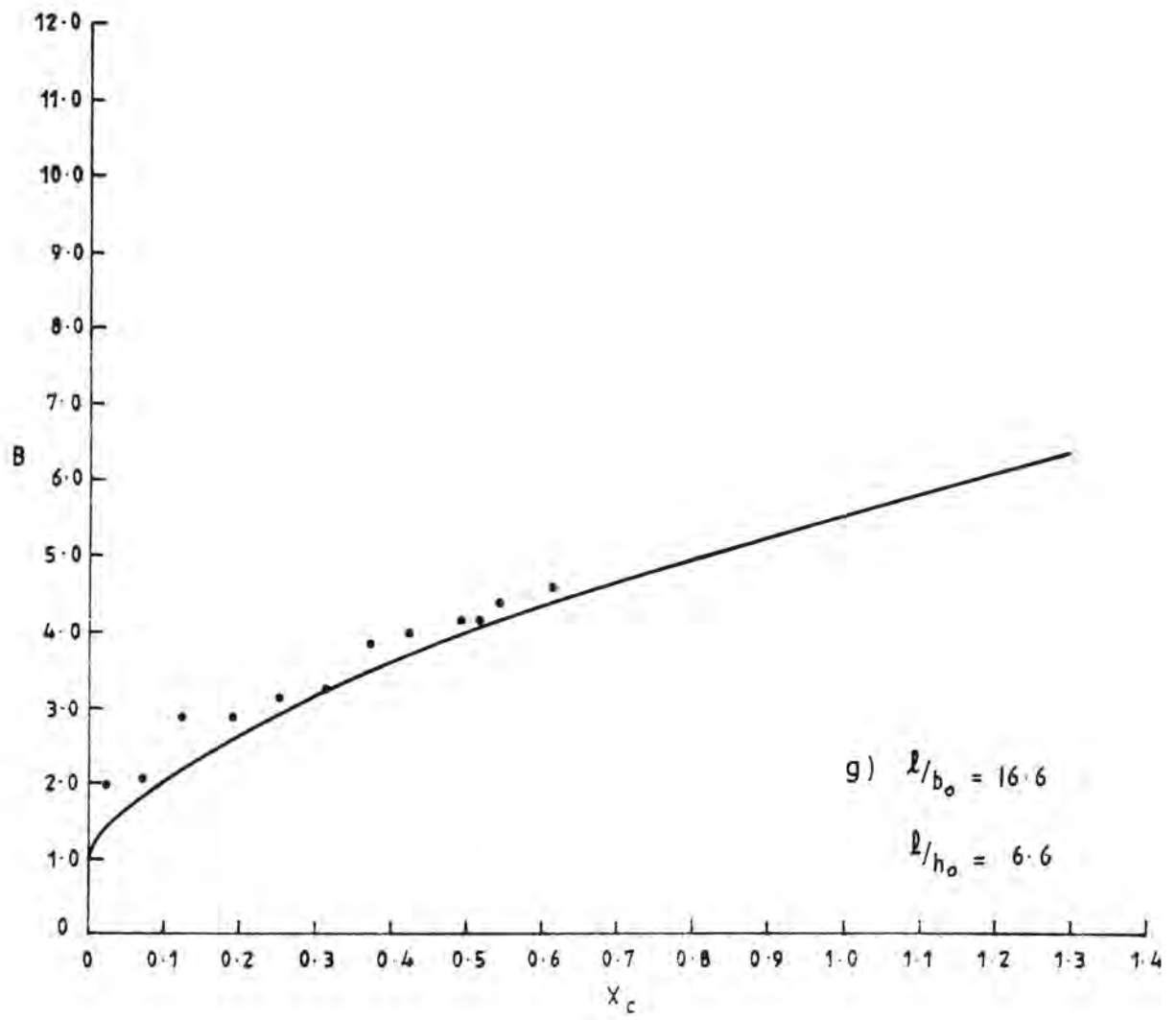
c) $\ell/b_o = 10.8$

FIGURE A3·6 (Cont.)

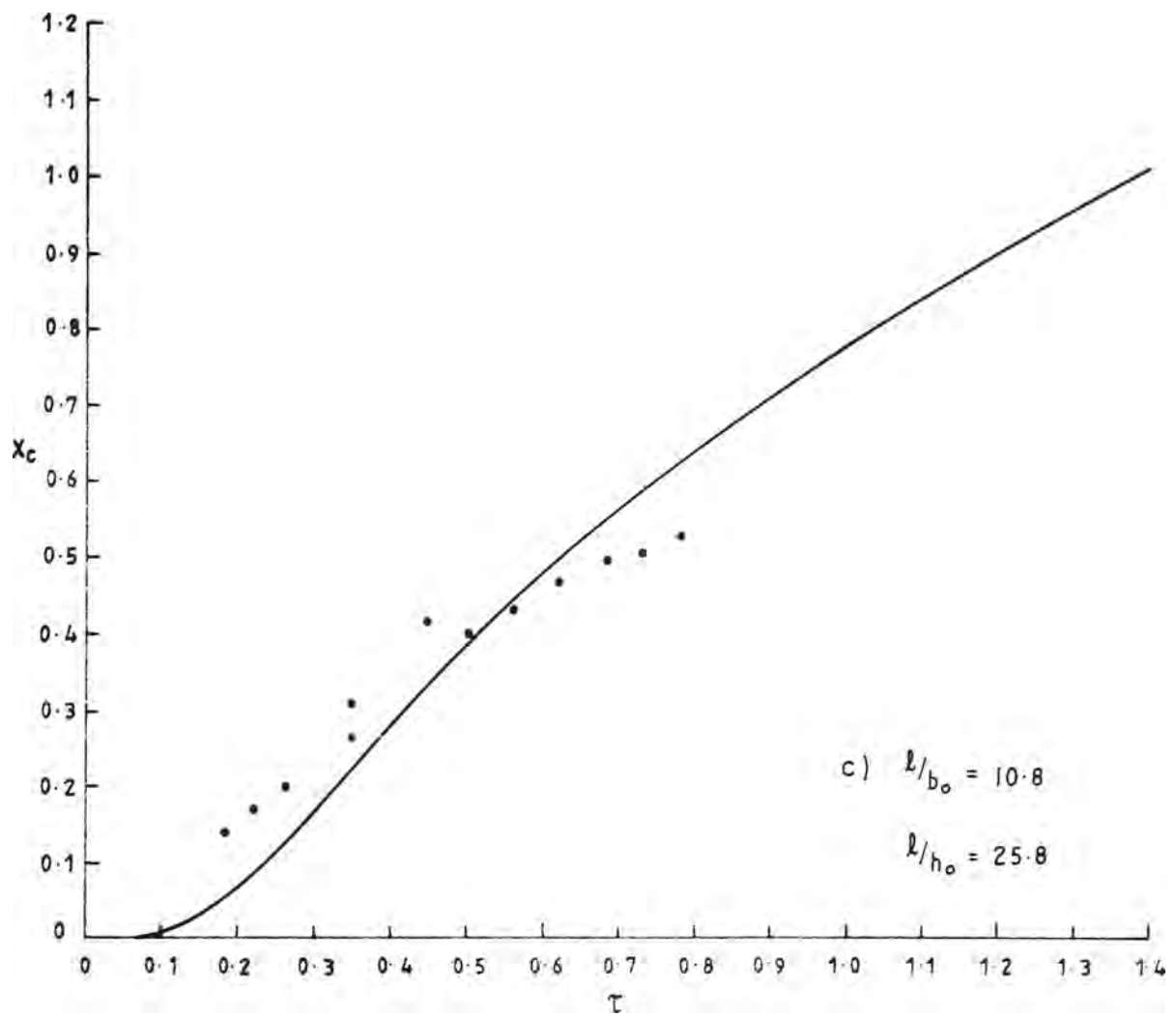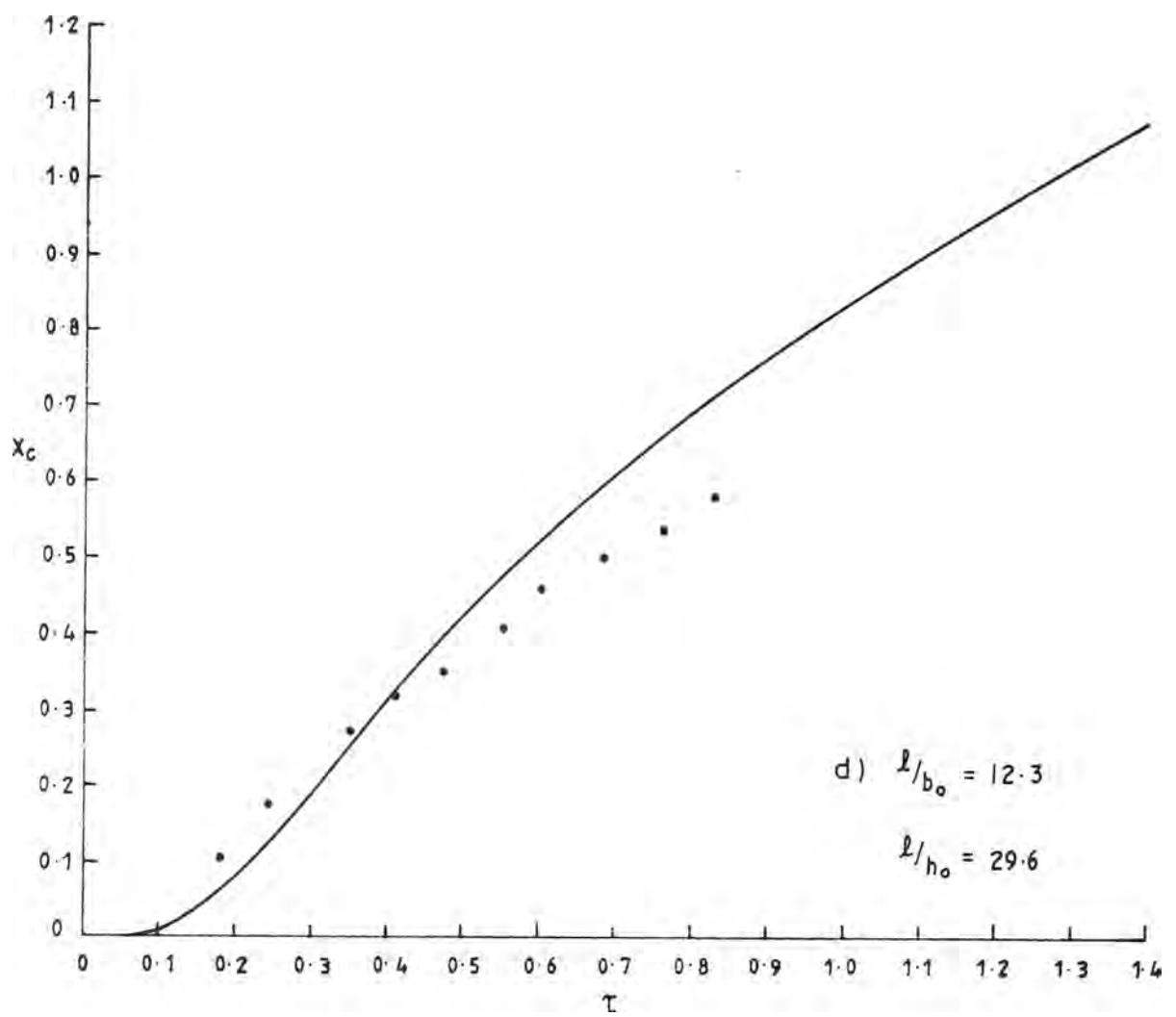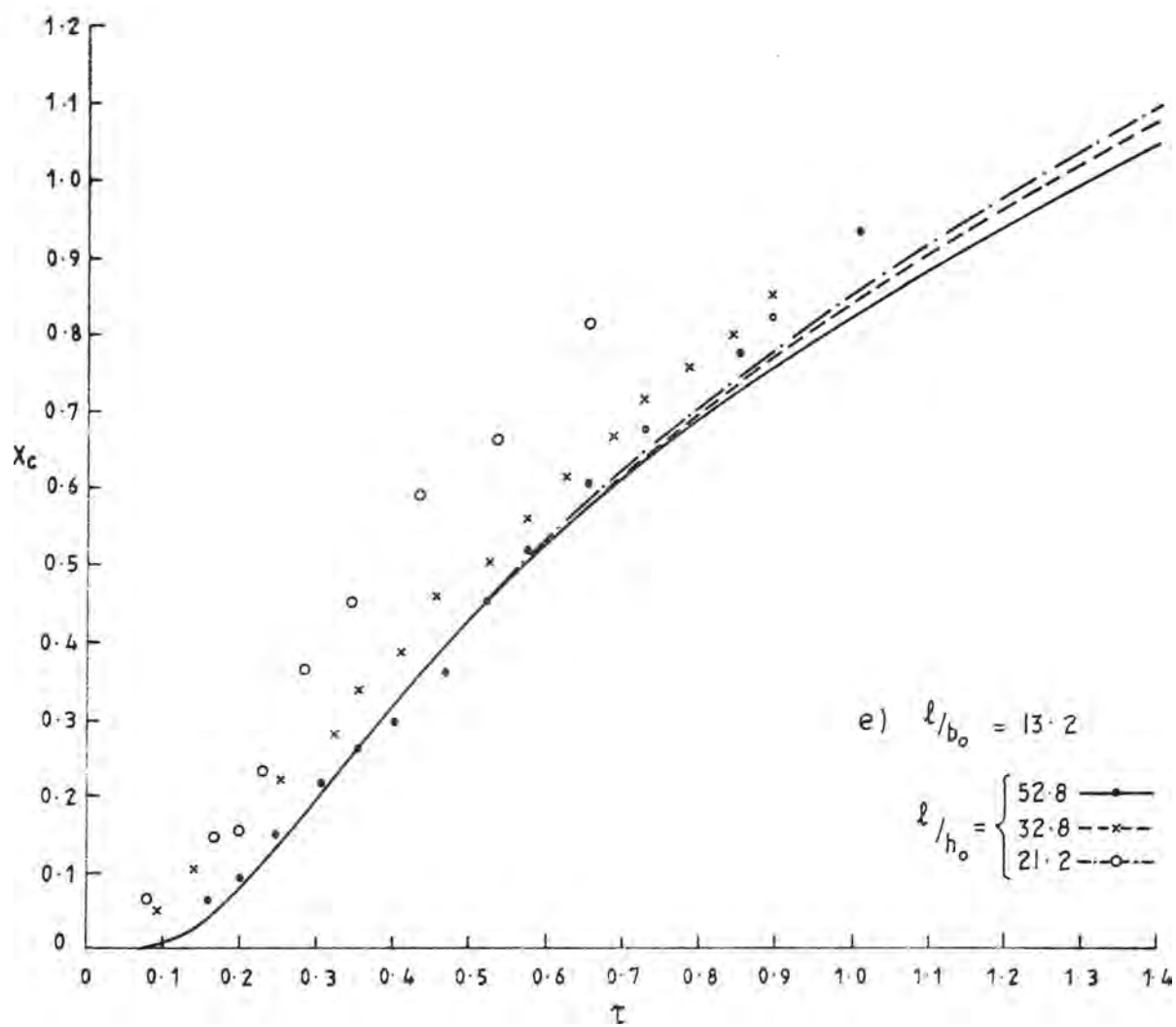d) $\ell/b_o = 12\cdot3$

$\ell/h_o = 29\cdot6$

FIGURE A3·6 (Cont.)

FIGURE A3·6 (Cont.)

FIGURE A3·6(Cont.)

FIGURE A3·6 (Cont.)
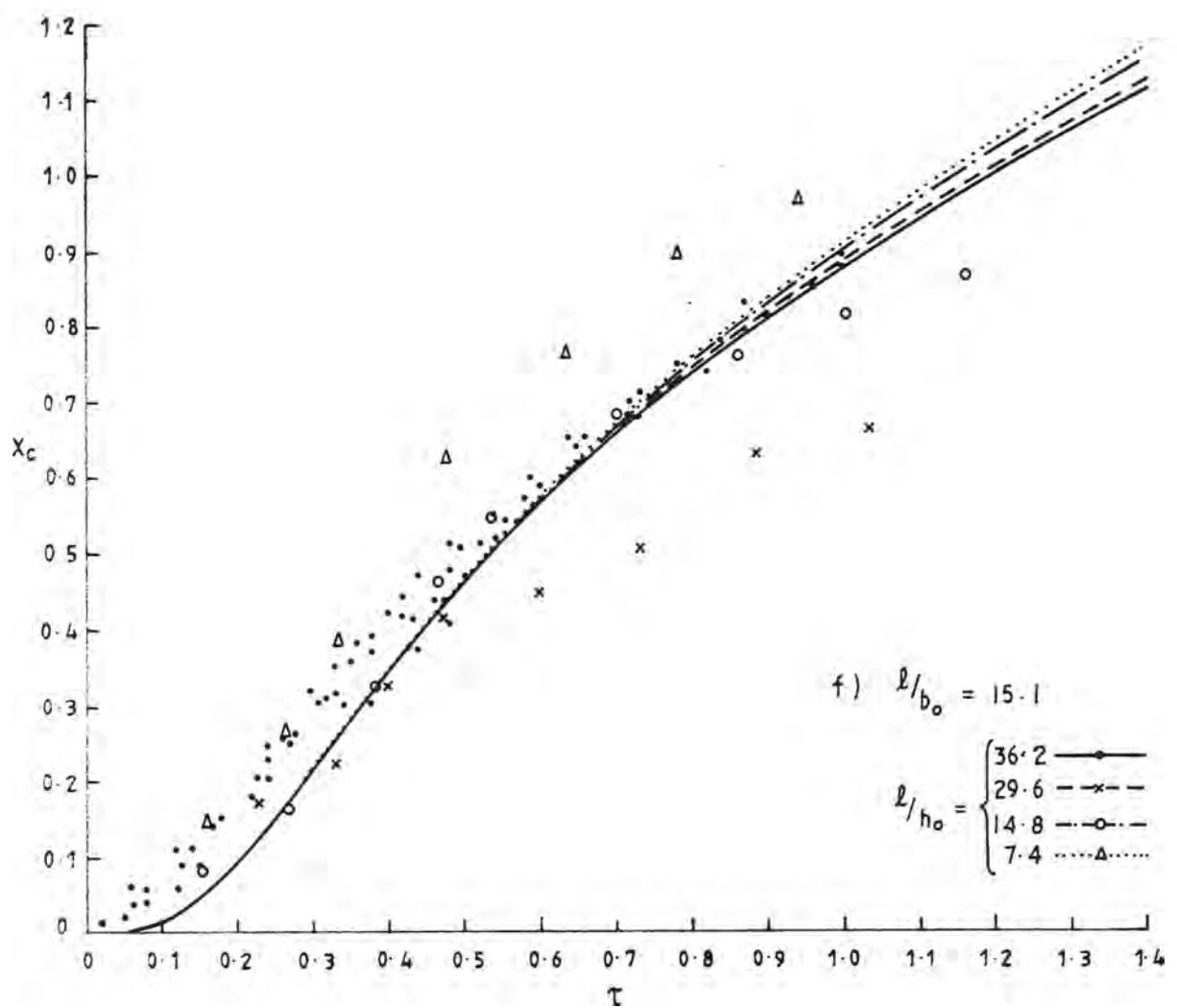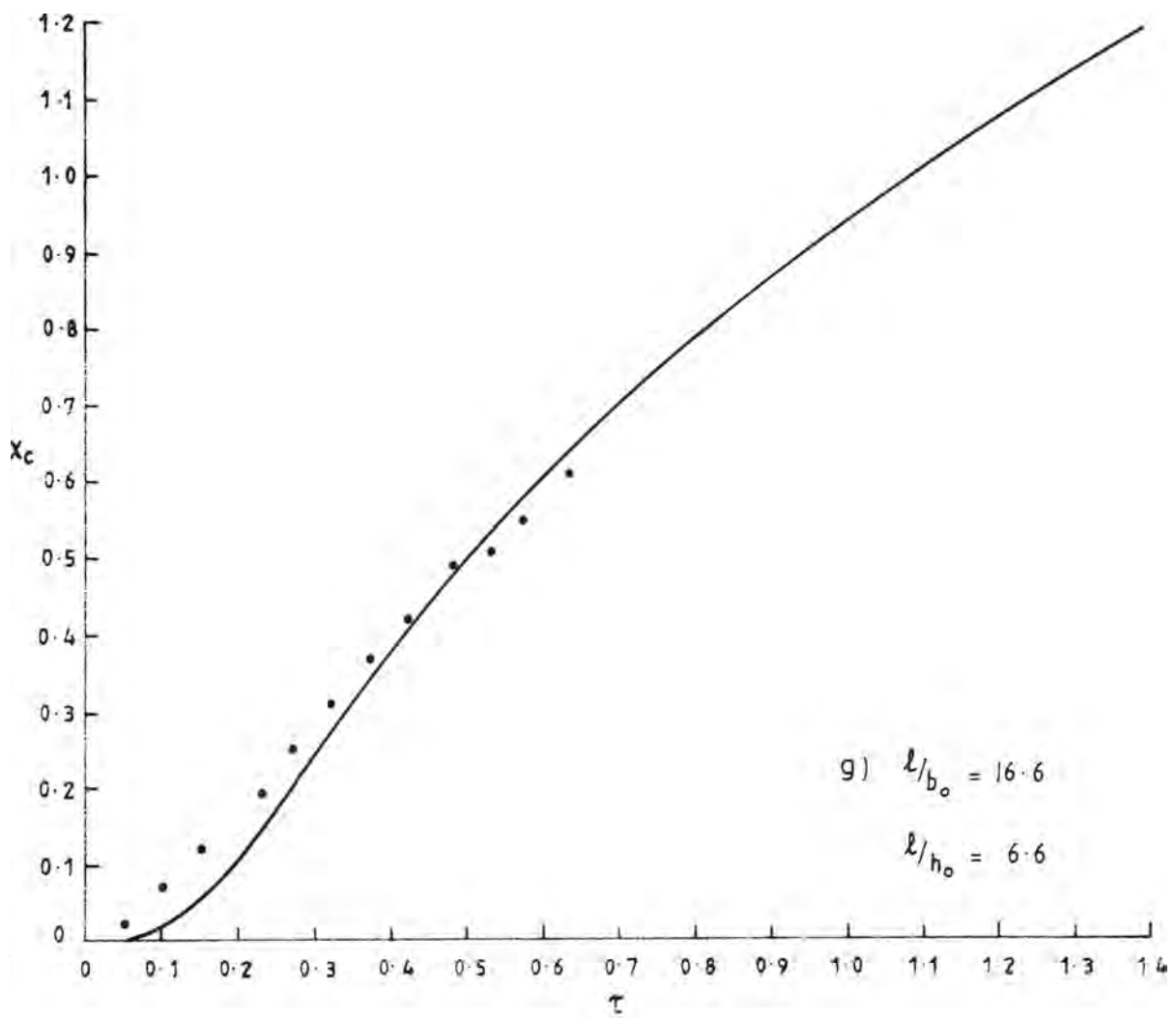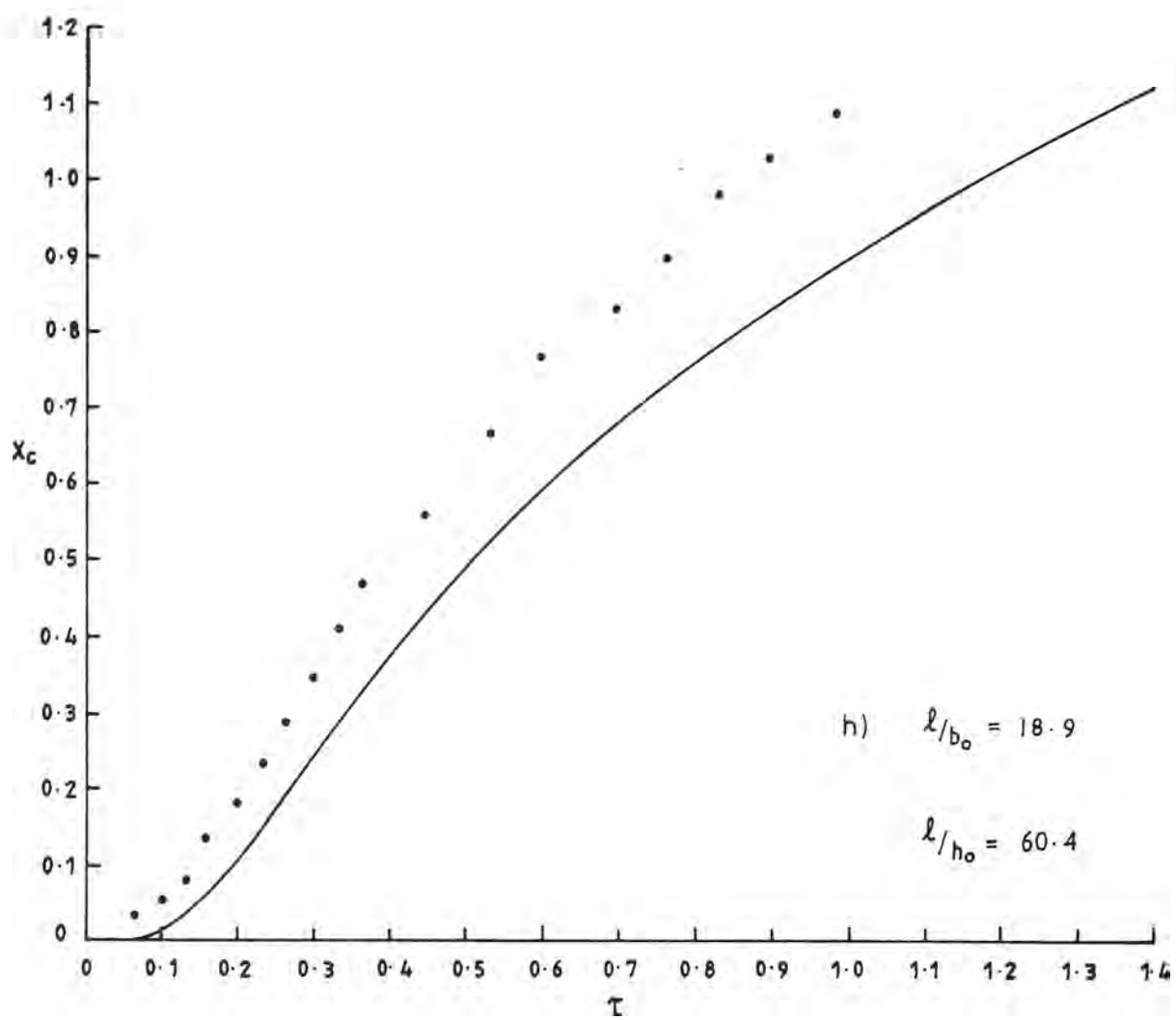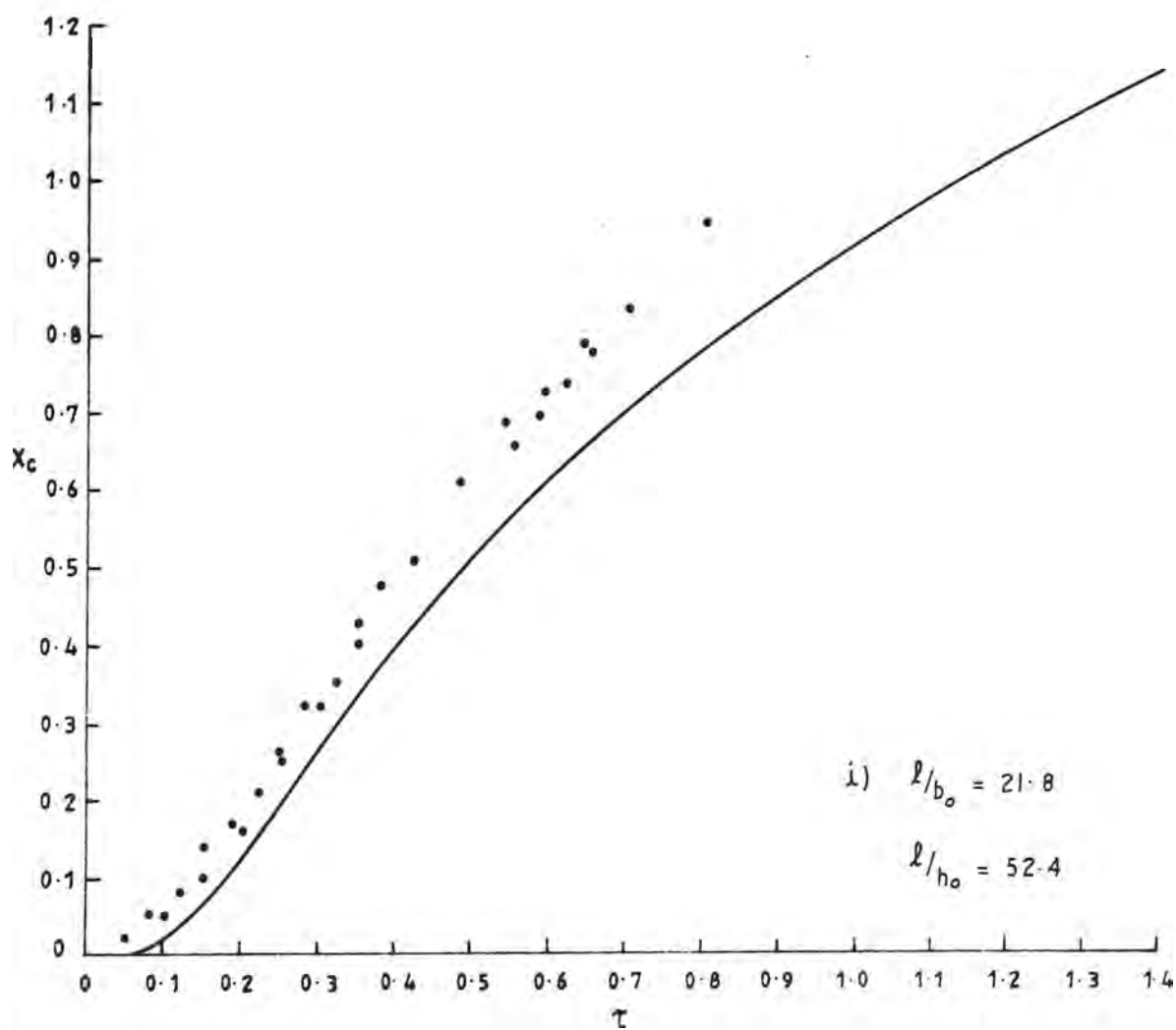
h) $\ell/b_o = 18 \cdot 9$

$\ell/h_o = 60 \cdot 4$

FIGURE A3·6(Cont.)

FIGURE A3·6(Cont.)

FIGURE A3·6 (Cont.)

FIGURE A 3·6 (Cont.)

FIGURE A3·6(Cont.)

m) $\ell/b_o = 39\cdot9$

$\ell/h_o = \begin{cases} 63\cdot8 \rule[0.5ex]{2em}{0.4pt} \\ 31\cdot9 \text{--x---} \end{cases}$

FIGURE A3·6 (Cont.)

n) $\ell/b_o = 118.4$

$\ell/h_o = 236.9$
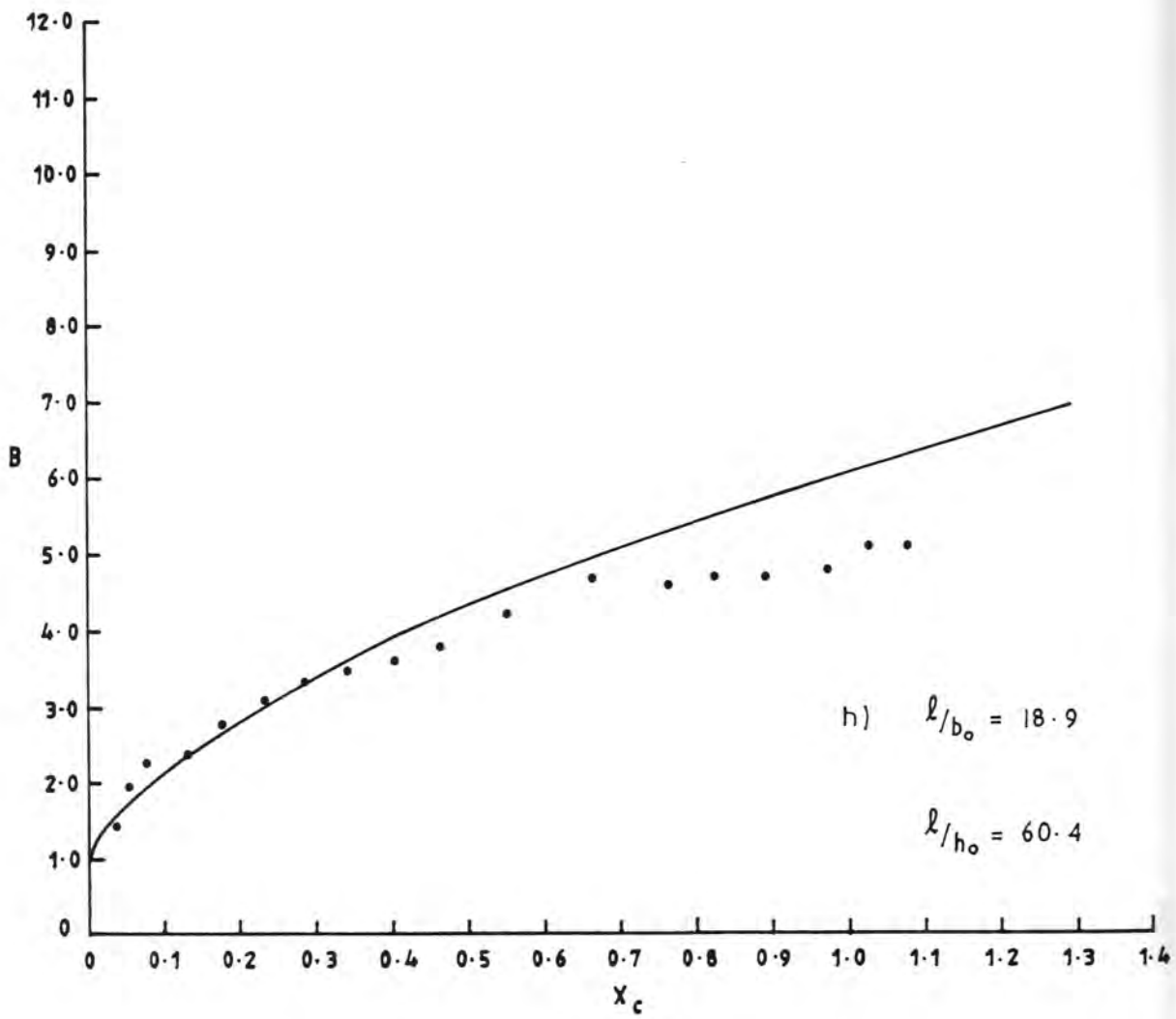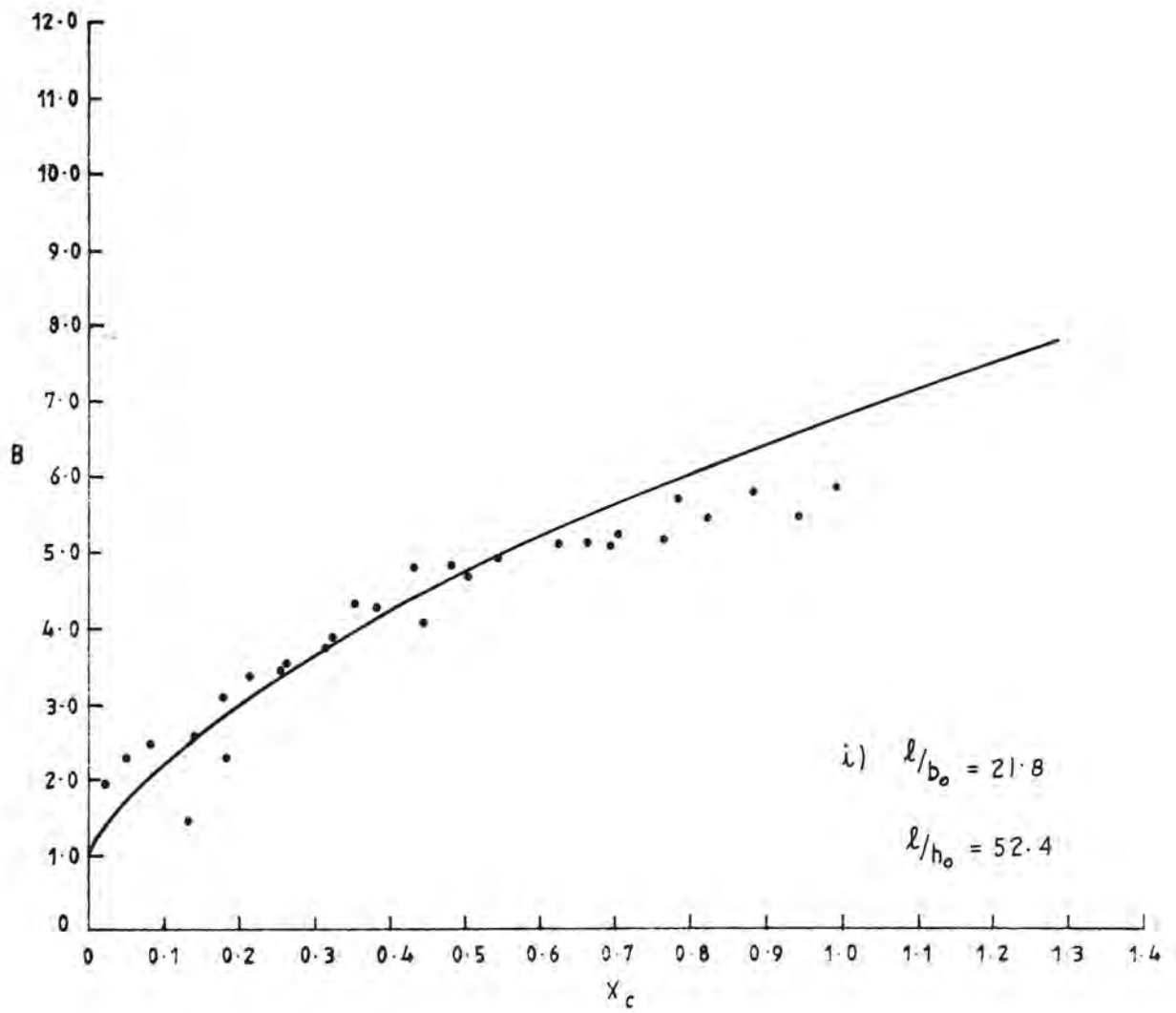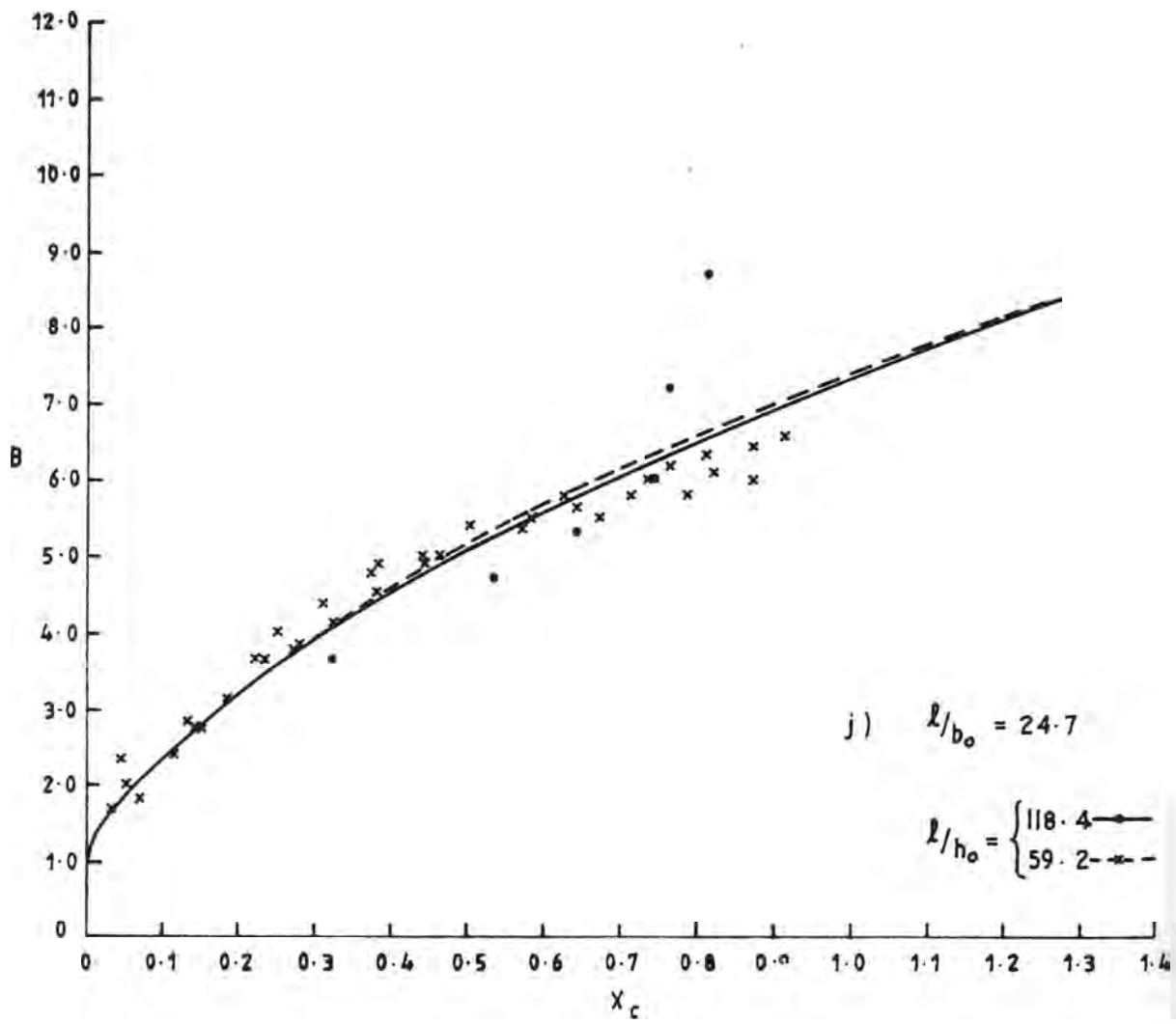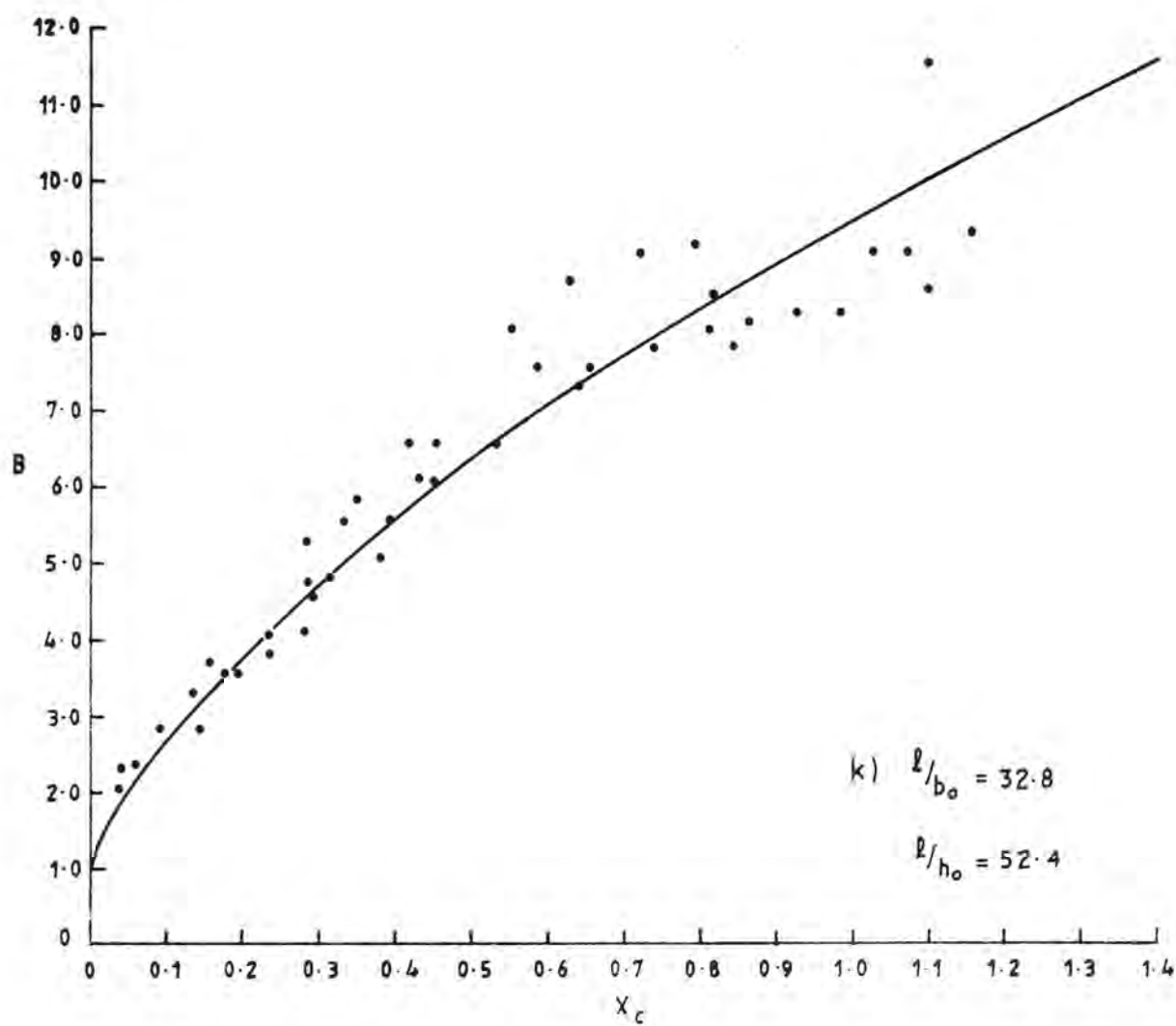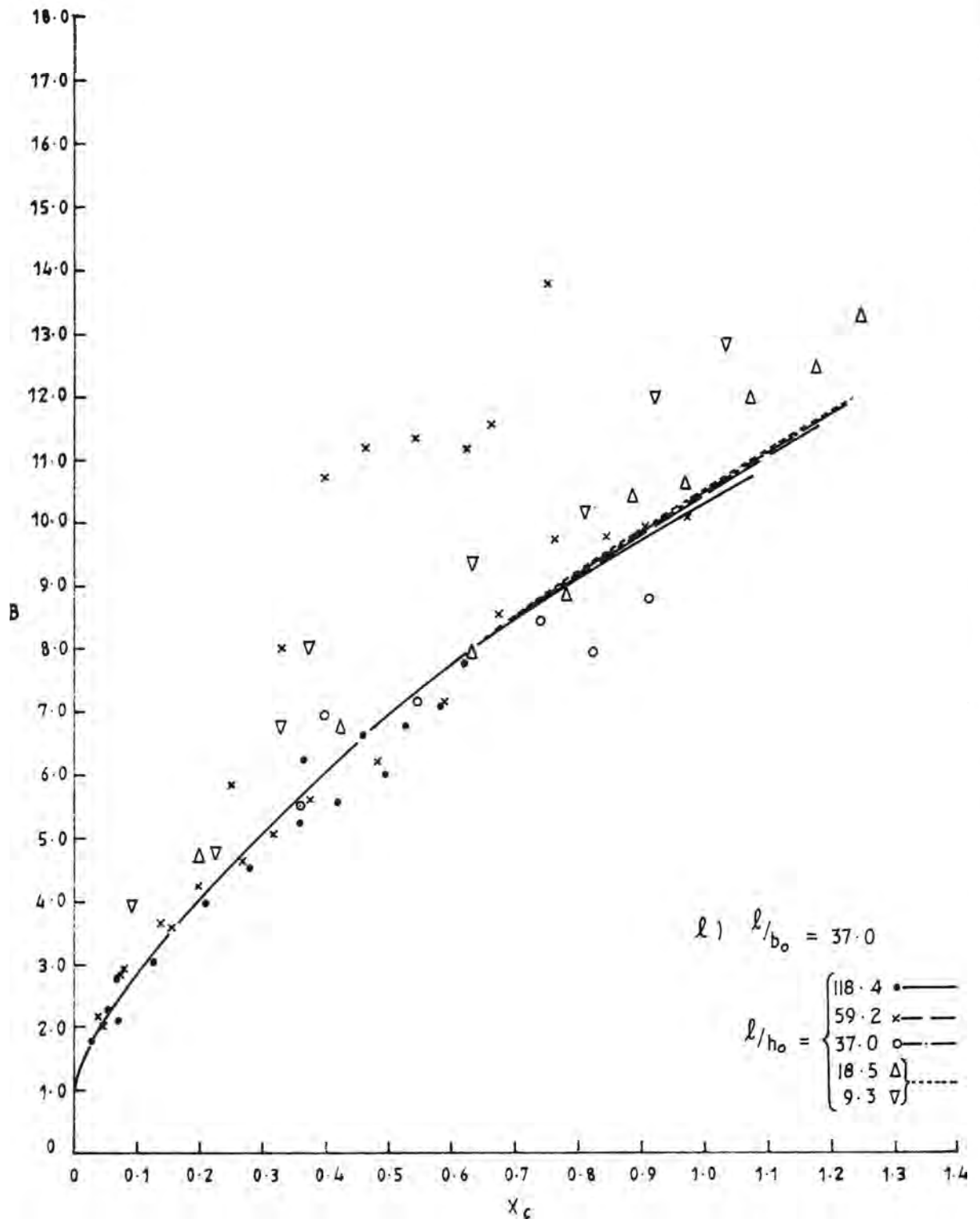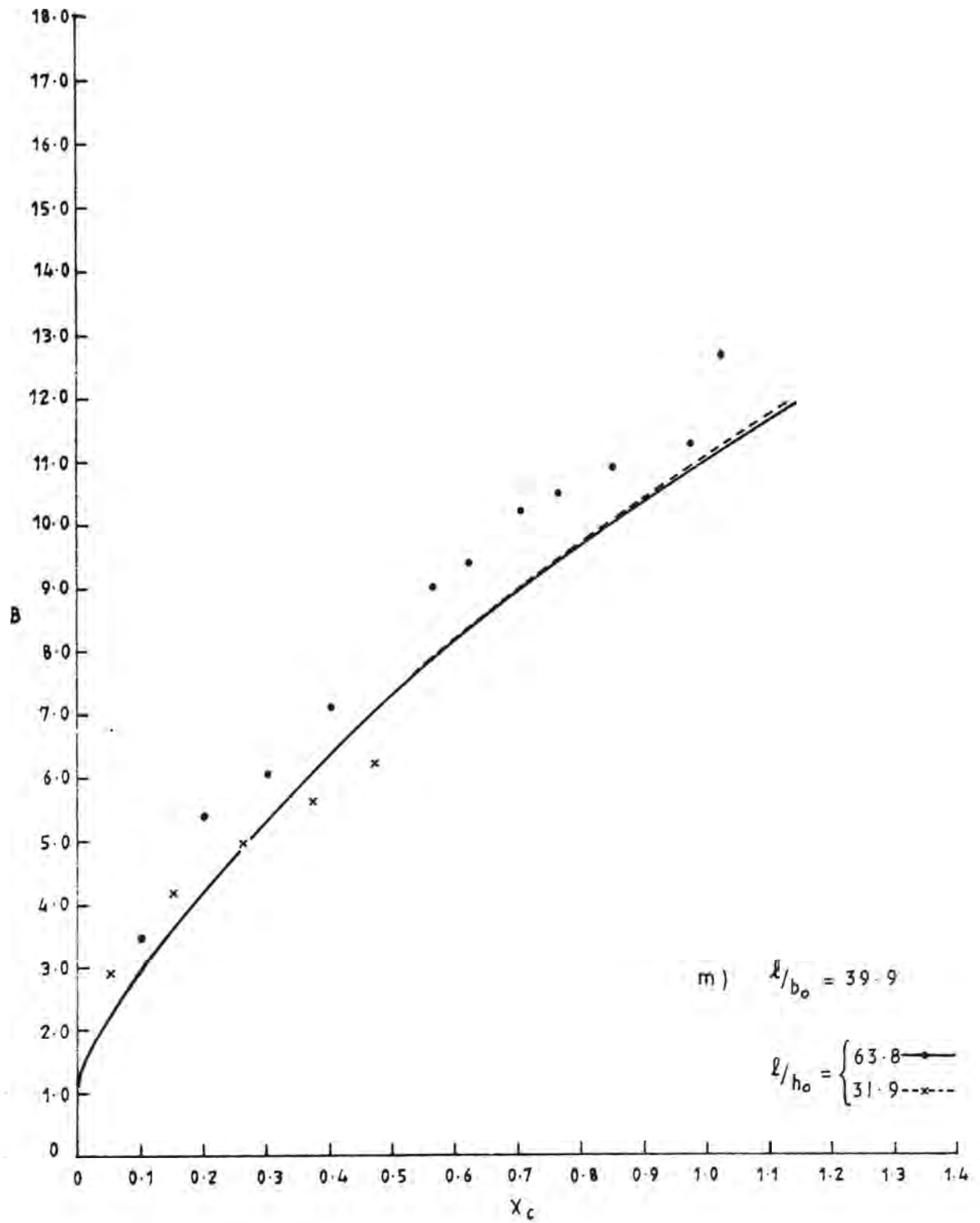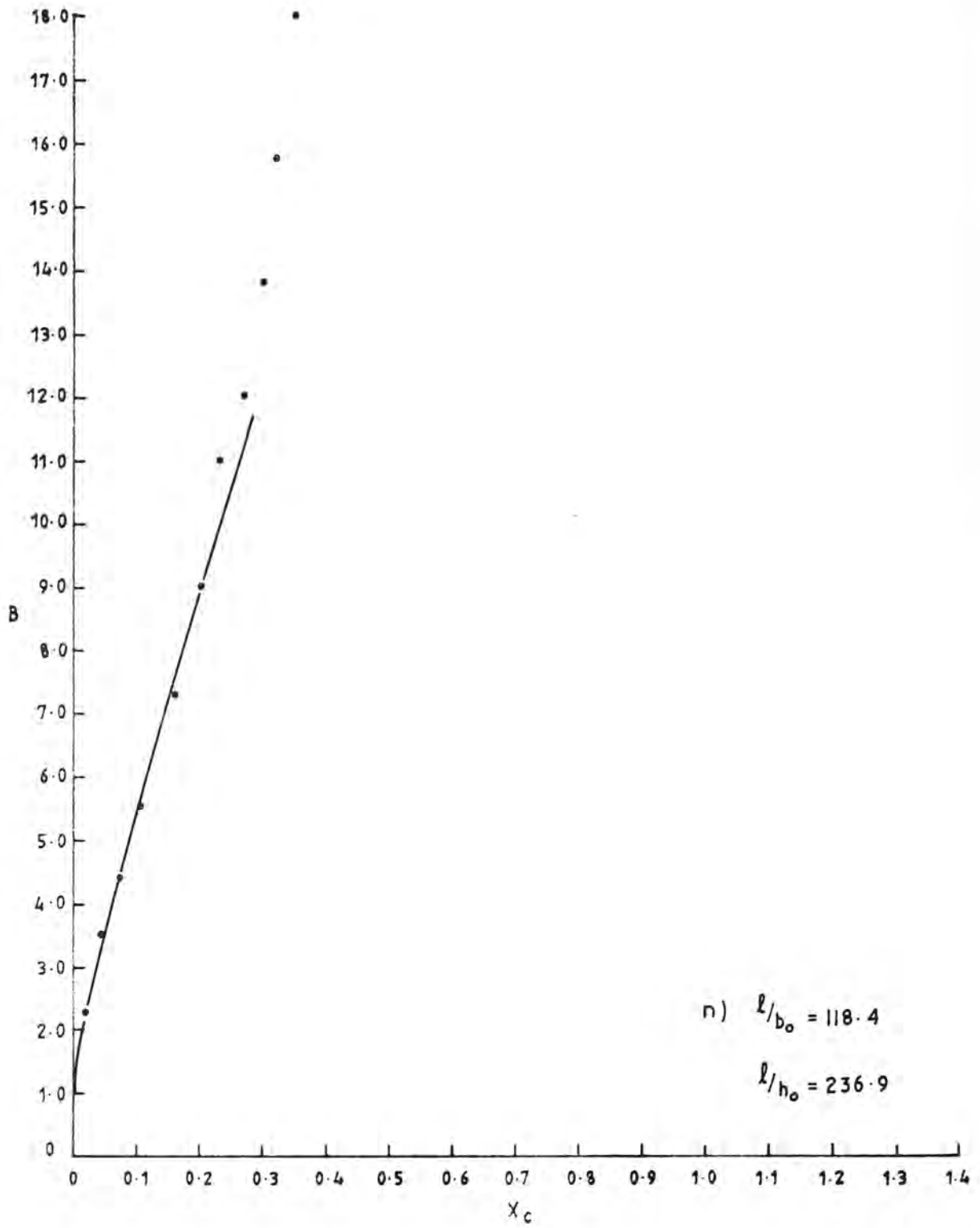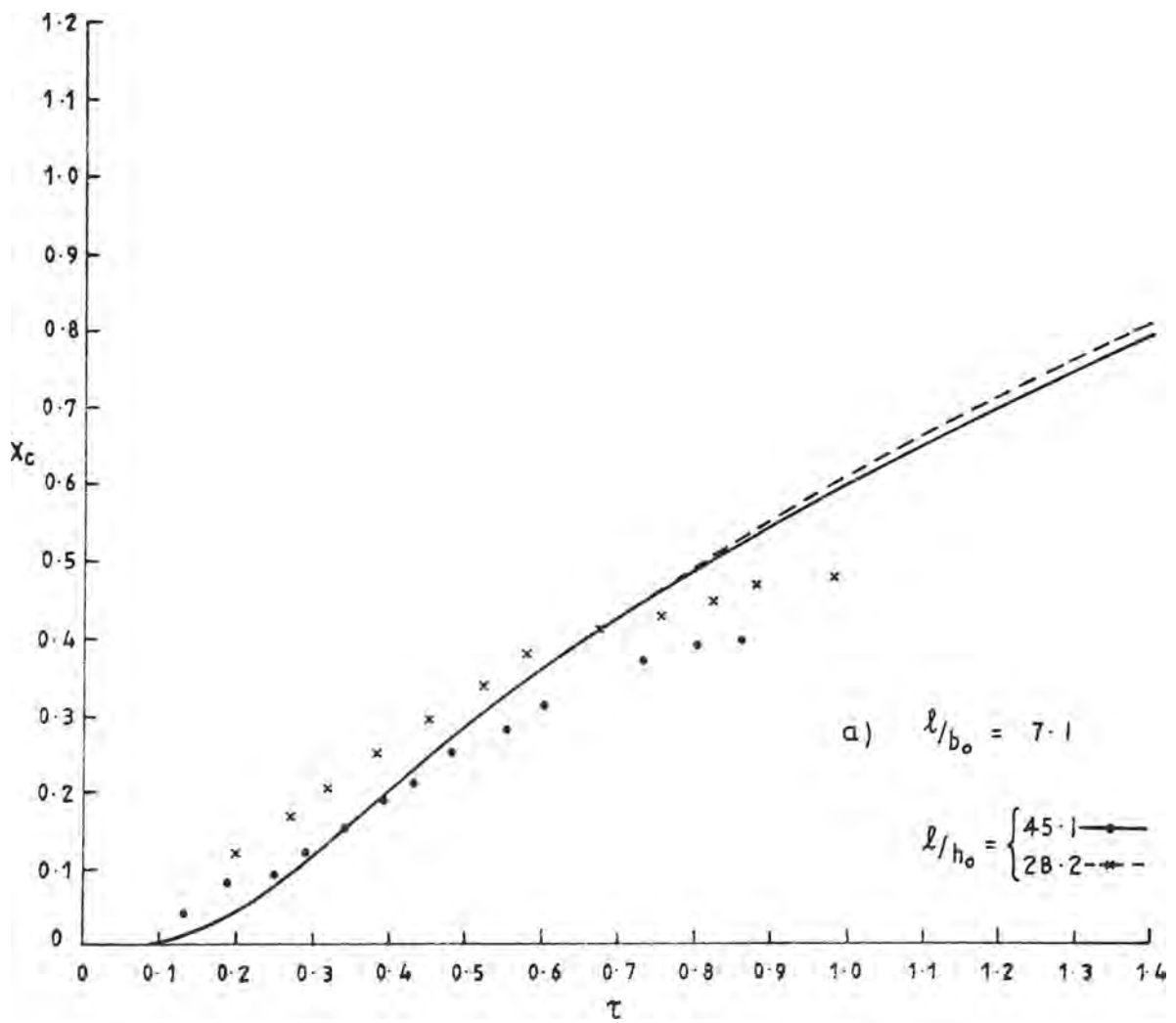
FIGURE A3·6(Cont.)

DIMENSIONLESS DISTANCE FROM THE INLET TO THE
VORTEX PAIR CENTRELINE, X_C, VERSUS DIMENSIONLESS
TIME, τ, FOR VARIOUS INLET WIDTH RATIOS

FIGURE A3·7

FIGURE A3·7 (Cont.)

c) $\ell/b_o = 10.8$

$\ell/h_o = 25.8$

FIGURE A3·7(Cont.)

d) $\ell/b_o = 12.3$

$\ell/h_o = 29.6$

FIGURE A3·7 (Cont.)

FIGURE A3·7 (Cont.)

f) $\ell/b_o = 15.1$

$\ell/h_o = \begin{cases} 36.2 & \rule{1cm}{0.4pt}\!\bullet\!\rule{1cm}{0.4pt} \\ 29.6 & \text{---}\times\text{---} \\ 14.8 & \text{---}\circ\text{---} \\ 7.4 & \cdots\triangle\cdots \end{cases}$

FIGURE A3·7 (Cont.)

g) $\ell/b_o = 16 \cdot 6$

$\ell/h_o = 6 \cdot 6$

FIGURE A3·7(Cont.)

h) $\ell/b_o = 18 \cdot 9$

$\ell/h_o = 60 \cdot 4$

FIGURE A3·7 (Cont.)

FIGURE A3·7 (Cont.)

j) $\ell/b_o = 24.7$

$$\ell/h_o = \begin{cases} 118.4 \text{ —●——} \\ 59.2 \text{ --×--} \end{cases}$$
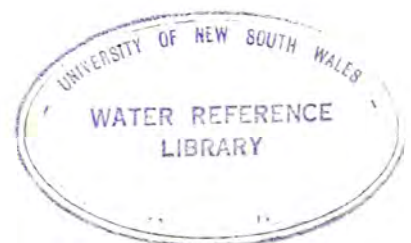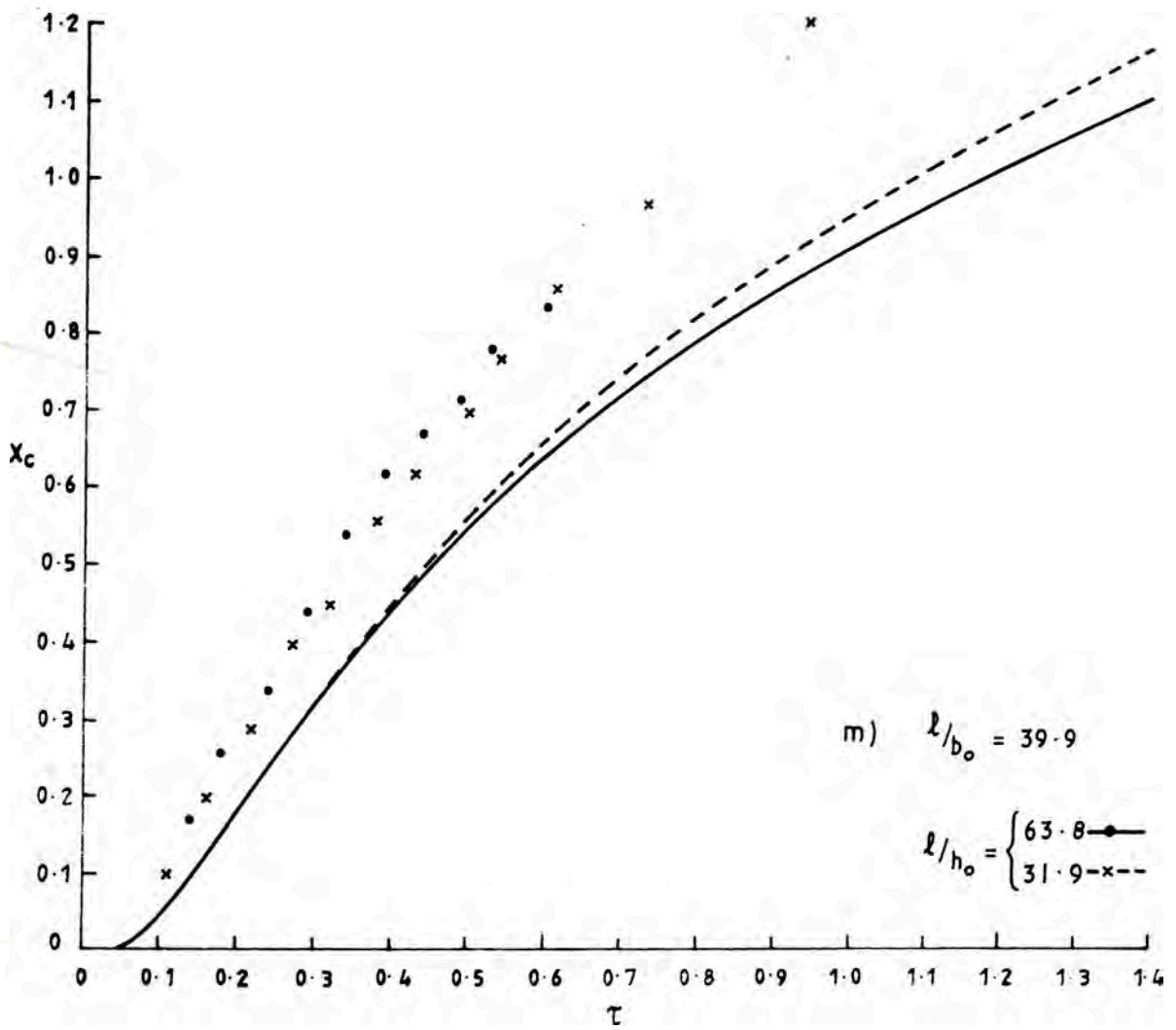
FIGURE A3·7 (Cont.)

k) $\ell/b_o = 32.8$

$\ell/h_o = 52.4$

FIGURE A3.7(Cont.)

FIGURE A3·7(Cont.)

m) $\ell/b_o = 39 \cdot 9$

$\ell/h_o = \begin{cases} 63 \cdot 8 \text{—} \bullet \text{—} \\ 31 \cdot 9 \text{—} \times \text{—} \end{cases}$

FIGURE A3·7(Cont.)

n) $\ell/b_o = 118.4$

$\ell/h_o = 236.9$

FIGURE A3·7(Cont.)